

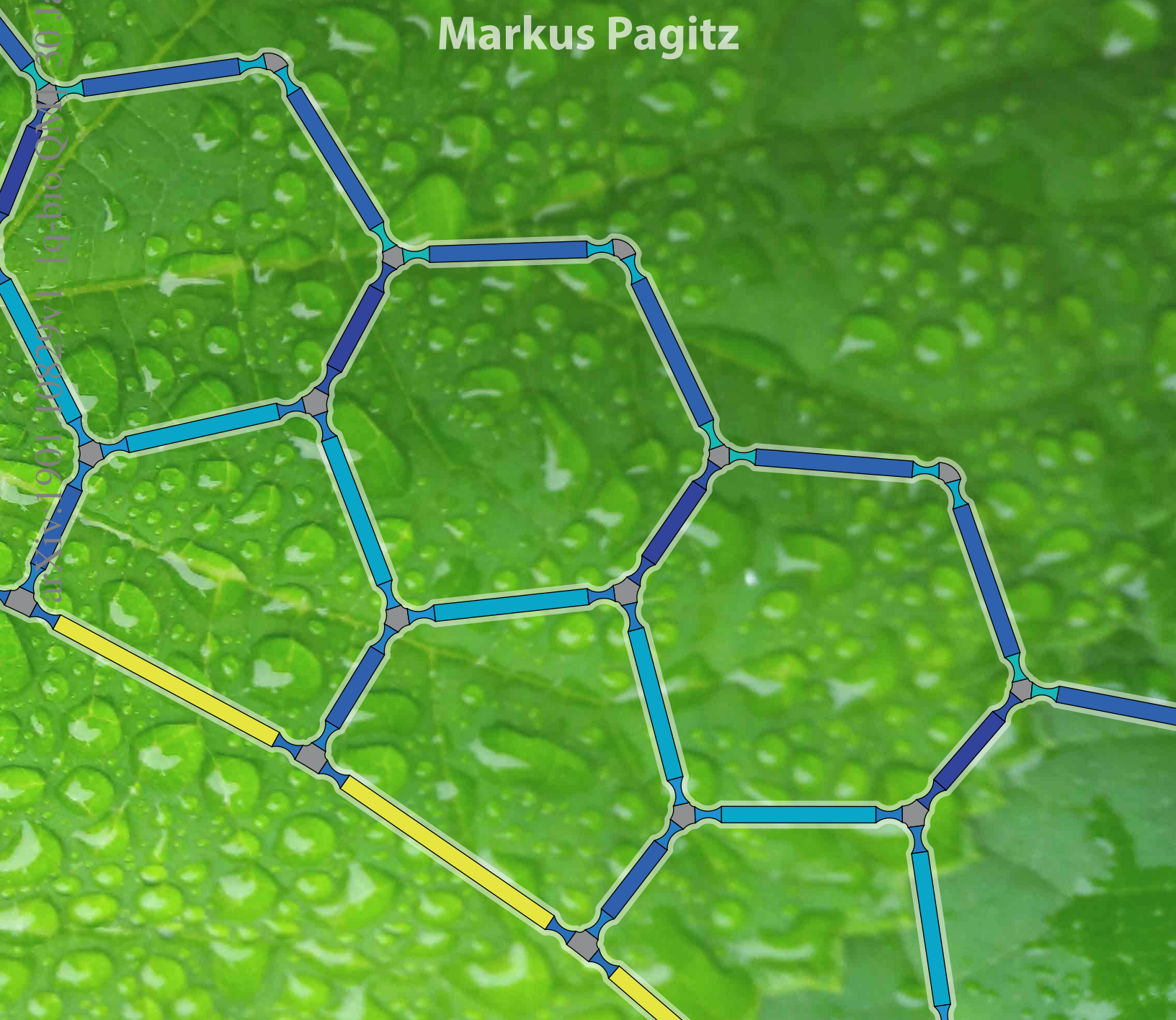


University of Stuttgart
Aerospace Engineering

Pressure Actuated Cellular Structures

Markus Pagitz

1901-10823v1 [q-bio.QN] 30 Jan 2019



The reasonable man adapts himself to the world;
the unreasonable one persists in trying to adapt the world to himself.
Therefore all progress depends on the unreasonable man.

George Bernard Shaw



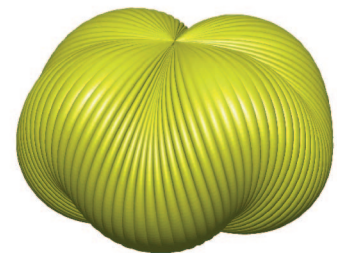
No students were used
or harmed in the
making of this thesis.

Preface

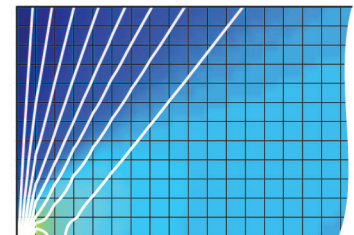
During my studies for a PhD at the University of Cambridge I have worked on the development of NASA's superpressure balloons. These balloons can partially replace satellites and serve as platforms for long-term high altitude experiments. The development of this technology started in the 1990s and was severely hindered for more than a decade by stability problems. My main contribution to this project was a re-designed cutting pattern that increased stability by up to 300 % without increasing the overall weight and membrane, tendon stresses [211, 212, 217, 223, 224]. A NASA balloon with a diameter of 80 m that is based on this design made a record flight above Antarctica in 2009. I received a research fellowship at St John's College, Cambridge for my work in this area. Google currently investigates the use of these balloons to establish a global, low cost access to the internet.

After my PhD I have been on the lookout for a new problem. I experimented, among others, with tensegrity structures and tension field theory. During that time I have developed a multi-grid approach for the simulation of wrinkled membranes [213]. This approach is capable of matching the analytical tension field of a rectangular membrane for pure shear deformations in the whole domain. Another result from that period is an algorithm for the form finding of tensegrity structures that is fast, robust and possesses an asymptotic quadratic convergence rate [221].

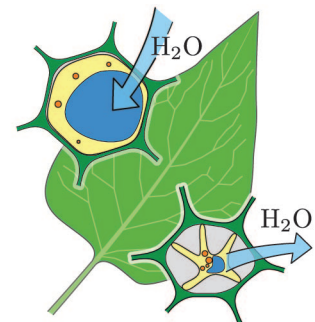
Subsequent to my time as a Research Fellow I have worked at TU Delft as an Assistant Professor. I was still on the lookout for a new problem when I started to investigate the nastic movement of plants. What was supposed to be a short stint turned out to be a problem that kept me occupied for more than seven years. During that time I have found that it is possible to create complex mechanisms by combining independently pressurized rows of specifically tailored prismatic cells [214, 215, 216, 218, 219, 220, 222]. A key advantage of this approach is the complete fusion between actuators and mechanisms. Pressure actuated cellular structures are lightweight, strong and capable of considerable shape changes. These properties make them particularly attractive



superpressure balloons



wrinkling of membranes



shape changing structures

for the aerospace industry that requires advanced high lift devices. At this point I moved from TU Delft to the German Aerospace Agency in Braunschweig to build a number of prototype mechanisms and to investigate various manufacturing techniques. However, I started to miss the rigor and relevance of an academic environment. Therefore, I am indebted to Professor Ricken for giving me the opportunity to write my postdoctoral thesis about pressure actuated cellular structures at the University of Stuttgart.

Abstract

A large number of important developments were initiated at the beginning of the last century by a series of manned flights with controlled airplanes. The underpowered vehicles that were used during these early days were mostly constructed from wood and textiles. Despite these humble beginnings, airplanes with a range of more than 40,000 km, a maximum speed of more than 7,000 km/h and a flight ceiling above the von Kármán line at 100 km were constructed within a century after these first flight attempts.

In view of these advancements, it is remarkable that the development approach for airplanes remained largely unchanged. Passenger airplanes still consist of a cylindrical fuselage, wings, high lift devices, engines and control surfaces that are, as far as possible, independently developed and manufactured. The performance improvements that were achieved so far are mostly driven by the steady improvement of individual components. With regard to airplane structures, these improvements are based on the availability of new materials and the development of computer aided simulation and manufacturing techniques.

Potential improvements that can be achieved by a decoupled optimization of individual components are largely exploited. This is reflected by the latest generation of passenger airplanes that achieved only a slight reduction of noise emissions and fuel consumptions while cruise speeds remained largely unchanged. On the other hand, fuel costs, passenger volumes and population densities around airports increase steadily. This puts additional pressure on the airplane industry as current noise and pollutant emissions are critically viewed by a large part of the general public.

It is likely that the improvements needed to counter these trends can only be achieved by an integral consideration of different airplane components. A fusion between high lift devices and wings seems to be particularly promising in this regard. The use of shape changing, gapless high lift devices that are tightly integrated into the wings would not only reduce the noise emissions during takeoff and landing but additionally

enable the use of advanced technologies that improve the laminarity of the airflow. These technologies have the potential to increase the lift to drag ratio of wings and thus to reduce the weight and fuel consumption of airplanes.

In contrast, the noise emissions and fuel consumption of military airplanes are not a main concern. More important are their flight speeds and stealth properties as they determine their survivability. A large part of the radar reflections of modern fighter jets and bombers can be traced back to discontinuities in their skins at component boundaries. As a consequence, stealth properties can only be significantly improved by a fusion of neighbouring components. For example, the use of gapless high lift devices would be beneficial as it eliminates many of the gaps that can be found in current airplane skins.

Similar to modern airplanes, commonly used high lift devices consist of several subcomponents that are, as far as possible, independently developed and manufactured. Aerodynamically shaped rigid bodies are connected to a wing at discrete points via simple mechanisms. Their positions are controlled by linear or rotary hydraulic or electric actuators. These punctual connections are disadvantageous as they prevent the rigid bodies from contributing to the wings stiffness and load carrying capacity.

The realization of gapless high lift devices requires skins that are stiff enough to carry the aerodynamic loads and soft enough to undergo the required shape changes. It is usually only possible to satisfy these conflicting demands with the help of complex mechanisms that tightly support the skins. This is one of the reasons why previously developed gapless high lift devices that are based on a separate consideration of actuators, skins and mechanisms are too heavy.

The development of a novel concept for gapless high lift devices that fuses actuators and mechanisms into a single structure is thus indispensable. The nastic movement of plants that is based on the pressure driven shape changes of a large number of cells with individually tailored geometries is subsequently used as a source of inspiration. A main advantage of these “pressure actuated cellular structures” is that they can be manufactured from a single piece of material that can range from plastics over composites and metals to ceramics. The cell sides of these structures are relatively thin as the pressure induced tension forces usually eliminate compression forces due to external loads. Furthermore, their stiffness and shape can be independently varied.

The design and manufacturing of structures that consist of a large number of three-dimensional cells with individually tailored geometries

and pressures is difficult. It is therefore of great advantage that the cell geometries and their pressure supplies can be greatly simplified for prismatic high lift devices. The pressure actuated cellular structures that are considered in this thesis are based on individually pressurized rows of prismatic cells that are connected to each other. These structures can be efficiently manufactured from fiber reinforced composites with the help of modern manufacturing techniques.

This postdoctoral thesis starts by reviewing the historic development of airplane structures and high lift devices from an engineering point of view. However, the main purpose of this document is the development of a novel concept for shape changing, gapless high lift devices that is inspired by the nastic movement of plants. A particular focus is put on the efficient simulation and optimization of compliant pressure actuated cellular structures.

Zusammenfassung

Die rasante Entwicklung der Luft- und Raumfahrt wurde zu Beginn des letzten Jahrhunderts durch eine Reihe von kurzen, bemannten Flügen eingeleitet. Die dafür verwendeten, untermotorisierten Fluggeräte, welche vorwiegend aus Holz und Textilien gefertigt wurden, waren nur sehr schwer zu kontrollieren. Seit diesen bescheidenen Anfängen wurden Flugzeuge mit einer Reichweite von mehr als 40,000 km, einer Maximalgeschwindigkeit von mehr als 7,000 km/h und einer Flughöhe von mehr als 100 km gebaut.

In Anbetracht dieser gewaltigen Fortschritte ist es bemerkenswert, dass sich der Ansatz für die Gesamtentwicklung vor allem von Passagierflugzeugen nur unwesentlich verändert hat. Moderne Passagierflugzeuge bestehen nach wie vor aus zylindrischen Rümpfen, Tragflächen, Hochauftriebssystemen, Triebwerke und Leitwerke, welche so weit wie möglich unabhängig voneinander entwickelt und hergestellt werden. Die bisher erzielten Leistungssteigerungen gehen daher vorwiegend auf die stetigen Verbesserungen einzelner Komponenten zurück. Bezüglich der Flugzeugstrukturen wurde dies vor allem durch den Einsatz neuer Metalllegierungen, Faserverbundwerkstoffen und der Entwicklung von rechnergestützten Simulationswerkzeugen und Fertigungsverfahren erreicht.

Das Potenzial einer entkoppelten Betrachtung einzelner Komponenten ist jedoch weitgehend ausgeschöpft. Dies spiegelt sich vor allem in den stagnierenden Reisegeschwindigkeiten, moderaten Lärmreduktionen und Treibstoffeinsparungen der letzten Flugzeuggenerationen wieder. Auf der anderen Seite steht ein zunehmendes Fluggastaufkommen, eine Verdichtung der Bevölkerung in der Nähe von Flughäfen und steigende Treibstoffkosten. Des Weiteren sinkt die Akzeptanz der Bevölkerung gegenüber Lärm- und Schadstoffemissionen, was eine beträchtliche Verbesserung von Flugzeugen erforderlich macht.

Derart weitgehende Verbesserungen sind wahrscheinlich nur durch eine integrale Betrachtung verschiedener Flugzeugkomponenten möglich. Am vielversprechendsten erscheint im Moment die Fusion von Hochauftriebssystemen und Tragflächen zu sein. Der Einsatz von formvariablen,

spaltfreien Hochauftriebssystemen welche formschlüssig mit den Tragflächen verbunden sind würde nicht nur die Lärmemissionen besonders während der Start- und Landephase reduzieren, sondern auch den Einsatz neuartiger Technologien ermöglichen, welche die Laminarität der Flügelumströmung verbessern und damit den Treibstoffverbrauch senken.

Eine ähnliche Entwicklung hat im militärischen Flugzeugbau stattgefunden, wo die Überlebensfähigkeit von Flugzeugen zunehmend von ihrer Radartarnung abhängt. Auch hier führten die bisherigen Entwicklungen dazu das weitere, signifikante Fortschritte nicht mehr nur durch die Optimierung einzelner Komponenten erzielt werden können. Ein großer Teil der Radarreflektionen von modernen Kampfflugzeugen haben ihren Ursprung an den Spalten und Kanten der Flugzeughüllen. Die Entwicklung von spaltfreien Hochauftriebssystemen ist daher auch hier von zentraler Bedeutung.

Die gängigen Hochauftriebssysteme moderner Flugzeuge bestehen, wie auch die Flugzeuge selbst, aus Subkomponenten welche so weit wie möglich unabhängig voneinander entwickelt und hergestellt werden. Aerodynamisch geformte Starrkörper sind über relativ einfache Mechanismen an einzelnen Punkten mit den Tragflächen verbunden und werden mithilfe hydraulisch oder elektrisch betriebener Aktuatoren ein- und ausgefahren. Diese punktuelle Verbindung zwischen Hochauftriebssystemen und Tragflächen hat den Nachteil, dass Hochauftriebssysteme in der Regel nur unwesentlich zur Lastabtragung und Steifigkeit der Tragflächen beitragen.

Die Realisierung formvariabler, spaltfreier Hochauftriebssysteme erfordert Flugzeughäute die steif genug sind, um die aerodynamischen Lasten ohne große Verformungen zu tragen und elastisch genug sind um die benötigten Formänderungen zu ermöglichen. Diese gegensätzlichen Anforderungen können in der Regel nur mithilfe komplexer Mechanismen erfüllt werden welche die Flugzeughäute an zahlreichen Stellen unterstützen beziehungsweise versteifen. Dies ist einer der Hauptgründe, warum bisherige Hochauftriebssysteme welche auf einer Trennung zwischen Flugzeughäuten, Mechanismen und Aktuatoren basieren in der Regel deutlich zu schwer sind.

Die Entwicklung eines neuen Konzepts für spaltfreie Hochauftriebssysteme, welches das Gesamtgewicht durch eine Fusion von Mechanismen und Aktuatoren signifikant reduziert, ist daher unumgänglich. Als Vorbild hierfür dient im Folgenden die nastische Bewegung von Pflanzen. Diese basiert auf den Gestaltsänderungen einer großen Anzahl von komplex geformten, dreidimensionalen Zellen, welche durch relative Zell-druckänderungen hervorgerufen werden. Ein Hauptvorteil dieser "Druck

Aktuierten Zellulären Strukturen” ist das sie in einem Stück und je nach Einsatzzweck aus verschiedenen Materialien gefertigt werden können. Des Weiteren werden Instabilitäten durch Druck induzierte Vorspannungen weitgehend verhindert, was den Einsatz dünner und dadurch leichter Zellwände ermöglicht. Weitere Vorteile liegen in einer veränderlichen, druckabhängigen Steifigkeit und der möglichen Zirkulation und Temperierung des Druckmediums um Vereisungen an einer Hochauftriebsfläche vorzubeugen.

Die Herstellung von dreidimensionalen Zellstrukturen, deren Zelldrücke einzeln geregelt werden ist schwierig. Es ist daher von großem Vorteil das die Zellgeometrien sowie deren Bedruckung für den Einsatz in prismatischen Hochauftriebssystemen beträchtlich vereinfacht werden können. Dies ermöglicht die Nutzung von miteinander verbundenen prismatischen Zellen, welche unter anderem mit modernen Webverfahren aus Faserverbundwerkstoffen in nahezu beliebigen Längen hergestellt werden können.

Diese Habilitationsschrift gibt einen Einblick in die geschichtliche Entwicklung von im Flugzeugbau gebräuchlichen Strukturkonzepten und Hochauftriebssystemen. Ein besonderer Schwerpunkt wird hierbei auf die verwendeten Mechanismen und Aktuatoren gelegt. Das Hauptziel dieser Arbeit liegt jedoch in der Entwicklung eines neuartigen Konzepts für formändernde, spaltfreie Hochauftriebssysteme, welches auf dem Funktionsprinzip von nastischen Pflanzen basiert. Besonderes Augenmerk wird hierbei auf die Entwicklung eines effizienten Ansatzes für die Simulation und Optimierung von “Druck Aktuierten Zellulären Strukturen”gelegt. Es wird gezeigt das diese Strukturen eine Reihe von Vorteilen besitzen, die sie für einen möglichen Einsatz in zukünftigen Hochauftriebssystemen prädestinieren.

Contents

Preface	i
Abstract	iii
Zusammenfassung	vii
1 Motivation	1
2 Structures	5
2.1 Concepts	5
2.1.1 Spaceframe	5
2.1.2 Semi-Monocoque	6
2.1.3 Monocoque	7
2.2 Materials	9
2.2.1 Wood	9
2.2.2 Metals	10
2.2.3 Composites	11
3 Actuators	13
3.1 Mechanical Actuators	14
3.1.1 Electromechanical	14
3.1.2 Pressure	15
3.2 Solid State Actuators	16
3.2.1 Piezoelectric and Piezomagnetic	17
3.2.2 Electrostrictive and Magnetostrictive	18
3.2.3 Electrostatic and Magnetostatic	18
3.2.4 Ionic	19
3.2.5 Phase Transition	20
3.2.6 Thermal	22
3.2.7 Swelling and Shrinking	23
4 Mechanisms	25
4.1 Mechanism Design	25
4.1.1 Complexity of Actuators and Mechanisms	25
4.1.2 Kinematic Pairs and Links	26

4.2	Conventional High Lift Devices	27
4.2.1	Leading Edge	27
4.2.2	Trailing Edge	29
4.3	Gapless High Lift Devices	30
4.3.1	Leading Edge	31
4.3.2	Trailing Edge	32
5	Skins	35
5.1	Poisson's Ratio	36
5.1.1	Material	36
5.1.2	Geometry	37
5.2	Leading Edge	38
5.3	Trailing Edge	39
5.3.1	Sandwich	40
5.3.2	Corrugated Shell	40
5.4	Variable Stiffness	41
5.4.1	Material	41
5.4.2	Friction	43
5.4.3	Geometry	43
6	Plant Movements	45
6.1	Automatic Movements	46
6.1.1	Passive Movements	46
6.1.2	Active Movements	49
6.2	Stimulated Movements	52
6.2.1	Tropisms	52
6.2.2	Nastic Movements	53
6.3	Cell Components	55
6.3.1	Geometry	56
6.3.2	Material	57
6.3.3	Cytoskeletons	59
6.3.4	Subcellular Motor	60
7	Biomimetics	63
7.1	Pressurized Cellular Structures	63
7.1.1	Beams	64
7.1.2	Plates	67
7.1.3	Shells	69
7.2	Pressure Actuated Cellular Structures	70
7.2.1	Potential	70
7.2.2	Shape Changing Modules	72
7.2.3	Application Range	73

8 Geometric Model	77
8.1 Corner Angles	78
8.1.1 Global State Variables	78
8.1.2 Pentagonal Cells	79
8.1.3 Triangular Cells	80
8.1.4 Transformation Matrices	81
8.2 Corner Geometries	82
8.2.1 Global State Variables	82
8.2.2 Local State Variables	82
8.2.3 Dependent Variables	83
8.2.4 Optimal Cell Corner Dimensions	83
8.3 Side Geometries	86
8.3.1 Global State Variables	86
8.3.2 Local State Variables	86
8.3.3 Dependent Variables	87
8.4 Summary	87
8.4.1 State Variables	87
8.4.2 Dependent Variables	88
8.4.3 Special Cases	88
9 Mechanical Model	89
9.1 Cell Side Deformations	90
9.1.1 Global State Variables	90
9.1.2 Local State Variables	91
9.1.3 Dependent Variables	92
9.2 Mechanical Properties	92
9.2.1 Global State Variables	92
9.2.2 Local State Variables	93
9.2.3 Dependent Variables	94
9.3 Summary	95
9.3.1 State Variables	95
9.3.2 Dependent Variables	95
9.3.3 Special Cases	96
10 Simulation	99
10.1 Potential Energy	99
10.1.1 Geometric Primitives	100
10.1.2 Structure	100
10.2 Stationarity	101
10.2.1 Equilibrium Configurations	101
10.2.2 Sensitivities	102
10.3 Target Shapes	103
10.3.1 Residuuum	103
10.3.2 Sensitivities	103
10.4 Optimization	103
10.5 Examples	105

10.5.1 Rigid Body Structures	106
10.5.2 Compliant Structures	114
10.5.3 Potential Improvements	117
11 Additional Topics	121
11.1 Material and Cell Sizes	121
11.1.1 Material Selection	122
11.1.2 Scaling	123
11.2 Cytoskeletons	124
11.2.1 Stiffness	124
11.2.2 Weight	125
11.3 End Caps	126
12 Conclusions	129
Nomenclature	133
Appendix	137
Distractions	137
Cantilever	139
Geometry	141
Bibliography	145

Chapter 1

Motivation

The first powered and controlled flights over very short distances in a heavier than air machine were most likely undertaken in 1901 by the German Gustave Weißkopf. Since then, airplanes were developed with a range of more than 40,000 km, a maximum speed of more than 7,000 km/h and a ceiling above the von Kármán line at 100 km that represents, by definition, the boundary between the Earth's atmosphere and outer space. Today, flying is one of the safest modes of transport where civil airplanes such as the Airbus A380 carry routinely more than 850 passengers over distances of up to 15,000 km at a travel speed of 900 km/h.

More than a century of research and development led to airplane structures that optimally combine existing materials, structural concepts and manufacturing techniques. The topology of a Boeing 777 wing that made its maiden flight in 1994 was optimized by Aage et al [1] in 2017. They discretized the wing with more than one billion voxels and achieved a potential weight reduction of 2-5% compared to the flight proven wing. However, it is currently not possible to economically manufacture the complex geometry of such a wing. The small potential weight savings that were found in this study are remarkable and a testimony of the maturity of modern airplane structures. As a consequence, significant performance improvements can only be achieved by using new technologies or an integral consideration of existing actuators, manufacturing techniques, materials, mechanisms and structures. Furthermore, solely reducing the weight of an airplane is not necessarily optimal. More important optimality criterions are, for example, the fuel consumption, noise emissions, maintenance requirements and stealth properties.

New technologies such as carbon fiber reinforced composites were widely introduced in the latest generation of civil airplanes to further reduce their overall weight [268]. As it appears today, one of the largest

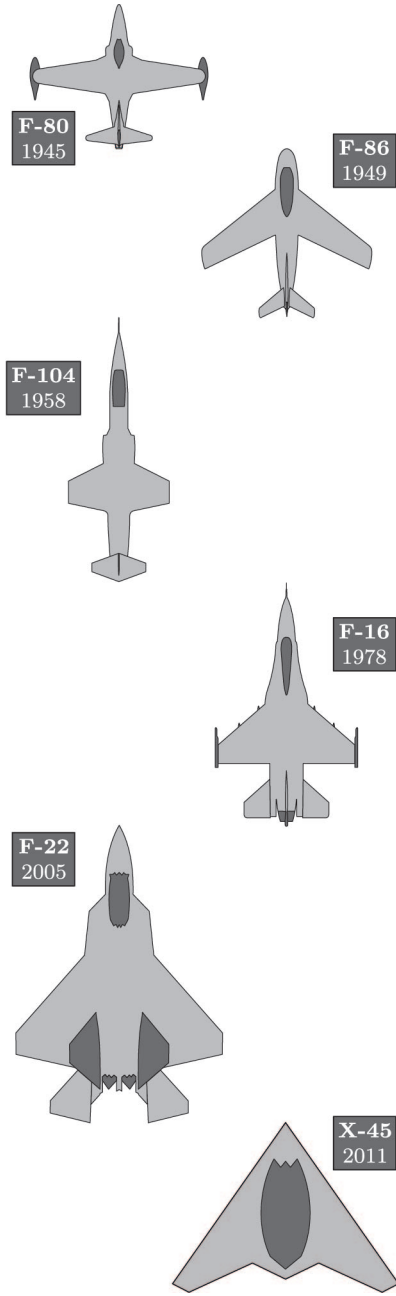


Figure 1.1: Typical airplane shapes during the last seven decades. Sixth generation fighter airplane will most likely be unmanned.

potential performance improvements in upcoming civil and military airplane generations might be achieved by a tight integration of high lift devices into the wing structures. This is highlighted by the development history of fighter jets that started towards the end of World War II with propeller machines that were upgraded with simple jet engines [171] as illustrated in Figure 1.1. Aerodynamic improvements during the last seven decades were mostly driven by the rapid development of computers that allowed the use of unstable designs. The relaxation of current design constraints is continued by the shift towards unmanned airplanes [74] with advanced stealth properties [104] and electronics. On the other hand, changes in the structural design were not as radical. For example, control surfaces are still rigid bodies that require gaps in an airplanes skin and thus create a source of radar reflections [135]. This is an increasingly big problem since these gaps limit an airplanes stealth properties and thus its survivability [17]. Hence, the development of technologies that minimize their impact is vital. One of the most promising approaches in this direction is the use of shape changing structures that avoid these gaps altogether.

In contrast, the radar signature of civilian airplanes is unimportant as long as they can be securely detected at all times. The weight and aerodynamic conditions of civilian airplanes differ significantly during takeoff, cruise and landing. As a consequence, their wing shapes are usually designed for average flight conditions during the cruise phase and additional high lift devices are deployed during low flight speeds to increase their lift. However, this approach is disadvantageous as the gaps between the wings and high lift devices increase noise emissions during takeoff and landing. This is a large problem for most airport operators due to the increasing number of flights and population densities. Furthermore, the joints between wings and high lift devices increase the turbulence of the flow during cruise and thus the fuel consumption. This was demonstrated by the flight testing of a Gulfstream III in 2014 that was retrofitted with shape changing, gapless trailing edges [157]. These flights indicated potential fuel savings of up to 10% and noise reductions during landings of up to 40%. The civilian airplane industry is highly competitive and economically driven. Nonetheless it is relatively conservative due to the increased passenger risk that comes with the introduction of new, safety critical technologies. On the other hand, the benefits of using shape changing structures in unmanned aerial vehicles is significantly higher and the risk for the loss of lives on the operator side is minimal. Hence it is likely that gapless high lift devices will be initially used in military airplanes.

Many applications both within and outside of the aerospace industry would benefit from structures that can continuously change their shapes such that they optimize one or more objectives in a varying environment.

These kind of structures are often referred to as being active, adaptive or even smart. Buzzwords like that are subsequently avoided since they are misleading and not clearly defined. Instead they are referred to as shape changing structures. Many authors have an illusive perception of potential performance improvements that come with the use of shape changing structures. High expectations are usually unrealistic since a shape changing structure is never lighter than an optimal rigid structure. This holds even if the structural loads are reduced by the shape changing capabilities. For example, safety considerations require an airplane to perform a wide range of flight maneuvers with deployed and retracted high lift devices [248]. These failsafe requirements prohibit the utilization of potential load reductions during nominal operations. Hence, the benefits of using a shape changing structure must clearly outweigh its additional complexity, weight and cost. This is reflected in nature by the fact that only a small number of plants are capable of nastic movements. These plants are predominantly found in biotopes with challenging environmental conditions where the exploitation of an additional food source is vital.

The development of new manufacturing techniques particularly in the field of three-dimensional weaving and the exponential growth of computing power enables the fast and inexpensive simulation, optimization and construction of advanced shape changing structures. The availability of these tools led to a point where an engineers competence is often the limiting factor. Competence can be rarely replaced by funding or a large workforce so that progress is often due to individuals. The aim of this postdoctoral thesis is the development of plant inspired shape changing structures. Unlike animals and humans, plants do not possess a central control system. Yet they are capable of fast reversible movements. Their relative simplicity and extremely tight integration of actuators, mechanisms and structures serves in the following as a source of inspiration for the design of future airplane structures.

The layout of this thesis is as follows: *Chapter 2* outlines the historic development of airplane structures and materials. It is shown that the underlying ideas were often inspired by nature. *Chapter 3* discusses the application range and limitations of existing actuation principles with regards to shape changing structures. *Chapter 4* reviews the development of high lift devices for airplanes. A particular focus is placed on existing concepts for gapless leading and trailing edges. Many of these concepts utilize rigid skins with a variable stiffness or tailored, soft deformation modes. *Chapter 5* shows that the design of skins that can sustain large strains and temperature differences as well as lightning and bird strikes is far from trivial. *Chapter 6* points out that nature often utilizes a tight integration of actuators, mechanisms and structures. Nastic plants are particularly outstanding as they have reached

a level of integration that makes a differentiation between their components nearly impossible. **Chapter 7** translates the working principle of nastic plants into a novel concept for pressure actuated cellular structures with a prismatic cross section. **Chapter 8** introduces a minimal set of state variables that are needed to describe the cross sectional geometry of compliant pressure actuated cellular structures. **Chapter 9** shows that the geometric model can be tightly coupled to a numerical model that is based on rigid cell sides, cell corners and rotational, axial springs. **Chapter 10** demonstrates by means of several examples that these models can be efficiently used for the simulation and optimization of compliant pressure actuated cellular structures. **Chapter 11** discusses various additional topics that range from the sealing of cells over subcellular structures to an optimal selection of cell sizes and materials. Finally, **Chapter 12** concludes this thesis.

Chapter 2

Structures

Architecture is the art of designing and building structures for habitats. Vitruvius [247] wrote in the 1st century BC that a good structure should be durable, suitable for the purpose and aesthetically pleasing. Durability and utility is easy to define but it is considerably harder to find optimality criteria for beauty. Engineers are thus fortunate that the design of structural components in aerospace, civil and mechanical engineering is mostly driven by their intended function. For example, a passenger airplane is usually designed for given flight profiles and cargo properties such that its life-cycle costs are minimal. This is done by taking aerodynamic, control, mass, propulsion and structural considerations into account. These aspects are coupled to each other so that small changes can significantly affect the whole design. Nonetheless, their dependencies can be relaxed by the use of advanced structural concepts and materials that minimize the overall weight of an airplane.

2.1 Concepts

2.1.1 Spaceframe

The symbiosis between structural concepts and the availability of large amounts of inexpensive materials is particularly highlighted by bridges. Nearly all major bridges before the 19th century were made out of stone, a material that can sustain large compression but only small tension forces. The Romans [65] took this into account by using arch like structures that carry the loads solely via compression forces. For example, the Alcántara bridge in Spain is one of the most famous arch bridges that is still fully functional. It was built in 106 AD and has a length of 194 m and a height of 71 m. Other examples include the relatively simple suspension bridges that were used in South America. They were made from ropes that can carry large tension but only small compression forces. As a consequence, their structural concept is based on an

inverted arch.

Large amounts of relatively inexpensive and durable materials that can carry tension as well as compression forces became available during the Industrial Revolution [10]. Furthermore, new manufacturing techniques and joining methods enabled the use of advanced structural concepts. As a consequence, truss bridges that combine tension and compression elements started to be widely used in the 19th century. For example, the first truss bridges in the United States used wood for the compression and iron for the tension elements whereas later bridges were fully made out of iron.

A similar concept was used for the first airplanes that were built from fabric, wood and steel wires. Their fabric covered wings were made out of wooden spars and ribs that defined its cross sectional shape. However, these wings could not sustain their flight loads so that they were supported by external wood struts and steel wires. Fuselages were built in a similar manner by using truss like structures where compression and tension forces were carried by struts and wires, respectively. For example, the Blériot XI that made its maiden flight in 1909 is based on this design principle, Figure 2.1. It was successfully used in many competitions and races and was the first airplane that crossed the English Channel.

2.1.2 Semi-Monocoque

The aerodynamic properties of truss like fuselages were improved by covering them with fabrics. It was soon realized that the tension bearing elements of the truss are redundant if the fabrics are sufficiently stiff and strong. As a consequence, the use of fabrics additionally reduced the weight and complexity of fuselages. The corresponding construction principle where a load carrying skin is supported by transverse frames and longitudinal stringers is known as a semi-monocoque design.

The fabric skins were subsequently replaced by plywood sheets that can carry compression and tension forces as well as out-of-plane bending moments. This further improved the aerodynamic properties and reduced the weight and complexity of the underlying support structure. The Deperdussin Monocoque that made its maiden flight in 1912 was based on such a design. It was the fastest airplane for several years and raised the air speed record for aircraft¹ to 204 km/h.

Biplanes were widely used during the First World War. Their truss like structures between the upper and lower wings increased the stiffness and reduced the overall weight. However, two wings and the additional

¹The speed record for cars was 228 km/h at that time. However, cars were soon eclipsed by airplanes.

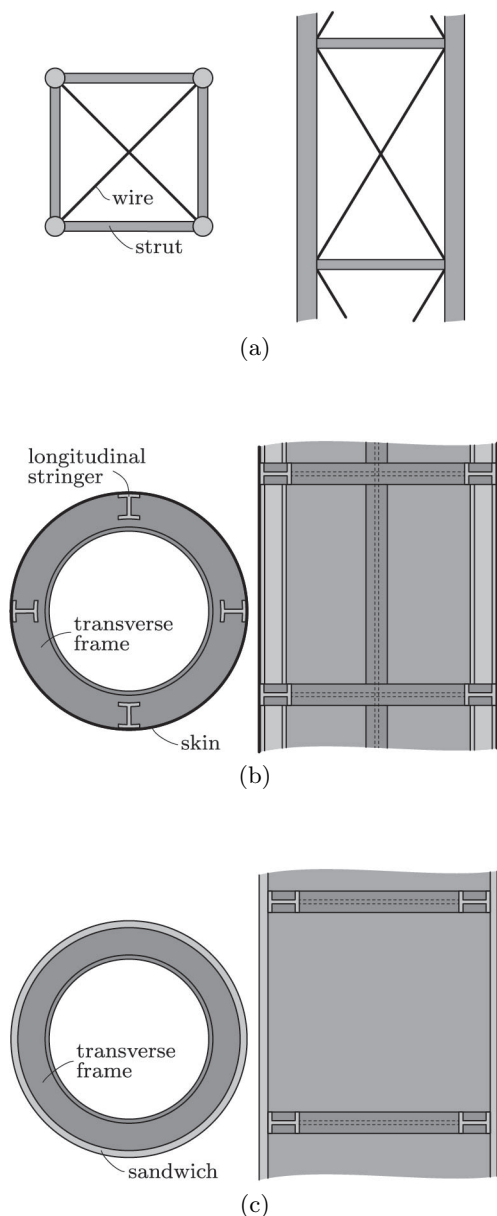


Figure 2.1: Cross sectional and top view of different construction principles for fuselages. (a) Spaceframe, (b) semi-monocoque and (c) monocoque construction.

support structures increased the drag and did not provide twice the lift. This was problematic as improved engines led to higher airspeeds so that aerodynamic requirements became increasingly dominant. As a consequence, monoplanes without external reinforcements were often used instead. This led to considerably higher wing forces that required plywood instead of fabric covered wings.

Semi-monocoque designs are widely used in modern airplanes. Their efficiency stems from the relatively thin skin that is locally supported against out-of-plane deformations such that it can carry most of the airplane loads. Furthermore, the construction and maintenance of semi-monocoque structures is relatively simple due to their clear separation between skins and support structures.

2.1.3 Monocoque

The skins of semi-monocoque designs can sustain large longitudinal forces as long as they are sufficiently supported against out-of-plane deformations. As a consequence, support structures are superfluous if compressive skin forces can be avoided or if their bending stiffness and therefore their resistance against buckling deformations is sufficiently large. Structures that consist of skins that are at most supported by transverse frames are known as monocoque designs.

Pressure Supported Structures

Compressive skin forces can be avoided by the application of sufficiently large prestresses. This approach was already used in the first manned flight of an aircraft that dates back to 1783 when the Montgolfier brothers pressurized their paper based envelope with the help of hot air [211]. To this day, pressure supported structures can be commonly found in aerospace and civil engineering. For example, Atlas rockets [61] can only carry their self weight if all tanks are sufficiently pressurized. Other rockets such as the Falcon 9 can carry their self weight during manufacturing, storage and transport but require pressurized tanks during flights.

Hundreds of pressurized radar domes were used by the United States Air Force during the 1950s [174]. They consisted of an air supported membrane and airlocks that minimized pressure losses during entries and exits as illustrated in Figure 2.2. Current applications of this concept include the Expandable Activity Module of the International Space Station [255] and sport stadiums that span large unobstructed spaces. Air supported buildings are based on a single, pressurized and inhabited space that usually requires a continuous operation of fans and an emergency power supply. In contrast, air inflated buildings are based on a large number of small, self contained and pressurized elements that are connected to each other. Depending on their use, these elements [159]

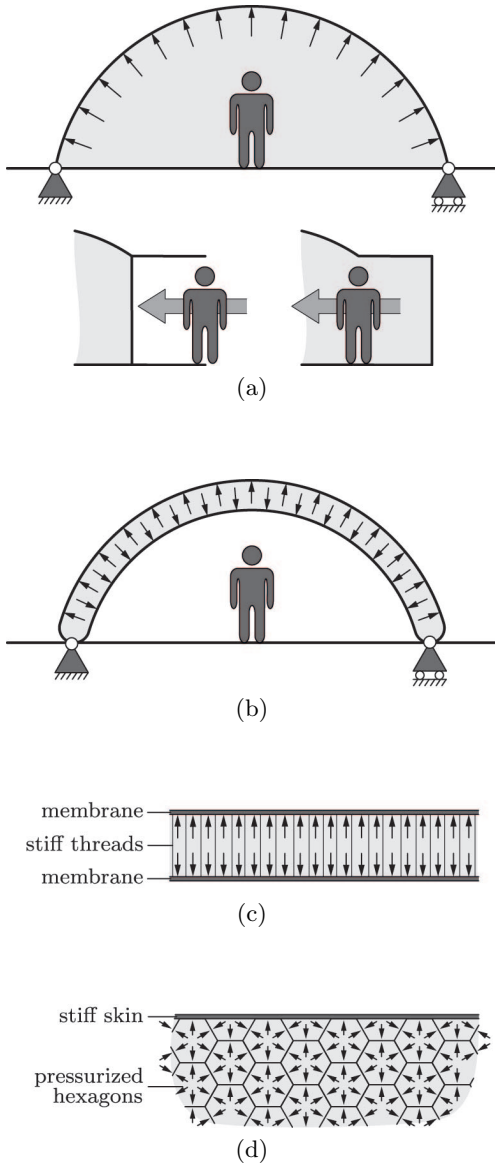


Figure 2.2: Pressure supported (a) membrane with an airlock that minimizes pressure losses. (b) Tubular arch, (c) Airmat and (d) honeycomb like structure.

may or may not be independently pressurized. Basic structural elements for air inflated buildings that are based on straight and curved prismatic tubes were developed by Sumovski [278] in 1893. One of the largest air inflated hangars that consists of these elements is currently operated by Airbus. It has a 23 m high ceiling and covers an area of nearly 6,000 m².

Early work on pressure stiffened wings and fuselages [98] was conducted by Robert Goddard in 1934. However, it took another two decades until the Inflatoplane from the Goodyear Tire & Rubber Company flew for the first time in 1956. The fully inflatable airplane was constructed from pressurized plate and shell like elements that are known as Airmats [101]. They consist of two parallel, airtight membranes that are connected by a large number of stiff threads. These threads preserve the membranes overall shape and carry most of its pressure loads. The Inflatoplane could be tightly packed and inflated by a bottle of compressed air or a manual pump. It was supposed to be dropped behind enemy lines to rescue grounded pilots. However, the work on the Inflatoplane was discontinued due to its limited military use. Nonetheless, Airmats are still widely used in applications that range from mattresses to Zorbing.

The current development of gun launched and air dropped drone swarms [252] created a renewed interest in inflatable wings. They might be used in the near future in conjunction with expendable inflation systems [205] to increase the packing density of drones. Cellular² wings that are based on a honeycomb like arrangement of separately pressurized tubes were proposed by Chutter [49] in 1967. The hexagonal grid of a honeycomb divides a surface into regions of equal area with the least total perimeter [113]. Hence it leads to regular, prismatic structures that can effectively carry internal cell pressures with a minimum amount of material. Modern manufacturing techniques such as the three-dimensional weaving of high strength fibers enable the monolithic construction of pressurized honeycomb wings with tailored cell geometries [46]. Furthermore, an automated integration of threads that support cell sides that are exposed to differential pressures seems to be possible.

Sandwich Structures

Monocoque skins are not supported in the longitudinal direction so that they are prone to buckling if exposed to compressive forces. As a consequence, they require an increased bending stiffness that limits their out-of-plane deformations. The efficiency of monocoque designs thus depends on the tradeoff between the additional weight that comes with

²The word “cell” was coined by Robert Hooke [131] in his book *micrographia* [125] that was published in 1665. He noticed the similarities between the structure of cork [97] and the cells that are inhabited by Christian monks in monasteries.

an increased skin stiffness and the savings that can be made due to the use of simpler support structures. Hence, it is essential to design mono-coque skins such that their in-plane stiffness is preserved while their out-of-plane stiffness is maximized for a given weight constraint.

Lightweight skins with a large in- and out-of-plane stiffness can be created by a combination of stiff face sheets and honeycomb cores that provide closely spaced supports against out-of-plane deformations [5]. Their use in airplane structures [141] was patented by Junkers in 1915. However, the connection between face sheets and cell cores turned out to be a major problem so that the Junkers J.I. [145] used corrugated metal sheets instead, Figure 2.3. The de Havilland Airplane Company circumvented these problems by gluing sheets of plywood to a lightweight balsa core, a naturally occurring material with a honeycomb like structure [29]. Their Mosquito airplane that was almost entirely made out of wood was one of the fastest operational airplanes at its introduction in 1941.

The remarkable performance of the Mosquito can be attributed to its superior structural concept. However, the balsa cores susceptibility to moisture led to weight increases, bonding problems and a degradation of mechanical properties in humid environments. This hindered the widespread use of the Mosquito during the Second World War particularly in the Pacific theater. Water ingress and condensation is still a big problem of modern honeycomb sandwich structures [257]. This is a reason why their use is commonly restricted to secondary airplane structures such as interior designs, fairings and control surfaces [123]. As a consequence, current developments focus on folded cores that ensure a sufficient ventilation through the introduction of drainage channels [120].

2.2 Materials

2.2.1 Wood

Wood is a widely available and inexpensive material that was used by humans at all times. It possesses anisotropic material properties and can carry relatively large tension and compression forces in the direction of its fibers. Selected lumbers reach the specific strength and modulus of aluminium alloys that were available in the first half of the twentieth century so that it is not surprising that early airplane structures were made out of wood. However, this changed in the second half of the twentieth century where the development of new alloys incrementally doubled the yield strength of aluminium [40]. The specific strength and modulus of various materials are summarized in Figure 2.4.

The lamination of several layers of veneer with glue was proposed by Samuel Bentham in 1797. The mechanical properties of this composite

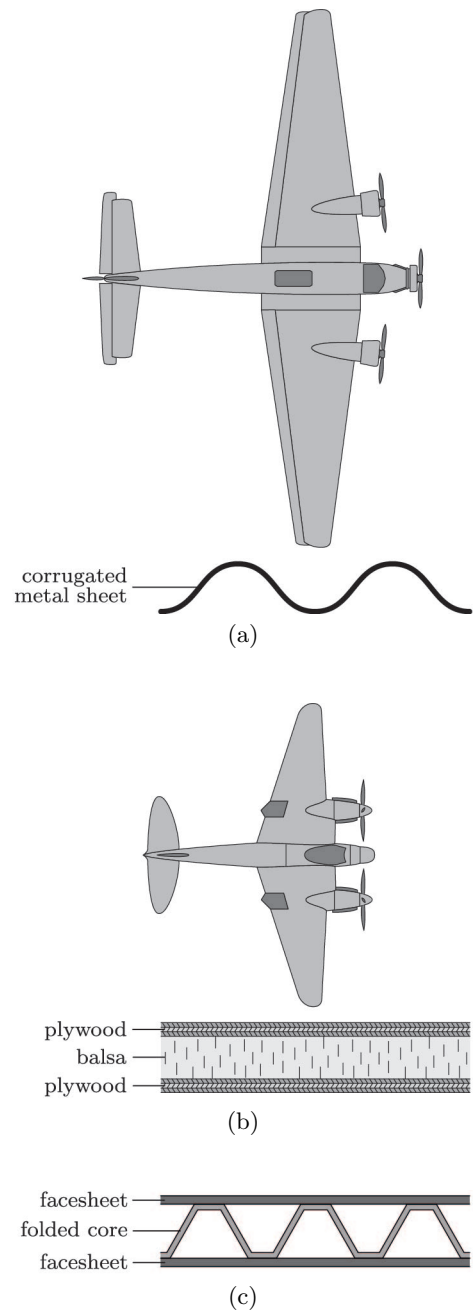


Figure 2.3: (a) Corrugated skin of a Ju 52. (b) Honeycomb sandwich of a mosquito airplane and (c) folded sandwich core.

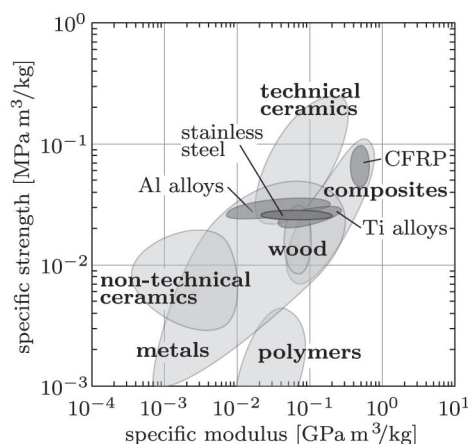


Figure 2.4: Specific strength and modulus of various materials (data from [9]).

material that is known as plywood can be tailored by varying the fiber direction of each layer. Furthermore, plywood defects such as veneer knots are better distributed and locally restricted to single layers. This minimizes potential stress concentrations and thus improves the average material properties. The inexpensive production of veneers became possible in the mid nineteenth century with the invention of the rotary lathe by Immanuel Nobel³. Material properties of veneers are limited by existing tree species so that the development potential of wood based materials was exhausted after the invention of the plywood. In contrast, the discovery of increasingly strong metal alloys continues to this day.

2.2.2 Metals

The transition from wood to metal started in 1915 with the maiden flight of the Junkers J 1 that was made out of steel. However, steel was soon replaced by aluminium due to its greater specific strength. The all aluminium DC-3 that made its maiden flight in 1935 is one of the most significant airplanes of all times. Many of the more than 16,000 DC-3's that were built until 1945 are still in service today. In contrast, the era of wooden airplanes ended in 1950 with the production of the last Mosquito. The current use of structural components that are made out of wood is limited to small airplanes.

The relatively fast transition from wood to metal is interesting since it was only partially driven by performance considerations [132]. Instead, a general inclination towards change and innovation might have been the main reason. This is underpinned by the performance of the Mosquito that could compete with comparable all metal airplanes of its time. Furthermore, wooden airplanes were cheap and easy to manufacture and their relatively short service life was not a limiting factor during war times. Hence it remains an open question if the rapid focus on all metal airplanes was, at least in the European theater, advantageous.

The first titanium alloys [229] were developed at the end of the 1940s. Their mechanical properties and corrosion resistance were found to be superior to those of aluminium so that they have been used in airplanes ever since. However, the complex and energy intensive production of titanium makes it relatively expensive. Furthermore, titanium alloys are difficult to machine [170] so that their use is often restricted to structural components that can not be made out of aluminium. An extreme example is the Lockheed SR-71 that raised the current air speed record for aircraft to 3,530 km/h in 1976. Its sustained high speed flights led to an aerodynamic heating so that 93% of its structure needed to be made out of titanium [189]. The performance improvements of military airplanes and the growing demand for lightweight commercial airplanes steadily

³Immanuel Nobel was an inventor who mainly worked in the defense industry. The Nobel Prize was endowed by his son Alfred who invented the dynamite.

increases the use of titanium alloys as shown in Figure 2.5. This trend will most likely continue due to the development of advanced manufacturing techniques such as rapid prototyping.

2.2.3 Composites

The use of aluminium in airplane structures diminished after the development of titanium alloys. This trend accelerated after the availability of high strength composite materials. Today, carbon fiber reinforced plastics are the most commonly used materials in commercial and military airplanes.

Carbon fibers with a yield strength that vastly exceeds those of aluminium and titan were developed in the 1960s. They are embedded in a polymer matrix to create structural components with tailored, anisotropic properties. Modern passenger airplanes from Airbus or Boeing are about 50% composite by weight. For example, the Boeing 787 airframe consists of 10% steel, 15% titanium, 20% aluminium and 50% composite. This material mix reduces the total weight by about 20% compared to an all aluminium design. However, the transition from aluminium to composite is considerably slower than the previous transition from wood to aluminium. This is even more striking since the performance differences between aluminium and carbon reinforced plastics are considerably larger than the differences between wood and aluminium.

Nonetheless, the trend towards composite airplanes will continue due to the development of increasingly strong fibers and the maturity of design, manufacturing and maintenance tools. The relatively slow progress in the airplane industry today is most likely due to the small number of competitors that have survived. Mergers and withdrawals led to a duopoly in the large jet airliner market that exists since the 1990s. Other aspects are the relatively high regulatory requirements and the increasing complexity of new airplanes.

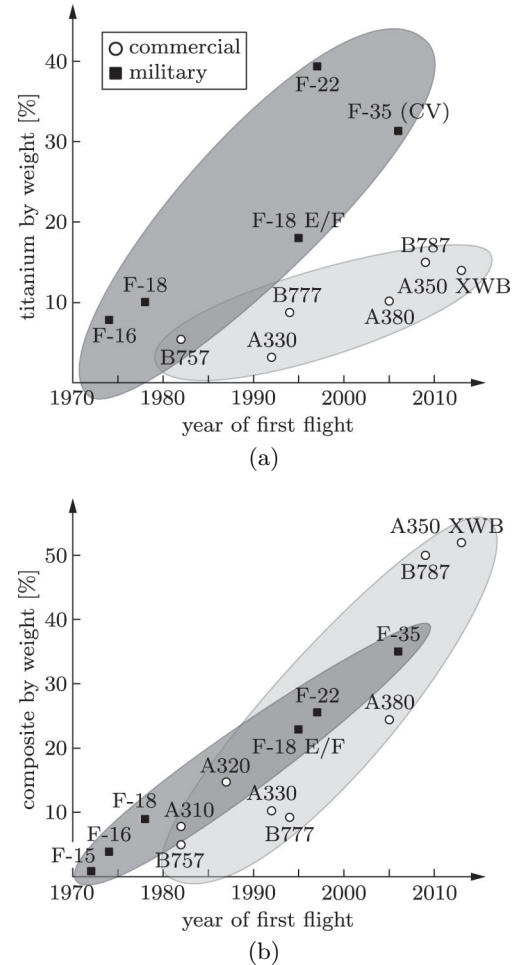


Figure 2.5: Percentage of (a) titanium and (b) composite structural weight of various commercial and military airplanes.

Chapter 3

Actuators

Humans usually approach complex tasks by splitting them into subtasks that are easier to solve. This is certainly true for high lift devices of airplanes where it is commonly assumed that rigid structures are translated and rotated by mechanisms that convert the simple input movements of one or more actuators into desired output movements. Actuators are widely used components that convert various kinds of energy into linear and rotary motions. In reverse conclusion, they can often be used as generators for the reciprocal task of converting motions into energy. Energy forms such as electric, magnetic, pressure and thermal are commonly used in engineering. These energy forms can be converted into each other although this inevitably leads to energy losses. Hence, the optimal actuator design depends, among others, on the available energy form, the required actuation stress, strain and speed. Achievable stresses, strains and frequencies of various actuation principles are summarized in Figure 3.1.

Actuators can be solid state materials or mechanisms themselves. Solid state actuators are usually driven by variations in their crystal or molecular structure so that they need to be described on a continuum level. In contrast, mechanical actuators are usually driven by the translation or rotation of discrete points or finite elements and are thus described on a structural level. Mechanical actuators can generate large actuation strains or in terms of motors unbounded rotations. In contrast, solid state actuators can generate only small strains but are usually capable of operating at higher frequencies. Mechanical actuators are widely used in engineering whereas solid state actuators are predominantly found in nature. The rotation motor that is used for the propulsion of bacteria [23] is one of the rare exceptions where a mechanical actuator is used in nature.

A brief overview of different mechanical and solid state actuators

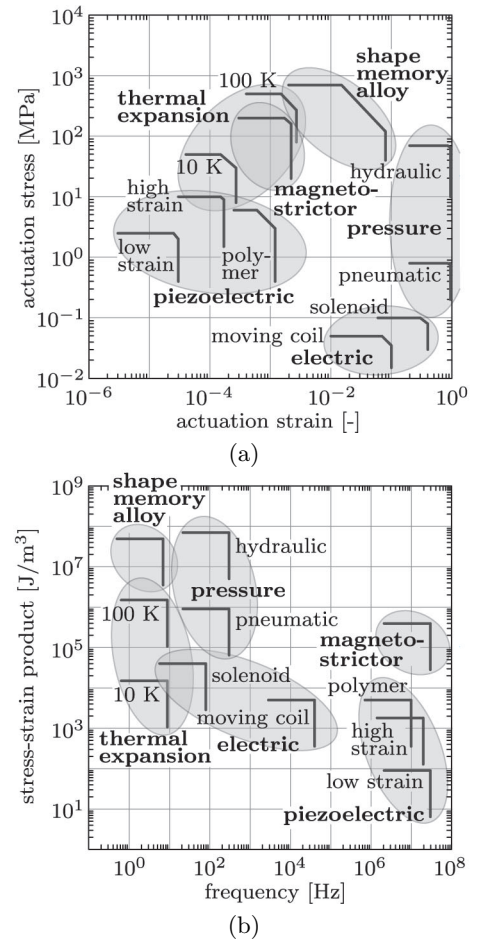


Figure 3.1: (a) Stress versus strain and (b) stress-strain product versus frequency of various actuation principles (data from [129]).

is subsequently given. The focus for the mechanical actuators is on the main types that are commonly used in heavy machinery such as airplanes. In contrast, currently available solid state actuators often lack the potential or maturity to replace mechanical actuators in these applications. This is taken into account by discussing a large number of different actuation principles, their potential, limitations and current developments.

3.1 Mechanical Actuators

3.1.1 Electromechanical

Electromechanical actuators are mechanisms that convert electrical energy into a rotary or linear motion. There exists a large number of different motor designs [130] that are widely used in engineering. All of them have in common that they are based on the interaction between winding currents and an electromagnetic field that is generated by permanent magnets or current carrying coils.

Linear actuators usually consist of an electric motor that is connected to a lead screw and a nut that is threaded into it. The nut is prevented from rotating with the lead screw so that a linear motion is created by driving it along the threads [179]. These kind of actuators are often combined with a brake system so that static loads can be carried by unpowered actuators. Solenoids and moving coils [26] are other types of linear actuators. Solenoids consist of an electromagnetic coil, a spring, and a ferromagnetic cylinder, rod. The coil is wound around the cylinder in which the rod can freely move. The electromagnetic field of the current carrying coil forces the rod towards its center and the spring returns it to its initial position after switch off. Moving coil actuators consist of a permanent magnet and an electromagnetic coil that is loosely wound around it. The electromagnetic field of the current carrying coil interacts with the magnetic field of the magnet and generates a force along its axis. Moving coils possess, unlike solenoids, a linear force displacement relationship where the force is proportional to the current.

Electric motors can be found in applications that range from the actuation of endoscopes [322] to the propulsion of large ships [226]. Solenoids are used in pneumatic or hydraulic control valves whereas moving coils are used in loud speakers that require large accelerations and a linear force displacement relationship. There is currently a strong trend towards the electrification of chemically powered machines. For example, trucks [286] and airplanes [246] use various kind of actuators that range from hydraulic cylinders to electric motors. Each kind of actuator requires a different energy form so that the weight and complexity of these machines can be often decreased and their energy efficiency increased by

minimizing the number of energy conversions. Hence it is not surprising that, wherever possible, hydraulic and pneumatic cylinders are replaced by lead screw driven actuators.

Most of the global electricity is generated by electric motors that convert motion into energy. On the other hand, electric motors consume about 45% of the electric energy [308]. This dual use magnifies the impact of new technologies that improve their energy efficiency. Current research in this field focuses particularly on the development of advanced magnetic materials [110] and optimized motor designs [68].

3.1.2 Pressure

Pressure actuators are mechanisms that convert a fluid flow into a rotary or linear motion. Pneumatic actuators use a gas whereas hydraulic actuators use a liquid for the power transmission. There exists a large number of different motor designs [227] where gear-, vane- and radial piston motors are among the most common. Their working principles are illustrated in Figure 3.2.

Pneumatic and hydraulic cylinders are linear actuators that are based on a rigid body mechanism where a prismatic joint between a piston rod and a cylinder provides a single degree of freedom. Pneumatic artificial muscles and bellows actuators are the compliant counterparts of pneumatic and hydraulic cylinders. Despite their name, both kind of actuators can be hydraulically and pneumatically operated [292]. Pneumatic muscles can generate large tension forces whereas bellows actuators can generate significant compression forces. The working principle behind both kind of actuators is based on the anisotropic stiffness of their cylindrical structure. Pneumatic muscles are relatively soft in radial and stiff in axial direction whereas bellows actuators are relatively stiff in radial and soft in axial direction. The anisotropy of pneumatic muscles is usually introduced on a material level by embedding axially oriented braided cords into an elastic cylinder [59]. In contrast, the anisotropy of bellows actuators is often introduced on a geometric level by using corrugated cylinders or on a material level by embedding equally spaced belt ribs around the circumference of an elastic cylinder. Pneumatic muscles and bellows actuators generate forces and displacements that are in the range of cylinder based actuators [234]. Unlike double acting cylinders they can perform work only in one direction so that they are often used in antagonistic pairs [188]. Furthermore, they possess a nonlinear force-displacement relationship [48] that depends on their pressurization, deformation and temperature. The latter is particularly difficult to describe since it fluctuates during operations and thus increases their control complexity [288].

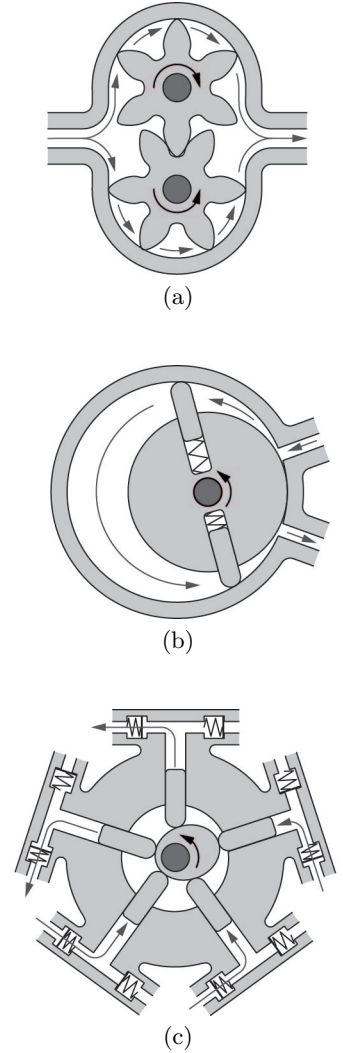


Figure 3.2: Different hydraulic motors. (a) Gear-, (b) vane- and (c) radial piston motor.

Pneumatic and hydraulic cylinders are relatively simple and inexpensive. They generate large actuation stresses and strains and can operate in challenging conditions. Pneumatic cylinders can be used in hazardous environments with temperatures between -40 to 300°C as they do not contain any flammable liquids. On the other hand, hydraulic cylinders have a very high power to weight ratio and their incompressible fluid allows them to steadily hold varying loads without a fluid supply. Due to their outstanding properties, pneumatic and hydraulic actuators are widely used. However, they often require additional parts such as fluid reservoirs, pumps, heat exchangers and valves which increases their overall complexity and weight. In contrast, pneumatic artificial muscles are rarely used since they have no clear advantage over their rigid body counterparts. Bellows actuators can be found in the suspension systems of some high end cars since they enable a smoother, adjustable ride than conventional steel springs [41]. Furthermore, they are used as lightweight lifting bags in recovery and rescue operations.

Particularly hydraulic actuators have not reached their full potential yet. Current research focuses on low friction seals [203] and energy efficient fluids [293] that allow the use of increasingly large operating pressures. Advances in manufacturing techniques [320] enabled a tight integration of actuators, fluid lines, valves and control electronics [256] which led to considerable weight savings. The current development of electro hydraulic actuators is driven by the ongoing trend towards the electrification of many machines. These actuators are a combination of hydraulic and electromechanical [299] or solid state actuators [44]. The main advantage of electrohydraulic actuators is their use of a localized hydraulic system that is electronically controlled and powered. This approach leads to significant weight savings [299] while it avoids some of the safety critical drawbacks of electromechanical actuators [14]. Nonetheless, pressure based actuators are still used in many heavy machines and it remains to be seen in how far they will be replaced by electromechanical systems.

3.2 Solid State Actuators

Sarcomeres are the smallest building blocks of muscles. They consist of three protein filaments that slide past one another at a length scale of about $2\text{ }\mu\text{m}$. Muscles consist of a large number of serial and parallel arranged sarcomeres so that their possible actuation strains and forces depend on their length and thickness. The underlying mechanism of single sarcomeres shares many similarities with mechanical actuators. However, they function at a different length scale and are only used in large numbers. Hence, a muscle is commonly considered to be a solid state actuator as it can be described on a continuum level.

Even within a single material class, solid state actuators can be based on a wide range of actuation principles. For example, polymers can be used to create electric, magnetic or thermal powered actuators. Generic terms such as electroactive polymers [42] or polymer artificial muscles [194] are thus not helpful. As a consequence, various solid state actuators are subsequently discussed on the basis of their actuation principle.

3.2.1 Piezoelectric and Piezomagnetic

Piezoelectric (*piezomagnetic*) materials generate an electric (*magnetic*) field in response to a deformation. Conversely, a deformation occurs when an electric (*magnetic*) field is applied. Piezoelectricity was discovered in 1880 by the brothers Jacques and Pierre Curie¹ [58] and piezomagnetism in 1960 by Borovik-Romanov [28]. Piezoelectricity (*piezomagnetism*) is a first order effect since deformations are proportional to the applied electric (*magnetic*) fields as illustrated in Figure 3.3. The subsequent focus is on piezoelectricity since piezomagnetic materials are rarely used.

Piezoelectricity of inorganic materials is understood as the interaction between the mechanical and the electric state of crystalline materials with no inversion symmetry. Out of the 32 crystal classes there are 20 that exhibit direct piezoelectricity [306]. Some organic materials such as the amorphous vinylidene cyanide [196] and the semi-crystalline polyvinylidene fluoride [143] are piezoelectric due to their molecular structure and arrangement. The properties of piezoelectric materials are described by strain and voltage coefficients. Strain coefficients are the ratios between the actuation strains and the applied electric fields whereas voltage coefficients are the ratios between the open circuit electric fields and the applied stresses. Large strain coefficients are required for actuators whereas large voltage coefficients are advantageous for sensors. Piezoelectric actuators are energy efficient and capable of high frequencies but limited to small strains and stresses. This makes them the ideal choice for applications such as vibration suppressors, precision positioners and ultrasonic motors [295].

The most common piezoelectric materials are the inorganic lead zirconate titanate that is toxic and brittle and the organic polyvinylidene fluoride that is biocompatible and flexible. Lead zirconate titanate has relatively large strain and small voltage coefficients whereas polyvinylidene fluoride has small strain and large voltage coefficients. The advantages of organic and inorganic piezoelectric materials are often combined in composites materials [305]. Current research focuses on the development of lead free inorganic materials [137] with a reduced toxicity and piezoelectric polymer composites for microfabricated devices [241].

¹Pierre Curie married Maria Skłodowska (Marie Curie) in 1895.

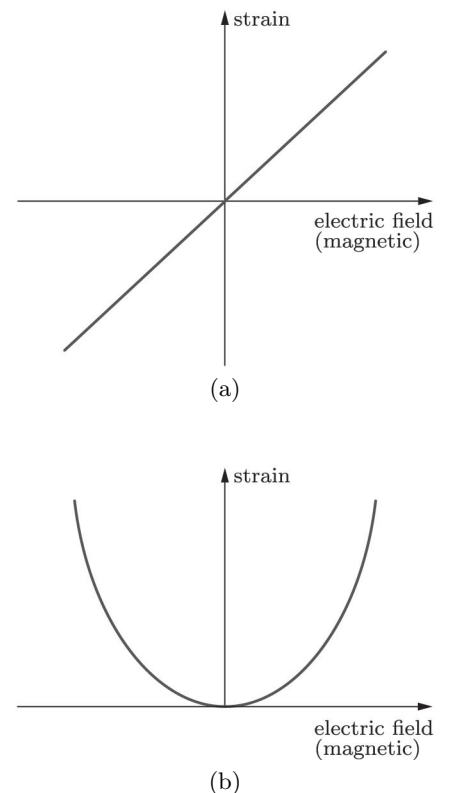


Figure 3.3: (a) First order effect of piezoelectric (*piezomagnetic*) materials. The actuation strain depends on the polarity of the electric (*magnetic*) field. (b) Second order effect of electrostrictive (*magnetostrictive*) materials.

3.2.2 Electrostrictive and Magnetostrictive

All non-conducting or dielectric (*ferromagnetic*) materials undergo a deformation in response to an electric (*magnetic*) field. These second order effects are independent of the polarity and proportional to the square of the electric (*magnetic*) field. Magnetostriction was first described by Joule [139] in 1842 and electrostriction by Volpicelli [154] in 1862.

Electrostriction of dielectric materials is due to the slight displacement of ions in a crystal lattice. These displacements accumulate throughout the material and lead to strains in the direction of the electric field. Some engineered ceramics that are known as relaxor ferroelectrics exhibit a remarkably large electrostriction. However, their underlying mechanism is not fully understood [56]. In contrast, magnetostriction occurs only in ferromagnetic materials. These materials possess uniformly polarized regions that align themselves to a magnetic field. Deformations from these rotations accumulate throughout the material and lead to strains in the direction of the magnetic field. Electrostrictive (*magnetostrictive*) actuators are energy efficient and capable of high frequencies. They can generate larger stresses and strains than piezoelectric actuators. However, electrostrictive (*magnetostrictive*) actuators are nonlinear and temperature sensitive. Nonetheless, particularly magnetostrictive actuators are widely used in vibration suppressors, sonar transducers and ultra sonic measuring devices [208].

Commonly used electrostrictive materials comprise the inorganic lead magnesium niobate [272] and some organic copolymers of polyvinylidene fluoride [318]. The highest known magnetostriction among alloys is exhibited by terbium iron dysprosium (Terfenol-D) [316]. Similar to piezoelectric materials, current research focuses on the development of inorganic materials that are lead free [325]. Despite its huge magnetostriction, the use of Terfenol-D is often limited by its susceptibility to fracture and its small tensile strength. Potential alternatives are iron gallium alloys that exhibit a moderate magnetostriction at very low magnetic fields. They possess a large tensile strength, small hysteresis and can be welded [12]. Furthermore, the material properties of polyvinylidene fluorides can be tailored for various applications by using fillers and different processing procedures [181].

3.2.3 Electrostatic and Magnetostatic

The electrostatic (*magnetostatic*) force between two charged (*magnetized*) plates is proportional to the square of the electric (*magnetic*) field and inversely proportional to the square of the distance between the plates and the relative permittivity (*permeability*) of the medium in-between. This relationship was discovered by Cavendish [185] in the early 1770s for the electrostatic and by Ampère [7] in 1820 for the mag-

netostatic force.

An electrostatic actuator that consists of two parallel plates is illustrated in Figure 3.4. The lower plate is fixed and the upper plate is connected to a spring. It can be seen that the nonlinear relationship between the electrostatic force and the gap between both plates leads to two potential equilibrium configurations. However, the left equilibrium configuration is unstable so that the electrostatic force can not be balanced by the spring beyond this point [201, 225]. This is widely known as a pull-in instability. Electrostatic actuators can be easily manufactured at small scales. Furthermore, their force increases nonlinearly with decreasing gaps. This makes them particularly suited for the use in micro-electromechanical systems (MEMS). In contrast, the use of magnetostatic actuators is currently limited by incompatibilities [202] with existing manufacturing techniques. Furthermore, the ratio between electrostatic and magnetostatic forces increases for decreasing actuator sizes. As a consequence, the subsequent focus is on electrostatic actuators.

MEMS are manufactured by bulk-, surface and high aspect silicon micromachining. Materials such as polymers, metals and ceramics can be deposited in layers on the silicon and patterned, etched to produce the required shapes [140]. Common electrostatic actuators are parallel plates [319], inchworms [321] and comp- [285], scratch drives [3]. They are used, for example, in micro mirrors [127] for cinema projectors, television sets and rapid prototyping machines. Electrostatic actuators are mature and well understood. Current developments focus on advanced actuator designs and manufacturing techniques as well as new materials. Furthermore, electrostatically actuated mechanisms for micro-fluidic devices receive a considerable amount of attention due to their potential impact on clinical diagnosis [249].

3.2.4 Ionic

The ions in electrostrictive actuators are only slightly displaced. In contrast, the displacements in ionic actuators can be considerably larger. Their movements lead to local volume changes that mostly preserve an actuators total volume. It should be noted that a magnetically actuated version of an ionic actuator is not possible as magnetic charges or magnetic monopoles do not exist. Depending on the chosen electrode material, ionic actuators are subsequently divided into two groups as illustrated in Figure 3.5.

An electrode storage actuator that consists of doped polymer electrodes and a separating electrolyte for the ion transport was proposed by Baughman et al [19] in the early 1990s. This kind of actuator became possible after the discovery of high conductivity polyacetylene deriva-

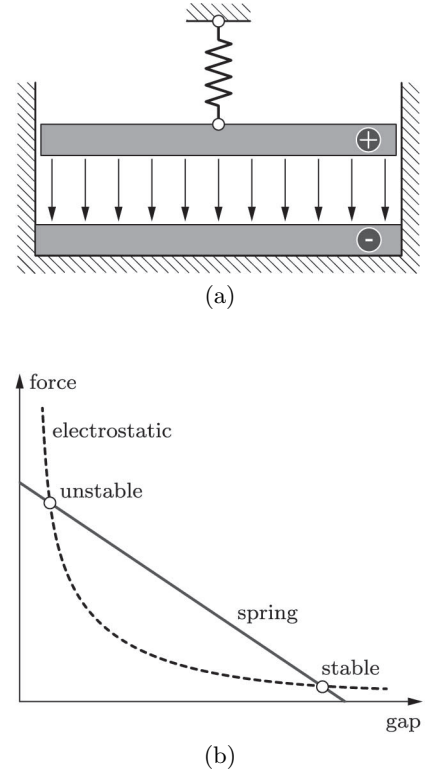


Figure 3.4: (a) Two parallel, separated and electrically charged plates. The lower plate is fixed and the upper plate is connected to a spring. (b) The electrostatic force depends nonlinearly on the gap between both plates so that a stable and an unstable equilibrium configuration exists for any electric field.

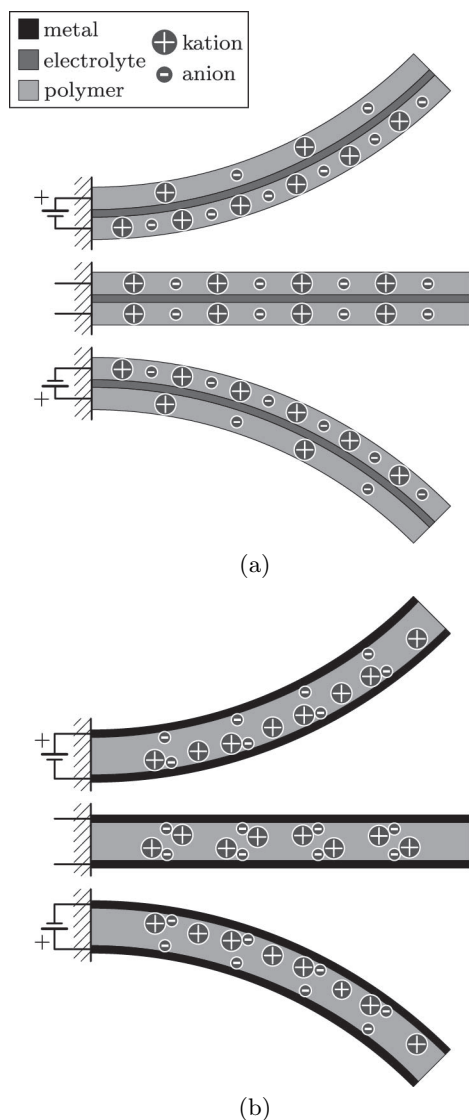


Figure 3.5: (a) Electrode storage actuator with doped polymer electrodes and separating electrolyte. (b) Polymer metal composite actuator with flexible metal electrodes and polyelectrolyte polymer.

tives at room temperatures by Shirakawa et al [260] in 1977. Current electrodes are often made from polypyrrole [27], polyaniline [281] or polythiophene [245].

Polymer metal actuators were first investigated by Oguro et al [207] in 1992. They are based on flexible metal electrodes that are plated on a polyelectrolyte where one ion type is provided by the polymer chains and the opposite type by solvated ions. Gold and platinum are often used as electrode materials whereas styrene/divinylbenzene polymers and perfluorinated alkenes [258] are commonly used as electrolytes. Current research focuses on advanced electrode and electrolyte materials where the main focus is on carbon nanotubes [20, 155] and polymers with zwitter ions [147].

Ionic actuators work with low voltages and their deformations depend on the polarity of the electric field. They are flexible, relatively inexpensive and easy to manufacture. However, their industrial use is currently limited as they can only operate at low frequencies, possess a low endurance and often suffer from irreversible deformations.

3.2.5 Phase Transition

A phase is a region of space throughout which all physical properties of a material are uniform. The transition of a material from one phase to another can affect its density, refractive index, magnetization or chemical composition. Phase transitions can be triggered by temperature, pressure and electric-, magnetic fields. Materials that reversibly vary their shape or volume during a phase transition can be used as actuators. Commonly used are the solid-solid phase transitions of shape memory alloys, the solid-liquid transition of paraffin [206] and the liquid-gas transition of ethanol [195]. Particularly shape memory alloys are widely used since they remain solid. Further advantages are their high strength, biocompatibility and workability.

Shape memory alloys are a group of metals that can repeatedly return from a deformed- to a memorized shape when heated or subjected to a magnetic field [133]. A thermally activated shape memory effect was first observed in 1932 in an Au-Cd alloy by Ölander [209] and in 1962 in a Ni-Ti alloy by Buehler et al [34]. The latter stands out of the large number of shape memory alloys that are known today [312] due to its remarkable properties [128]. A subgroup within the thermally actuated shape memory alloys that can also be magnetically actuated was discovered by Ullakko [297] in 1996. However, magnetically actuated alloys are rarely used and the only commercially available material is a Ni-Mn-Ga alloy [80]. Shape memory alloys possess three potentially stable crystal structures (twinned martensite, detwinned martensite and austenite).

The austenite crystal structure is the preferred material phase at high temperatures. A shape memory alloy returns to its austenite structure upon heating even if it is heavily loaded. Transformations between crystal structures can be categorized into pseudoelastic, one- and two way shape memory effects as illustrated in Figure 3.6.

Due to instant phase transitions, shape memory alloys can undergo large pseudoelastic strains at high temperatures. Loads lead to a transition from the austenitic to the martensitic phase which is instantaneously reversed upon unloading [31]. In contrast, a one way shape memory alloy remains in the deformed configuration upon unloading if the environmental temperature is not sufficiently high for a phase transformation. However, it eventually recovers to its initial shape if the temperature is raised.

A one way shape memory alloy can only remember its austenitic shape whereas a two way shape memory alloy can remember its austenitic and martensitic shape. Depending on the temperature, a two way shape memory alloy can repeatedly cycle between both shapes. Hence it does not require external forces that deform the austenite crystal structure into a certain martensite structure upon cooling. However, potential actuation strains of two way shape memory alloys are considerably smaller than those of one way alloys. Furthermore, they suffer from strain deteriorations that can be observed within a small number of cycles [253].

A two way shape memory alloy needs to be “trained” in order to remember its austenitic and martensitic shapes [173]. This can be done by repeatedly performing the following steps:

1. Heating of unloaded alloy to its austenitic phase.
2. Deformation into desired cold shape.
3. Preservation of cold shape and cooling to its martensitic phase.
4. Unloading of alloy.

The hysteresis of a shape memory alloy is the difference in transition temperatures between heating and cooling. Shape memory alloys with a small hysteresis are used in applications that require fast shape changes [57] whereas alloys with a large hysteresis are used in applications that need to maintain certain shapes within a large temperature range.

The low energy efficiency, fatigue life [72] and phase stability [324] of shape memory alloys limits their applicability. However, there exists a number of industrially relevant applications that exploit their pseudoelasticity and biocompatibility. For example, Ni-Ti alloys are widely used in eyeglass frames, dental wires, stents, vena cava filters and aortic valves [231].

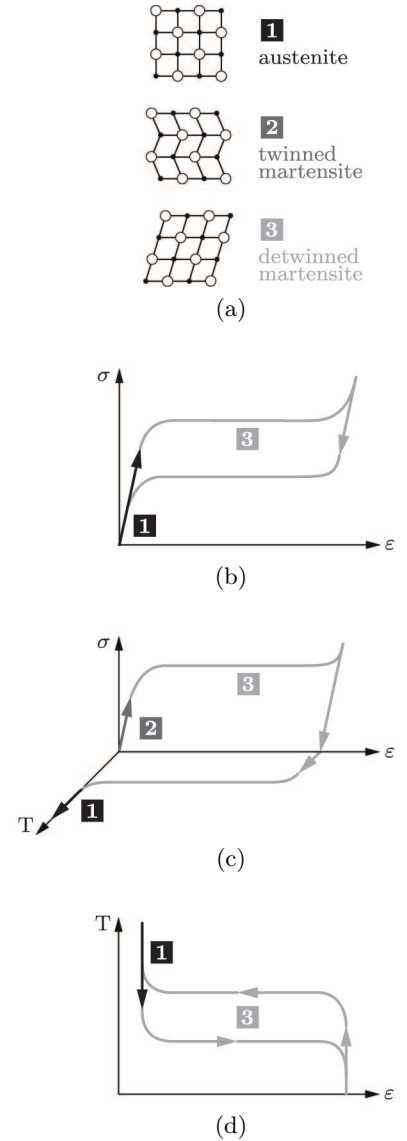


Figure 3.6: (a) Potentially stable crystal structures of shape memory alloys. (b) Pseudoelastic behavior at high temperatures and (c) one way shape memory effect at lower temperatures. (d) Two way shape memory effect of “trained” alloys.

3.2.6 Thermal

The densities of existing materials depend to a varying degree on the temperature. Thermal expansion coefficients and conductivities as well as Young's moduli of various material classes are illustrated in Figure 3.7. Based on their stress-strain-temperature relationships, thermal actuators can be made from a wide range of materials. Actuators that consist of a single, solid piece of material that is actively heated or cooled can generate large forces but only small strains. Different approaches that can be used to increase the actuation strains for given temperature changes at the cost of reduced actuation forces are subsequently discussed.

It was shown by Lima et al [165] in 2012 and subsequently by Haines et al [112] in 2014 that it is possible to significantly increase the effective axial strains of anisotropic fibers by coiling them. For example, the thermal expansion coefficient of nylon fibers with axially oriented polymer chains is negative in axial and positive in radial direction. A reorientation of the polymer chains into helices can be achieved by twisting. Straight nylon fibers with helical polymer chains experience a torsional deformation upon heating. This deformation is magnified by the different signs of the thermal expansion coefficients in radial and axial direction. An actuator that translates this torsional deformation into a linear motion can be created by fiber coiling. Such an actuator can generate contractile strains of more than 30% at the cost of a reduced actuation force [111].

Microarchitected materials that consist of two or more material phases can be designed for a wide range of properties. This makes them particularly attractive for the use in thermal actuators since they can occupy regions of the material property space that were previously empty [82]. Sigmund pioneered the topology optimization of microarchitected materials with extreme thermal expansion coefficients for two [264] and three [265] phases. Large thermal expansion coefficients come at the cost of a low bulk modulus. A simple relationship between the thermal expansion coefficients and bulk modulus of two phase materials [163] is known whereas a corresponding relationship for three phase materials does not exist. However, bounds for the thermal expansion of microarchitected multiphase materials are well known [94].

The energy efficiency and actuation frequency of thermal actuators is relatively low. Hence they are particularly suited for applications that need to respond to slow changes in the environmental temperature. For example, thermal actuators are widely used in greenhouse ventilation systems and thermostats. The steady progress of additive manufacturing techniques for multiple materials [298] enables the creation of increasingly sophisticated microarchitected actuators with desired shape changing properties. This might enable one day the construc-

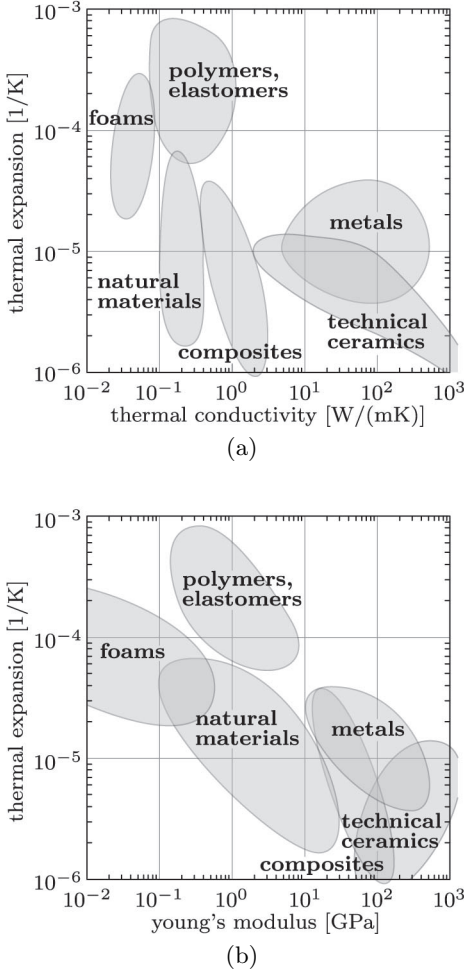


Figure 3.7: (a) Thermal expansion, conductivity and (b) Young's modulus of various materials (data from [9]).

tion of multiphase materials with properties similar to those of a shape memory alloys.

3.2.7 Swelling and Shrinking

Gels consist of three-dimensional networks of polymer chains. Their structures differ from soluble materials as their chains are connected by cross links so that they can enclose large amounts of liquids (hydrogels) or gasses (aerogels) as shown in Figure 3.8. For example, aerogels are excellent insulators as more than 99% of their volume is made up of immobile air². In contrast, the water content of hydrogels [315] can be varied within a wide range or redistributed with the help of different mechanisms. This leads to large potential volume changes that can be used to create various actuators.

Volume changes can be triggered by a wide range of external stimuli. For example, osmotic gradients can be generated by ionizing ultraviolet light [178] or in ionic hydrogels by electric fields [284]. Other mechanisms include a breakdown [283] of hydrogel networks or a variation of their hydrophilicity [182] due to temperature variations. The speed of volume changes and the mechanical properties of hydrogels depend heavily on the network structure. Response times can be significantly reduced by large, interconnected pores [45] whereas mechanical properties depend largely on the cross links. Haraguchi and Takehisa [114] showed in 2002 that cross links can be modified by the inclusion of nanoparticles. Another approach that leads to stiff and ductile hydrogels was proposed by Gong et al [100] in 2003. It is based on two interlaced networks where one is stiff and brittle and the other soft and ductile. Further improvements seem to be possible by tailoring the network structure with the help of carefully designed, self-assembling building blocks [230].

The relatively slow and size dependent response times of hydrogel actuators vary between shrinking and swelling. Hence they are currently not used in industry. However, the working principle and potential of hydrogels is intriguing as it has much in common with the nastic movement of plants.

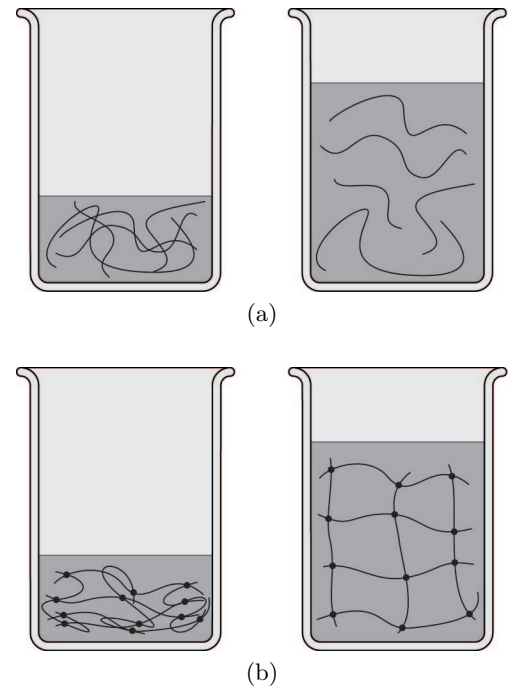


Figure 3.8: Dilution of polymer chains (a) without and (b) with cross links.

²Graphene aerogels with a density of about 160 g/m³ are the least dense solids known [279]. They are nearly eight times lighter than air.

Chapter 4

Mechanisms

Roll movements of the first airplanes were controlled by twisting their wings in opposite directions. This required structures with a low torsional stiffness that could only be used at low flight speeds. Rigid wings with hinged ailerons were employed as flight speeds became too large. The airfoils of these wings were optimized for cruise so that they did not provide enough lift at previous takeoff and landing speeds. This led to increasingly long runways and the development of various high lift devices that were widely used since the 1930s. For example, the deployed high lift devices of a Boeing 747-400 increase the wing area by 21% and the lift by 90%.

High lift devices are usually made from rigid structures that are rotated and translated with the help of relatively simple mechanisms and linear or rotary actuators. This chapter discusses the major principles that are used for the design of mechanisms and the difficulties that are encountered. It is shown that the historic development of high lift devices will ultimately lead to gapless leading and trailing edges that are required to further reduce the fuel consumption, noise emissions and radar reflections of airplanes.

4.1 Mechanism Design

4.1.1 Complexity of Actuators and Mechanisms

Geneva drives are simple mechanisms that translate the continuous rotation of an actuator into an intermittent rotary motion of a wheel as illustrated in Figure 4.1. These drives were widely used in movie projectors during the twentieth century for the stepwise movement of films. In contrast, modern projectors avoid complex mechanisms by using computer controlled stepper motors. This example highlights that it is possible to

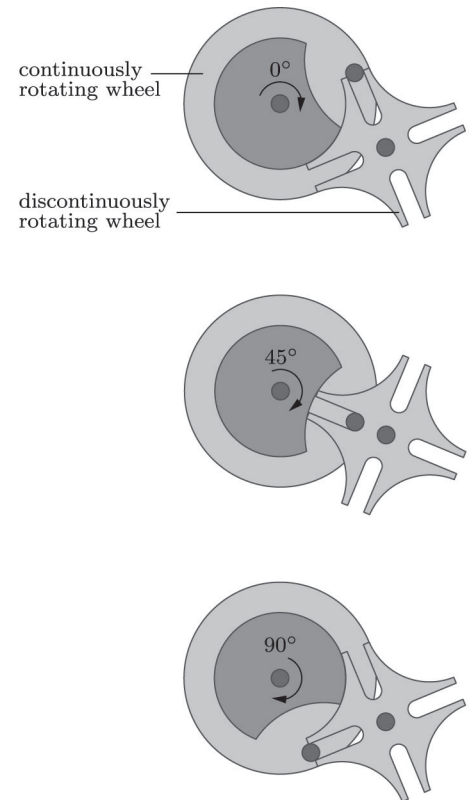


Figure 4.1: Three discrete positions of a Geneva drive during the phase where both wheels rotate.

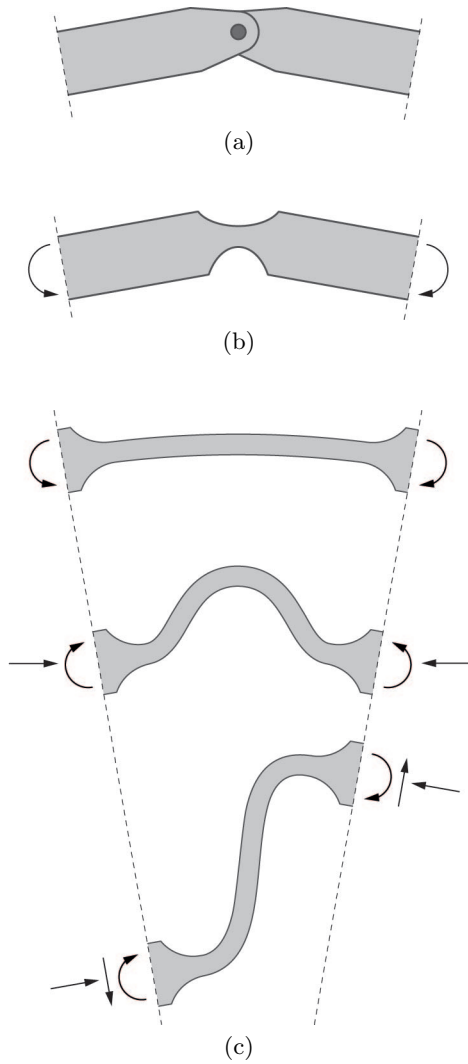


Figure 4.2: Equilibrium shapes of three different rotational joints for a fixed rotation angle. (a) Frictionless hinge and (b-c) compliant hinges with a (b) lumped and (c) distributed compliance. Equilibrium shapes of the latter are not unique and depend on the stress resultants and loading history.

either use a sophisticated mechanism and a simple actuator or a simple mechanism and a complex, computer controlled actuator with sensors. Furthermore, there exists a wealth of possible solutions in-between that combine different mechanisms, actuators and control systems of varying complexities [309]. As a consequence, the design approach of modern machines often shifted from the mechanical (hardware) to the actuator (software) side. This holds particularly for machines whose weight and reliability are not important. Nowadays it is relatively simple to design machines with arbitrary output movements. However, it is still an art to design machines that are lightweight, reliable and that function without a complex control system.

4.1.2 Kinematic Pairs and Links

Reuleaux abstracted mechanisms into rigid bodies (links) whose relative movements are constrained by joints (kinematic pairs) [243]. He further abstracted joints into lower and higher pair joints. The difference between both kind of joints is that lower pair joints lead to surface contacts whereas higher pair joints to line or point contacts. Commonly used lower pair joints are hinges and sliders whereas gears and cams (wheels) are higher pair joints. Lower and higher pair joints can be commonly found in man made machines whereas lower pair joints are nearly exclusively used in nature due to the larger contact areas. A rare exception are the gears of some insects that synchronize their leg movements [35]. Furthermore, wheels are completely absent in nature. Stiff wheels are an effective way of propulsion if the underground is hard, level and free of obstacles [66]. However, even humans abandon wheels if the underground is too soft or uneven [103]. The main problem is that their versatility is limited [161] whereas limbs can be used for walking, climbing, swimming and jumping.

Rotational joints can be realized as frictionless or compliant hinges [126] if the rotations are small. The use of compliant hinges is often advantageous since it reduces the part count, self-weight and maintenance requirements. However, cyclically loaded compliant hinges are susceptible to fatigue [169]. One way of increasing their fatigue life is to distribute their compliance over a larger region [8]. The equilibrium shapes of a frictionless and compliant hinge with a lumped and distributed compliance are shown in Figure 4.2 for a fixed rotation angle. It can be seen that the equilibrium shapes for a distributed compliance depend on the stress resultants and loading history. In contrast, the equilibrium shapes of the other joints are unique. As a consequence, only frictionless hinges and hinges with a lumped compliance are subsequently considered.

Three different cutters are exemplarily used in Figure 4.3 to illustrate some simple mechanisms with lower pair joints. The optimal mechanism

of these cutters depends on the materials that need to be processed and the force, movements that can be comfortably applied by humans. Paper is usually cut with scissors that are based on a 2-bar linkage whereas a 4-bar linkage is often used for metal shears and a 5-bar linkage for bolt cutters. Furthermore, a clear discrimination between mechanisms and joints is often difficult since many natural joints are mechanisms themselves. For example, the cruciate ligament in a knee can be considered to be a 4-bar linkage [199].

The topological synthesis of mechanisms for given input and output movements is a mixture of art and science [47]. It is often approached by using topology optimization [263] if the in- and output movements are relatively small. Otherwise it is approached by combining simple building blocks such as 2-bar linkages or Geneva drives. Until today, the search for a good mechanism can generally not be fully automated and thus requires trial and error, experience and ingenuity.

4.2 Conventional High Lift Devices

An optimal airplane wing is capable of changing its entire shape in response to the current flight regime. However, the design and construction of such wings is not possible with current technologies. Wings are therefore often split into wing boxes and leading, trailing edges. Wing boxes are rigid structures that carry most of the loads whereas the design of the movable leading and trailing edges is dominated by aerodynamic considerations. This section provides a brief overview of the historic development [269] of currently used high lift devices and their mechanisms for both leading and trailing edges.

4.2.1 Leading Edge

Fixed leading edge slats or slots as illustrated in Figure 4.4 were invented by Lachmann in 1917 after he stalled his airplane during training. They consist of a small, separate airfoil shaped device that is rigidly placed in front of the wing. The corresponding patent application was initially rejected by the German Patent Office in 1918 and retroactively granted [162] in 1922 after experiments confirmed an increased lift of about 63%. Slots can considerably reduce an airplanes stall speed and improve its handling properties at low speeds. However, they are rarely used in modern airplanes since the slot induced drag becomes prohibitive at higher speeds. As a consequence, they are mostly used in slow flying, low maintenance bush planes that need to takeoff and land on short runways.

Slots were independently developed in the United Kingdom by Handley Page who applied for a patent in 1919. In order to avoid a patent

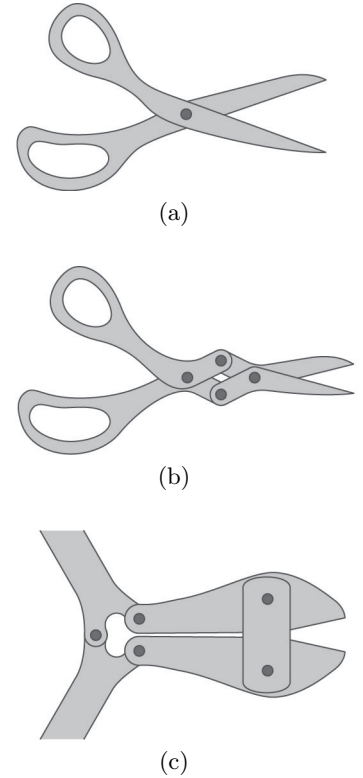


Figure 4.3: (a) Scissor with a 2-bar linkage, (b) metal shear with a 4-bar linkage and (c) bolt cutter with a 5-bar linkage.

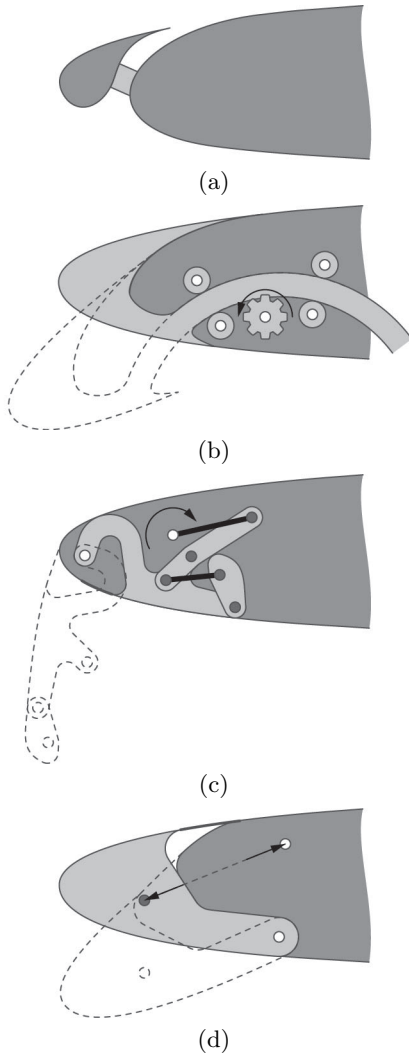


Figure 4.4: Various high lift devices for leading edges. (a) Fixed slat or slot. (b) Three position slat. The sealed configuration is used during takeoffs whereas the slotted configuration is used during landings. Mechanism is based on constant radius tracks and a rotary actuator. (c) In-board bull nose Krüger flap. Mechanism consists of two connected 4-bar linkages and a rotary actuator. (d) Rigid droop nose. Mechanism is based on a 2-bar linkage and a linear actuator.

challenge he joined forces with Lachmann who moved to the United Kingdom in 1929. They continued their work on high lift devices by investigating moveable slats that increase an airplanes lift at low speeds without increasing its drag at high speeds. The first slats made use of the relationship between flight speeds and aerodynamic leading edge forces. They were automatically deployed by springs at low speeds (*low aerodynamic forces*) and retracted at high speeds (*high aerodynamic forces*). Automatic slats were widely used during the Second World War due to their simplicity and reliability. However, they were soon replaced by actively controlled slats that are commonly used today.

The first actively controlled slats were either fully deployed or retracted. Two position slats were widely used in passenger airplanes such as the Boeing B707 that made its maiden flight in 1957. However, it was soon realized that it is advantageous to use different slat positions during takeoff and landing. This led to the development of three position slats that are slotted during landing to maximize lift and sealed during takeoff. Examples of modern airplanes with three position slats include the Airbus A380 that made its maiden flight in 2005 and the Boeing B787 that made its maiden flight in 2009.

Krüger flaps were invented in 1943 at the Aerodynamische Versuchsanstalt in Göttingen. Three different kind of Krüger flaps with increasingly refined aerodynamic surfaces are commonly used. Simple Krüger flaps deploy a single and bull nose flaps two connected and aerodynamically shaped rigid bodies from the lower wing surface. The latter can be found, for example, in the Boeing B747 that made its maiden flight in 1969. Variable camber flaps are a further development of the bull nose design. They consist of a flexible skin that is bend in the deployed configuration. Despite their advanced aerodynamic properties, variable camber flaps are rarely used since they require relatively complex and heavy mechanisms. Krüger flaps are generally lighter, simpler and less expensive than moveable slats. However, they can only be deployed into one position so that their aerodynamic performance is, particularly during takeoff, inferior to three position slats. Nonetheless, they are currently attracting a lot of attention since they avoid gaps on the suction side of a wing. This is particularly important for the design of laminar flow airfoils that are considered for the next generation of passenger airplanes.

Rigid droop noses were already investigated by Harris and Bradfield [116] in 1920. They differ from slats insofar that the entire leading edge rotates downwards without moving away from the wing. Rigid droop noses can generally not achieve the lift performance of slotted slats since the stall angles are limited by the large curvatures of their upper surfaces. Nonetheless, they are easier to manufacture and require

a smaller construction space than slats. Hence they are particularly suited for supersonic airplanes such as the F-5 that made its maiden flight in 1959. Furthermore, the use of rigid droop noses in passenger airplanes turned out to be advantageous under certain conditions. For example, the Airbus A350 and A380 use rigid droop noses between the fuselage and inboard engines.

4.2.2 Trailing Edge

Ailerons were already used by Esnault-Pelterie in 1904 to control the roll movement of a glider. Plain flaps as illustrated in Figure 4.5 often resemble ailerons with the difference that they solely move downwards to increase lift. They have been tested in the United Kingdom by The Royal Aircraft Factory and the National Physical Laboratory between 1913 and 1914. Plain flaps were first used in a floatplane for the Royal Naval Air Service that was built in 1916 by the Fairey Aviation Company. They are inexpensive, compact and easy to construct. However, their performance is usually inferior to other kind of flaps so that they are mostly used in small airplanes and fighter jets with relatively thin wings. Examples include the MiG-29 and the F-15E that made their maiden flights in 1977 and 1986, respectively.

Split flaps were invented by Orville Wright and James Jacobs [317] in 1921. They can be considered to be a variation of plain flaps where the upper part is rigidly connected to the wing and the lower part hinges downwards. Split flaps were widely used during the 1930s in passenger airplanes such as the DC-3 that made its maiden flight in 1935 and in military airplanes such as the Focke-Wulf Fw 190 that made its maiden flight in 1939. The lift forces of split flaps are approximately the same as those of plain flaps. However, their drag forces are considerably larger. This enables steeper approaches during landings but leads to longer take-off rolls. Modern airplanes avoid this problem by using flaps with a larger lift to drag ratio and additional air breaks that increase the drag during landings.

An eccentric center of rotation can be used to increase the lift to drag ratio of plain flaps. This leads to gaps between wings and flaps in the deployed configurations that stabilize the boundary layers of the upper surfaces. The working principle of single slotted flaps is similar to those of leading edge slats so that it is not surprising that their development coincided at Handley Page Ltd [191] in 1920. The lift to drag ratios of single slotted flaps were further improved by Fowler in 1924. He proposed the use of larger flaps that are partially covered by the wings in the retracted configurations. Fowler flaps are rotated and translated backwards by relatively complex mechanisms so that they increase the

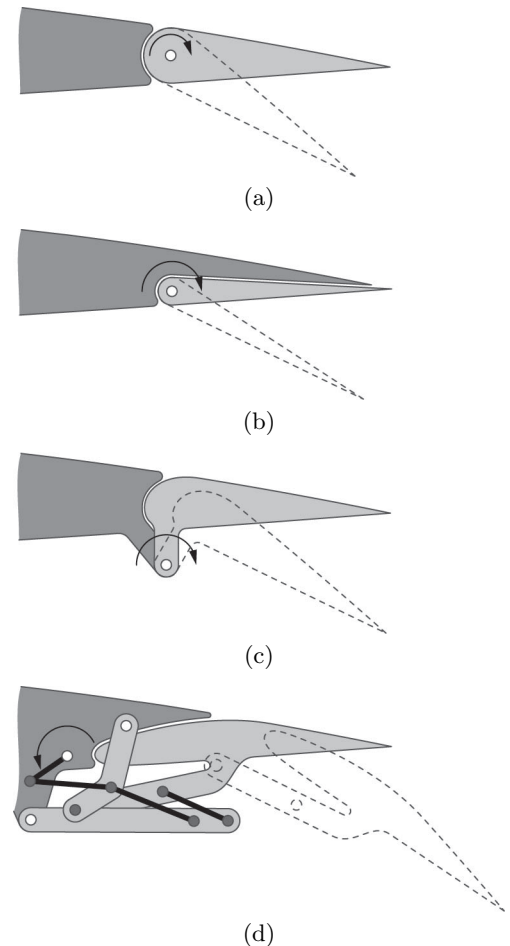


Figure 4.5: Retracted and deployed high lift devices for trailing edges that consist of an aerodynamically shaped rigid body, struts, beams and a rotary actuator. (a) Plain flaps are used in small airplanes and fighter jets with relatively thin wings. (b) Split flaps as used in fighter planes during the Second World War were found to be inferior to single or multi slotted flaps. (c) Single slotted and (d) outboard Fowler flap. The latter increases the wing area and thus the lift forces in the deployed configuration.

wing areas and thus the lift forces in the deployed configurations. They were first used in the Martin 146 that made its maiden flight in 1935.

The performance of Fowler flaps was further improved by splitting them into two or more segments. These segments separate during deployment so that they increase the number of slots and thus the lift. Double slotted flaps were first used in the Piaggio P.32 and triple slotted flaps in the Boeing B727 that made their maiden flights in 1936 and 1963, respectively. However, the performance gain of double and triple slotted flaps comes at the cost of relatively complex mechanisms and increased maintenance requirements. The development of powerful computers and simulation tools during the last decades enabled the design of increasingly refined flaps. This led to a reversal of this trend [242] so that single slotted flaps can be found in many modern airplanes. Examples include the Boeing B787 that made its maiden flight in 2009 and the Airbus A350 that made its maiden flight in 2013.

4.3 Gapless High Lift Devices

The effective perceived noise of various passenger airplanes during take-off is illustrated in Figure 4.6. It can be seen that the noise emissions¹ decreased significantly since the 1950s. Furthermore it can be seen that this development started to slow down in the 1990s. Other design aspects that reached a high level of maturity include the energy efficiency and stealth properties of airplanes. As a consequence, significant improvements in these fields can only be achieved by the development of new technologies. A promising approach in this regard is the development of gapless high lift devices. They can not only reduce an airplanes noise emissions, fuel consumption and radar reflections but also provide a basis for the use of new technologies such as laminar flow control [274].

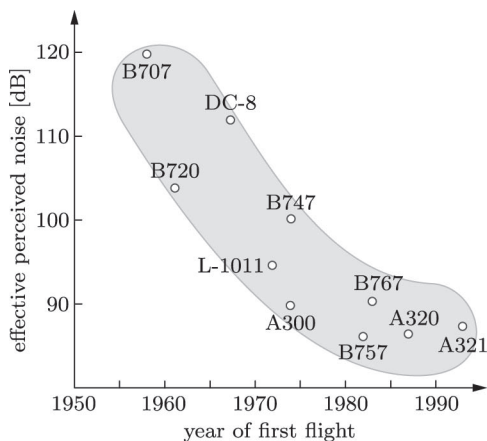


Figure 4.6: The effective perceived noise of passenger airplanes during takeoff since the 1950s (data from [81]).

Gapless wings that can completely change their shapes were already investigated in 1915 by the Varioplane Company [172]. However, the realization of such wings is far from trivial and not possible with current technologies. These difficulties led to the development of separate concepts for gapless leading and trailing edges that can be connected to existing wing boxes. The cruise and low speed configurations of a gapless leading and trailing edge are shown in Figure 4.7. It can be seen that mechanisms for gapless leading edges can be designed such that their skins undergo only bending deformations. In contrast, the discontinuous trailing edge geometries lead to mechanisms that can not preserve the arc-lengths of their upper and/or lower skins. Potential mechanisms

¹Noise emissions of passenger airplanes reduced by about 30 dB since the 1950s. This is comparable to the reductions that can be achieved by using a silencer on a rifle.

for gapless leading and trailing edges are subsequently reviewed. Corresponding concepts for skins with an invariant and tunable stiffness that can undergo bending and stretching deformations are investigated in the following chapter.

4.3.1 Leading Edge

One of the first gapless leading edges was proposed by Pierce in 1970. It consists of a flexible skin, rigid struts and a cam that is rotated by a linear actuator as illustrated in Figure 4.8. The skin that is locally supported by struts is deformed by the contact forces that are exerted by the cam. A major advantage of this approach is that the arc-length of the skin is preserved as long as the friction forces are relatively small. However, the sliding motions between the skin and cam can lead to increased maintenance requirements. Furthermore, large skin deformations on the suction side can not be prevented.

A gapless leading edge that avoids any sliding motions was developed by Zimmer [327] in 1979. It is based on a segmented skin that consists of three flexible segments and two rigid cams. The upper and lower segments are deformed by the underlying mechanism whereas the segment at the front of the leading edge is deformed by the rolling contact forces that are exerted by both cams. This approach has the drawback that the continuity of the skin in the deployed configuration is limited by the rigid cams. Furthermore, although rolling contacts are an advancement compared to sliding contacts, their use can still increase the maintenance requirements. A similar, less complex leading edge was subsequently proposed by Cole [53] in 1982. It is based on a skin that consists of a flexible segment and a rigid body. Contact forces are avoided and the part count of the underlying mechanism is considerably reduced. However, this comes at the cost of a kink at the bottom of the leading edge in the deployed configuration.

A gapless leading edge with an unsegmented skin that is continuous in the retracted and deployed configuration was proposed by Kintscher et al [149] in 2009. It avoids any contact forces and possesses a relatively simple mechanism that consists of a beam, rigid struts and a rotary actuator. The stringers that reinforce the skin in spanwise direction serve as attachment points for the underlying mechanism. A variation of this mechanism that additionally enforces the gradient of the skin at the front of the leading edge was proposed by Grip et al [108] in 2014.

Despite a massive research effort, gapless leading edges are currently not used in commercial or military airplanes. This is in part due to the heavy mechanisms and actuators. Another problem is the need for skins

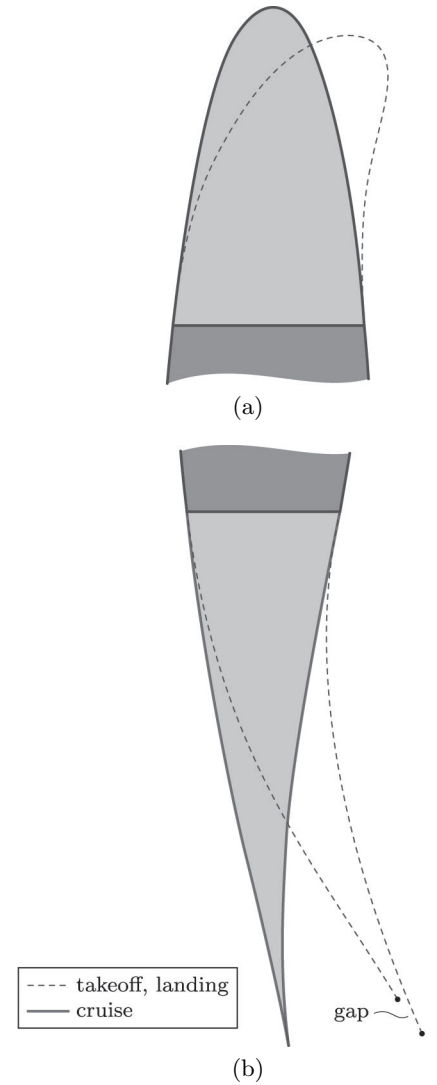
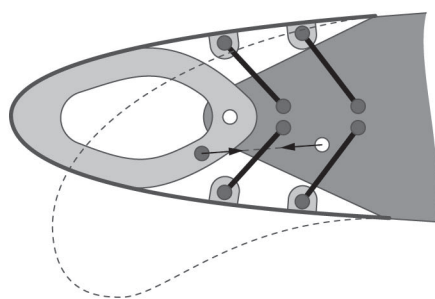
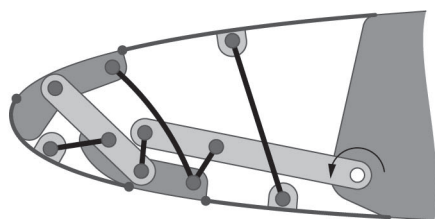


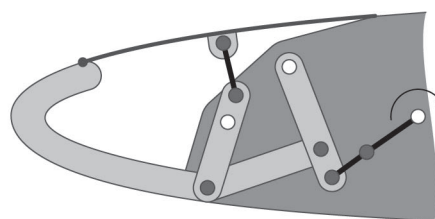
Figure 4.7: Cruise and low speed configuration of a gapless (a) leading and (b) trailing edge. Leading edge mechanisms can be designed such that their skins undergo only bending deformations. Discontinuous trailing edges require skins that can undergo bending and stretching deformations.



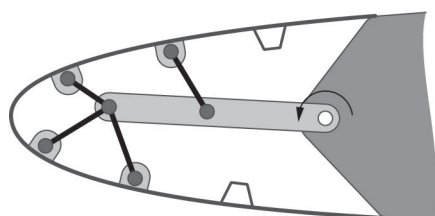
(a)



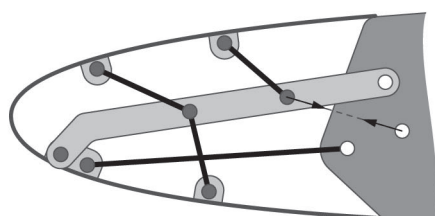
(b)



(c)



(d)



(e)

that are soft enough to undergo large deformations and stiff enough to carry the aerodynamic loads. In addition, leading edge skins have to protect the wing against erosion, icing, lightning- and bird strikes. Nonetheless, these problems might eventually be overcome by the availability of increasingly advanced materials and manufacturing techniques.

4.3.2 Trailing Edge

There exists an astonishingly large number of different mechanisms for gapless trailing edges. This variety is mostly due to the false assumption that the design of mechanisms is not constrained by the stretching deformations of their skins. A few interesting mechanisms that are based on different concepts are subsequently reviewed. It is shown that the required stretching deformations of their skins vary significantly.

Truss structures for fuselages and wings were widely used since the early days of aviation. For example, the wings of the Junkers Ju 52 that made its maiden flight in 1932 are based on a relatively complex, three-dimensional truss structure. It is likely that the idea to actively change the shape of a truss by varying the lengths of its members goes back to these early days. Shape changing truss structures are periodically revisited since then although they were never used in commercial or military airplanes. For example, Lyon [176] investigated a wing with a flexible skin and an internal, shape changing truss structure in 1960. Forty years later, Perez [228] proposed a gapless trailing edge that is based on a similar mechanism as shown in Figure 4.9. It possesses a large number of degrees of freedom that can be either separately actuated or merged into a single degree of freedom with the help of a drive train. A major drawback of this approach is that the lower skin has to undergo large stretching deformations whereas the arc-length of the upper skin is preserved. Furthermore, it requires a large number of ac-

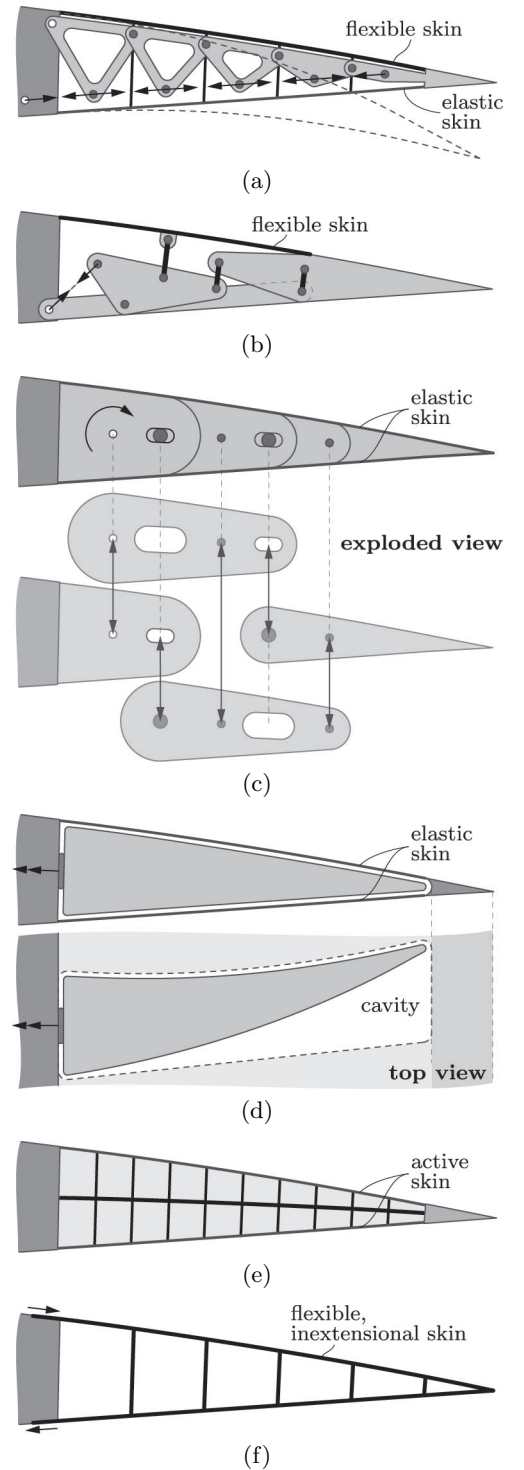
Figure 4.8: Gapless leading edges with mechanisms that preserve the arc-lengths of their skins. (a) Flexible skin with a cam mechanism, rigid struts and a linear actuator. (b) The segmented skin consists of three flexible segments and two rigid cams. The underlying mechanism is based on beams, rigid struts and a rotary actuator. (c) A similar approach with a skin that is based on a flexible segment and a rigid body. The skin is continuous during cruise and discontinuous on the pressure side during takeoff and landing. (d) An unsegmented, flexible skin and a relatively simple mechanism that consists of a beam, rigid struts and a rotary actuator. (e) A variation of the previous mechanism that additionally enforces the gradient of the skin at the front of the leading edge.

tuators or a relatively heavy drive train.

A mechanism with fewer parts and a single degree of freedom was proposed by Cole [52] in 1975. It is based on three rigid bodies, three struts and a linear actuator. The upper skin consists of a flexible segment and a rigid body whereas the lower skin is formed by two rigid bodies. As a consequence, the continuity of the lower skin is not preserved during takeoff and landing. A similar approach [271] was successfully used by the National Aeronautics and Space Administration during the 1980s to evaluate the performance of an upgraded F-111A fighter jet.

Gapless trailing edges with continuous surfaces require mechanisms that equally distribute the deformations between the upper and lower skins. Such a mechanism with a single degree of freedom was developed by Piening and Monner [233] in 1997. It consists of a chain of overlapping rigid bodies that are connected to each other via hinges and sliders. The mechanism was initially proposed in conjunction with segmented, discontinuous skins. Nonetheless it can be used together with elastic, flexible skins that avoid these discontinuities. However, potential shape changes are limited and the weight penalty due to the overlapping rigid bodies is large.

Figure 4.9: Various mechanisms for gapless trailing edges. (a) A truss that is based on triangular elements. The arc-length of the upper skin is preserved whereas the bottom skin has to undergo large stretching deformations. The degrees of freedom between the triangular elements can be merged into a single degree of freedom by using a drive train. (b) Single degree of freedom mechanism that consists of three rigid bodies, three struts and a linear actuator. It preserves the arc-length of the upper, flexible skin segment. The lower skin is continuous during cruise and discontinuous during takeoff and landing. (c) Mechanism with a single degree of freedom that is based on a chain of rigid bodies and a rotary actuator. The rigid bodies are connected to each other with hinges and sliders. Both, the upper and lower skins of the mechanism are stretched. (d) Single degree of freedom mechanism that is based on a three-dimensional cam and a rotary actuator. It stretches both, the upper and lower skins. (e) Compliant mechanism that consists of a central, flexible plate and two honeycomb cores that act as spacers between the plate and the skins. The mechanism is actuated by skins that can actively change their lengths. (f) Compliant mechanism that completely integrates the flexible, inextensional skins. The trailing edge is deformed by shear deformations that are caused by moving both ends of the skins in and out of the wing box.



A completely different mechanism was proposed by Müller [198] in 1996. It is based on a three-dimensional, rigid cam with a horn like shape that is rotated inside a cavity of an elastic, compliant trailing edge. The geometries of the line contacts between the cam and the upper, lower skin vary considerably during actuation so that both skins are usually stretched in the deployed configuration. This concept requires, due to the sliding line contacts, low friction surfaces that minimize actuation forces and wear. Another problem is the load transfer between the skins and the horn particularly on the suction side.

A compliant mechanism that avoids any moving parts, friction forces and discontinuities was developed by Maclean et al [177] in 1993. It is based on a central, flexible plate that is sandwiched between two honeycomb cores that act as spacers between the plate and the skins. The mechanism is either actuated by internally placed tendons that induce a bending moment at the tip of the trailing edge [21] or by skins that can actively change their length [177].

Arguably one of the most promising mechanisms for compliant, shape changing wings was developed by Campanile and Hanselka [39] in 1997. It is based on a closed, flexible skin whose upper and lower surfaces are connected via spokes. The wing is deformed by internally placed actuators that cause shear deformations. The shape of the deformed wing is thus defined by the stiffness, position and angle of each spoke. This concept was taken up by Kota and Hetrick [158] in 2003 for the development of a gapless trailing edge. It differs from previous approach insofar that shear deformations are created by moving the ends of the trailing edge skins in and out of the wing box. Such a trailing edge was apparently tested in a modified Gulfstream III that underwent a series of successful flight tests in 2014. These tests indicated potential fuel savings of up to 10% and noise reductions during landings of up to 40%. Although not directly related to high lift devices, a similar mechanism for grippers was patented by Bannasch and Kniese [16] in 2007.

Chapter 5

Skins

A wide range of applications require stiff skins with tailored, soft deformation modes. For example, an umbrella is a relatively simple structure with moderate shape and stiffness requirements in its deployed configuration. It consists of a watertight membrane that is locally supported and prestressed by a mechanism with a single degree of freedom in the deployed configuration. A deployed umbrella can carry large wind loads without significant deformations due to its prestressed skin. On the other hand, the bending stiffness of the unstressed skin is negligible so that even small compressive stresses lead to wrinkles. This drastically reduces the in-plane stiffness of the skin and thus enables a tight packaging of the umbrella as illustrated in Figure 5.1. A similar approach is used, for example, in nature for the wings of bats [119].

Currently used high lift devices of commercial and military airplanes are rigid bodies that are deployed and retracted with the help of relatively simple mechanisms and actuators. Despite being inexpensive and reliable, their inherent surface gaps are a bottleneck that limits potential noise reductions, fuel savings and stealth properties. This limitation led to the development of various approaches towards gapless high lift devices that can be incorporated into existing wings. Most of them have in common that they separate the design of mechanisms and skins [289]. Although tempting, such a separation is usually not helpful. Instead, it is necessary to design the soft deformation modes of otherwise rigid skins such that their shapes are fully defined by the displacements at a small number of points that are connected to the underlying mechanisms. Some general approaches for the design of anisotropic skins with a constant and variable in-plane and bending stiffness are subsequently presented.

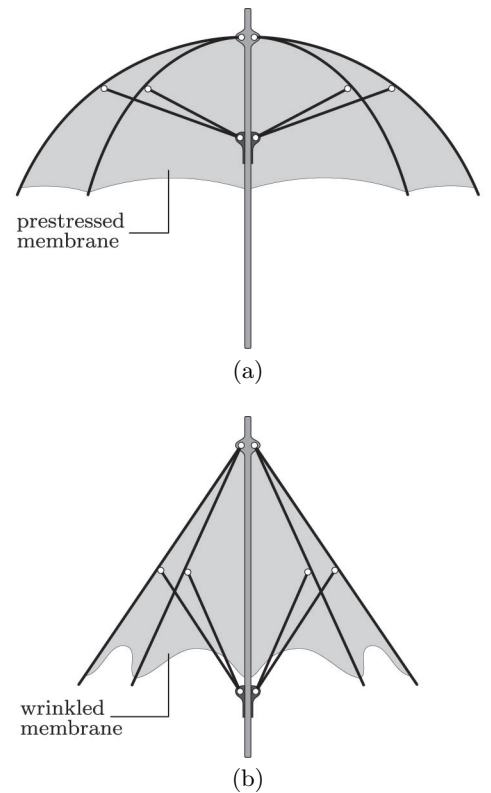


Figure 5.1: Mechanism and skin of a (a) deployed and (b) partially folded umbrella.

5.1 Poisson's Ratio

The complexity of a skin depends to a large degree on its Gaussian curvature [92]. An unstressed skin that possesses a zero Gaussian curvature is known to be developable. Wings with a constant chord length along their span are widely used in small airplanes. This is often a reasonable tradeoff with respect to their design complexity, manufacturing cost and aerodynamic efficiency. On the other hand, wings with a double tapered chord are often used in large passenger airplanes [105]. The variation of the outer taper is usually small so that skins of most high lift devices can be considered to be developable.

Developable surfaces with an infinitesimally small thickness have the benefit that their in-plane and bending strains are decoupled. However, skins of gapless high lift devices possess a finite thickness. This leads to a coupling between in-plane and bending strains if they are made from a material with a non-zero Poisson's ratio. This coupling either causes anticlastic curvatures or, if out-of-plane deformations are constrained, large in-plane stresses and support forces. Hence it is advantageous to use skin materials with a zero or nearly zero Poisson's ratio. Various design approaches for materials with a zero or negative Poisson's ratio¹ are subsequently reviewed. It is shown that a zero or negative Poisson's ratio can be introduced on a material and geometric level.

5.1.1 Material

Negative Poisson's ratios in single crystals were already observed by Voigt [306] in 1920. Many natural and biological materials that exhibit this property were discovered since then [164]. It is well known from the linear theory of elasticity that the Poisson's ratio of isotropic materials is bounded [106] between -1 and 0.5. In contrast, the Poisson's ratio of anisotropic materials [291] is unbounded which enables the design of fiber reinforced composites with extreme properties.

Fiber reinforced composites [79] with a negative Poisson's ratio in the in-plane direction were studied by Tsai and Hahn [294] in 1980. Composites with a negative Poisson's ratio in the out-of-plane direction were studied by Herakovich [122] in 1984. The achievable auxeticity of conventional laminates depends on the stacking sequence, fiber volume fraction and fiber stiffness. However, the negative Poisson's ratios that were realized thus far are moderate. For example, Miki and Morotsu [190] manufactured an unbalanced, bi-directional laminate with a negative in-plane Poisson's ratio of -0.4 in 1989 and Hine et al [124]

¹Auxetic is another commonly used term to designate materials with a negative Poisson's ratio. It was coined by Ken Evans and stems from the Greek word *auxesis* which means "increase".

manufactured an angle-ply laminate with a negative out-of-plane ratio of -0.5 in 1997.

Composites with a considerably smaller Poisson's ratio can be created with the help of auxetic fibers and/or an auxetic matrix [204]. Milton [193] showed in 1992 that rigid inclusions can be used to lower the Poisson's ratio of a composite matrix. However, these inclusions would have to be numerous and carefully placed as shown in Figure 5.2. Furthermore, they might have a detrimental effect on other composite properties so that auxetic matrices are currently not used.

The fiber volume fraction of round fibers is usually between 50-65% whereas the maximum achievable fraction is about 90%. As a consequence, due to the rule of mixtures, the gain from using auxetic fibers clearly exceeds that of an auxetic matrix. It was found by Caddock and Evans [36] in 1989 that the Poisson's ratio of polymers can be considerably lowered by a three stage process that consists of compaction, sintering and extrusion. Otherwise identical polypropylene fibers with a Poisson's ratio of -0.6 and 0.3 were used in different composite structures by Alderson et al [4] in 2002. They found that the pull-out force of auxetic fibers is twice as large as those of conventional fibers [266].

A fiber with a remarkably small Poisson's ratio was studied by Miller et al [192] in 2006. It consists of a helical and straight tread. The helical thread is relatively stiff and thin whereas the straight thread is soft and thick in the unstressed configuration. Upon loading, the fiber thickness increases as the helical thread becomes straight and the straight thread becomes helical. This geometric effect that alters the fiber thickness resulted in a Poisson's ratio of -2.1 during first tests. An auxetic knit structure with a similar mechanism was subsequently developed by Ugbolue et al [296] in 2007.

5.1.2 Geometry

Evans et al [78] pointed out that structures with a single, soft deformation mode and a Poisson's ratio of -1 were already developed during the 1950s for nuclear reactors [238]. Their graphite cores were designed to sustain large earthquakes and deformations due to non-uniform temperature distributions. Each core consisted of about 44,000 rigid bricks that were connected at their corners and sides via sliding joints. However, it took another three decades until structures with a geometrically induced negative Poisson's ratio were systematically investigated. Closed form expressions for the material properties of regular, compliant honeycombs were developed by Gibson and Ashby [96] in 1982. They showed that the material properties of a honeycomb cell can be tailored within a wide range by varying its geometry. A honeycomb with reentrant cell corners

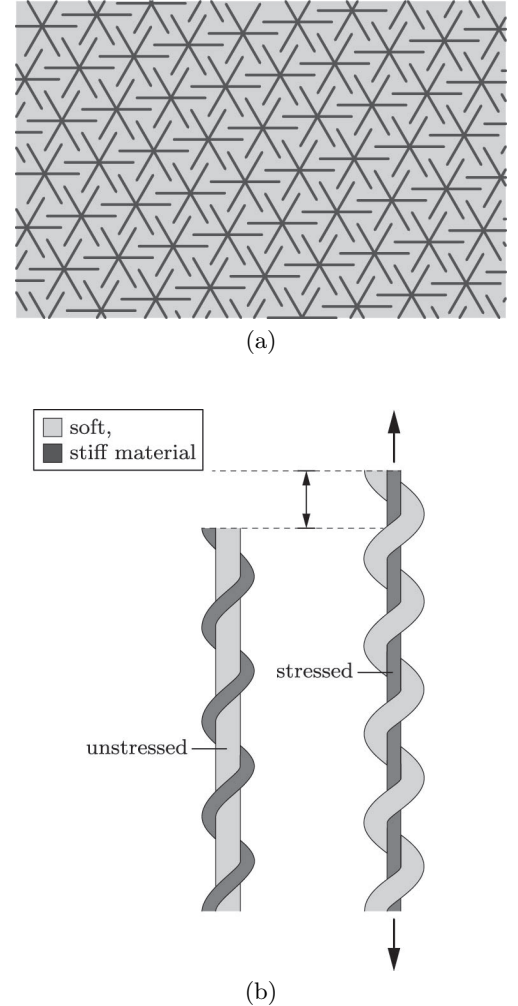


Figure 5.2: (a) The Poisson's ratio of a composite matrix can be reduced with the help of rigid, star shaped inclusions. (b) An auxetic fiber that consists of a helical and a straight thread. The helical thread is relatively stiff and thin whereas the straight thread is soft and thick in the unstressed configuration. The fiber thickness increases in the stressed configuration as the helical thread becomes straight and the straight thread becomes helical.

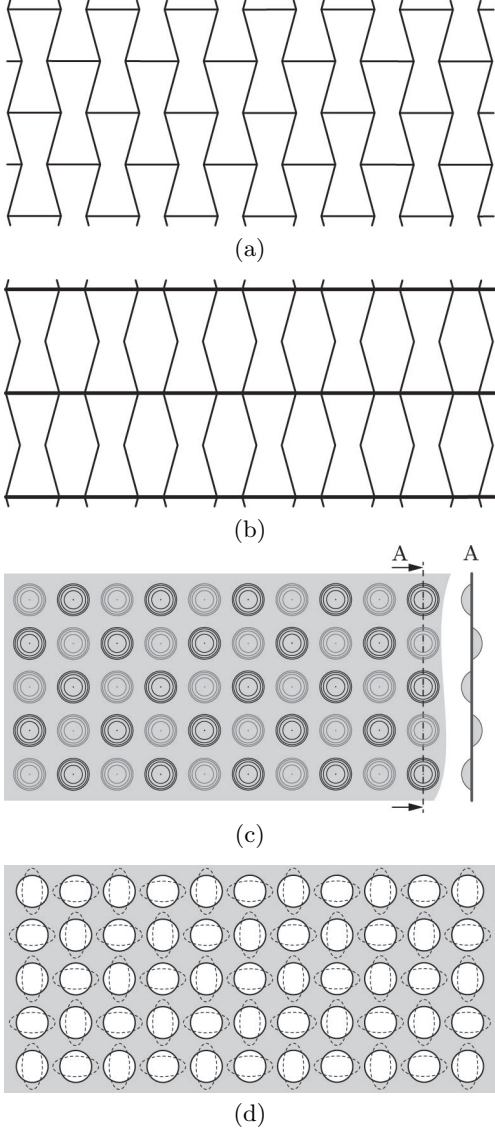


Figure 5.3: Different structures with a negative or zero Poisson's ratio. (a) Reentrant honeycomb with a negative Poisson's ratio. (b) Rectangular structure with a zero Poisson's ratio and a large, uniaxial in-plane and bending stiffness. (c) Sheet with spherical dimples that are arranged on both sides in a checkerboard pattern. (d) Sheet with a lattice of circular holes and superimposed deformation modes.

that possesses a small Poisson's ratio is shown in Figure 5.3. Various cellular structures with a negative or zero Poisson's ratio were published since then. Most of them were derived by using intuition or trial and error. Two approaches that can be used to systematically design these structures are subsequently discussed.

Linear topology optimization was used by Sigmund in 1994 for the design of regular cellular structures with desired material properties in two- [261] and three-dimensions [262]. This work was improved upon by Clausen et al [50] in 2015. They additionally considered nonlinear effects that enabled the design of structures with a constant Poisson's ratio for a wide range of strains. Rapid prototyping was used to manufacture a large number of structures with a Poisson's ratio between ± 0.8 . Experiments confirmed a nearly constant Poisson's ratio for strains of up to 20%.

Cellular structures with a regular, two-dimensional geometry are ultimately based on the triangular, rectangular or hexagonal tiling of a plane. Körner and Liebold-Ribeiro [153] showed in 2015 that a simple eigenvector analysis of a unit cell with straight sides is sufficient to find a large number of auxetic structures. Furthermore, they showed that this approach can be generalized to three-dimensions and semiregular structures. Hence it can be used to systematically classify previously published auxetic, cell based structures. For example, the eighth eigenvector of a triangular unit cell has close similarities with the chiral honeycomb that was published by Prall and Lakes [239] in 1997.

A completely different approach towards auxetic structures was developed by Golabchi and Guest [99] in 2009. They observed that the positive Poisson's ratio of a homogeneous and isotropic sheet can be lowered by regularly denting its surface on both sides in a checkerboard pattern. This effect that stems from the out-of-plane deformations of its dimples was rediscovered by Javid et al [134] in 2015. A similar effect that is driven by elastic instabilities was discovered by Bertoldi et al [24] in 2010. They found that the otherwise positive Poisson's ratio of an elastic sheet with regularly placed holes can become negative under compression loads. This work was extended to three-dimensions by Babaei et al [13] in 2013. However, the usefulness of this approach is limited due to the nonlinear relationship between the loading and the effective material properties.

5.2 Leading Edge

An airplanes leading edge skin needs to protect the wing against erosion, icing, lightning- and bird strikes. For example, commercial passenger jets are hit about once a year by a lightning strike [90]. In addition, more

than 65,000 bird strikes that led to nine human fatalities were reported [51] in the United States during a fifteen year period. The design of lightweight skins that can safely operate under these conditions is difficult. Leading edge skins of modern passenger airplanes such as the Boeing 787 are made from carbon fiber metal laminates. Their deicing system is based on an integrated metal layer that is sandwiched between two insulating glass fiber fabrics as illustrated in Figure 5.4.

The mechanism of a shape changing leading edge can be designed such that it preserves the arc-length of its skin. As a consequence, the required actuation energy depends solely on the skins bending stiffness in chordwise direction. On the other hand, the skin needs to be stiff enough to minimize deformations due to external loads. These conflicting demands can only be satisfied by highly anisotropic skins whose bending stiffness is large in spanwise and small in chordwise direction. Furthermore, it is advantageous if the impact protection and deicing systems are decoupled from the skins. The front spar of a wing and thus the fuel reservoir can be protected against bird strikes with the help of secondary structures that are placed inside of the leading edge [43]. The deicing can be realized by internally placed ventilation systems that circulate hot bleed air [102].

A skin with a varying thickness that breaches under impact was investigated by Kintscher et al [149] in 2009. It consists of an anisotropic glass fiber laminate that is reinforced by stringers in spanwise direction. The positions of the stringers are chosen such that they additionally serve as attachment points for the underlying mechanisms. Geier et al [93] investigated the attachment of a deicing system to such a skin. They found that the outer skin strains can be considerably reduced if a thin rubber layer with a low shear stiffness is placed between the glass fiber laminate and the deicing system. The use of a rubber layer has the additional benefit that it reduces the energy consumption of the deicing systems since it acts as an insulator. Furthermore, it slightly increases the impact resistance of the skin and thus reduces the requirements for the internally placed, secondary structure.

5.3 Trailing Edge

Skins for shape changing leading- and trailing edges differ insofar that the latter have to additionally undergo large in-plane strains in chordwise direction. These strains, that are caused by the discontinuous trailing edge geometries, increase the overall design complexity. However, trailing edge skins do not require a deicing- or impact protection system. Furthermore, they are less susceptible to erosion.

Leading edge skins usually consist of thin laminates that are based

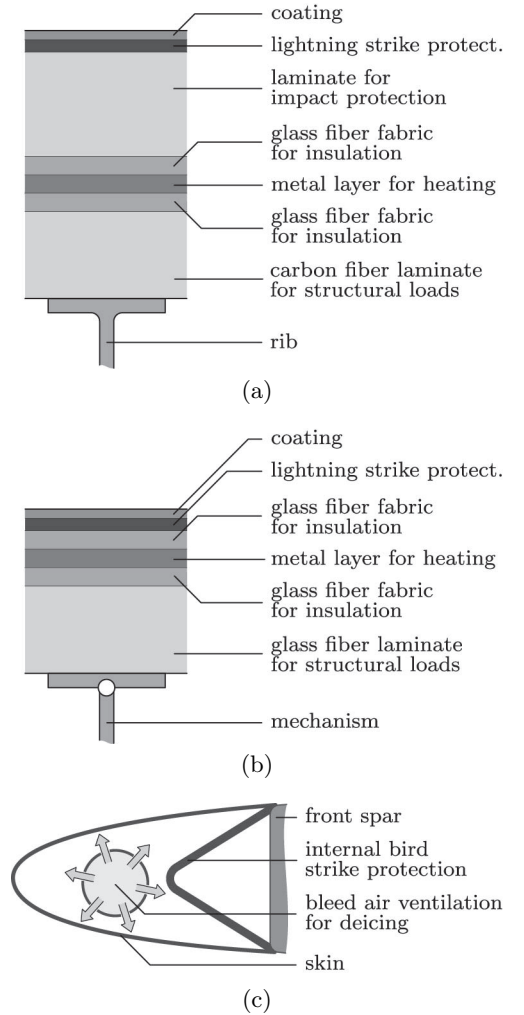


Figure 5.4: (a) The impact resistive leading edge skin of a Boeing 787 is made from a carbon fiber metal laminate. Its deicing system is sandwiched between two insulating glass fiber fabrics. (b) A similar approach for a shape changing, non-impact resistive leading edge skin that consists of a glass fiber laminate. (c) Its impact protection and deicing system can be placed inside of the leading edge.

on low modulus fibers. However, these kind of laminates can not undergo the large in-plane strains in chordwise direction that are required by trailing edge skins. As a consequence, the anisotropy of trailing edge skins needs to be even more extreme. Their carefully tailored soft deformation modes have to be fully controlled by the underlying mechanisms. The design of such skins has, due to their extreme anisotropy, many similarities with the development of rigid body mechanisms. Hence it is not surprising that they are mostly designed on a geometric level.

5.3.1 Sandwich

Some of the most promising approaches towards trailing edge skins are based on sandwich structures with hyperelastic face sheets and cell cores with a zero Poisson's ratio. For example, an anisotropic core with a rectangular unit cell as illustrated in Figure 5.5 was investigated by Olympio and Gandhi [210]. The face sheets are supported by the straight, rigid sides in spanwise direction whereas the accordion like structure of the core enables large shape changes in chordwise direction.

A drawback of this approach is that the face sheets are only supported in spanwise direction. Other cell sides can not be connected due to different relative motions. As a consequence, these sides can only provide contact forces against out-of-plane deformations on the pressure side of an airfoil. Another problem is the relatively small bending stiffness of the core in chordwise direction. Bubert et al [33] showed that this stiffness can be increased with the help of guided beams. However, the required sliding mechanisms have a detrimental impact on the skins weight, complexity and maintenance requirements.

5.3.2 Corrugated Shell

Other approaches for the design of trailing edge skins are based on corrugated shells that possess a relatively small in-plane and bending stiffness in chordwise direction due to their prismatic, wavy geometry as shown in Figure 5.6. Similar to previously discussed cell cores, corrugated shells can only support the face sheets in spanwise direction. Hence it does not make much of a difference if the face sheets are supported by cell cores or corrugated shells.

The use of corrugated shells for trailing edge skins was first proposed by Yokozeki et al [323] in 2006. A large number of different geometries and various combinations of corrugated shells were investigated since then. For example, the use of two symmetrically stacked shells was studied by Thill et al [290] in 2007. This arrangement leads to closed, rectangular cells that considerably increase a skins torsional stiffness.

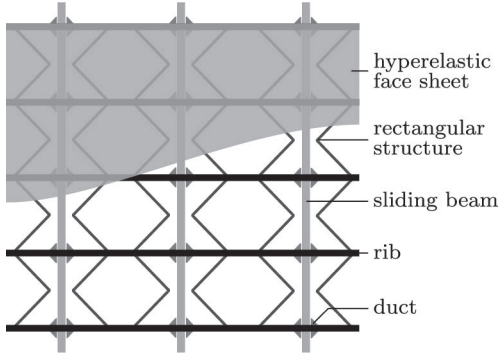


Figure 5.5: Top view of a trailing edge skin that consists of a cell core with a zero Poisson's ratio and hyperelastic face sheets. Additional sliding beams can be incorporated into the core to vary the bending stiffness in chordwise direction.

A further advantage of this approach is that the in-plane and bending deformations are decoupled. Furthermore, the stiffness of single cells can be varied with the help of foam inserts. A similar approach that is based on a nested combination of two corrugated shells was proposed by Previtali et al [240] in 2014. This arrangement preserves the decoupling between in-plane and bending deformations and additionally increases the outer thickness and thus the bending stiffness in spanwise direction.

The use of corrugated skins is, at least from an aerodynamic point of view, disadvantageous. Their wavy surfaces can be smoothed by filling one side of the shells with an elastomer that might or might not be reinforced in spanwise direction as illustrated in Figure 5.7. Unfortunately, the weight penalty of such an approach is usually prohibitive. Airolidi et al [2] proposed the incorporation of lightweight honeycomb cores that act as fillers between the corrugations and thin, elastic face sheets. However, as before, it is not possible to directly connect the face sheet to the honeycombs due to different relative motions. Thill et al [290] avoided these problems by using segmented face sheets instead. Two neighboring segments can be connected via simple sliding mechanisms to reduce out-of-plane deformations. This approach is widely used in nature and can be found, for example, in shark skins and bird wings [22].

5.4 Variable Stiffness

The carefully tailored deformation modes of otherwise stiff skins enable large shape changes. However, their deformations can only be controlled by the underlying mechanisms at a few locations so that large, undesired displacements can generally not be avoided. As a consequence, it is either necessary to tightly support the skins with complex mechanisms or to actively control their stiffness. The weight penalty of closely spaced supports is usually prohibitive so that different approaches for variable stiffness structures were developed. Some of the most promising approaches that are based on a variation of the material and geometric properties of substructures as well as friction forces between them are subsequently reviewed.

5.4.1 Material

A programmable structural element that can switch between different nonlinear stiffness functions can be realized on the basis of feedback controlled actuators, Figure 5.8. These actuators utilize force and position sensors as well as microprocessors and complex algorithms [251]. Programmable elements are mainly used in robotics where they enable a fast, software centered development. The complexity of a programmable element can be significantly reduced if it only needs to switch between two constant stiffness values. Such an element that functions without

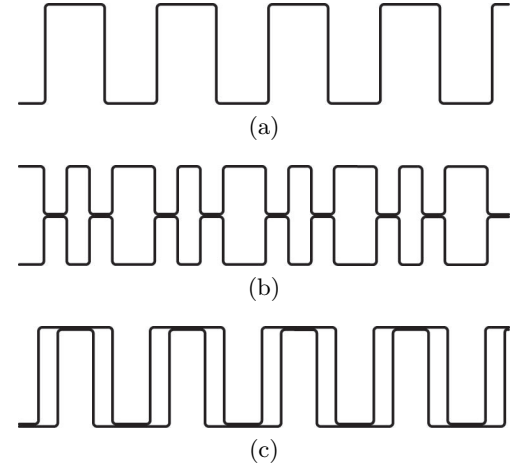


Figure 5.6: Side views of corrugated trailing edge skins. (a) A single, (b) symmetrically stacked and (c) nested shell.

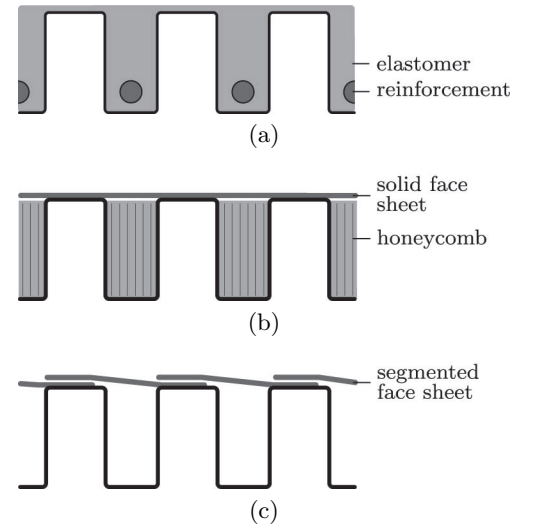


Figure 5.7: Smoothing of corrugated shell surfaces. (a) An elastomer filled shell with additional reinforcements in spanwise direction. (b) A face sheet is supported by an internal honeycomb core against pressure induced out-of-plane deformations. (c) Segmented face sheet.

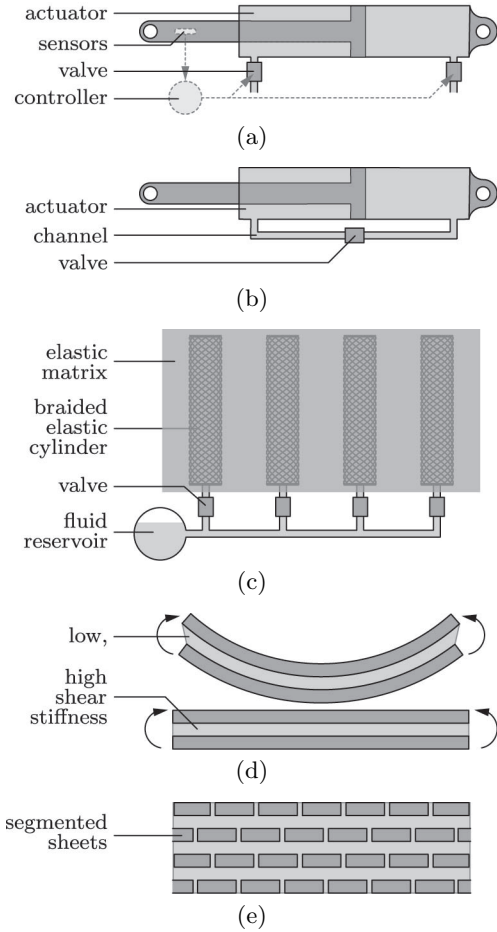


Figure 5.8: Material based approach for variable stiffness structures. (a) Feedback controlled actuator with a microprocessor, sensors and valves that can switch between arbitrary force displacement relationships. (b) A simplified actuator with connected ports and a single valve that can switch between two constant stiffness values. (c) A similar approach that is based on a number of compliant, pneumatic muscles that are embedded in an elastic matrix. (d) A sandwich structure with continuous face sheets and a variable stiffness core. (e) A sandwich structure with a large number of layers that alternately consist of a polymer and hexagonal platelets.

sensors, microprocessors and complex algorithms was developed by Kobori et al [151] in 1993. It consists of a double acting, hydraulic cylinder whose ports are connected via a valve. A closed valve leads to a large stiffness that is only limited by the compressibility of the fluid and the elasticity of the cylinder. In contrast, an open valve enables a flow between both ports so that the elements stiffness becomes negligible. This relatively simple and robust approach has a fast response time and requires only a small amount of energy. Hence, it is widely used in buildings that need to vary their stiffness during earthquakes. However, the one-dimensional nature of these elements renders them unsuitable for an application in airplane skins.

A plate like element with a variable stiffness that is based on a similar approach was proposed by Shan et al [259] in 2009. It consists of a large number of pneumatic muscles that are embedded in an elastic matrix. These actuators can be arranged in several layers and their orientations might vary between layers or even within a single layer. Actuators can be combined into groups of varying sizes such that their in- and outflow is controlled by a single valve. This reduces the control complexity and enables tailored stiffness variations within a plate.

A sandwich structure with a variable bending stiffness was proposed by Martin et al [180] in 1998. It consists of a thermoplastic polymer core² and continuous, flexible face sheets. The material for the core is chosen such that its glass transition temperature is well above the structures operating temperatures. The highly nonlinear relationship between the polymers temperature and shear modulus around its glass transition temperature is exploited to vary the bending stiffness of the sandwich. This can be done by using heating and/or cooling elements that are embedded in the sandwich core. The performance of these structures is limited by the continuous face sheets that allow only developable deformations. Inspired by bio-composites [136, 311] such as nacre and dentin, McKnight et al [187] overcame this problem by using a large number of layers that alternately consist of a thermoplastic polymer and hexagonal platelets.

The response times of these structures is limited by the heat capacity and thermal conductivity of their polymer layers. Furthermore, the use of heating and/or cooling elements is energy intensive. Alternative materials [160] with a variable stiffness that improve upon some of these aspects include phase transition, magnetorheological and electrorheological materials. For example, shape memory alloys such as Ni-Ti can

²High melting thermoplastics such as the semi-crystalline polyether ether ketones (PEEK) and the amorphous polyether sulfones (PES) are commonly used. The shear modulus of a thermoplastic polymer can decrease by up to two orders of magnitude if it is heated above its glass transition temperature.

undergo a solid-solid phase transition. The Young's modulus of their high temperature phase is about 80 GPa whereas their low temperature modulus is about 30 GPa.

5.4.2 Friction

A granular material can have, depending on its loading, temperature, density, geometric and material properties, the characteristics of a solid and a fluid [166]. The jamming of a granular material can therefore be considered to be a special case of a solid-solid phase transition, Figure 5.9. For example, the vacuum packaging of coffee beans that is done since the early 1900s leads to rigid bodies whereas the unpacked beans can flow from a storage tank into the grinder of a coffee machine. This effect was subsequently exploited by Suits [277] in 1952 for portable shelters and by Campanaro et al [38] in 1962 for shapeable structures.

Granular materials possess a large number of degrees of freedom so that they can be formed into a wide range of shapes. However, this is usually neither required nor desirable so that simpler systems with only a few degrees of freedom are commonly used instead. For example, rotary clutches possess only a single degree of freedom. Their torsional stiffness is often varied by changing the normal force induced friction forces between two layers. These normal forces can be generated with the help of pressure, mass inertia, electric charges or electromagnetism.

A similar approach can be used for layered bars, beams and plates. The available publications in this field differentiate themselves with respect to the normal force generation and the layer geometry. For example, Tabata et al [282] proposed the use of one-dimensionally stacked plates with patterned electrodes in 2001. Electrostatic forces between plates are generated by alternately connecting them to a high voltage source. The use of vacuum induced pressure forces and two-dimensionally stacked beams that enable biaxial stiffness variations was subsequently proposed by Kawamura et al [144] in 2002. It was pointed out by Kim et al [148] in 2012 that the previous approach can be easily extended towards beams with a varying in-plane and bending stiffness.

5.4.3 Geometry

The second moment of area of a layered structure is indirectly affected by the friction forces between its substructures. Instead of using friction forces, it is possible to directly vary a structures geometric properties by applying translations or rotations to its otherwise rigidly connected substructures. For example, Griffin et al [107] filed a patent in 1998 where they describe a rotating, elliptic trailing edge spar that varies a

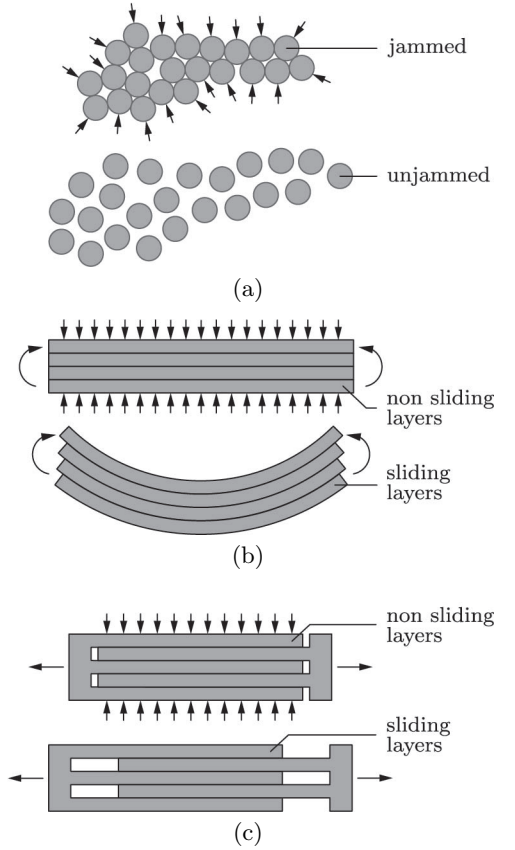


Figure 5.9: (a) Jamming induced stiffness variation of a granular material. Friction induced stiffness variations of a layered (b) beam and (c) bar.

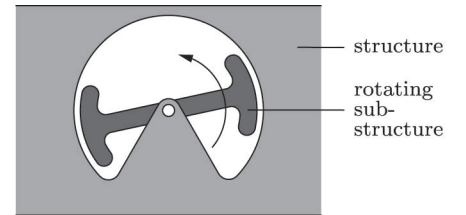


Figure 5.10: A structure's second moment of area and thus its stiffness is varied by the rotation of a substructure.

wings second moment of area.

Chapter 6

Plant Movements

None of the previously developed gapless high lift devices is currently used in commercial or military airplanes. This is due to the additional weight and complexity that primarily stems from the moderate integration of actuators, mechanisms and structures. The development of a novel concept for highly integrated shape changing structures is therefore indispensable. Structures with various integration levels can be found in nature [15]. For example, humans tend to build heavy machinery from rigid bodies, frictionless hinges and hydraulic cylinders as illustrated in Figure 6.1. A similar approach is used in humans and large animals where the hydraulic cylinders are substituted by compliant muscles. This approach is further refined in smaller animals such as bees where the segmented joints are additionally substituted by compliant hinges. Nonetheless, the integration level of these structures is still relatively small in comparison to plants [109] where it is often impossible to distinguish between their components. Plants achieve such an integration by using a large number of compliant cells with tailored geometries and a pressure medium for actuation. Furthermore, unlike humans and animals, they do not possess a central control system. If well understood, their working principle might enable the creation of gapless high lift devices with a reduced part count, weight and complexity.

Depending on the species and intended purpose, the complexity and speed of plant movements vary significantly. A comprehensive selection of automatic and stimulated movements is discussed in the following. A focus is put on the movements that are triggered by non-directional stimuli as they are of particular interest for the development of shape changing structures. It is pointed out that the interactions between cell geometries, cell materials, cytoskeletons and osmotic hydration motors are far-reaching and well beyond the movement of plants.

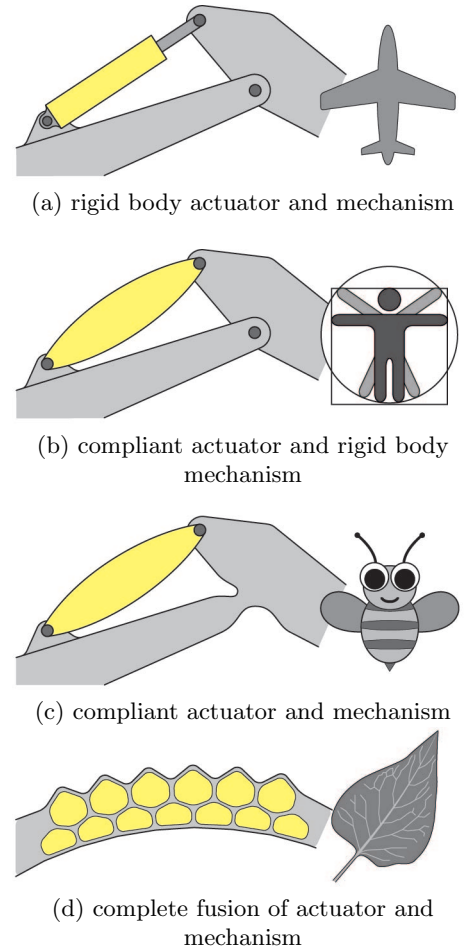


Figure 6.1: Implementation of a single degree of freedom mechanism and actuator in (a) heavy machinery, (b) humans (c) bees and (d) plants.

6.1 Automatic Movements

Plants are bound to the place where they germinate. Nonetheless, they are far from being immobile as they can adapt to their environment by changing the shape of their roots, stems and leaves. These movements are either automatically initiated or triggered by directional or non-directional external stimuli. Fully automatic movements are commonly used by plants to disperse their pollen and seeds or to find mechanical support [275]. Their speed varies between the slow growth of shoots and roots to the explosive rupture of seed pods. Automatic movements are either passive or active. Active movements depend on the plant metabolism whereas passive movements are driven by external energy sources such as temperature and humidity gradients. Furthermore, the energy can be continuously translated into movements or stored inside the plant to enable rapid, discontinuous shape changes.

6.1.1 Passive Movements

Continuous

Some of the simplest plant movements are driven by the swelling and shrinking of cell walls. The matrix of these fiber reinforced composite structures can undergo large volume changes due to the influx and efflux of water whereas the fiber lengths remain unchanged. The different characteristics of the cell wall constituents enable tailored plant movements that are driven by humidity gradients. This principle is widely used by plants to disperse their seeds and to improve the conditions for germination. For example, pine seeds are protected within a cone during their growth phase that can take up to three years. Upon maturation, they are automatically released if the weather is warm and dry [60] so that they can be carried away by the wind. The cone opening is accomplished by the bending of a large number of scales as illustrated in Figure 6.2. Scales are bi-layered structures with different fiber orientations. The fibers of the upper and lower layers are in the radial and tangential directions, respectively. This leads to different axial strains in each layer as the swelling and shrinking deformations are orthogonal to the fiber directions. Poppinga et al [236] showed that this simple approach works reliably even in 15 million year old conifer cones.

Another example for humidity driven passive movements can be found in wheat awns [76]. Each seed is attached at its rear to two awns that help to improve its germination conditions. Awns stabilize the seeds free fall after the separation from the ear and propel it along and into the ground. They are curved towards the outside during daytime when the humidity is relatively low and nearly straight during nighttime when the humidity is high. The seeds mobility is further improved by a large

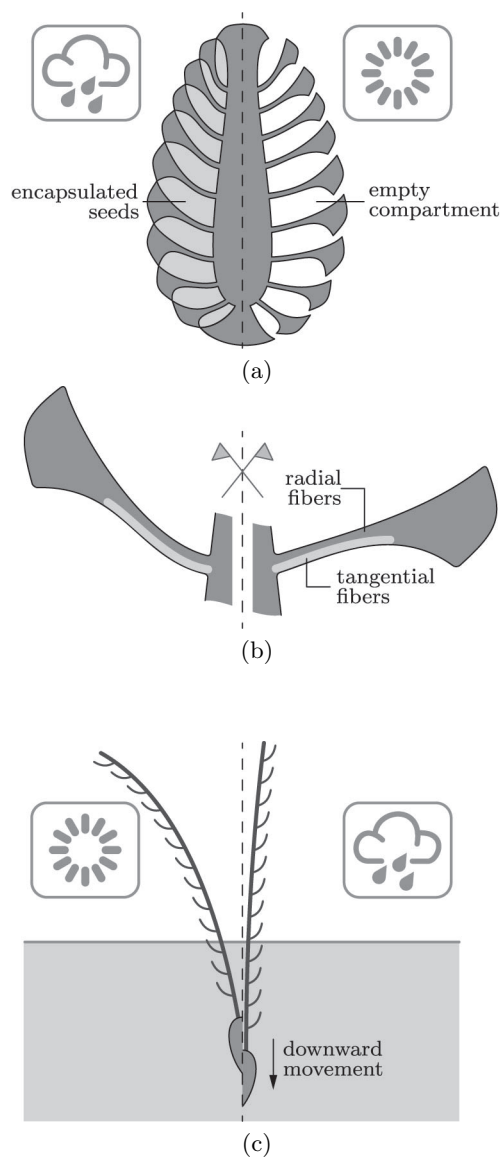


Figure 6.2: Plant movements that are driven by the continuous swelling and shrinking of cell walls. (a) Pine cone and (b) scale in a humid and dry environment. Pine cones open in a dry environment to release seeds. (c) Self burial of wheat due to awn movements. Seed depth increases during each dry-humid cycle.

number of hairs that cover the awns. These hairs act as hooks and point towards the tip of the awn. They support the seeds movement into the ground and hinder its pull-out. A similar approach that is based on a single awn that undergoes helical instead of bending movements is used by *Erodium cicutarium* [273]. These awns can bury their seed into a favourable, porous ground over the course of five day-night cycles. A further increase in the complexity of passive plant movements can be observed in ice plant seed capsules [115]. Their valves are shell like structures that translate the swelling and shrinking of cell walls via curved hinge lines into two-dimensional shape changes.

Discontinuous

Continuous plant movements that are driven by the swelling and shrinking of cell walls are relatively slow. They are thus often used for the release of winged seeds that can independently travel over large distances. In contrast, the ballistic dispersal of reproduction units requires considerably faster movements. Based on the same actuation principles, a significant speedup can only be achieved by the storage and sudden release of elastic energy.

The fruit of *Cardamine parviflora* from the mustard family Brassicaceae contains about 300 seeds that each weighs about $150\text{ }\mu\text{g}$. The seeds are attached to a replum and protected by two valves as illustrated in Figure 6.3. The elastic bending energy that is stored in the bilayered valves through water evaporation is suddenly released upon reaching a critical stress between valves and replum [304]. The subsequent coiling motions of the valves accelerate the seeds to velocities of up to 12 m/s that is sufficing for distances of about 2 m. An interesting property of

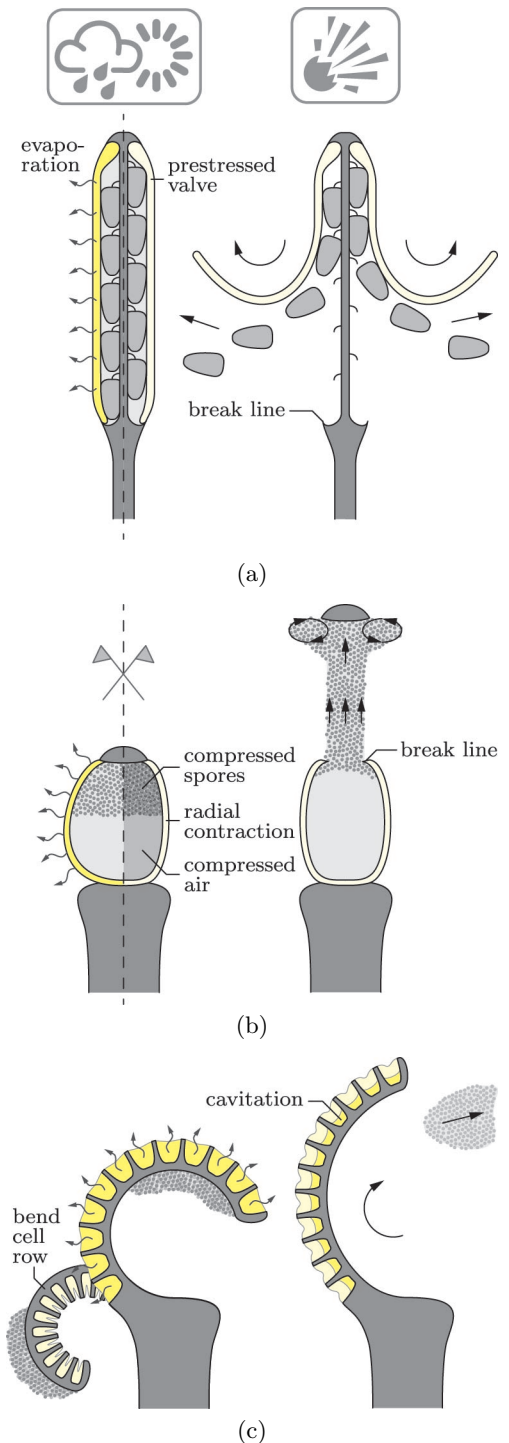


Figure 6.3: Discontinuous plant movements that are driven by water evaporation. (a) Valves of *Cardamine parviflora* (Brassicaceae) are prestressed through water evaporation. Fracture between valves and replum leads to rapid coiling movements. Seeds are accelerated by adhesion forces that decrease with increasing valve curvatures. (b) Capsule of genus *Sphagnum* (Sphagnaceae) is equally filled with air and spores. Water evaporation leads to a radial contraction and thus to an increased air pressure. Spore dispersal is triggered by a fracture between capsule and lid. The spore range is considerably increased by turbulent vortex rings near the ejected lid. (c) *Phlebodium aureum* (Polypodiaceae) disperses its pollen without predetermined breaking lines. Water evaporation from a cell row leads to large bending deformations. Rapid movements are triggered by the cavitation of the remaining cell water upon reaching a critical pressure. Spore dispersal occurs after a sudden retardation around the midway due to an internal damping system.

this ejection mechanism is that the valves move away from the seeds and thus do not exert any contact forces upon them. Instead they are accelerated by adhesion forces that decrease with increasing valve curvatures. However, the sensitivity of the adhesion forces to variations of the valve moisture leads to a high variability of the launch performance.

A similar approach that is based on contact instead of adhesion forces is used by *Tetraberlinia moreliana* from the family Leguminosae that is native in Gabon and the south-west of Cameroon [300]. Its fruit consists of two connected valves that cover up to four seeds with an average weight of about 2.5 g. Drying of the valves leads to the buildup of elastic energy that is suddenly released upon reaching a critical stress between both valves. The subsequent helical valve motions catapult the seeds to distances of up to 60 m by accelerating them to velocities of 37 m/s. Even greater speeds are achieved by *Hura crepitans* from the family Euphorbiaceae. This evergreen tree is domiciled in the tropical regions of North and South America and the Amazon Rainforest. Its fruit is a pumpkin shaped capsule that contains 7-16 seeds that each weighs about 1 g. Water evaporation from the fruit tensions the carpels and thus compresses the seeds. The carpels split at a critical stress into two halves and separate from the rotation axis of the fruit [280]. This disintegration leads to squeeze forces that accelerate the seeds to velocities of 70 m/s. Despite the relatively small seed mass, ejection distances of up to 45 m were observed. Due to the emitted noise at dispersal, *Hura crepitans* is sometimes known as the monkey's dinner bell. However, the raw seeds are poisonous for humans and most animals.

Plants such as *Sphagnum fimbriatum* of the family Sphagnaceae store the elastic energy for the spore dispersal in compressed air instead of elastic cell walls. They use spherical capsules that are divided into two compartments. Up to 240,000 spores are developed in the upper part whereas the lower part is filled with air. The airtight capsule wall that is relatively dark on the outside consists of four to five layers. Water evaporation from the wall at sunny days leads to a cylindrically shaped capsule with a smaller volume and a nearly identical height [302]. Spore ejection is initiated at a differential pressure of about 400 kPa by the failure of a breaking line between the capsule and the lid. The compressed air ejects the spores at maximum speeds of 30 m/s. The vertically launched spores that are 22 to 45 μm in size reach altitudes of nearly 20 cm so that they can be carried away within the turbulent boundary layer. These impressive altitudes are enabled by the relatively low drag coefficients of turbulent vortex rings that form in the vicinity of the ejected lid [313].

The water potential of air with a relative humidity of 50% is about -94 MPa. It is a measure for the work that needs to be done to add a unit volume of water from the air to the plant. As a consequence,

water evaporation in conjunction with stiff cell walls can lead to negative pressures that exceed the cohesion of the cell water. This causes a vaporization of the water and thus large volume changes that release most of the elastic cell wall energy. The sudden release of elastic energy due to cavitation is utilized during the spore dispersal of ferns such as *Polypodium aureum* from the family Polypodiaceae [167]. Their main component is a cell row that encloses the spores in its hydrated configuration. Loss of water from the 12 to 25 cells through evaporation leads to a slow bending deformation and to a collapse of the lateral cell walls. The cavitation that occurs at pressures of about -10 MPa causes a rapid movement towards the fully hydrated shape. The ejection angle of the spores during this movement is determined by an internal damping system that causes a sudden retardation around the midway. The spores that are about 45 μm in size are accelerated to speeds of up to 10 m/s and dispersed over distances of 20 mm. This approach is outstanding as it does not require any predetermined breaking lines.

6.1.2 Active Movements

Continuous

Active movements differ from passive movements insofar that they receive the required energy from the plant metabolism. Hence they are tightly controlled by the plant and independent of the environmental conditions. The energy for these movements is usually provided by the pressure variations and/or directed growth of cells. As for passive movements, the energy can be stored and rapidly released [250] or continuously translated into shape changes.

Plants rarely grow in one direction. Instead they oscillate around a mean growth direction [32]. These movements that are known as circumnutation follow an elliptical orbit if viewed from the mean growth direction and thus resemble a helix as the plant grows as shown in Figure 6.4. The amplitude, period and shape of circumnutations can vary greatly and depends on the species, the involved plant organs and the developmental stage. For example, the shoots and tendrils of many climbing plants move regularly on circular orbits whereas other, non-climbing plants may exhibit highly irregular movements that hardly resemble an elliptical orbit. Furthermore, the purpose of circumnutations can differ significantly. Climbing plants use these regular movements to find mechanical supports for shoots and tendrils whereas the benefit of circumnutations in many non-climbing plants remains unclear.

Plant growth is, to a varying degree, driven by plant hormones that are known as auxins [87]. They influence the cell divisions and cell elongations that lead to plant movements. Subdivided cells are elongated by increased cell pressures and reinforced by the deposition of additional cell

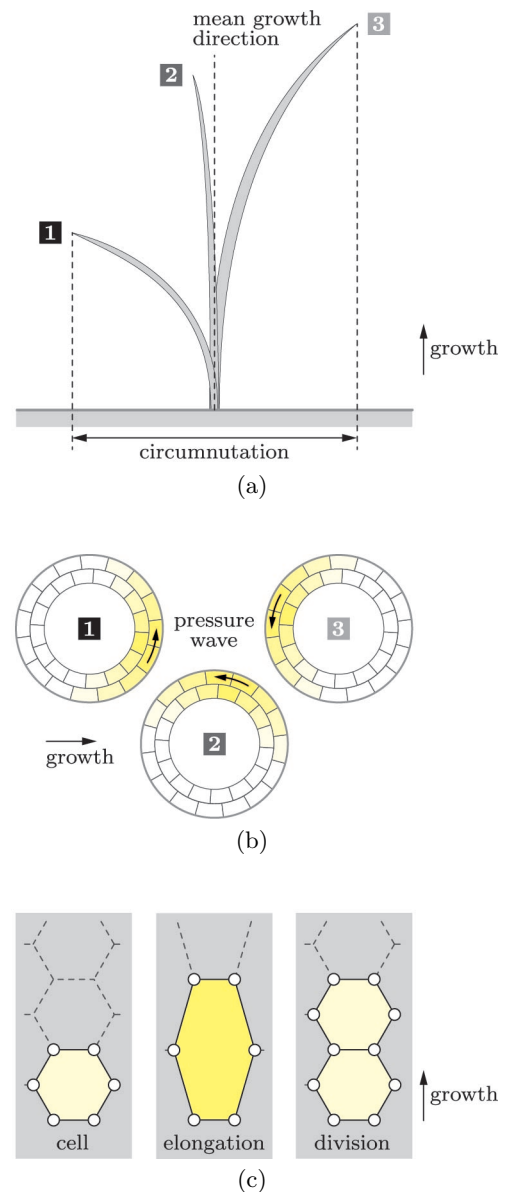
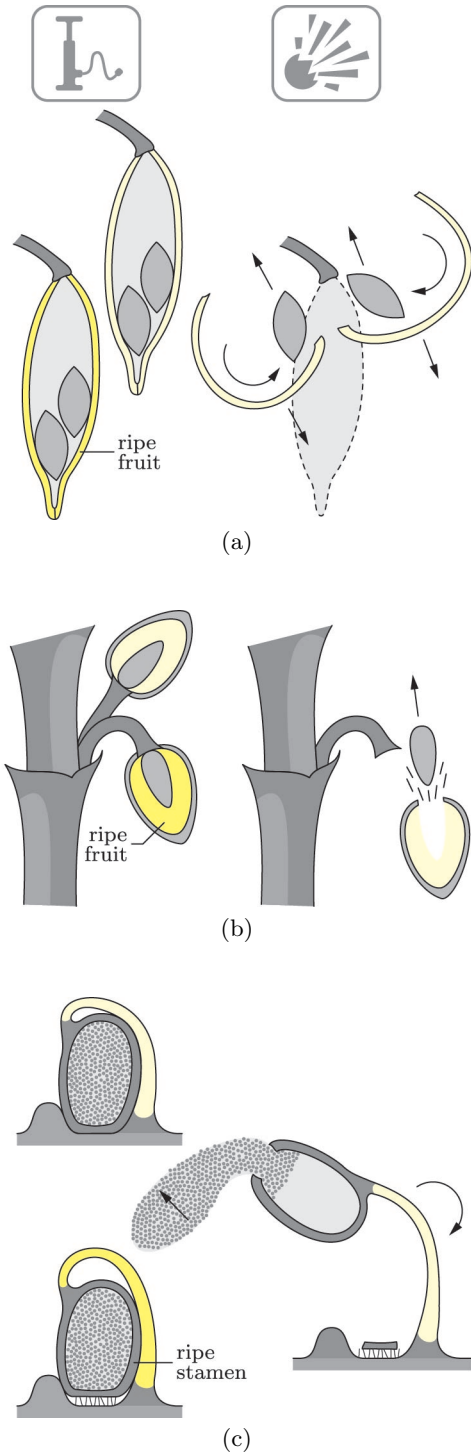


Figure 6.4: Circumnutation of plants due to local cell elongations and cell divisions. (a) Oscillation around the mean growth direction. (b) Cross section of stem and pressure wave that travels in counterclockwise direction. (c) Longitudinal growth through pressure driven cell elongation and cell division.



wall materials. Although not fully understood, it is likely that circumnutations are caused by rotating turgor waves during growth [121]. The period of these waves differs significantly and ranges between twenty and three-hundred minutes in most plants. For example, cell walls in *Phycomyces* can grow in longitudinal directions with strain rates of more than fifty per day [138]. Nonetheless, circumnutations are considerably slower than the speeds that can be achieved by the sudden release of energy due to fracture or cavitation. Furthermore, they are far more complex and less understood. Particularly the interaction of auxins with other plant processes and their detailed involvement in the division and elongation of cells is still an open question.

Discontinuous

Impatiens glandulifera from the family Balsaminaceae is a highly invasive plant that conquered much of the Northern Hemisphere. Part of *I. glandulifera*'s success can be attributed to its efficient seed dispersal mechanism. Each of its seed pods consists of five valves that enclose 5 to 10 seeds that each weighs about 7 mg. The valves are bilayer structures where water absorption shortens the inner and expands the outer layer. This leads to tension stresses in the inner and compression stresses in the outer layer as deformations are constrained by connections between the valves. It is speculated that the elastic bending energy that is stored in the valves is at least partially generated by plant controlled cell pressures [118]. Hence it seems plausible that the fracture between the valves and thus the seed dispersal can be actively triggered. About 45% of the elastic energy that is released during valve coiling is transferred into the kinetic energy of the seeds [64]. Initial velocities of 12 m/s were observed

Figure 6.5: Discontinuous plant movements that are driven by cell pressures. (a) Valves of *Impatiens glandulifera* (Balsaminaceae) are pre-stressed by cell pressures. Fracture between valves and a subsequent separation from the stem leads to rapid coiling movements. Seeds are accelerated by momentum exchange. (b) Seeds of the genus *Arceuthobium* (Santalaceae) are embedded in a sticky layer of viscin cells that is surrounded by the exocarp. Unripe fruits point upwards whereas pressurized, ripe fruits bend downwards. Elastic energy due to the hydrostatic pressure of the viscin cells is stored in the exocarp. Thermogenesis leads to a separation between the pedicel and the fruit. A contraction of the exocarp causes squeeze forces that accelerate the seed upwards. (c) *Morus alba* (Moraceae) resembles a classical catapult. A pollen filled anther is attached to a curved filament that stores elastic energy. The anther is accelerated on a circular trajectory after slippage past a mechanical restraint.

that catapult the seeds to distances of up to 10 m. This is particularly remarkable as the less invasive *Impatiens capensis* from the same genus utilizes only about 0.5 % of the elastic valve energy for the acceleration of its seeds.

The plants of the genus *Arceuthobium* from the family Santalaceae are commonly known as dwarf mistletoes. They cause considerable economic damage by parasitizing species of Pinaceae and Cupressaceae in North and Central America, Asia, Europe and Africa. The ellipsoidal fruits of dwarf mistletoes contain a single seed with a weight of about 2 to 3 mg. The seed is embedded in a sticky layer of viscin cells that is surrounded by the exocarp as illustrated in Figure 6.5. The pedicel of a ripe fruit changes its shape so that the fruit apex points downwards. Furthermore, an abscission zone develops between the pedicel and the fruit. The elastic energy for the fruit dispersal that is stored in the exocarp is generated by the hydrostatic pressure of the viscin cells. A remarkable property of these plants is that the seed dispersal is actively triggered by thermogenesis [63] that initiates a failure in the abscission zone. The fruit is sheared from the pedicel and the rapid contraction of the exocarp causes squeeze forces that accelerate the aerodynamically shaped seeds to velocities of up to 25 m/s [117]. The vertically ejected seeds can reach altitudes of 20 m. Some of them stick to upright needles during their descent at which they slide down during rainfall to get in contact with the bark.

Morus alba from the family Moraceae is a small to medium-sized tree that is native to North China. Its male inflorescence possesses about 60 individual flowers where each floral bud incorporates four stamens [287] that have much in common with manmade catapults. The pollen filled anther is connected to a curved filament that stores the elastic energy generated by cell pressures. Anther movements are prevented by fine threads and a mechanical restraint. Slippage past the restraint is triggered by increasing cell pressures. The anther that is torn open during the slippage is moving on a circular trajectory so that the pollens are accelerated by centrifugal forces. Velocities of up to 240 m/s were observed which is one of the fastest movements recorded in biology thus far. It is particularly remarkable as it approaches the physical limits for plant movements. The pollens of *M. alba* that have a diameter of about $25\text{ }\mu\text{m}$ are dispersed by this mechanism over distances of up to 65 mm.

A slightly different approach is used by *Cornus canadensis* from the family Cornaceae that is native to Eastern Asia. Its dispersal mechanism differs from *M. alba* insofar that it resembles more a trebuchet than a classical catapult [71]. Each flower consists of an inset and four anthers that are flexibly connected to filament tips as illustrated in Figure 6.6. A characteristic of *C. canadensis* is that the elastic energy for the pollen

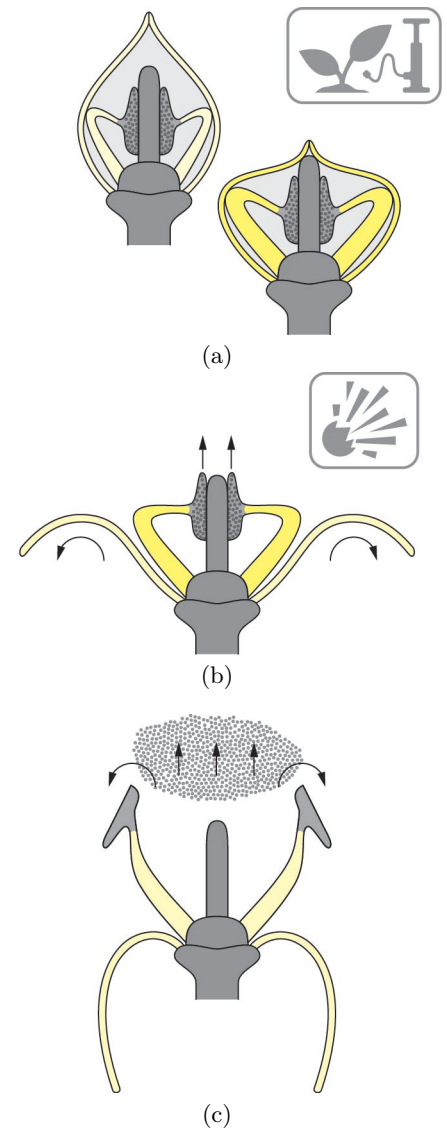
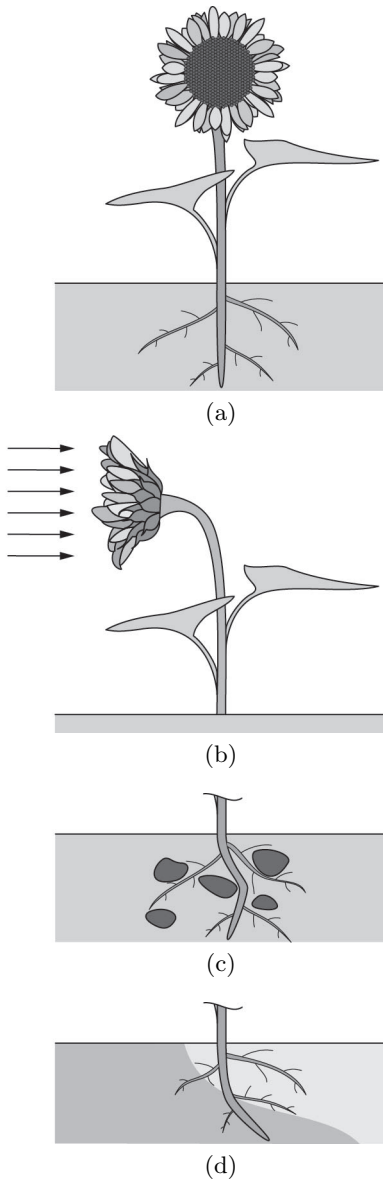


Figure 6.6: Pollen dispersal of *Cornus canadensis* (Cornaceae). (a) Elastic energy is stored in the petals and filaments through differential growth and cell pressures. (b) Petal opening is triggered by cell pressures or large insects. Anthers start to accelerate vertically. (c) Separation from the inset leads to anther rotations that increase the tip velocities for the pollen dispersal.



dispersal is partially generated through differential growth as the filaments grow faster than the petals during flower development. The rapid opening of the prestressed petals is triggered by cell pressures or the touch of large insects such as bumblebees. This leads to an initially vertical acceleration of the anthers that start to rotate after the separation from the inset. The rotational velocity of the anther increases its vertical tip velocity so that the pollens are accelerated to speeds of up to 7.5 m/s [314]. Pollens that weight about $24 \mu\text{g}$ are dispersed by this mechanism to altitudes of 25 mm. They are either carried away by the wind or by the pollinated insect that triggered the release.

6.2 Stimulated Movements

Plant movements that occur in response to an external stimulus can be divided into preprogrammed, nastic movements that do not depend on the direction of the stimulus and the more sophisticated tropisms that depend on the magnitude and direction of the stimulus. The latter are of little interest for most engineering structures as the required shape changes are usually known in advance.

6.2.1 Tropisms

Circumnutations and tropisms are growth driven movements. They differ from each other insofar that tropisms react to directed, external stimuli whereas circumnutations do not. Common stimuli are irradiation (*phototropism*, *heliotropism*), gravity (*geotropism*), nutrients (*hydrotropism*) and touch (*thigmotropism*) as illustrated in Figure 6.7. The close link between circumnutations and tropisms is highlighted by many climbing plants. They minimize their supportive tissue and thus energy consumption during vertical growth by utilizing external supports. Circumnutations are used to randomly search for new supports whereas touch induced growth movements are initiated upon contact.

A more sophisticated approach is used by climbing plants such as *Epipremnum giganteum* from the family Araceae that is native to the tropical forests of Indochina. These plants avoid random searches by using negative phototropism (*skototropism*) that directs them towards dark, solid objects [276]. This is remarkable as they initially impair their light exposure before they can start to climb towards the canopy. Phototropism that directly improves a plants exposure to light can be observed at different timescales. Most plants optimize their orientation with respect to average light conditions that occur over a longer period of time. Other plants such as juvenile sunflowers directly track the motion of the sun during a diurnal cycle which is known as heliotropism. They even reorient the flowers after sunset to directly face the sunrise the next

Figure 6.7: Various forms of tropism. (a) *Geotropism* drives the vertical growth of stems and roots. (b) *Phototropism* optimizes the irradiation of plant organs. (c) Obstacle avoidance of roots is based on *thigmotropism*. (d) Growth of roots towards nutrient rich soil is known as *hydrotropism*.

morning [11]. The latter movement that is not driven by phototropism seems to be triggered by the circadian clock [186].

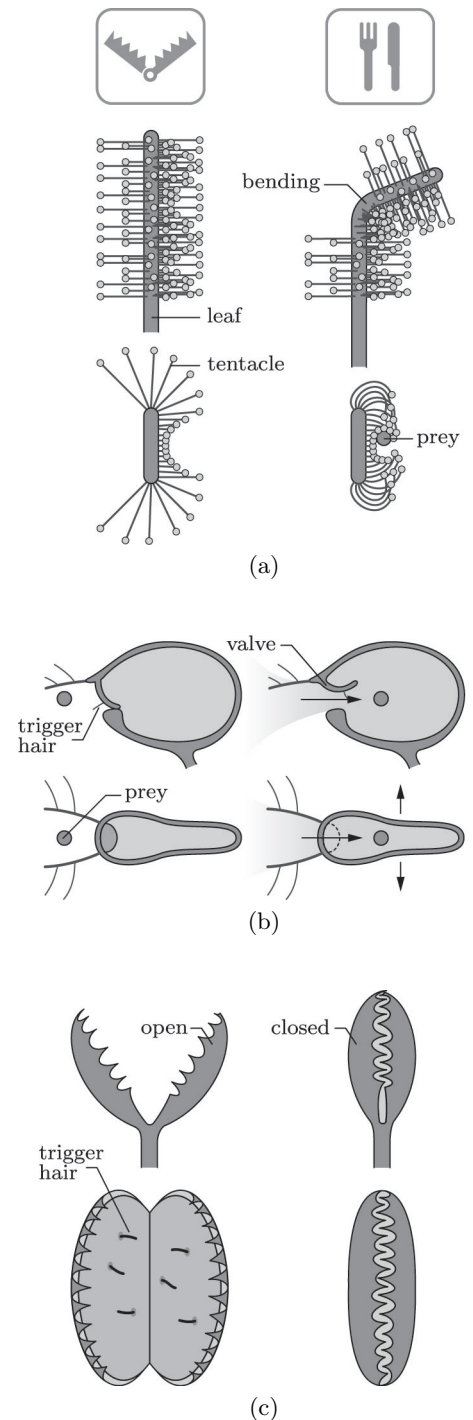
The study of tropisms is often complicated by their mutual interactions. For example, the growth of roots is driven by geotropism that aligns the mean growth direction to the gravitational field, thigmotropism that uses touch responses to avoid obstacles and hydrotropism that directs the growth towards nutrient and water rich soil. It is thus difficult to quantify the influence of each tropism on the growth direction [70]. Some of these interactions can be switched off with the help of mutants or microgravity environments that can be found on space stations. However, despite a considerable research effort, a detailed understanding of the mechanisms behind tropisms remains elusive.

6.2.2 Nastic Movements

Nastic movements occur, unlike tropisms, in response to non-directional stimuli. They are often preprogrammed into a plants structure so that they are relatively fast. The difference to previously introduced automatic, passive movements lies in the fact that they are fully controlled by the plant and do not require external energy sources such as temperature or humidity gradients. Instead they are driven by cell pressure variations or by fast growing cells. These movements are initiated by stimuli such as irradiation (*photonastic*), temperature (*thermonastic*), touch (*thigmonastic*), vibration (*seismonastic*) and the circadian clock (*nyctinastic*).

Photonastic and thermonastic movements play a major role in the opening and closing of flowers. Some species open their flowers only once whereas others open and close them regularly [301]. The latter has the advantage that they are protected against environmental conditions during the time of day when a pollination is unlikely. Diurnal flowers such as Iridaceae are open during the day and closed during the night whereas nocturnal flowers such as Cactaceae or Bromeliaceae are open during the night and closed during the day. Diurnal flowers are often pollinated by butterflies or bees whereas nocturnal flowers are pollinated by moths

Figure 6.8: Side and top view of various carnivorous plants. (a) *Drosera capensis* uses nastic growth movements to clutch tentacles around prey and tropic movements to subsequently bend the leaf. (b) *Utricularia vulgaris* stores elastic energy in the bladders by pumping out water through osmosis. Valve seal breaks if trigger hairs are touched. Prey is sucked in by rapid water inflow. (c) *Dionea muscipula* uses cell pressure variations to store elastic energy in the leaves and to trigger rapid shape changes if trigger hairs are touched.



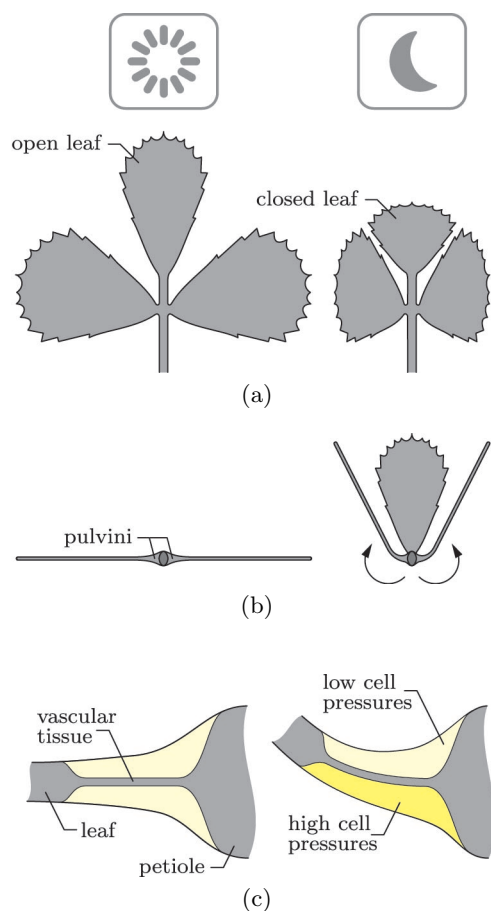


Figure 6.9: (a) Top and (b) side view of an open, closed *Medicago truncatula* (Fabaceae) leaf. Its closure and opening is driven by seismonastic, thigmonastic or nyctinastic movements. (c) Cross section of a simplified pulvinus that translates cell pressure variations into leaf movements.

and bats. The opening and closing of most flowers is based on growth movements. Opening times can vary significantly. Flowers that open only once can store elastic energy in bracts or sepals that accelerates the opening after abscission. For example, *Hedera helix* from the family Araliaceae that opens its flowers only once requires about five minutes whereas *Oenothera biennis* from the family Onagraceae that opens its flowers every evening requires about twenty minutes.

Plants that are capable of fast, reversible movements have several advantages over their conspecific, static rivals. For example, carnivorous plants grow in places where the soil is extremely poor in nutrients. They use rapid movements to supplement their diet by catching insects and arachnids [77]. *Drosera capensis* from the family Droseraceae that is native to South Africa [168] possesses strap like leaves that are covered by long tentacles on the marginal sides and by short tentacles on the central part of the leaf. The glands at the top of the tentacles secrete a sticky, sugar containing mucilage that attracts prey. A struggling animal that sticks to a tentacle is transported towards the center of the leaf and covered by the remaining lateral tentacles via fast bending movements. These growth driven, thigmonastic movements are followed by the thigmotropic bending of the leaf at the location of the prey to improve digestion as illustrated in Figure 6.8. A remarkable property of many carnivorous plants is that they can distinguish between different stimuli that are unrelated to food such as rain or wind.

A trapping mechanism that functions without complex growth movements is used by *Utricularia vulgaris* from the family Lentibulariaceae. The aquatic plant that can be found in Asia and Europe uses bladder like traps to capture small animals. The in- and outflow of a bladder is controlled by a compliant valve that opens inwards. The valve is sealed by an adhesive so that underpressures of up to 15 kPa can be generated within the bladder by pumping out water via osmosis. Animals are attracted towards the bladder by a sugar containing mucilage that is excreted around the valve. Trigger hairs that are connected to the valve serve as levers that break the seal upon touch. This leads to a rapid release of the elastic energy that is stored in the bladder material. The rapid inflow of water through the open valve carries the prey, if small enough, into the bladder. It is subsequently dissolved by digestive secretions within a few hours. The trap continuously pumps out water during this process to increase the nutrient concentration so that it can be reused within half an hour after digestion.

Dionaea muscipula from the family Droseraceae is native to the subtropical wetlands of North and South Carolina. Its leaves are divided into a heart shaped petiole for the photosynthesis and a pair of terminal lobes that form the trap. The lobes secrete, like many other carnivorous

plants, mucilage to attract prey. The upper, red dyed surface of each lobe contains three hair like trichomes. They trigger rapid thigmonastic movements if one hair is touched twice in rapid succession or two hairs are touched within twenty seconds. *D. muscipula* exploits a geometric instability to close its leaves within a fraction of a second [84]. This discontinuous, repeatable movement is particularly interesting as it does not require complex growth processes or subcomponents such as valves. Instead it is based on cells with carefully designed geometries whose total elastic energy is generated and partially released by cell pressure variations [214]. The edges of the trap are seamed by stiff hairs that interlock as the leaves close. Gaps between the hairs allow small animals to escape whereas larger prey is digested if the trigger hairs are further stimulated. The digestion takes about ten days and the reopening up to twelve hours.

The discontinuous, rapid movements of *Dionaea muscipula* are fascinating. However, they can rarely serve as an inspiration for engineering structures as they require, at least for most applications, fully controllable, continuous movements. Plants such as *Mimosa pudica* or *Medicago truncatula* from the family Fabaceae use continuous movements to close their leaves within seconds, Figure 6.9. These movements are driven by a pulvinus at the base of each petiole that consist of a stiff core of vascular tissue that is surrounded by thin walled cells. Leaf closure minimizes a plants radiative heat losses during nighttime (*nyctinastic*) and creates the illusion of being a less voluminous meal during daytime if touched by a predator (*thigmonastic*). Furthermore, the defensive capabilities of *M. pudica* improve during closure as the relative angles between protective thorns and predators vary [75]. Leaf closure during daytime is energetically costly as the plants photosynthesis reduces drastically. Hence there is a tradeoff between the protection against potential threats and the vital harnessing of energy. An impressive property of *M. pudica* is its ability to habitually learn which kind of seismonastic and thigmonastic stimuli require leaf closure [89]. This property is more pronounced and persistent for plants that grow in challenging environments as they have a smaller margin for superfluous movements.

6.3 Cell Components

Nastic plants such as *Mimosa pudica* are highly integrated, lightweight and energy efficient. Their continuous movements are preprogrammed into the cell geometries and driven by cell pressure variations. The main components and processes that are involved in these movements include cell walls, cytoskeletons and subcellular osmotic hydration motors as illustrated in Figure 6.10.

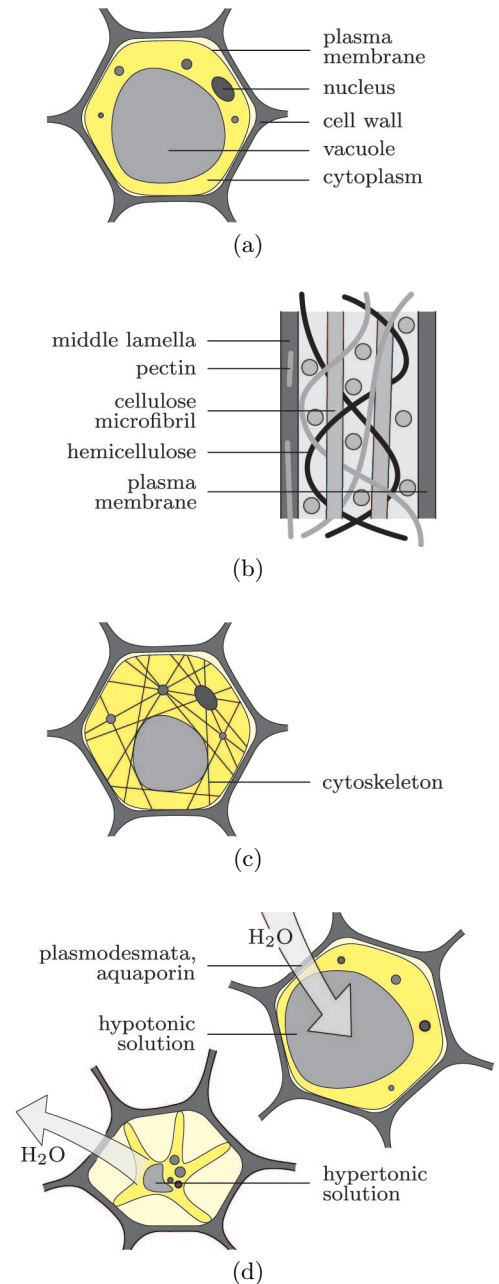


Figure 6.10: Cell components that are involved in nastic movements. (a) Cell organization. (b) Middle lamella, primary cell wall and plasma membrane. (c) Cytoskeletons and (d) osmotic hydration motors.

6.3.1 Geometry

The Weaire-Phelan structure possesses the smallest total surface area observed thus far [310] for a packing of equal volume cells. It utilizes two kind of cell geometries where one is a dodecahedron with pyritohedral symmetry and the other is a truncated hexagonal trapezohedron. This structure is used, for example, in the Beijing Aquatic Center. Plant cells rarely form this ideal structure as their geometries are driven by more than one objective. However, like the Weaire-Phelan structure, they always pack their cells such that only three edges meet at a single point. The diversity of cell geometries can be highlighted with the help of epidermal plant cells [152]. Their basic geometries depend to a certain degree on the habitat that can range from deserts to wetlands. Plants that are exposed to intense irradiation and heat are often protected by fine hairs against water evaporation. In contrast, wetland plants often use self cleaning surfaces to reduce contaminations and pathogen attacks.

The periclinal cell walls that form a plants outer surface can be seen with a light microscope. Their tetragonal or polygonal outlines can be isodiametric (constant cell side lengths) or elongated as illustrated in Figure 6.11. The basic geometry of these cell walls can vary even within a single leaf. For example, cells of the lower leaf side of *Poa annua* (Poaceae) are tetragonal elongated whereas cells of the upper side are polygonal. The boundaries between periclinal cell walls can be straight or undulated with U, V, Ω and S shapes. These undulations can be regular or non-regular and their amplitudes may vary. It is widely believed that the mechanical properties of the epidermis are improved by the interlocking between undulated cell boundaries.

Anticline cell walls are orthogonal to the periclinal cell walls. Related to the plant surface they can be flush, sunken or exposed. The periclinal cell walls that are bounded by the anticlines can be tabular (flat), concave or convex. Tabular surfaces can be often found in submerged and floating water plants such as *Anubias barteri* from the fam-

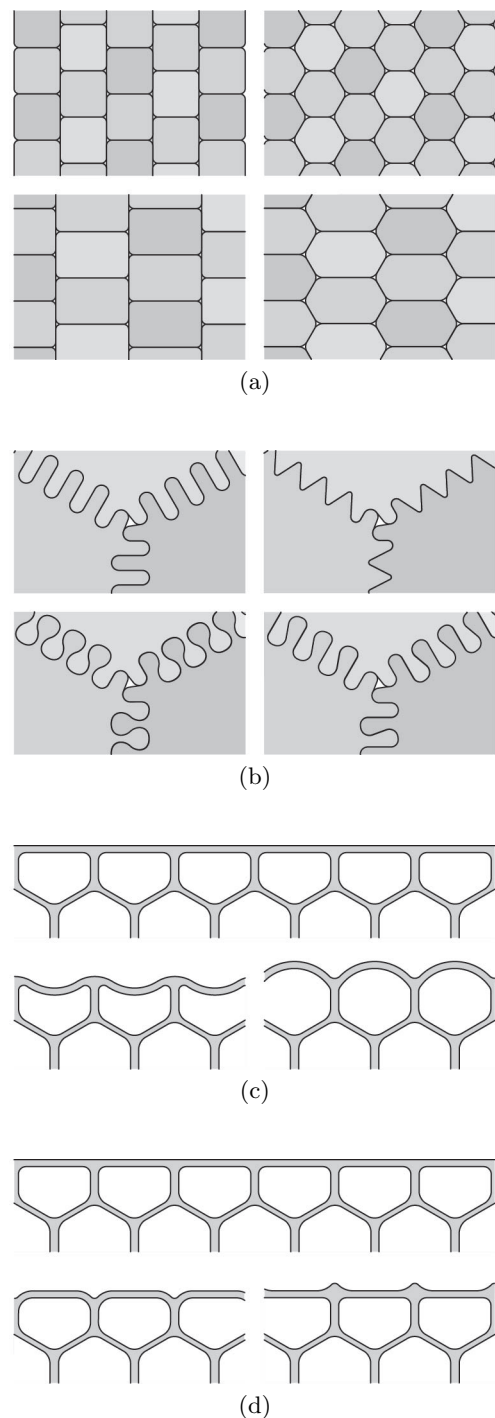


Figure 6.11: Basic epidermal plant cell geometries. (a) The plant surface is formed by periclinal cell walls. Their tetragonal or polygonal outlines can have sides with identical (isodiametric) or varying lengths (elongated). (b) The boundaries between periclinal cell walls are not necessarily straight. There exist undulated boundaries with U, V, Ω and S shapes. (c) Periclinal cell walls can be flat, concave or convex. For example, plant hairs are formed by highly convex cell walls. (d) The anticline cell walls that are perpendicular to the surface can be flush, sunken or exposed.

ily Araceae. In contrast, concave periclinal cell walls are rarely present in water containing cells as the concavity is usually caused by water evaporation. Hence they are commonly found in dry seeds such as the wind dispersed seeds of *Aeginetia indica* from the family Orobanchaceae. Convex periclinal cell walls are the most common. Underwater plants are usually hydrophilic whereas emerged (above the water) and wetland plants are often hydrophobic. Plants such as *Nelumbo nucifera* from the family Nelumbonaceae possess convex walls with optimized shapes that improve their self cleaning capabilities [200]. This reduces their susceptibility to contaminations and pathogen attacks that are promoted by the high, constant moisture of their habitat.

Plant hairs are formed by extremely elongated convex cell walls. They can be dead or living and based on single or multiple periclinal cell walls. Many plants use hairs as a protection against intense irradiation. For example, the straight, air filled hairs of the South African tree *Leucadendron argenteum* consist of a single cell wall. They form a dense layer that appears to be white as it reflects most of the visible light. Other densely covered plants such as *Encelia farinosa* reflect mainly the near infrared radiation (700-3000 nm) whereas the photosynthetically useful radiation (400-700 nm) can reach the leaves [73]. Although hairs are common in the plant kingdom they are absent in underwater plants as their periclinal walls are mostly tubular. Rough, hairy surfaces can be found on the floating leaves of water ferns of the genus *Salvinia*. The water repelling, multicellular hairs increase the buoyancy of the leaves by retaining an air layer for several days even if fixed underwater. Other multicellular hairs with glands that secrete adhesives and enzymes for the capture and digestion of prey can be found in carnivorous plants such as *Drosera capensis*.

The study of internal cell geometries is far more difficult as they can not be directly observed. Hence it is not surprising that the available literature in this field is relatively sparse. Irrespective of the limited knowledge, a direct translation of cell geometries into technical applications is unrealistic as their shapes are driven by various objectives whose interactions are little understood. In contrast, cell geometries for engineering structures are potentially simpler as they need to be optimized solely for the shape changing requirements.

6.3.2 Material

Unlike animal cells, plant cells are surrounded by a stiff cell wall with a thickness that varies between a tenth to several μm . This is necessary as plants do not possess a centralized skeleton that carries most of the loads. Hence it is not possible for them to use muscles like actuators in the same way as animals do. Instead they can generate large cell

pressures that are contained by the surrounding cell walls. Commonly used turgor pressures are between 0.4-0.8 MPa but can reach 5 MPa in guard cells that control the gas exchange of plants. Cell walls are a living material that can grow and reorganize its constituents. It is thus difficult to quantify the mechanical properties of this composite material particularly on the microscopic level as they are highly dynamic [6].

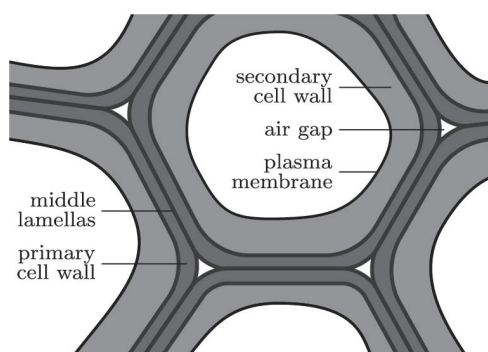


Figure 6.12: Neighbouring cells are glued together by middle lamellas. This can lead to air filled gaps at cell corners that are known as intercellular spaces. Fully grown cells of woody plants develop a secondary cell wall inside the primary cell wall to increase their load carrying capacity. Secondary cell walls additionally reduce a cells permeability and increases its resistance against pathogens.

A cell wall consist of a primary cell wall that is sandwiched between the plasma membrane and the middle lamella. Some fully grown plant cells additionally possess a secondary cell wall that is located between the plasma membrane and the primary cell wall as illustrated in Figure 6.12. The primary cell wall is a thin, flexible and extensible layer that is formed during growth. It consists of a network of cellulose microfibrils that are connected by hemicellulose tethers. This network is embedded in a pectin matrix, a hydrated gel that pushes the microfibrils apart, thus easing their sideways motion [55]. For example, primary cell walls in dicotyledonous plants consist of approximately 35% pectin, 30% cellulose, 30% hemicellulose and 5% protein on a dry weight basis [88]. The cellulose fibers possess a Young's modulus of about 130 GPa and a tensile strength of about 1 GPa [95]. In contrast, the Young's modulus of hemicellulose is between 5-8 GPa and thus considerably smaller. As a consequence, the mechanical properties of a primary cell wall depends mainly on the orientation of its microfibrils. Cellulose fibers are widely used in natural fiber composites as their mechanical properties and biodegradability make them a serious competitor to glass fiber reinforced plastics [232]. Another remarkable property of primary cell walls is the ability to vary their stiffness with the help of enzymes. This enables them to undergo large plastic strains that are driven by pressure induced tension forces during cell division.

The plasma membrane is a semipermeable lipid bilayer that separates the cytoplasm from the cell wall. It forms through the process of self assembly and has a thickness between 7-10 nm. The lipid bilayer possesses a hydrophobic internal phase and a hydrophilic external phase on both sides. The hydrophobic phase creates a barrier between the interior and exterior of the cell that can not be easily passed by water whereas the hydrophilic surfaces on both sides are in contact with aqueous fluids. A plasma membrane possesses passive and active mechanisms that transport molecules in both directions so that it can influence the osmotic gradient. Furthermore, it contains sensors that receive signals from the environment and hormones that control the plant growth and cell division.

Pectin based middle lamellas are the outmost cell wall layers that glue neighbouring cells together. The finite curvatures of cell walls often lead to air filled gaps at cell corners that are known as intercellular

spaces. It is often difficult to distinguish between the middle lamellas and the primary cell walls so that they are often referred to as a compound middle lamella. A separation of cells is usually accomplished by enzymes that dissolve the middle lamellas. This happens for example during the separation of petals and leaves.

Secondary cell walls are relatively thick layers between the primary cell walls and plasma membranes of woody plants. They usually account for most of the biomass and are formed in fully grown cells that need to carry large external loads. Similar to primary cell walls, secondary cell walls contain cellulose, hemicellulose and pectin. However, their composition differs as their cellulose fraction and thus their strength, stiffness and durability is considerably higher. Furthermore, their permeability is lower so that they can efficiently protect a cell against pathogens. Attributed to their large stiffness, secondary cell walls can carry tension as well as compression stresses. In contrast, primary cell walls carry mostly tension forces due to cell pressures. However, the large stiffness of secondary cell walls and their low permeability hinders nastic movements so that they are of little interest for the work that is presented in this thesis.

6.3.3 Cytoskeletons

Cytoskeletons are complex networks that extend throughout the cytoplasm. They support the cell shape, anchor subcellular components and participate in intracellular transports and communications [83]. They can rapidly adapt their structure to varying cell requirements through rapid growth and disassemblies.

Cytoskeletons consist of interconnected microfilaments, intermediate filaments and microtubules that are anchored in the plasma membrane. Microtubules are highly dynamic, polar structures with an outer diameter of about 24 nm and an inner diameter of about 12 nm. They create a scaffold for the cell and serve as tracks for intracellular transports. These transports are accomplished by motor proteins that are powered by adenosine triphosphate. Kinesin transports towards the positive and dynein towards the negative pole of a microtubule as illustrated in Figure 6.13. Most microtubules possess a half life of five to ten minutes whereas others remain stable for hours. Microtubules grow faster at the positive end and slower at the negative end. It is believed that their dynamic growth and disassembly is used to probe a cells three-dimensional space [150].

Microfilaments are less dynamic than microtubules as they can grow, shrink or remain stable. They consist of two helical, interlaced strands

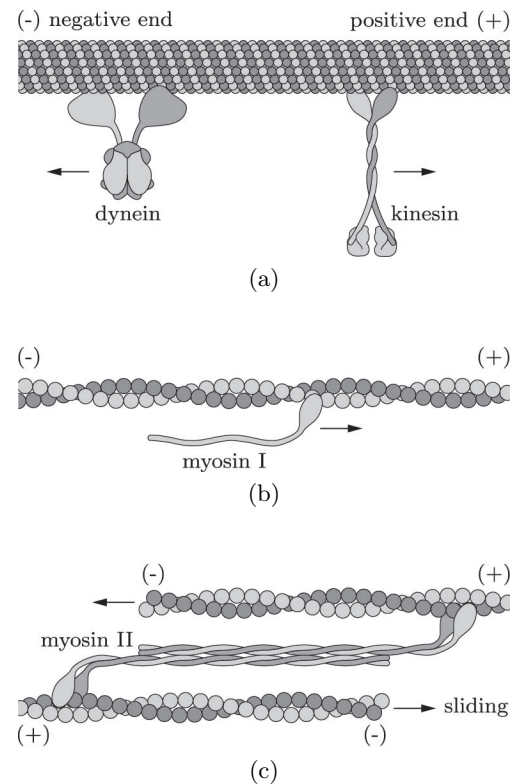


Figure 6.13: (a) Most intracellular transports are based on microtubules and motor proteins. Dynein transports towards the negative and kinesin towards the positive end. (b) Alternatively, microfilaments can serve as tracks for myosin I motors. (c) Muscle like fibers are constructed from myosin II motors and microfilaments. They are used to tension the cytoskeleton and to vary the cell shape.

that form a polarized structure with a diameter of about 7 nm. Much like microtubules, microfilaments grow faster at the positive and slower at the negative end. Different myosin motors that are powered by adenosine triphosphate can bind to the microfilaments. The myosin I protein that moves towards the positive end of a microfilament is particularly used for transports in regions that are poor in microtubules. Muscle like fibers are created with the help of myosin II proteins that connect two or more microfilaments. Fiber contractions are accomplished by the relative sliding motions of microfilaments. The tension forces that result from these contractions rigidify the cytoskeletons or vary the cell shape. For example, a contracting ring of microfilaments is used to divide the cytoplasm into two parts during cell division.

Intermediate filaments have a diameter of about 10-13 nm so that they are thicker than microfilaments and thinner than microtubules. They are less dynamic and more elastic than microfilaments and microtubules. It is estimated that they can be stretched between three to five times their initial length. Elastic strains of these magnitude are enabled by a hierarchical structure where deformation mechanisms vary with strain levels. A common occurrence of intermediate filaments in plant cells has not been unequivocally demonstrated [156] so that little is known about their function. However, it seems likely that they support the cytoskeletal structures.

The involvement of cytoskeletons in the nastic movement of plants is mostly unknown [197]. It is known that local tensile stresses of up to 0.3 MPa can be exerted by muscle like fibers [30] whereas turgor pressures that act on the whole cell wall can reach up to 5 MPa. This discrepancy makes it unlikely that microfilaments are actively involved in plant movements. However, it is shown in a subsequent chapter that subcellular structures with inherent mechanisms can carry a significant portion of the cell pressures. This reduces the required cell wall thicknesses and thus the rigidity of cells. Furthermore, cytoskeletons might be used to constrain cell geometries prior to shape changes. This hypothesis is supported by the observations of Kanzawa et al [142]. They found that the highly organized cytoskeletons in motor cells of *Mimosa pudica* become fragmented after shape changes. Hence it seems that they support plant movements by a rapid disintegration.

6.3.4 Subcellular Motor

Plant movements are driven by cell pressures that can be as low as -10 MPa in *Phlebotidium aureum* and as high as 5 MPa in guard cells [85]. This is impressive as the pressures of hydraulic aircraft systems in

the 1940s¹ were between 3.5-7 MPa. The subcellular osmotic hydration motors that generate and control these large pressures without the need for external energy sources are of particular interest for engineering applications. The main principles behind these motors are well understood whereas the understanding of many details remains elusive.

As illustrated in Figure 6.14, the water transport in plants occurs through three different pathways [69]. The apoplastic pathway is a flow through the porous cell walls and intercellular spaces. It depends mainly on the cell wall porosity that is driven by the pectin deposition in the primary, secondary cell wall and the middle lamella. The symplastic pathway is a direct flow through the cytoplasm continuum via plasmodesmata that cross the cell walls of neighbouring cells. In contrast, the transcellular pathway is a flow through cell walls and plasma, vacuolar membranes. It needs to pass two plasma membranes at each cell wall so that its solute conductivity is relatively small.

An osmotic hydration motor is based on a semipermeable plasma membrane whose expansion is restrained by adjacent cell walls. A flow through the cell walls (apoplastic pathway) is mostly driven by pressure gradients as the cell wall continuum is permeable to most solutes. In contrast, a flow through the plasma membrane requires an osmotic gradient that is the difference in solute concentrations on both sides of the membrane. Water flows towards the solution with the higher concentration until an equilibrium with the pressure gradient is reached. The osmotic gradient is controlled by passive and active transports through the plasma membrane. Passive transports are directly driven by gradients and thus do not require any additional energy. They can be based on diffusion or non-specific and specific transporters such as aquaporins. Active transports against a gradient require additional energy. Primary active transporters use adenosine triphosphate as an energy source whereas secondary active transporters gain energy from the transport of two substances where one is moved against and the other in the direction of its osmotic gradient.

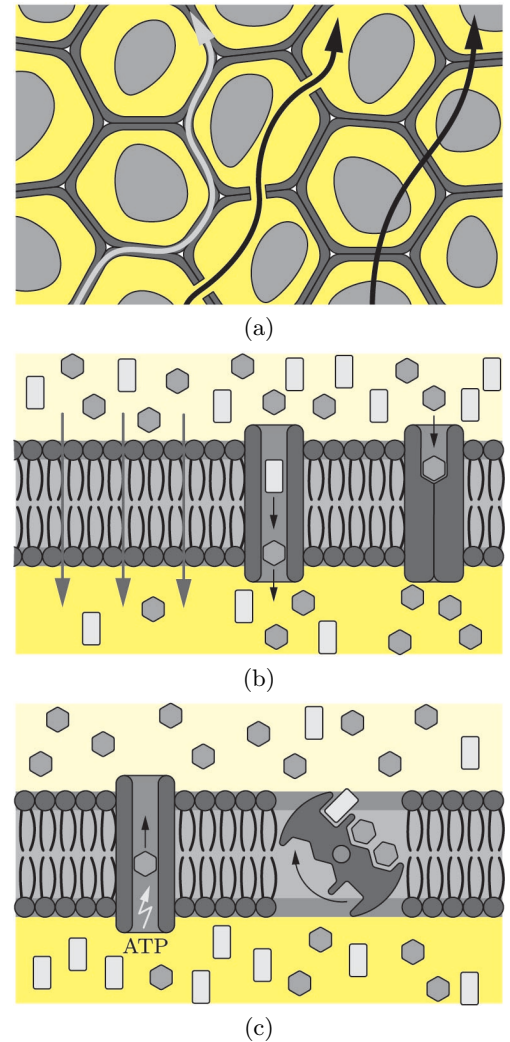


Figure 6.14: (a) Water transport in plants is based on three pathways. Apoplastic pathway through porous cell walls and intercellular spaces. Symplastic pathway through cytoplasm continuum via plasmodesmata. Transmembrane pathway through cell walls, cytoplasm and vacuoles. (b) Passive transport across the plasma membrane through diffusion and non-specific, specific transporters. (c) Active transport against concentration gradients through primary and secondary transporters.

¹Weight savings led to progressively increasing hydraulic pressures that reached 21 MPa (3,000 psi) in the 1950s, 28 MPa (4,000 psi) in the 1970s and 34 MPa (5,000 psi) in the early 1980s. Pressures will most likely increase to 56 MPa (8,000 psi) in the near future.

Chapter 7

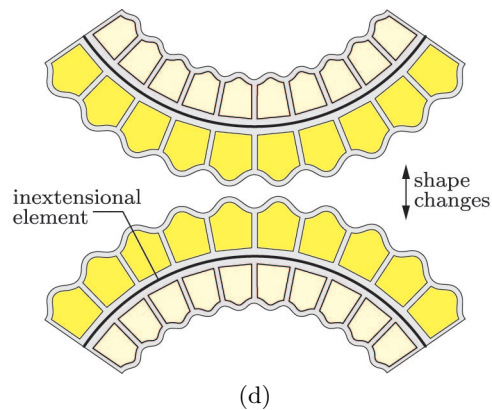
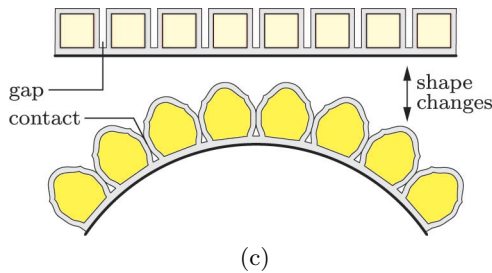
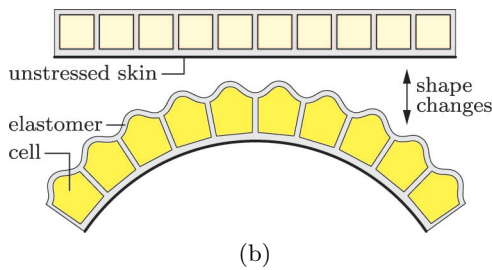
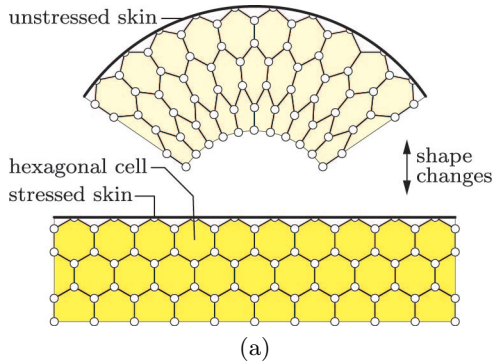
Biomimetics

The working principles of nature are often used in various contexts and at different length scales [86]. For example, cells are the basic structural, functional and biological units of all living organisms. They recur at different scales in compound eyes or the nests of bees. Furthermore, not all manmade structures that use these principles were consciously inspired by nature. This complicates a review about plant inspired, shape changing structures. The first part of this section focuses on technologies that, irrespective of their inspiration and length scale, are based on pressurized cellular structures that can undergo significant shape changes. A novel approach towards pressure actuated cellular structures [216] on which this thesis builds is subsequently presented and its potential is demonstrated with the help of several examples.

7.1 Pressurized Cellular Structures

As pointed out in Chapter 2, pressure supported structures are widely used in applications that range from balloons and rockets to large sport stadiums and modules for space stations. Furthermore, they were considered for pressure stiffened wings and fuselages in the 1930s and served as a backbone for the inflatable airplanes that were build in the 1950s. Pressurized cellular structures that can undergo large shape changes have been recently revisited for the use in gapless high lift devices. The subsequently presented approaches have in common that they mostly focus on the cell geometries. It is usually assumed that cell pressures are generated by an external source such as a compressors. Furthermore, cytoskeletons are utterly neglected and cell sides are either assumed to be rigid or composed of an isotropic homogeneous and linear elastic material. The cellular structures are grouped in the following according to their shape changing capabilities into beam, plate and shell like structures.

7.1.1 Beams



Cellular structures that can undergo large, uniaxial bending deformations can be split into two groups. The first group comprises structures that are based on equally pressurized cells and energy storing elements such as compliant hinges, cell sides and flexible skins. These structures possess a unique relationship between shape and cell pressures and thus an invariant stiffness. The second group comprises structures that possess two or more connected and independently pressurized cell rows. This enables them to vary both, their shape and stiffness. Hence, they do not require compliant cells or other auxiliary elements that store elastic energy.

An approach for shape changing structures that has close links to the pressure stiffened airplane wings by Chutter [49] and the inflatable housing structures by Khire et al [146] was investigated by Vos [307] in 2009. It is based on a curved skin that is connected to a large number of equally pressurized hexagonal cells as shown in Figure 7.1. The cells are assembled from rigid sides and frictionless hinges so that they can not store any strain energy. The structures equilibrium shapes are thus bounded by the shape of the unstressed skin (zero cell pressures) and the shape that maximizes the cross sectional area of the cells (infinite cell pressures). However, the use of multiple cell rows is disadvantageous as the outer cells need to undergo large deformations. This is particularly problematic for compliant cells as potential strains are limited.

Figure 7.1: Shape changing structures that undergo bending deformations due to cell pressure variations. (a-c) Different assemblies of equally pressurized cells that are connected to a flexible skin. The bending deformations depend on the skins shape and stiffness as well as on the cells elasticity, geometry and pressure. There exists a unique relationship between the skins curvature and cell pressures so that the stiffness of these structures is invariant. (a) Cellular structure that is assembled from a curved skin and a large number of identical hexagonal cells that are arranged in several rows (third row is only partially shown). The cells consist of rigid sides and frictionless hinges so that their inherent stiffness is zero. (b) Cellular structure with a straight skin and a single row of elastic, quadrilateral cells that contribute to the overall stiffness. (c) A similar structure where the cells are separated by gaps to reduce the cell wall strains during deformations. (d) Combination of two separately pressurized cell rows into an agonist-antagonist pair. The shape of this structure depends on the ratio and its stiffness on the magnitude of the cell row pressures. Hence it does not require compliant cells or other auxiliary structures that can store elastic energy.

A similar approach that is based on a straight skin and a single row of quadrilateral cells was investigated by Correll et al [54] in 2010. The use of quadrilateral cells is rather unusual and was motivated by the casting based manufacturing process. Quadrilateral cells that are made from rigid sides and frictionless hinges possess a single degree of freedom whereas pentagonal and hexagonal cells possess two and three degrees of freedom, respectively. Hence, quadrilateral cells that share a common side can only be used in shape changing structures if they are made from an elastic material that indirectly increases their degrees of freedom. However, this leads to relatively large strains as the cell geometry needs to be transformed upon pressurization. An improved version with small gaps between neighbouring cells was subsequently developed by Polygerinos et al [235] in 2013. Nonetheless, it would be best to use cells with a tailored pentagonal geometry instead that can be constructed from rigid sides and frictionless hinges.

Two separately pressurized cell rows can be combined into an agonist-antagonist pair. The shape of such a structure depends mostly on the pressure ratio and its stiffness on the magnitude of the cell row pressures. Hence, it does not require an energy storing element such as a flexible skin or compliant cells. However, axial deformations need to be constrained by a straight assembly of rigid cell sides or an inextensional element. Another advantage of shape changing structures with separately pressurized cell rows is the possibility to improve their energy consumption during shape changes. This can be done by enabling a direct fluid flow between rows that is supported by a pressure booster.

The aim of this thesis is the advancement of shape changing structures with an arbitrary number of cell rows and individually tailored cell geometries as first proposed by Pagitz et al [216, 218] in 2011. The main idea behind these “Pressure Actuated Cellular Structures” or “PACS” is subsequently outlined. Rows of equally pressurized cells with an identical pentagonal or hexagonal cross section are assembled from rigid cell sides and frictionless hinges as illustrated in Figure 7.2. These rows de-

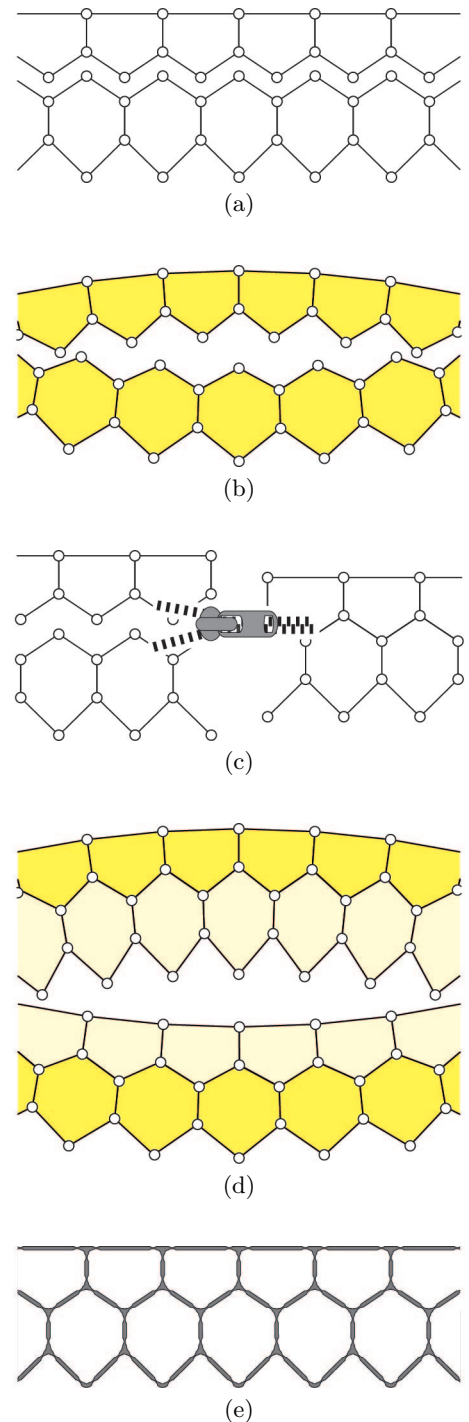
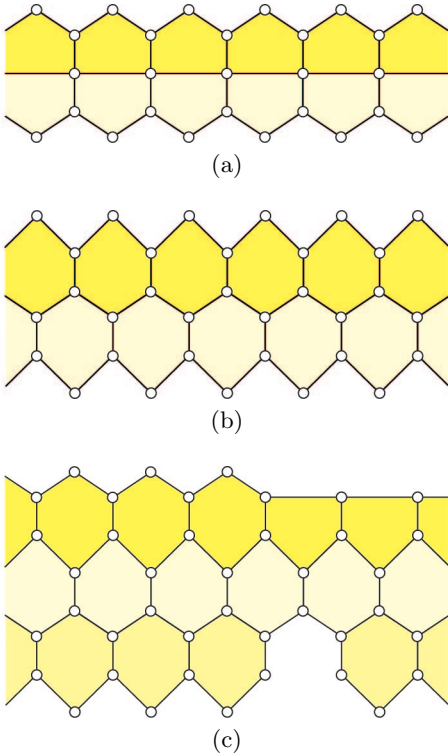


Figure 7.2: Working principle of pressure actuated cellular structures. (a) Two separate cell rows with a number of identical pentagonal and hexagonal cells are assembled from rigid sides and frictionless hinges. (b) Cell rows deform into circular arcs upon pressurization. Their radii depends solely on the cell geometries. (c) Cell rows can be connected if opposite sides are of equal length. (d) The equilibrium shape and stiffness of a structure with two cell rows can be independently altered by a variation and scaling of cell row pressures, respectively. (e) Alternatively, pressure actuated cellular structures can be made from a single piece of elastic material with compliant hinges around cell corners.

form into circular arcs upon pressurization. Their radii depends solely on the cell side lengths as both, hinges and cell sides can not store any strain energy. Two cell rows can be connected if the opposite cell sides are of equal length. This leads to a structure that can vary its stiffness and shape within the bounds that are defined by the cell geometries and admissible cell row pressures.

The use of rigid cell sides and frictionless hinges increases the part count and weight of a pressure actuated cellular structure. It is therefore often best to use a monolithic structure instead where bending deformations are localized in regions (compliant hinges) around cell corners. However, this comes at the cost of an increased design complexity as their inherent stiffness, fatigue properties and producibility needs to be considered. This requires a detailed geometric model that does not only take into account the cell side lengths but additionally the cell corner geometries and the cell side thicknesses as well as their variations.



The underlying principle is by no means limited to the combination of two cell rows with pentagonal and hexagonal cells. A few alternative arrangements and topologies are illustrated in Figure 7.3. It can be seen that the previously introduced compliant structure with two rows of quadrilateral cells can be polygonalized by using two rows of pentagonal cells with rigid sides and frictionless hinges. The base sides of the pentagonal cells form a straight, inextensional element that prevents axial deformations. The axial stiffness of this structure can be reduced by using hexagonal cells instead. This leads to a coupling between axial and bending deformations that enables sophisticated shape changes particularly in conjunction with more than two cell rows. Hence, the number of cell rows and their topologies that need to be used for a certain application depends on the shape changing requirements. The subsequent focus is on pressure actuated cellular structures that consist of a pentagonal and one or more hexagonal cell rows as they possess a relatively smooth, inextensional surface and a regular topology. Shape changes in the axial direction are thus neglected.

Figure 7.3: Alternative cell row arrangements and topologies. Two connected cell rows of (a) pentagonal and (b) hexagonal cells. The latter leads to a coupling between axial and bending deformations. (c) Pressure actuated cellular structure with three cell rows and varying topologies.

Another perspective on possible cell topologies can be gained by looking at the three regular tessellations of a plane. They are based on triangles, quadrilaterals and hexagons where the latter possesses the smallest possible total cell side length for a given cell area and the largest number of degrees of freedom. The eight semiregular tessellations are of little interest as they have a larger total cell side length. Furthermore, the degrees of freedom are unevenly distributed as the shape changing capabilities of polygons depend on their number of cell corners. A regular tessellation of hexagonal cells can not be directly used in pressure actuated cellular structures for high lift devices as it lacks a smooth surface. An additional constraint that enforces an inextensional, smooth

boundary leads to a topology with a pentagonal and one or more hexagonal cell rows as previously discussed.

Equilibrium shapes for given cell row pressures can be preprogrammed into the cell geometries of pressure actuated cellular structures. This enables structures whose shape changing capabilities increase with the number of cell rows. It is thus usually pointless to use more than two cell rows if their cells possess an identical geometry. The following chapter presents an algorithm that deals with the optimization of compliant pressure actuated cellular structures for given target shapes, cell row pressures and stress constraints.

7.1.2 Plates

Beam and plate like structures differ from each other insofar that the in-plane dimensions of the latter are usually of the same order of magnitude. It is subsequently assumed that the plane strain compatibility condition [37] is satisfied so that plates undergo only in-plane shape changes. These kind of structures are thus of potential interest for applications that require continuous shape changes along their boundary. However, the same capability can be achieved by connecting both ends of a beam like structure. This has the additional benefit that it frees up internal space that can be used to accommodate other components or that can be partially or fully filled with active or passive mechanisms that support the boundary. Hence there exists a smooth transition between beam and plate like structures.

Due to these similarities it is possible to use the same design approach as for beam like structures. A closed row of pentagonal cells provides a smooth boundary with an invariant length whereas the interior can be, at least partially, filled with additional rows of hexagonal cells. How-

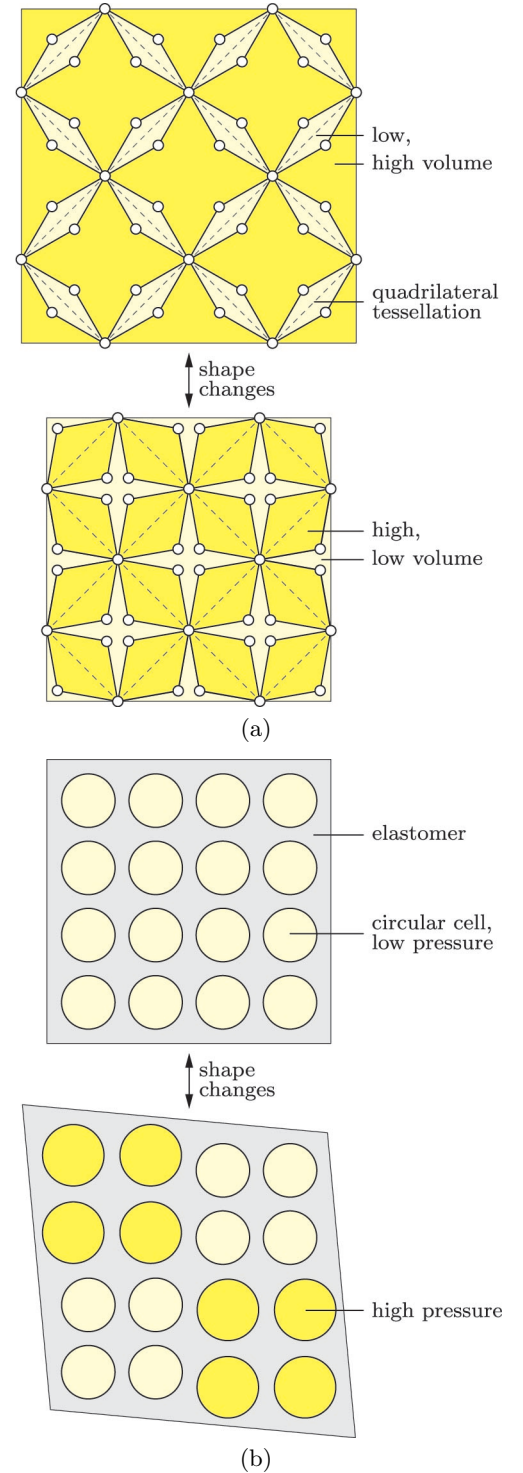


Figure 7.4: Shape changing structures that undergo in-plane deformations due to cell pressure variations. (a) Cellular structure that is generated from a quadrilateral tessellation of a plane. Each cell side is cut at its center and split along its axial direction. The four loose ends are connected by two central cell corners. The cross-sectional area of the actuator is minimized, maximized by pressurizing the convex, concave cells respectively. These kind of actuators can be either monolithic or assembled from stiff cell sides that are connected by frictionless hinges. (b) Shape changing structure that is made from a monolithic, elastic plate by cutting out a regular lattice of circular cells. Pressurization of one or more cells leads to local, elastic cell deformations that can accumulate throughout the plate to generate large shape changes.

ever, the design of plate like structures is complicated by the increased coupling between cells. Furthermore, an optimal grouping of cells with identical pressures is, for the most general case, difficult to find. Hence, relative little work about shape changing plates was published so far as they do not provide a clear benefit with regards to beam like structures. Nonetheless, two different approaches that enable relatively simple shape changes are subsequently reviewed.

A concept for plate like structures that comprises different topologies was patented by Dittrich [67] in 2003. It is based on the regular tessellation of a plane where rigid cell sides are connected at cell corners via frictionless hinges. Some or all of the cell sides are then modified to increase the structures total number of degrees of freedom. This is done by cutting them at their center and/or splitting them along their axial direction. The free cell side ends are subsequently connected by additional hinges. The three possibilities are:

1. A single side is cut at its center.
2. A single side is cut at its center and split in its axial direction.
3. Two neighbouring sides are split in their axial direction.

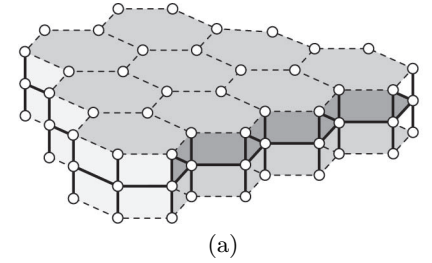
A cellular structure that is generated from a quadrilateral tessellation by cutting all cell sides at their center and splitting them in their axial direction is shown in Figure 7.4. This structure can vary its stiffness and is capable of large, uniform shape changes. Hence it can be used instead of double acting hydraulic or pneumatic cylinders. However, it suffers from the occurrence of cell corners where only two cell sides meet. The axial forces of these sides can vary greatly as they vanish for identical cell pressures. Furthermore, it is prone to snap through buckling as it can be subjected to compression forces. As a consequence, these kind of structures are of little interest for practical applications.

A different approach towards shape changing, plate like structures that is relatively conceptual in nature was proposed by Matthews et al [183] in 2006. It is based on a monolithic, elastic plate from which a regular lattice of circular cells is cutout. Pressurization of one or more cells leads to local deformations that accumulate into global shape changes. The required shape changes are not preprogrammed into the cell geometries so that it can be difficult, if not impossible to split the single cutouts into a small number of groups with equally pressurized cells. It differs from the previous approach insofar that its stiffness depends on the Young's modulus of the material. Furthermore, large material strains are another problem that limit its shape changing potential such that this approach becomes merely an interesting thought experiment.

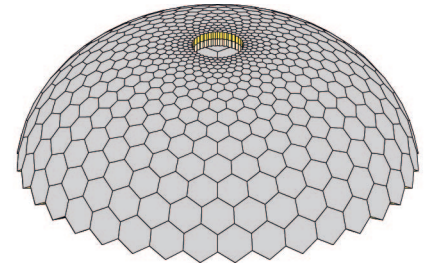
7.1.3 Shells

Shape changing plate and shell like structures differ from each other insofar that the latter can additionally undergo arbitrary out-of-plane deformations. They do not satisfy the plane strain compatibility condition if the Gaussian curvature of their surface needs to be changed. Hence they can generally not be replaced by beam like structures. Furthermore, their design and manufacturing is far more complex so that very little work was published so far.

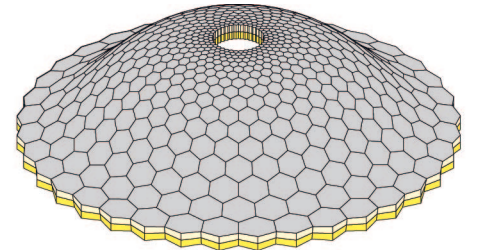
Pagitz and Bold [214, 215] developed a novel approach for shape changing shell like structures in 2012 that is based on three plane layers of hexagonal cells as illustrated in Figure 7.5 (a). The undeformed cell layers possess an identical geometry but differ with respect to their material properties. Cell sides of the central layer are rigid whereas those of the outer layers are elastic. Cell sides of each layer are connected at cell corners via frictionless hinges so that the cells of the central layer can vary the angles between their sides whereas the cells of the outer layers can additionally vary their cell side lengths. Furthermore, opposite cell corners of all layers are connected by beams that remain straight for arbitrary deformations. It is assumed that the single cell layers and the boundary of the structure are sealed by membranes that possess a negligible in-plane and a large out-of-plane stiffness. This leads to the formation of an upper and lower compartment that can be independently



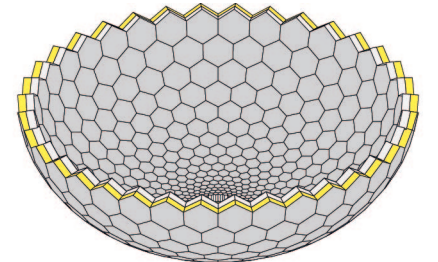
(a)



(b)



(c)



(d)

Figure 7.5: (a) Segment of a shape changing shell like structure that consists of three plane layers of hexagonal cells. The undeformed layers possess an identical geometry but differ with respect to their material properties. The hexagonal cells of the central layer possess rigid sides whereas the cell sides of the outer layers are elastic. As a consequence, central cells can only vary the angles between their sides whereas the outer cells can additionally vary their side lengths. The opposite cell corners of all three layers are connected by rigid beams that remain straight for arbitrary deformations. This creates an upper and lower compartment that can be independently pressurized. (b) The hemispherical equilibrium shape of a plane, circular shell with a central hole after the pressurization of the upper compartment. This shape is pre-programmed into the structure as individual cell side lengths are tailored to maximize the cell areas in the deformed configuration. (c) The shell develops regions of negative curvatures if the pressure is subsequently decreased in the upper and increased in the lower compartment. (d) Rapid shape changes into a hemisphere with a negative mean curvature are triggered if the remaining pressure in the upper compartment is decreased below a critical value.

pressurized.

Two symmetric equilibrium configurations can be preprogrammed into the structure by individually tailoring the length of cell sides. This can be done in a first approximation by maximizing the cell areas of all layers upon deformation into the desired target shapes. However, an exact solution needs to additionally consider the coupling between cell areas and cell side strains. This is highlighted by the fact that out-of-plane deformations of shells require, unlike the previously introduced beam and plate like structures, cell side elongations.

The shape changing capabilities of an annulus shaped structure are illustrated in Figure 7.5 (b-d). The circular opening at its center is required as the assembly of hexagonal cells needs to satisfy the Euler characteristic [244]. The cell side lengths are tailored such that the structure deforms into a hemisphere upon pressurization of the upper or lower compartment. It can be seen that regions of negative curvatures develop if the pressure in the other compartment is subsequently increased. Rapid shape changes that are driven by the release of strain energy occur if a critical pressure ratio between both compartments is reached. This is remarkable as it shows that the fast nastic movements as known from the trapping leaves of *Dionea muscipula* can be triggered by a pressure release. Hence, these kind of plants do not necessarily have to overcome an energy barrier that would have to be sufficiently large to prevent unintended closures.

Similar to the previously introduced beam like structures, additional cell layers can be added to increase the number of potential target shapes at the cost of a reduced shape changing capability. Furthermore, non-symmetric cell layers can be used to increase the design space and thus the potential shape changing capabilities. Another potential improvement is the fusion of shell and beam like structures to create smooth boundaries. However, the optimization and manufacturing of shape changing shell like structures is relatively complex so that it is uncertain if sufficiently powerful tools and manufacturing techniques can be developed in the near future. Nonetheless, the corresponding work does not have to start from scratch as many of the underlying geometric problems are similar to those of freeform architectural designs that are based on hexagonal grids [237].

7.2 Pressure Actuated Cellular Structures

7.2.1 Potential

The potential of pressure actuated cellular structures depends to a large degree on their shape changing capabilities, stiffness and selfweight. A

one meter long cantilever as shown in Figure 7.6 (a) is subsequently used to provide a first insight. It consists of two cell rows that are assembled from pentagonal and hexagonal cells with identical geometries. The inherent stiffness of the cells is negligible as they consist of rigid sides and frictionless hinges. The movements of cell corners at both ends are constrained by supports or a rigid endplate such that edge effects are eliminated. The pressurized structure thus deforms into a circular arc upon pressurization. Cell row pressures of either 0.4 or 2.0 MPa lead to subtended angles of about 60° and 110° . Angle changes between adjacent pentagonal cells are thus about 5° .

The equilibrium configurations of the cantilever for tip loads of 5 and 10 kN/m are shown in Figure 7.6 (b-c) where the unit “kN/m” refers to a depth of one meter. It can be seen that the cantilever is capable of moving a tip load of 10 kN/m over a vertical distance that nearly equals its own length. A remarkable property of pressure actuated cellular structures is that their cell side forces are mostly driven by cell pressures. This makes them highly resilient against unexpectedly large loads and deformations. For example, the maximum axial cell side forces for all load cases are less than 250 kN/m. The required cell side thicknesses due to normal forces are therefore less than half a millimeter if modern materials such as carbon fiber reinforced polymers are used. The nodal coordinates and cell side forces of the cantilever with a tip load of 5 kN/m are summarized in the appendix for both equilibrium configurations. This enables a verification of the presented results via simple hand calculations.

Cell sides that are located at the boundary or between cell rows are subjected to differential pressures. These additional loads lead to bending moments that considerably increase the required cell side thicknesses and thus the overall weight. Bending moments can be minimized with the help of cytoskeletons or efficiently carried by cell sides with a variable thickness. Furthermore, the stiffness and load carrying capacity of the cantilever increases linearly and its weight sublinearly with increasing

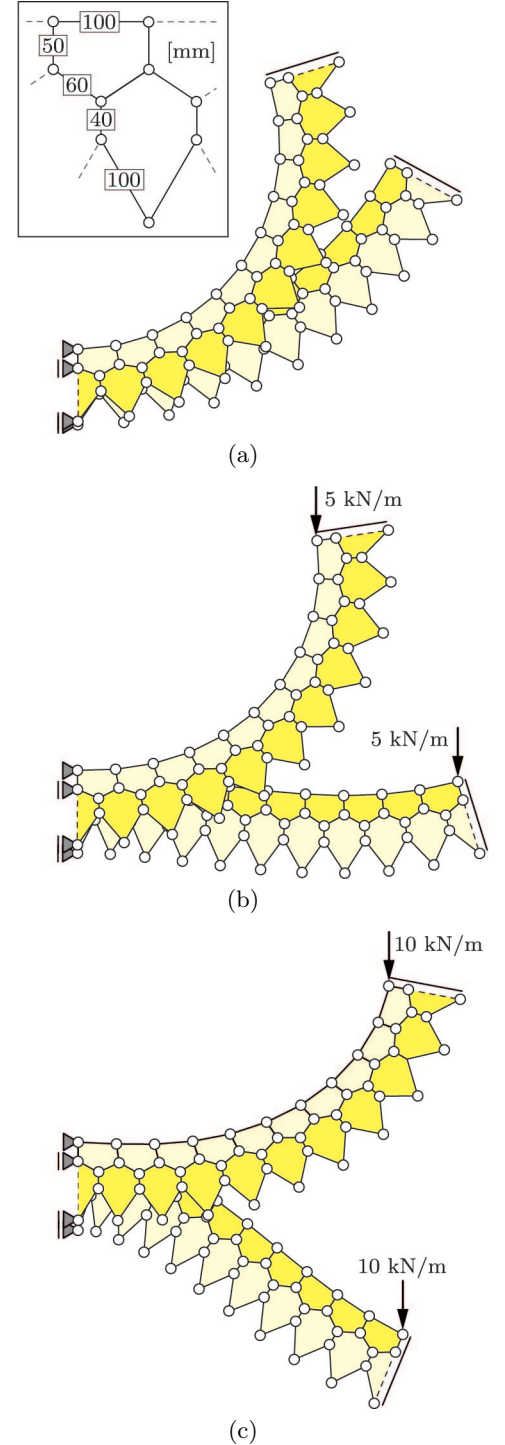


Figure 7.6: Shape changing capability and load carrying capacity of a pressure actuated cellular structure. The one meter long cantilever consists of two cell rows that are assembled from identical pentagonal and hexagonal cells. Cell sides are rigid and connected at cell corners via frictionless hinges. Edge effects are eliminated by constraining the displacements of end nodes to a common plane so that the unloaded structure deforms into a circular arc upon pressurization. Cell row pressures are either 0.4 or 2.0 MPa. Equilibrium shapes of (a) an unloaded and loaded cantilever with a tip load of (b) 5 and (c) 10 kN/m where “kN/m” refers to a unit depth.

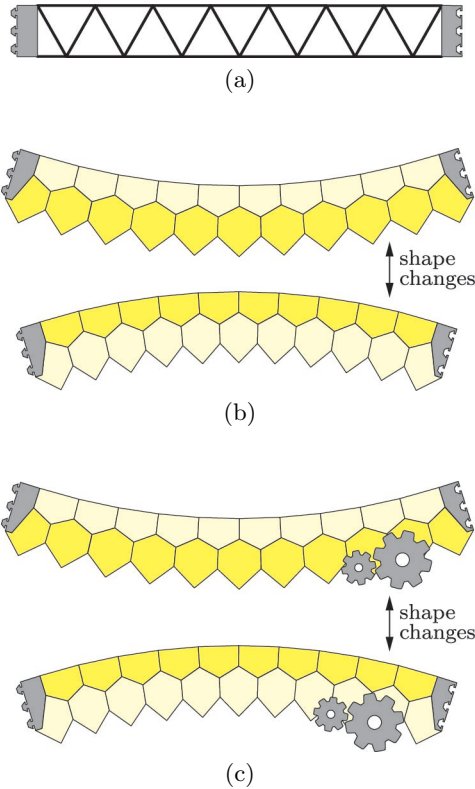


Figure 7.7: Three kind of modules with an increasing shape changing capability and weight. Modules possess connectors at both ends so that they can be arbitrarily combined. (a) Rigid module that is based on a truss structure. (b) Pressure actuated cellular module whose equilibrium shapes resemble circular arcs. Its potential shape changing capabilities are limited by stiffness requirements. (c) A mechanical module that combines a pressure actuated cellular structure and a passive or active mechanisms to increase its shape changing capabilities and stiffness.

cell row pressures. This is due to the superlinear relationship between the bending stiffness and cell side thicknesses. Commonly used pressures of pneumatic systems reach values of up to 5 MPa so that the chosen cell row pressures for this example are relatively moderate. A preliminary sizing of the cantilever indicates that a selfweight of as low as 10 kg/m^2 seems to be possible. In comparison, the projected area of an A380 wing is 845 m^2 and its selfweight is about 66,000 kg so that the corresponding weight per unit area is 78 kg/m^2 .

7.2.2 Shape Changing Modules

Truss and pressure actuated cellular structures have much in common as they both consist of cells that can be pressurized to increase their stiffness. Hence they differ only with respect to their inherent degrees of freedom that depend on the cell topologies. It is generally pointless to use pentagonal and hexagonal cells in regions of pressure actuated cellular structures that need to undergo only small shape changes. A tight integration of triangular and pentagonal, hexagonal cells can thus be advantageous. A reversible transition between different cell topologies can be achieved with the help of cytoskeletons. These subcellular structures are relatively thin so that they can carry large tension but only minor compression forces. Hence they can be used to fully or partially subdivide a cell into triangles upon reaching limit deformations that put them into tension [222].

The achievable change of angles between adjacent pentagonal base sides is limited. As a consequence, potential shape changes of pressure actuated cellular structures depend on the number of pentagonal cells. However, structures with a larger number of smaller cells possess a reduced stiffness so that the use of additional supports that can be provided by passive or active mechanisms might be necessary. This can even lead to pressure actuated cellular structures that resemble not much more than a flexible skin whose shape is fully controlled by active mechanisms. It is remarkable that rigid structures are commonly used in classical high lift devices whereas gapless leading edges that are based on flexible skins and active mechanisms are currently developed. However, both approaches are rather extreme and most likely not optimal. Pressure actuated cellular structures can be used instead to create a wide range of intermediate solutions that might even function without additional mechanisms.

A detailed investigation of pressure actuated cellular structures with different cell topologies, cytoskeletons and rigid body mechanisms is beyond the scope of this thesis. However, three kind of modules with an increasing shape changing capability as illustrated in Figure 7.7 are sub-

sequently used to outline the potential of an integral approach. These modules possess connectors at both ends so that they can be arbitrarily combined. Furthermore, their outer surfaces resemble circular arcs with a constant arc-length and a constant or variable radius. Rigid modules are based on truss structures so that their surface shapes are invariant. In contrast, the shape changing capabilities of modules that are based on pressure actuated cellular structures are only limited by stiffness constraints. These constraint can be overcome with the help of passive or active mechanisms that provide additional supports at the cost of an increased weight, complexity and construction space. Similar to Lego bricks [18], modules can be manufactured with different, standardized lengths, surface radii and shape changing capabilities. Their equilibrium shapes can then be adjusted within these bounds by cell pressure variations.

7.2.3 Application Range

The determination of different, one-dimensional geometries that optimize certain properties for a given set of environmental conditions is relatively simple. For example, optimal airfoil geometries for high lift and flight configurations are well known. However, it is much harder to translate these geometries into shape changing structures that are sufficiently lightweight, strong and manufacturable. It is therefore often advantageous to gain a first insight with the help of prototype structures that can be assembled from a set of shape changing modules.

The one-dimensional geometries can be broken down into C^1 continuous sequences of circular arcs with different radii and identical arc-lengths. The properties of these arcs can be optimized such that they approximate the geometries in a least square sense. This requires a discontinuous optimization approach as the arc-lengths need to be chosen from a set of admissible values. The optimization results can then be

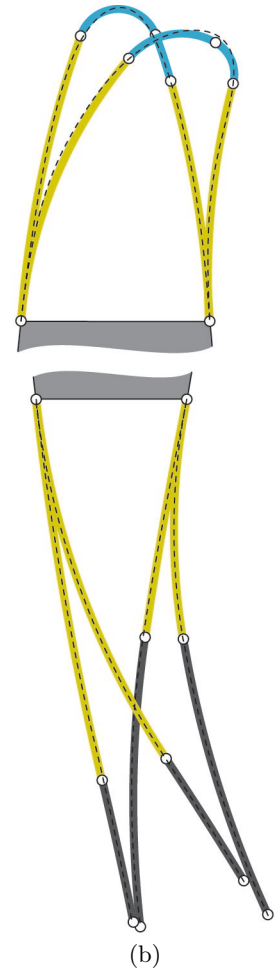
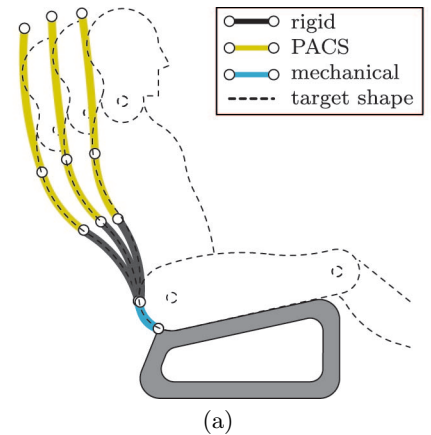


Figure 7.8: Two example structures that highlight the approximation power and application range of shape changing modules. (a) A passenger seat that can adapt to 1.7-1.9 m tall persons. It consists of one rigid, one mechanical and two pressure actuated modules. The backward, central and forward position is shown for a 1.8 m tall person. (b) Superimposed high lift and flight configuration of a gapless leading and trailing edge. The leading edge is assembled from two pressure actuated modules that are separated by two mechanical modules. Both, the upper and lower trailing edge sides are based on a rigid and pressure actuated module. The gap between the two rigid modules in the high lift configuration is inevitable as modules possess an invariant arc-length.

used to assemble the corresponding structure with the help of shape changing modules. This is subsequently demonstrated by means of two examples.

Car Seat

The first example deals with a passenger seat that can vary its inclination and adapt to persons with a body height between 1.7-1.9 m. Boundary geometries of humans with different sizes and postures were derived from a model where the head, torso and extremities are assumed to be rigid bodies that are connected via central hinges. Details about the geometry of the rigid bodies and their connection points can be found in the appendix. The radii and discrete arc-lengths of circular arcs that serve as a basis for the shape changing modules were optimized for 1.7, 1.8 and 1.9 m tall persons in a backward, central and forward position. The optimized arc-lengths \mathbf{L} from top to bottom are

$$\mathbf{L} = \begin{bmatrix} 0.40 & 0.20 & 0.25 & 0.10 \end{bmatrix}^T \text{ m}$$

and the corresponding minimum and maximum subtended angles for all considered positions are

$$\begin{bmatrix} \alpha_{\min} \\ \alpha_{\max} \end{bmatrix} = \begin{bmatrix} -19^\circ & -42^\circ & 42^\circ & -80^\circ \\ 6^\circ & -33^\circ & 45^\circ & -48^\circ \end{bmatrix}.$$

Therefore, the required shape changing capabilities per unit length are

$$(\alpha_{\max} - \alpha_{\min}) = \begin{bmatrix} 63^\circ & 45^\circ & 12^\circ & 320^\circ \end{bmatrix} \text{ m}^{-1}.$$

It can be seen that the shape changes of the third arc are relatively small in comparison to those of the fourth arc. Furthermore, due to the chosen boundary conditions, the bending moments in the backrest increase towards the base of the seat. Hence it is best to use pressure actuated modules for the first two arcs, a rigid module for the third arc and a mechanical module for the fourth arc as illustrated in Figure 7.8 (a). This result is rather unsurprising as most car seats are based on a mechanism that connects a rigid backrest to its base. Nonetheless, they usually do not possess an upper part that can vary its shape. It can be seen that the approximation errors are remarkably small despite the use of only four modules.

Gapless Leading and Trailing Edge

The second example deals with a gapless leading and trailing edge that can continuously vary their shapes between a high lift and flight configuration. Details about the geometries of the corresponding airfoils can be found in the appendix. The optimized arc-lengths \mathbf{L} of the circular

arcs for the leading edge that start from the support in counterclockwise direction are

$$\mathbf{L} = \begin{bmatrix} 0.50 & 0.10 & 0.20 & 0.60 \end{bmatrix} \text{ m}$$

and the corresponding minimum and maximum subtended angles for both positions are

$$\begin{bmatrix} \alpha_{\min} \\ \alpha_{\max} \end{bmatrix} = \begin{bmatrix} -18^\circ & 5^\circ & 80^\circ & 15^\circ \\ 13^\circ & 75^\circ & 140^\circ & 35^\circ \end{bmatrix}.$$

Therefore, the required shape changing capabilities per unit length are

$$(\alpha_{\max} - \alpha_{\min}) = \begin{bmatrix} 62^\circ & 700^\circ & 300^\circ & 33^\circ \end{bmatrix} \text{ m}^{-1}.$$

It can be seen that the second and third arc need to undergo relatively large whereas the first and fourth arc need to undergo only moderate shape changes. The leading edge can thus be assembled from two pressure actuated and two mechanical modules as shown in Figure 7.8 (b).

The corresponding arc-lengths \mathbf{L} for the trailing edge that start from the support in counterclockwise direction are

$$\mathbf{L} = \begin{bmatrix} 0.80 & 0.30 & 0.60 & 0.50 \end{bmatrix} \text{ m}$$

and the minimum and maximum subtended angles for both positions are

$$\begin{bmatrix} \alpha_{\min} \\ \alpha_{\max} \end{bmatrix} = \begin{bmatrix} 7^\circ & -2^\circ & -15^\circ & -21^\circ \\ 27^\circ & -2^\circ & -15^\circ & -3^\circ \end{bmatrix}.$$

Data for the geometry of the high lift configuration is not available so that it is assumed that the radii of the circular arcs at the rear of the trailing edge are invariant. The required shape changes thus are

$$(\alpha_{\max} - \alpha_{\min}) = \begin{bmatrix} 25^\circ & 0^\circ & 0^\circ & 36^\circ \end{bmatrix} \text{ m}^{-1}.$$

It can be seen that the first and fourth module need to undergo only small shape changes so that the upper and lower side of the trailing edge can be each assembled from a pressure actuated and rigid module. The gap between the two rigid modules in the high lift configuration is inevitable as the arc-lengths of the considered modules are invariant. Hence, a closed boundary would either require modules that can vary their arc-length or an approach where the shape of the complete airfoil is changed instead.

It is rather surprising that a wide range of shape changing structures can be realized with the help of a few standardized modules that resemble circular arcs. However, such an approach inevitably leads to an increased weight and a reduced stiffness. Furthermore, compromises are made with

respect to approximation errors so that it is often best to use tailored shape changing structure instead. It is shown in the subsequent chapters how the cell corner geometries, cell side lengths and cell side thicknesses of pressure actuated cellular structures can be efficiently optimized for arbitrary sets of target shapes.

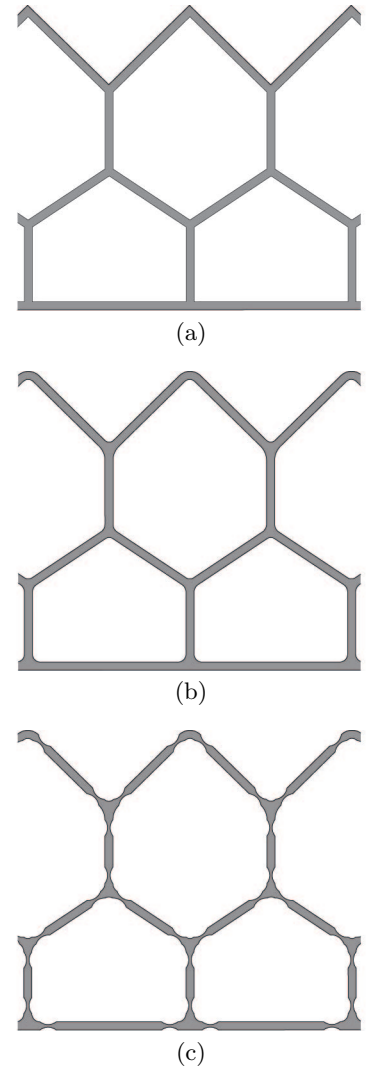
Chapter 8

Geometric Model

The compliant pressure actuated cellular structures that are considered in this thesis are based on prismatic cells whose geometries can be fully described in two-dimensions. Potential cell topologies are limited to pentagonal and hexagonal cells as they maximize the inherent degrees of freedom, provide a smooth outer surface and minimize the total cell side length for a given cross sectional area. It is therefore rather surprising that some authors approach the design of pressurized cellular structures with the help of topology optimization [184, 303]. Despite a predetermined topology, it is still of utmost importance that their geometry is described as efficiently as possible to simplify their simulation and optimization.

It is therefore assumed in the following that compliant pressure actuated cellular structures are generated in three steps as illustrated in Figure 8.1. Rectangular cell sides with individual lengths and thicknesses are joined into a cellular structure for given cell corner angles. The pointed cell corners are rounded out and cutouts are made to create compliant hinges that localize bending deformations. It is subsequently shown how the cell corner angles can be represented by a minimal set of global state variables. Furthermore, additional global state variables for the computation of optimal cell corner and hinge geometries are introduced.

Figure 8.1: Generation of a compliant pressure actuated cellular structure. (a) Structure is assembled from rectangular cell sides with individual lengths and thicknesses for given cell corner angles. (b) Pointed cell corners are rounded out with circular arcs and (c) cutouts are made to create compliant hinges that localize bending deformations.



8.1 Corner Angles

8.1.1 Global State Variables

The cell corner angles of pressure actuated cellular structures can be expressed in terms of global state variables \mathbf{u} and effective cell side lengths \mathbf{v} as illustrated in Figure 8.2. It can be seen that the cell side lengths are defined with respect to fictitious, centric cell corners where

$$\mathbf{v} = [\mathbf{b}_1^\top \quad \mathbf{c}_1^\top \quad \dots \quad \mathbf{b}_{n_R}^\top \quad \mathbf{c}_{n_R}^\top \quad \mathbf{a}^\top]^\top \in \mathbb{R}^{n_v} \quad (8.1)$$

and, for example $\mathbf{b}_i = [b_{i,1} \quad \dots \quad b_{i,n_P+2-i}]^\top$. Herein, n_P denotes the number of base pentagons and n_R the number of cell rows. It can be seen from the vector \mathbf{b}_i that it is assumed that each additional cell row contains one cell less than the previous row. This is not a limitation of the proposed framework since arbitrary topologies at both ends can be modeled with the help of constraints. Therefore, the total number of hexagonal cells n_T and cell sides n_v of the considered pressure actuated cellular structures are

$$n_T = \frac{1}{2}(2n_P - n_R)(n_R - 1) \quad (8.2)$$

and

$$n_v = 4n_P + 3n_T + n_R. \quad (8.3)$$

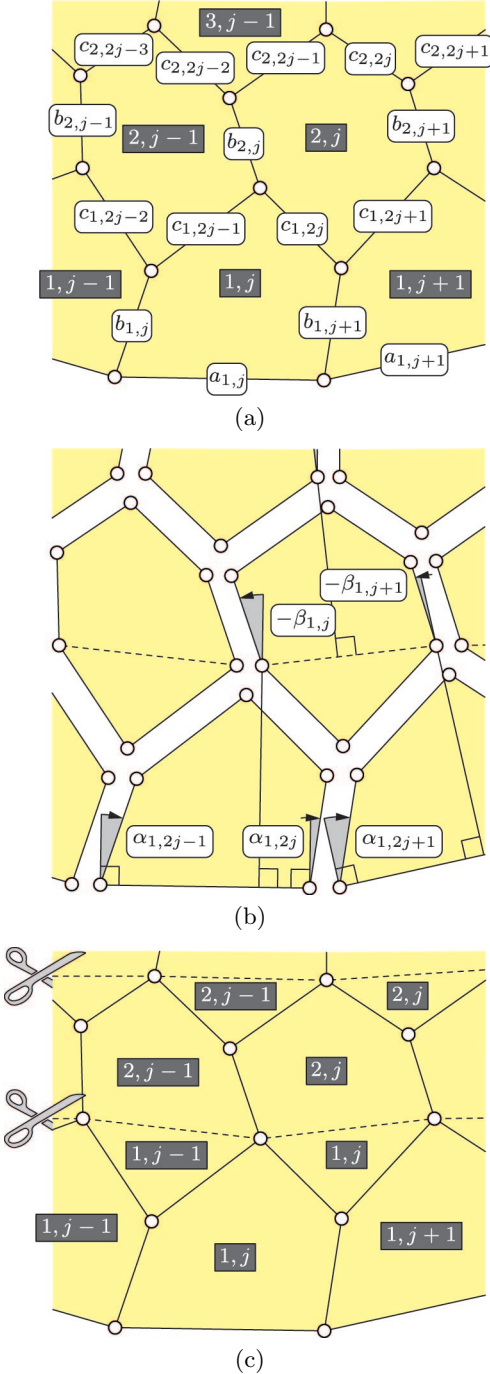
The global state variables \mathbf{u} that define the inclinations of the cell sides \mathbf{b} are

$$\mathbf{u} = [\alpha_{1,1} \quad \dots \quad \alpha_{1,2n_P} \quad \beta_{1,1} \quad \dots \quad \beta_{n_R-1,n_P-n_R+2}]^\top \in \mathbb{R}^{n_u} \quad (8.4)$$

where the number of state variables n_u is

$$n_u = 2n_P + n_T + n_R - 1. \quad (8.5)$$

Figure 8.2: A minimal set of global state variables that fully defines the cell corner angles of pressure actuated cellular structures with an arbitrary number of cell rows. (a) Cell numbering and effective cell side lengths \mathbf{v} between fictitious, centric cell corners. (b) Global state variables \mathbf{u} that define the inclinations of cell sides. An exploded view is used to increase the clarity of the presentation. (c) Different cell numbering of pressure actuated cellular structures with more than one cell row that are cut into strips of triangular and/or pentagonal cells. Global state variables \mathbf{u} can be transformed into local state variables for the pentagonal \mathbf{u}^P and triangular \mathbf{u}^T cells. They serve as a basis for the computation of cell corner angles.



8.1.2 Pentagonal Cells

Local State Variables

Pressure actuated cellular structures with more than one cell row can be cut into strips that consist of triangular and/or pentagonal cells. The internal lengths \mathbf{x} , y , z and cell corner angles γ of the j -th pentagonal cell in the i -th cell row can be expressed in terms of the effective cell side lengths

$$\mathbf{v}_{i,j}^P(\mathbf{v}) = [b_{i,j} \quad b_{i,j+1} \quad c_{i,2j-1} \quad c_{i,2j}]^T \quad (8.6)$$

and the local state variables

$$\mathbf{u}_{i,j}^P(\mathbf{u}, \mathbf{v}) = [\alpha_{i,2j-1} \quad \alpha_{i,2j} \quad a_{i,j}]^T \quad (8.7)$$

as shown in Figure 8.3. It can be seen that a superscript “P” is used to denote the local state variables of pentagonal cells. The base side a is a part of \mathbf{u}^P since it is an abstract term for hexagonal cells that are cut into a triangular and pentagonal part.

Dependent Variables

The local state variables of a pentagonal cell can be used to derive a number of dependent variables. The length y that divides the pentagonal cell into a triangular and quadrilateral part is

$$\begin{aligned} y_{i,j} &= \sqrt{x_{i,2j-1}^2 + x_{i,2j}^2} \\ &= \sqrt{(a + \sin(\alpha_2)b_2 - \sin(\alpha_1)b_1)^2 + (\cos(\alpha_2)b_2 - \cos(\alpha_1)b_1)^2} \end{aligned} \quad (8.8)$$

and the altitude z of the triangular part can be expressed as

$$z_{i,j} = \sqrt{c_1^2 - \frac{1}{4y_{i,j}^2} (y_{i,j}^2 + c_1^2 - c_2^2)^2}. \quad (8.9)$$

Previous expressions are based on the abbreviations

$$\mathbf{v}_{i,j}^P = [b_1 \quad b_2 \quad c_1 \quad c_2]^T \quad (8.10)$$

and

$$\mathbf{u}_{i,j}^P = [\alpha_1 \quad \alpha_2 \quad a]^T \quad (8.11)$$

that are used for the sake of clarity. The internal angle $\gamma_{i,2j-1}$ of a pentagonal cell from which the cell corner angles can be derived is completely

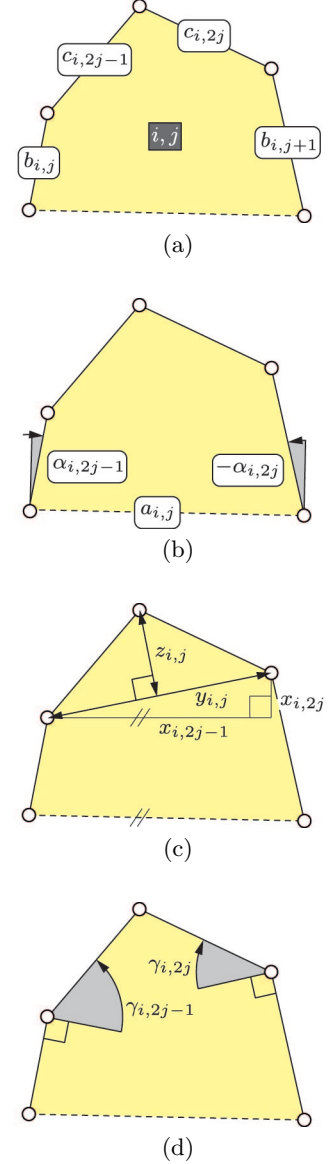


Figure 8.3: Variables of the j -th pentagonal cell in the i -th cell row. Local state variables (a) \mathbf{v}^P for the cell side lengths and (b) \mathbf{u}^P for the cell side inclinations and base length. (c) Internal lengths \mathbf{x} , y , z and (d) internal angles γ .

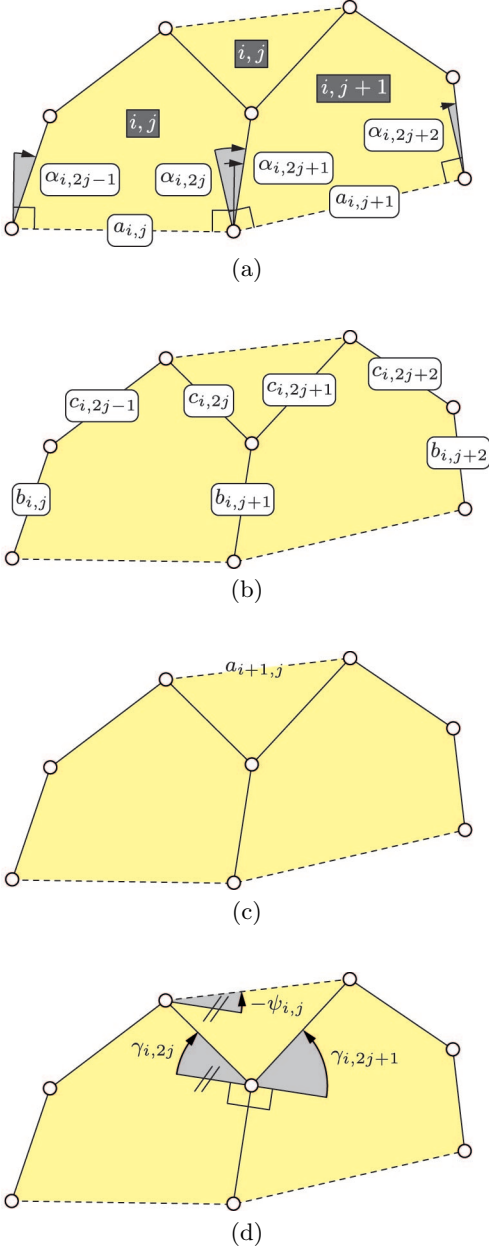


Figure 8.4: Variables of the j -th triangular cell in the i -th cell row. Local state variables (a) \mathbf{v}^T for the cell side lengths and (b) \mathbf{u}^T for the cell side inclinations and base lengths. (c) Internal length a and (d) internal angles γ , ψ .

determined by the local state variables through

$$\gamma_{i,2j-1} = \begin{cases} \alpha_1 + \arcsin\left(\frac{x_{i,2j}}{y_{i,j}}\right) + \arcsin\left(\frac{z_{i,j}}{c_1}\right) & c_2^2 \leq y_{i,j}^2 + c_1^2 \\ \alpha_1 + \arcsin\left(\frac{x_{i,2j}}{y_{i,j}}\right) - \arcsin\left(\frac{z_{i,j}}{c_1}\right) + \pi & c_2^2 > y_{i,j}^2 + c_1^2. \end{cases} \quad (8.12)$$

The corresponding expressions for the internal angle $\gamma_{i,2j}$ are derived in a similar manner. The previous equation could be written without a distinction of cases. However, this would result in lengthier expressions. The cross sectional area A^P of a pentagonal cell that is required for the simulation and optimization of pressure actuated cellular structures results in

$$A_{i,j}^P = \frac{1}{2} ((\cos(\alpha_1) b_1 + \cos(\alpha_2) b_2) a + \sin(\alpha_2 - \alpha_1) b_1 b_2 + y_{i,j} z_{i,j}) \quad (8.13)$$

where the superscript “P” is used to distinguish it from the cross sectional area of triangular cells. However, despite its notation, it is not a state variable.

8.1.3 Triangular Cells

Local State Variables

A triangular cell is generated from a hexagonal cell by cutting it into a triangular and pentagonal part. The total number of triangular cells n_T is therefore equal to the total number of hexagonal cells. The cell corner angles of the j -th triangular cell in the i -th cell row can be expressed in terms of the effective cell side lengths

$$\mathbf{v}_{i,j}^T (\mathbf{v}^P) = [b_{i,j} \quad b_{i,j+1} \quad b_{i,j+2} \quad c_{i,2j-1} \quad c_{i,2j} \quad c_{i,2j+1} \quad c_{i,2j+2}]^T \quad (8.14)$$

and the state variables

$$\mathbf{u}_{i,j}^T (\mathbf{u}^P) = [\alpha_{i,2j-1} \quad \alpha_{i,2j} \quad \alpha_{i,2j+1} \quad \alpha_{i,2j+2} \quad a_{i,j} \quad a_{i,j+1}]^T. \quad (8.15)$$

The local state variables of a triangular cell that are denoted by a superscript “T” can thus be fully assembled from the local state variables of its neighbouring pentagonal cells as illustrated in Figure 8.4.

Dependent Variables

The length a that divides a hexagonal cell into a triangular and pentagonal part can be derived from the local state variables of a triangular

cell so that

$$a_{i+1,j} = \sqrt{c_{i,2j}^2 + c_{i,2j+1}^2 + 2c_{2j}c_{2j+1} \cos(\gamma_{i,2j} + \gamma_{i,2j+1})}. \quad (8.16)$$

Similarly, the internal angle ψ of the triangular part results in

$$\psi_{i,j} = \gamma_{i,2j} - \arccos\left(\frac{a_{i+1,j}^2 + c_{i,2j}^2 - c_{i,2j+1}^2}{2a_{i+1,j}c_{i,2j}}\right). \quad (8.17)$$

Finally, the cross sectional area A^T of a triangular cell is

$$A_{i,j}^T = \frac{1}{2}c_{i,2j}c_{i,2j+1} \sin(\gamma_{i,2j} + \gamma_{i,2j+1}). \quad (8.18)$$

It can be seen that the length a , the angle ψ and the cross sectional area A^T are functions of the internal angles γ of the neighbouring pentagonal cells.

8.1.4 Transformation Matrices

The local state variables of the pentagonal $\mathbf{u}_{i,j}^P$ and triangular $\mathbf{u}_{i,j}^T$ cells can be directly assembled from the global state variables \mathbf{u} and \mathbf{v} if they are located in the first cell row ($i = 1$). In contrast, local state variables of cells in other rows depend on both, the global state variables β that are contained in \mathbf{u} and the local state variables of the previous cell row. As illustrated in Figure 8.5, the state variables $\mathbf{u}_{i+1,j}^P$ of the j -th pentagonal cell in the $(i+1)$ -th cell row can be expressed in terms of the state variables $\mathbf{u}_{i,j}^T$, $\beta_{i,j}^T = [\beta_{i,j} \ \beta_{i,j+1}]^T$ and $\mathbf{v}_{i,j}^T$ of the j -th triangular cell in the i -th cell row such that

$$\mathbf{u}_{i+1,j}^P(\mathbf{u}_{i,j}^T, \mathbf{v}_{i,j}^T, \beta_{i,j}^T) = \mathbf{T}_{i,j}^\beta \beta_{i,j}^T + \mathbf{T}_{i,j}^{\text{lin}} \mathbf{u}_{i,j}^T + \mathbf{T}_{i,j}^{\text{nl}}(\mathbf{u}_{i,j}^T, \mathbf{v}_{i,j}^T) \quad (8.19)$$

where the linear matrices are

$$\mathbf{T}_{i,j}^\beta = \begin{bmatrix} 1 & 0 \\ 0 & 1 \\ 0 & 0 \end{bmatrix} \quad (8.20)$$

and

$$\mathbf{T}_{i,j}^{\text{lin}} = \begin{bmatrix} 0 & -1 & 0 & 0 & 0 & 0 \\ 0 & 0 & -1 & 0 & 0 & 0 \\ 0 & 0 & 0 & 0 & 0 & 0 \end{bmatrix}. \quad (8.21)$$

The nonlinear matrix that depends on the internal length a and angle ψ of a triangular cell is

$$\mathbf{T}_{i,j}^{\text{nl}}(\mathbf{u}_{i,j}^T, \mathbf{v}_{i,j}^T) = \begin{bmatrix} -\psi_{i,j}(\mathbf{u}_{i,j}^T, \mathbf{v}_{i,j}^T) \\ -\psi_{i,j}(\mathbf{u}_{i,j}^T, \mathbf{v}_{i,j}^T) \\ a_{i+1,j}(\mathbf{u}_{i,j}^T, \mathbf{v}_{i,j}^T) \end{bmatrix}. \quad (8.22)$$

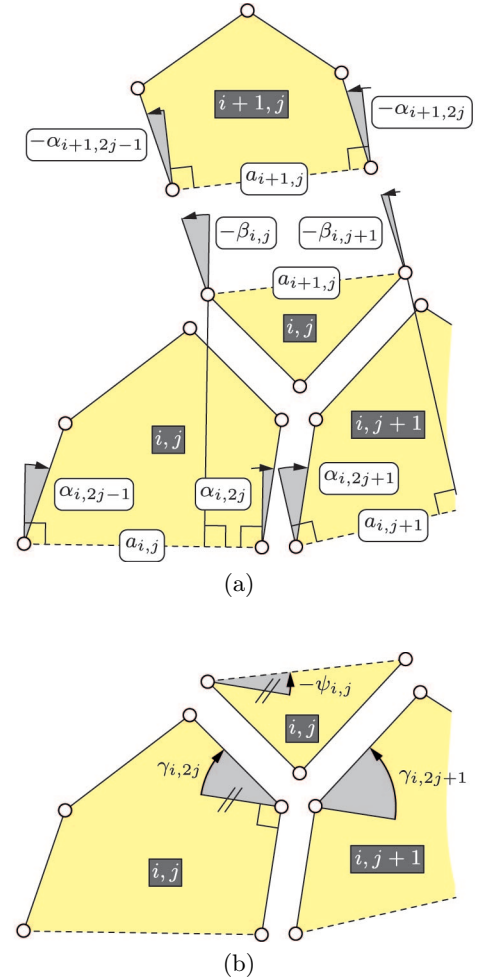


Figure 8.5: (a) Global, local state variables and dependent variable of a hexagonal cell that is cut into a pentagonal and triangular part. (b) Internal angles of triangular and neighbouring pentagonal cells. An exploded view is used to increase the clarity of the presentation.

Previous matrices can be used to assemble the transformation matrix \mathbf{T}^u that relates the pentagonal state variables \mathbf{u}^P to the triangular state variables \mathbf{u}^T

$$\mathbf{T}_{i,j}^u = \frac{\partial \mathbf{u}_{i+1,j}^P}{\partial \mathbf{u}_{i,j}^T} = \mathbf{T}_{i,j}^{\text{lin}} + \frac{\partial \mathbf{T}_{i,j}^{\text{nl}}}{\partial \mathbf{u}_{i,j}^T}. \quad (8.23)$$

Similarly, the transformation matrix \mathbf{T}^v relates the pentagonal state variables \mathbf{u}^P to the triangular state variables \mathbf{v}^T so that

$$\mathbf{T}_{i,j}^v = \frac{\partial \mathbf{u}_{i+1,j}^P}{\partial \mathbf{v}_{i,j}^T} = \frac{\partial \mathbf{T}_{i,j}^{\text{nl}}}{\partial \mathbf{v}_{i,j}^T}. \quad (8.24)$$

Hence it is possible to sequentially compute the local state variables of triangular and pentagonal cells from the local state variables of previous cell rows.

8.2 Corner Geometries

8.2.1 Global State Variables

Compliant pressure actuated cellular structures that are assembled from rectangular cell sides possess pointed cell corners. These corners are subsequently rounded out with circular arcs to increase their aesthetics and stiffness and to minimize stress concentrations. This requires, besides the global state variables \mathbf{u} and \mathbf{v} from which the cell corner angles are derived, additional global state variables that describe the cell side thicknesses \mathbf{t} and the target curvature κ^{tar} of all cell corner fillets. The ordering of the cell side thicknesses is similar to that of the cell side lengths \mathbf{v} so that

$$\mathbf{t} = [\mathbf{t}_{b,1}^\top \quad \mathbf{t}_{c,1}^\top \quad \dots \quad \mathbf{t}_{b,nR}^\top \quad \mathbf{t}_{c,nR}^\top \quad \mathbf{t}_a^\top]^\top \in \mathbb{R}^{nv} \quad (8.25)$$

where, for example $\mathbf{t}_{b,i} = [t_{b,i,1} \quad \dots \quad t_{b,i,nP+2-i}]^\top$.

8.2.2 Local State Variables

The geometry of the k -th cell corner that connects n_s cell sides can be expressed in terms of the cell side thicknesses

$$\mathbf{t}_k^C(\mathbf{t}) = [t_{k,1} \quad \dots \quad t_{k,n_s}]^\top \quad (8.26)$$

and the local state variables \mathbf{u}^C that are composed of the cell corner angles $\boldsymbol{\theta}$ so that

$$\mathbf{u}_k^C(\mathbf{u}^P, \mathbf{v}^P) = [\theta_{k,1} \quad \dots \quad \theta_{k,n_s-1}]^\top. \quad (8.27)$$

The latter contains only $n_s - 1$ angles since $\theta_{k,n_s} = 2\pi - \sum_{i=1}^{n_s-1} \theta_{k,i}$. It can be seen that the superscript “C” is used to denote local state variables of cell corners. Variables of the k -th cell corner that connects $n_s = 3$ cell sides are illustrated in Figure 8.6.

8.2.3 Dependent Variables

The angles ω between the cell sides and chords of the circular fillets as well as the chord lengths \mathbf{x} can be computed from the local state variables \mathbf{u}^C , \mathbf{t}^C and the unknown cell corner dimensions ξ . However, their derivations are straightforward so that they are not explicitly given. A C^1 continuous transition between cell corners and sides requires that $\sum_{i=1}^{n_s} (\omega_{k,2i} - \omega_{k,2i-1})^2 = 0$. This can not be satisfied for arbitrary cell side thicknesses and cell corner angles. Hence it is necessary to average the kinks between the cell sides and circular arcs so that the fillet curvatures κ become

$$\kappa_{k,i} = \frac{2}{x_{k,i}} \cos\left(\frac{\theta_{k,i}}{2}\right) \quad (8.28)$$

where $i = 1, \dots, n_s$.

8.2.4 Optimal Cell Corner Dimensions

It is not possible to directly compute the cell corner dimensions ξ from the local state variables of a cell corner. Instead they have to be optimized such that they minimize both, the kinks between the cell sides and circular arcs as well as the deviations of the fillet curvatures from the target value κ^{tar} . This is subsequently done in two steps.

First Step

Kinks between cell sides and fillets can be minimized in a least square sense by computing

$$\tilde{\xi}_k(\mathbf{t}_k^C, \mathbf{u}_k^C, \xi_k^{\text{tar}}) = \underset{\substack{\xi_k \\ \mathcal{C}_k(\xi_k, \xi_k^{\text{tar}}) = 0}}{\operatorname{argmin}} \mathcal{F}_k(\mathbf{t}_k^C, \mathbf{u}_k^C, \xi_k) \quad (8.29)$$

where the objective \mathcal{F} is

$$\mathcal{F}_k(\mathbf{t}_k^C, \mathbf{u}_k^C, \xi_k) = \sum_{i=1}^{n_s} (\omega_{k,2i} - \omega_{k,2i-1})^2 \quad (8.30)$$

and the constraint \mathcal{C} that restricts the solution space for ξ is

$$\mathcal{C}_k(\xi_k, \xi_k^{\text{tar}}) = \xi_k^{\text{tar}} - \sum_{i=1}^{n_s} \xi_{k,i}. \quad (8.31)$$

Hence, the Lagrangian of the first optimization step can be written as

$$\mathcal{L}_k(\xi_k, \lambda_k) = \underset{\mathbf{u}_k^C, \mathbf{t}_k^C, \xi_k^{\text{tar}}}{\mathcal{F}_k(\xi_k)} + \lambda_k \mathcal{C}_k(\xi_k). \quad (8.32)$$

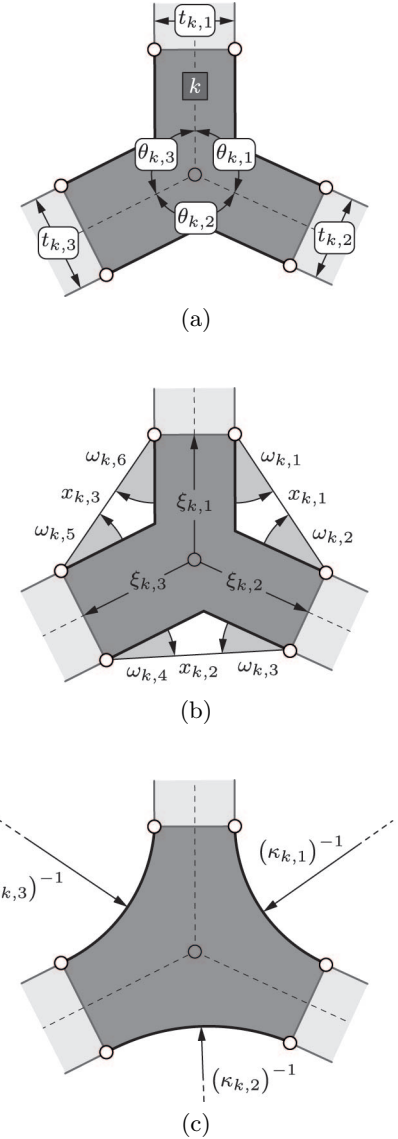


Figure 8.6: Variables of the k -th cell corner. (a) Local state variables \mathbf{u}^C and \mathbf{t}^C . (b) Internal angles ω , chord lengths \mathbf{x} and cell corner dimensions ξ . (d) Fillet curvatures κ .

The variables $\tilde{\mathbf{v}} = [\tilde{\boldsymbol{\xi}} \quad \tilde{\lambda}]^\top$ that satisfy the stationarity condition can be iteratively computed by using a Newton based approach. Variables of the $(i+1)$ -th iteration are

$$\mathbf{v}_k^{i+1} = \mathbf{v}_k^i - (\mathbf{H}_k^i)^{-1} \mathbf{g}_k^i \quad (8.33)$$

where the gradient \mathbf{g} is

$$\mathbf{g}_{\mathbf{u}_k^C, \mathbf{t}_k^C, \boldsymbol{\xi}_k^{\text{tar}}}^i(\mathbf{v}_k^i) = \left[\frac{\partial \mathcal{L}_k^i}{\partial \boldsymbol{\xi}_k} \quad \frac{\partial \mathcal{L}_k^i}{\partial \lambda_k} \right]^\top \quad (8.34)$$

and the Hessian \mathbf{H} is

$$\mathbf{H}_{\mathbf{u}_k^C, \mathbf{t}_k^C, \boldsymbol{\xi}_k^{\text{tar}}}^i(\mathbf{v}_k^i) = \begin{bmatrix} \frac{\partial^2 \mathcal{L}_k^i}{\partial \boldsymbol{\xi}_k^2} & \frac{\partial^2 \mathcal{L}_k^i}{\partial \lambda_k \partial \boldsymbol{\xi}_k} \\ \frac{\partial^2 \mathcal{L}_k^i}{\partial \boldsymbol{\xi}_k \partial \lambda_k} & \mathbf{0} \end{bmatrix} = \begin{bmatrix} \left(\mathbf{H}_k^{i-1} \right)_{11} & \left(\mathbf{H}_k^{i-1} \right)_{12} \\ \left(\mathbf{H}_k^{i-1} \right)_{21} & \left(\mathbf{H}_k^{i-1} \right)_{22} \end{bmatrix}^{-1}.$$

Coupling Terms

The first and second optimization step are coupled by the sensitivities $\partial \tilde{\boldsymbol{\xi}} / \partial \boldsymbol{\xi}^{\text{tar}}$ and $\partial^2 \tilde{\boldsymbol{\xi}} / \partial \boldsymbol{\xi}^{\text{tar}2}$. Stationarity of $\tilde{\mathbf{g}} = \mathbf{g}(\mathbf{t}^C, \mathbf{u}^C, \boldsymbol{\xi}^{\text{tar}}, \tilde{\mathbf{v}})$ requires that

$$\tilde{\mathbf{g}}_k(\mathbf{t}_k^C, \mathbf{u}_k^C, \boldsymbol{\xi}_k^{\text{tar}} + \Delta \boldsymbol{\xi}_k^{\text{tar}}, \tilde{\mathbf{v}}_k + \Delta \mathbf{v}_k) = \mathbf{0}. \quad (8.36)$$

Linearization of the stationarity condition at the optimum leads to

$$\tilde{\mathbf{g}}_k(\mathbf{t}_k^C, \mathbf{u}_k^C, \boldsymbol{\xi}_k^{\text{tar}}, \tilde{\mathbf{v}}_k) + \frac{\partial \tilde{\mathbf{g}}_k}{\partial \boldsymbol{\xi}_k^{\text{tar}}} \Delta \boldsymbol{\xi}_k^{\text{tar}} + \frac{\partial \tilde{\mathbf{g}}_k}{\partial \mathbf{v}_k} \Delta \mathbf{v}_k = \mathbf{0} \quad (8.37)$$

so that

$$\frac{\partial \tilde{\mathbf{v}}_k}{\partial \boldsymbol{\xi}_k^{\text{tar}}} = - \left(\frac{\partial \tilde{\mathbf{g}}_k}{\partial \mathbf{v}_k} \right)^{-1} \frac{\partial \tilde{\mathbf{g}}_k}{\partial \boldsymbol{\xi}_k^{\text{tar}}}. \quad (8.38)$$

Hence the sensitivities of $\tilde{\boldsymbol{\xi}}$ with respect to $\boldsymbol{\xi}^{\text{tar}}$ are

$$\frac{\partial \tilde{\boldsymbol{\xi}}_k}{\partial \boldsymbol{\xi}_k^{\text{tar}}} = \left(\tilde{\mathbf{H}}_k^{-1} \right)_{12} \quad (8.39)$$

and

$$\frac{\partial^2 \tilde{\boldsymbol{\xi}}_k}{\partial \boldsymbol{\xi}_k^{\text{tar}2}} = - \left(\tilde{\mathbf{H}}_k^{-1} \right)_{11} \begin{bmatrix} \frac{\partial^3 \tilde{\mathcal{L}}_k}{\partial \boldsymbol{\xi}_k^2 \partial \xi_{k,1}} \left(\tilde{\mathbf{H}}_k^{-1} \right)_{12} \\ \vdots \\ \frac{\partial^3 \tilde{\mathcal{L}}_k}{\partial \boldsymbol{\xi}_k^2 \partial \xi_{k,ns}} \left(\tilde{\mathbf{H}}_k^{-1} \right)_{12} \end{bmatrix}^\top \frac{\partial \tilde{\boldsymbol{\xi}}_k}{\partial \boldsymbol{\xi}_k^{\text{tar}}}. \quad (8.40)$$

Second Step

The optimal value for ξ^{tar} is determined in a second step by computing

$$\tilde{\xi}_k^{\text{tar}}(\mathbf{t}_k^{\text{C}}, \mathbf{u}_k^{\text{C}}) = \underset{\xi_k^{\text{tar}}}{\operatorname{argmin}} \mathcal{G}_k(\mathbf{t}_k^{\text{C}}, \mathbf{u}_k^{\text{C}}, \tilde{\xi}_k(\mathbf{t}_k^{\text{C}}, \mathbf{u}_k^{\text{C}}, \xi_k^{\text{tar}})) \quad (8.41)$$

where the difference between target and fillet curvatures is taken into account by the objective

$$\mathcal{G}_k(\mathbf{u}_k^{\text{C}}, \mathbf{t}_k^{\text{C}}, \tilde{\xi}_k(\mathbf{u}_k^{\text{C}}, \mathbf{t}_k^{\text{C}}, \xi_k^{\text{tar}})) = \sum_{i=1}^{n_s} (\kappa_{k,i} - \kappa_k^{\text{tar}})^2. \quad (8.42)$$

Similar to the first step, a Newton based approach is used to compute the variable $\tilde{\xi}^{\text{tar}}$ that satisfies the stationarity condition. The variable of the $(i+1)$ -th iteration is

$$\xi_k^{\text{tar}, i+1} = \xi_k^{\text{tar}, i} - \Delta \xi_k^{\text{tar}, i} \quad (8.43)$$

where

$$\Delta \xi_k^{\text{tar}, i} = \begin{cases} \left(\frac{\partial \mathcal{G}_k^i}{\partial \xi_k^{\text{tar}}} \right)^{-1} \mathcal{G}_k^i & \text{for } \frac{\partial^2 \mathcal{G}_k^i}{\partial \xi_k^{\text{tar}^2} } \leq 0 \\ \left(\frac{\partial^2 \mathcal{G}_k^i}{\partial \xi_k^{\text{tar}^2} } \right)^{-1} \frac{\partial \mathcal{G}_k^i}{\partial \xi_k^{\text{tar}}} & \text{for } \frac{\partial^2 \mathcal{G}_k^i}{\partial \xi_k^{\text{tar}^2} } > 0. \end{cases} \quad (8.44)$$

The corresponding derivatives are

$$\frac{\partial \mathcal{G}_k^i}{\partial \xi_k^{\text{tar}}} = \frac{\partial \mathcal{G}_k^i}{\partial \tilde{\xi}_k} \frac{\partial \tilde{\xi}_k^i}{\partial \xi_k^{\text{tar}}} \quad (8.45)$$

and

$$\frac{\partial^2 \mathcal{G}_k^i}{\partial \xi_k^{\text{tar}^2}} = \frac{\partial \tilde{\xi}_k^i}{\partial \xi_k^{\text{tar}}}{}^{\top} \frac{\partial^2 \mathcal{G}_k^i}{\partial \tilde{\xi}_k^2} \frac{\partial \tilde{\xi}_k^i}{\partial \xi_k^{\text{tar}}} + \frac{\partial \mathcal{G}_k^i}{\partial \tilde{\xi}_k} \frac{\partial^2 \tilde{\xi}_k^i}{\partial \xi_k^{\text{tar}^2}}. \quad (8.46)$$

It can be seen that both derivatives are based on the previously derived coupling terms.

Sensitivities

The optimization of compliant pressure actuated cellular structures requires the sensitivities of $\tilde{\xi}$ with respect to state variables \mathbf{u}^{C} and \mathbf{t}^{C} . They can be expressed as

$$\frac{d\tilde{\xi}_k}{d\mathbf{u}_k^{\text{C}}} = \frac{\partial \tilde{\xi}_k}{\partial \xi_k^{\text{tar}}} \frac{\partial \xi_k^{\text{tar}}}{\partial \mathbf{u}_k^{\text{C}}} + \frac{\partial \tilde{\xi}_k}{\partial \mathbf{u}_k^{\text{C}}} \quad (8.47)$$

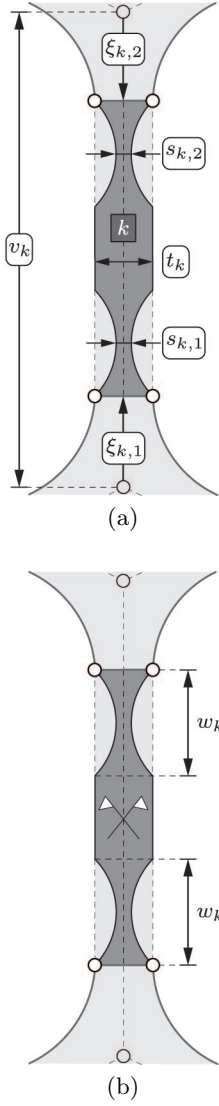


Figure 8.7: (a) Local state variables \mathbf{u}^S , v^S , \mathbf{s}^S and t^S of the k -th cell side. (b) Internal lengths \mathbf{w} .

and

$$\frac{d\tilde{\xi}_k}{d\mathbf{t}_k^C} = \frac{\partial \tilde{\xi}_k}{\partial \xi_k^{\text{tar}}} \frac{\partial \xi_k^{\text{tar}}}{\partial \mathbf{t}_k^C} + \frac{\partial \tilde{\xi}_k}{\partial \mathbf{t}_k^C} \quad (8.48)$$

where

$$\frac{\partial \xi_k^{\text{tar}}}{\partial \mathbf{u}_k^C} = - \left(\frac{\partial^2 \tilde{\mathcal{G}}_k}{\partial \xi_k^{\text{tar}2}} \right)^{-1} \frac{\partial^2 \tilde{\mathcal{G}}_k}{\partial \xi_k^{\text{tar}} \partial \mathbf{u}_k^C} \quad (8.49)$$

and

$$\frac{\partial \xi_k^{\text{tar}}}{\partial \mathbf{t}_k^C} = - \left(\frac{\partial^2 \tilde{\mathcal{G}}_k}{\partial \xi_k^{\text{tar}2}} \right)^{-1} \frac{\partial^2 \tilde{\mathcal{G}}_k}{\partial \xi_k^{\text{tar}} \partial \mathbf{t}_k^C}. \quad (8.50)$$

The rounding out of cell corners with circular arcs is surprisingly complex as two coupled objectives need to be minimized. Nonetheless, the computation of optimal cell corner geometries is robust and usually requires only a few iterations.

8.3 Side Geometries

8.3.1 Global State Variables

The bending deformations of rectangular cell sides are localized by circular cutouts that are symmetrically arranged next to the cell corners as illustrated in Figure 8.7. The description of the cell side geometries thus requires, besides the global state variables \mathbf{u} , \mathbf{v} , \mathbf{t} and κ^{tar} additional global state variables for the central hinge thicknesses \mathbf{s} . The ratio μ between the width and central hinge thickness is assumed to be constant and identical for all hinges. The ordering of the hinge thicknesses is similar to that of the cell side lengths \mathbf{v} so that

$$\mathbf{s} = [\mathbf{s}_{b,1}^\top \quad \mathbf{s}_{c,1}^\top \quad \dots \quad \mathbf{s}_{b,nR}^\top \quad \mathbf{s}_{c,nR}^\top \quad \mathbf{s}_a^\top]^\top \in \mathbb{R}^{2nv} \quad (8.51)$$

where, for example $\mathbf{s}_{b,i} = [s_{b,i,1} \quad s_{b,i,2} \quad \dots \quad s_{b,i,2(nP+2-i)}]^\top$. It can be seen that the two hinge thicknesses of a cell side are grouped together.

8.3.2 Local State Variables

The hinge geometries of the k -th cell side are fully defined by the cell side thickness

$$t_k^S(\mathbf{t}) = t_k \quad (8.52)$$

and the central hinge thicknesses

$$\mathbf{s}_k^S(\mathbf{s}) = \begin{bmatrix} s_{k,1} & s_{k,2} \end{bmatrix}^\top. \quad (8.53)$$

The localization of these hinges requires additional variables that include the effective cell side length

$$v_k^S(\mathbf{v}) = v_k \quad (8.54)$$

and the cell corner dimensions

$$\mathbf{u}_k^S(\mathbf{t}^C, \kappa^{\text{tar}}, \mathbf{u}^C) = \begin{bmatrix} \xi_{k,1} & \xi_{k,2} \end{bmatrix}^\top \quad (8.55)$$

that depend on the local state variables of the neighbouring cell corners. It can be seen that the superscript “S” is used to denote the local state variables of a cell side.

8.3.3 Dependent Variables

The widths \mathbf{w}^S of compliant hinges are assumed to be proportional to the central hinge thicknesses \mathbf{s} so that

$$\mathbf{w}_k^S = \mu \mathbf{s}_k^S. \quad (8.56)$$

The use of a linear relationship is advantageous since it leads to relatively simple expressions. Nonetheless, different hinge geometries that are not based on circular arcs could be used instead. Furthermore, cell side geometries with a nonconstant thickness can be used to minimize the weight of a cellular structure. However, this is not done in this thesis as it unnecessarily complicates the presented approach.

8.4 Summary

8.4.1 State Variables

In summary it can be said that the centerlines of compliant pressure actuated cellular structures with straight cell sides can be fully described by the global state variables \mathbf{u} and \mathbf{v} . The additional global state variables \mathbf{s} , \mathbf{t} , κ^{tar} and μ are required if thickness variations of cell corners and sides need to be considered. Hence, the design variables \mathbf{e}^G of the geometric model are

$$\mathbf{e}^G = \begin{bmatrix} \mathbf{u}^\top & \mathbf{v}^\top & \mathbf{t}^\top & \mathbf{s}^\top & \kappa^{\text{tar}} & \mu \end{bmatrix}^\top. \quad (8.57)$$

These global state variables can be sequentially transformed into the local state variables of pentagonal and triangular cells as well as cell corners and cell sides. Their dependencies are

geometric primitive	local state variables
pentagonal cell	$\mathbf{u}^P(\mathbf{u}, \mathbf{v}), \mathbf{v}^P(\mathbf{v})$
triangular cell	$\mathbf{u}^T(\mathbf{u}^P), \mathbf{v}^T(\mathbf{v}^P)$
cell corner	$\mathbf{u}^C(\mathbf{u}^P, \mathbf{v}^P), \mathbf{t}^C(\mathbf{t}), \kappa^{\text{tar}}$
cell side	$\mathbf{u}^S(\kappa^{\text{tar}}, \mathbf{u}^C, \mathbf{t}^C), v^S(\mathbf{v}), \mathbf{s}^S(\mathbf{s}), t^S(\mathbf{t}^C), \mu.$

8.4.2 Dependent Variables

Various geometric properties that are required for the simulation and optimization of compliant pressure actuated cellular structures can be derived from the local state variables of the geometric primitives. They include

geometric primitive	local state variables
pentagonal cell	$\gamma(\mathbf{u}^P, \mathbf{v}^P), A^P(\mathbf{u}^P, \mathbf{v}^P)$
triangular cell	$\psi(\mathbf{u}^T, \mathbf{v}^T), A^T(\mathbf{u}^T, \mathbf{v}^T)$
cell corner	$\xi(\kappa^{\text{tar}}, \mathbf{u}^C, \mathbf{t}^C)$
cell side	$\mathbf{w}(\mu, \mathbf{s}^S).$

8.4.3 Special Cases

The geometric model for pressure actuated cellular structures can be considerably simplified if frictionless hinges are used instead of compliant hinges. The corresponding simplifications depend greatly on the hinge locations as illustrated in Figure 8.8. The use of centric hinges reduces the design variables \mathbf{e}^G of the geometric model to

$$\mathbf{e}^G = [\mathbf{v}^\top \quad \mathbf{t}^\top]^\top \quad (8.58)$$

since frictionless hinges enable arbitrary rotations and cell corners do not exist. The local state variables of a cell side thus reduce to $v^S(\mathbf{v})$ and $t^S(\mathbf{t})$.

Compared to structures with centric hinges, the use of eccentric hinges considerably complicates the geometric model so that

$$\mathbf{e}^G = [\mathbf{u}^\top \quad \mathbf{v}^\top \quad \mathbf{t}^\top \quad \kappa^{\text{tar}}]^\top. \quad (8.59)$$

The additional global state variables \mathbf{u} and κ^{tar} are required to describe the cell corner geometries so that their local state variables are identical to those of compliant structures. In contrast, the local state variables of cell sides reduce to $\mathbf{u}^S(\kappa^{\text{tar}}, \mathbf{u}^C, \mathbf{t}^C)$, $v^S(\mathbf{v})$ and $t^S(\mathbf{t}^C)$ since detailed hinge geometries are not considered.

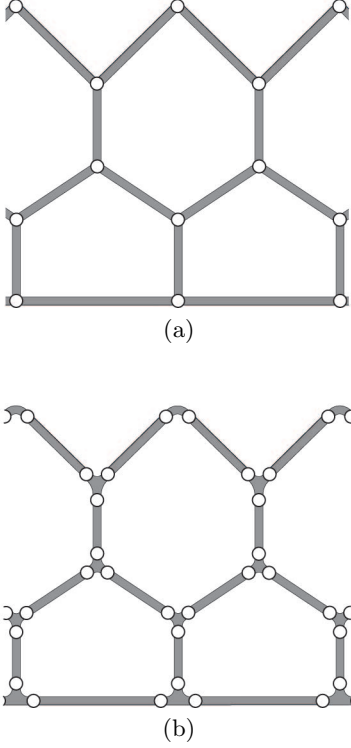


Figure 8.8: Pressure actuated cellular structure with (a) centric and (b) eccentric hinges.

Chapter 9

Mechanical Model

The simulation of compliant pressure actuated cellular structures with an arbitrary number of cell rows and geometries is relatively simple and can be done with various numerical tools such as the boundary element [91], finite difference [270] or finite element [326] method. Particularly the latter is commonly used in engineering as it can be applied to a wide range of linear and nonlinear problems with complex geometries and loading conditions [254]. Depending on the geometry of the structure and the desired accuracy, it is possible to use different kind of finite elements that range from one-dimensional bars and beams to two-dimensional membrane elements. A numerical simulation of pressure actuated cellular structures is thus only limited by the available computing power. If structures with an exceedingly large number of cells need to be simulated it is possible to use multiscale methods [62, 175] that trade off accuracy against speed. However, these kind of structures are usually not of practical interest as their increased manufacturing complexity clearly outweighs any additional benefits that come with a large number of cells.

Unfortunately, the optimization of cell geometries for given target shapes, cell pressures and material properties is much harder. This is due to the fact that the geometric and mechanical models are highly coupled. Variation of a single cell side thickness changes the optimal geometries of the neighbouring cell corners and sides. This affects the corresponding hinge eccentricities, cell side stiffness and thus all equilibrium configurations of the mechanical model. The latter leads to different maximum hinge and cell side stresses throughout the structure and therefore, in return, alters the optimal geometry of all cell corners and sides. A detailed mechanical model for the simulation and optimization of compliant pressure actuated cellular structures that can be tightly coupled to the geometric model is subsequently presented.

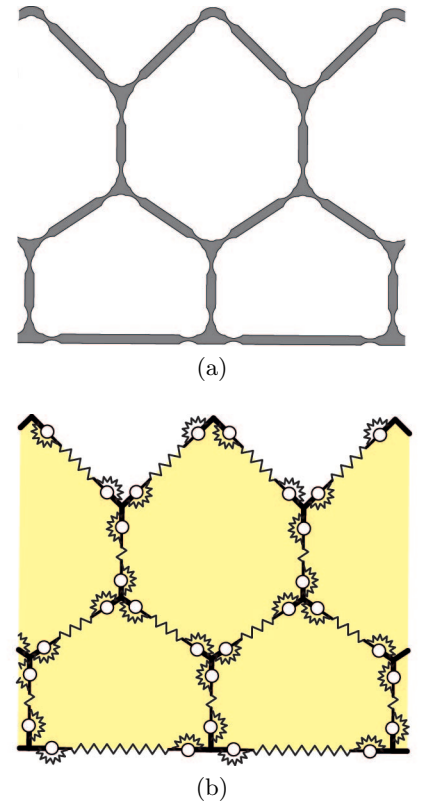


Figure 9.1: (a) Geometric and (b) mechanical model of a compliant pressure actuated cellular structure. The mechanical model is based on rigid cell corners, frictionless hinges and axial, rotational springs.

9.1 Cell Side Deformations

9.1.1 Global State Variables

The considered geometric and mechanical models of compliant pressure actuated cellular structures are shown in Figure 9.1. It can be seen that the compliant hinges are modeled by rotational springs and frictionless hinges whereas the central cell sides are modeled by axial springs. The hinge eccentricities \mathbf{d} can be derived from the global state variables of the geometric model where it is assumed that

$$\mathbf{d}(\mathbf{e}^G) = \boldsymbol{\xi}(\mathbf{e}^G) + \frac{1}{2}\mathbf{w}(\mathbf{e}^G). \quad (9.1)$$

This assumption is justified as compliant hinges possess two reflection symmetry planes that concentrate their bending deformations at their centers. Furthermore, cell corners are relatively stiff due to their bulky geometry and compliant hinges relatively small so that their axial elongations can be neglected. The chosen ordering of the hinge eccentricities is illustrated in Figure 9.2. It can be seen that is similar to the ordering of the central hinge thicknesses \mathbf{s} . Hence, the geometry of an undeformed mechanical model is fully described by

$$\mathbf{e}^M(\mathbf{e}^G) = \begin{bmatrix} \mathbf{u}_0^\top & \mathbf{v}_0^\top & \mathbf{d}(\mathbf{e}^G)^\top \end{bmatrix}^\top \quad (9.2)$$

where the subscript “0” is used to highlight the variables of the reference, undeformed configuration. However, these variables are insufficient to describe the deformed cell sides so that they need to be augmented by the additional global state variables $\boldsymbol{\kappa}$ where

$$\boldsymbol{\kappa} = \begin{bmatrix} \boldsymbol{\kappa}_1^\top & \dots & \boldsymbol{\kappa}_{n_{R+1}}^\top \end{bmatrix}^\top \in \mathbb{R}^{n_\kappa} \quad (9.3)$$

and the total number of cell corners n_κ is

$$n_\kappa = 3n_P + 2n_T + n_R + 1. \quad (9.4)$$

The state variables $\boldsymbol{\kappa}$ are defined with respect to the cell sides \mathbf{b} . As a consequence, the upper cell corners of a pressure actuated cellular structure need to be described with respect to imaginary cell sides that possess only one hinge so that

$$\boldsymbol{\kappa}_i = \begin{cases} \begin{bmatrix} \kappa_{i,1,1} & \kappa_{i,1,2} & \dots & \kappa_{i,n_P-i+2,1} & \kappa_{i,n_P-i+2,2} \end{bmatrix}^\top & i \leq n_R \\ \begin{bmatrix} \kappa_{n_R+1,1,1} & \dots & \kappa_{n_R+1,n_P-n_R+1,1} \end{bmatrix}^\top & i > n_R. \end{cases} \quad (9.5)$$

Hence, the deformed geometry of a mechanical model is fully described by the global state variables \mathbf{e}^M and

$$\mathbf{h}^M = \begin{bmatrix} \mathbf{u}^\top & \mathbf{v}^\top & \boldsymbol{\kappa}^\top \end{bmatrix}^\top. \quad (9.6)$$

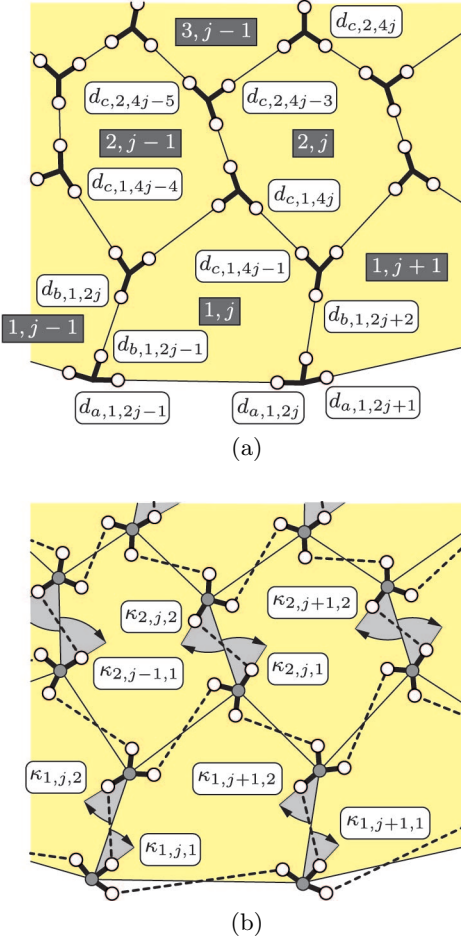


Figure 9.2: Additional global state variables that are required to describe the deformed configuration of the mechanical model. (a) Hinge eccentricities \mathbf{d} and (b) cell corner rotations $\boldsymbol{\kappa}$.

9.1.2 Local State Variables

The deformed geometry of the k -th cell side is fully defined by the hinge eccentricities

$$\mathbf{d}_k^S(\mathbf{e}^M) = [d_{k,1} \quad d_{k,2}]^\top \quad (9.7)$$

the effective cell side length

$$v_k^S(\mathbf{h}^M) = v_k \quad (9.8)$$

and the cell corner rotations

$$\mathbf{u}_k^S(\mathbf{e}^M, \mathbf{h}^M) = [\kappa_{k,1} \quad \kappa_{k,2}]^\top \quad (9.9)$$

as shown in Figure 9.3. The cell corner rotations are special as their values depend on the cell side location within a cell. Hence, only the rotations for the cell sides \mathbf{b} can be directly expressed in terms of the global state variables $\boldsymbol{\kappa}$. The corresponding rotations for the other cell sides are subsequently derived with the help of the j -th pentagonal cell in the i -th cell row as illustrated in Figure 9.4. The local state variables for the cell corner rotations

$$\boldsymbol{\kappa}_{i,j}^P(\boldsymbol{\kappa}) = [\kappa_{i,2j-1} \quad \kappa_{i,2j} \quad \kappa_{i,2j+1} \quad \kappa_{i,2j+2} \quad \kappa_{i+1,2j-1}]^\top \quad (9.10)$$

of the pentagonal cell are linked to the cell sides \mathbf{b} so that they can be directly obtained from the global state variables $\boldsymbol{\kappa}$. As a consequence, it is necessary to augment the local state variables \mathbf{u}^P and \mathbf{v}^P with the variable

$$\beta_{i,j}^P(\mathbf{u}) = \beta_{i,j} \quad (9.11)$$

that describes the inclination of the cell side $b_{i+1,j}$ and thus provides a basis for the upper cell corner rotation. The internal angles $\boldsymbol{\kappa}_c$ between the rigid cell corners and, for example, the fictitious, straight cell side $c_{i,2j}$ of a pentagonal cell thus become

$$\begin{bmatrix} \kappa_{c,i,4j-1} \\ \kappa_{c,i,4j} \end{bmatrix} = \begin{bmatrix} \kappa_{i,2j+2} - \Delta\gamma_{i,2j} \\ \kappa_{i+1,2j-1} - \Delta\gamma_{i,2j} - \Delta\alpha_{i,2j} + \Delta\beta_{i,j} \end{bmatrix} \quad (9.12)$$

where, for example $\Delta\alpha = \alpha - \alpha_0$ is the difference of the local pentagonal state variable α between the current (deformed) and the reference (undeformed) configuration. It is assumed that $\Delta\beta = 0$ for pentagonal cells that are located in the top, boundary cell row. This is due to the fact that global state variables $\boldsymbol{\beta}$ are not required in the top row as there are no further pentagonal cells. Instead, they serve as the basis for the variables $\boldsymbol{\kappa}$ and thus can have any value, including zero. The corresponding angles for the pentagonal base sides \mathbf{a} that exist for $i = 1$ are

$$\begin{bmatrix} \kappa_{a,i,2j-1} \\ \kappa_{a,i,2j} \end{bmatrix} = \begin{bmatrix} \kappa_{i,2j-1} + \Delta\alpha_{i,2j-1} \\ \kappa_{i,2j+1} + \Delta\alpha_{i,2j} \end{bmatrix}. \quad (9.13)$$

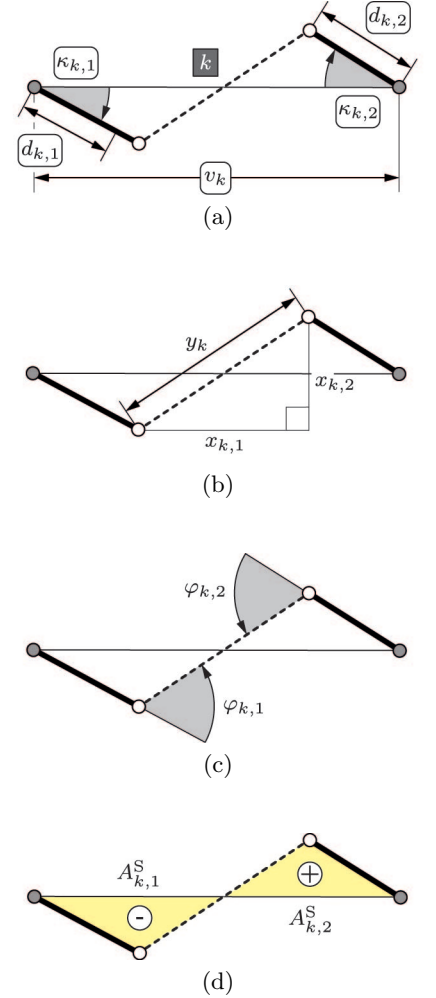


Figure 9.3: Variables of the k -th cell side. (a) Local state variables \mathbf{d}^S , v^S and $\boldsymbol{\kappa}^S$. (b) Internal lengths \mathbf{x} , y and (c) internal bending angles $\boldsymbol{\varphi}$. (d) Effective cell side area A^S that varies the cross sectional area of neighbouring cells. The shown signs highlight the positive and negative terms.

9.1.3 Dependent Variables

The internal lengths \mathbf{x} of a deformed cell side with eccentric hinges are

$$\begin{bmatrix} x_{k,1} \\ x_{k,2} \end{bmatrix} = \begin{bmatrix} v_k - \cos(\kappa_{k,1}) d_{k,1} - \cos(\kappa_{k,2}) d_{k,2} \\ \sin(\kappa_{k,1}) d_{k,1} + \sin(\kappa_{k,2}) d_{k,2} \end{bmatrix} \quad (9.14)$$

so that the hinge rotations or bending angles φ result in

$$\varphi_k = \kappa_k + \arcsin\left(\frac{x_{k,2}}{y_k}\right) \begin{bmatrix} 1 & 1 \end{bmatrix}^\top \quad (9.15)$$

where the central cell side length is

$$y_k = \sqrt{x_{k,1}^2 + x_{k,2}^2}. \quad (9.16)$$

The effective cell side area A^S that varies the cross sectional area of a neighbouring cell thus becomes

$$A_k^S = \frac{1}{2} (\sin(\kappa_{k,2}) \cos(\kappa_{k,2}) d_{k,2}^2 - \sin(\kappa_{k,1}) \cos(\kappa_{k,1}) d_{k,1}^2 + (\sin(\kappa_{k,2}) d_{k,2} - \sin(\kappa_{k,1}) d_{k,1}) x_{k,1}). \quad (9.17)$$

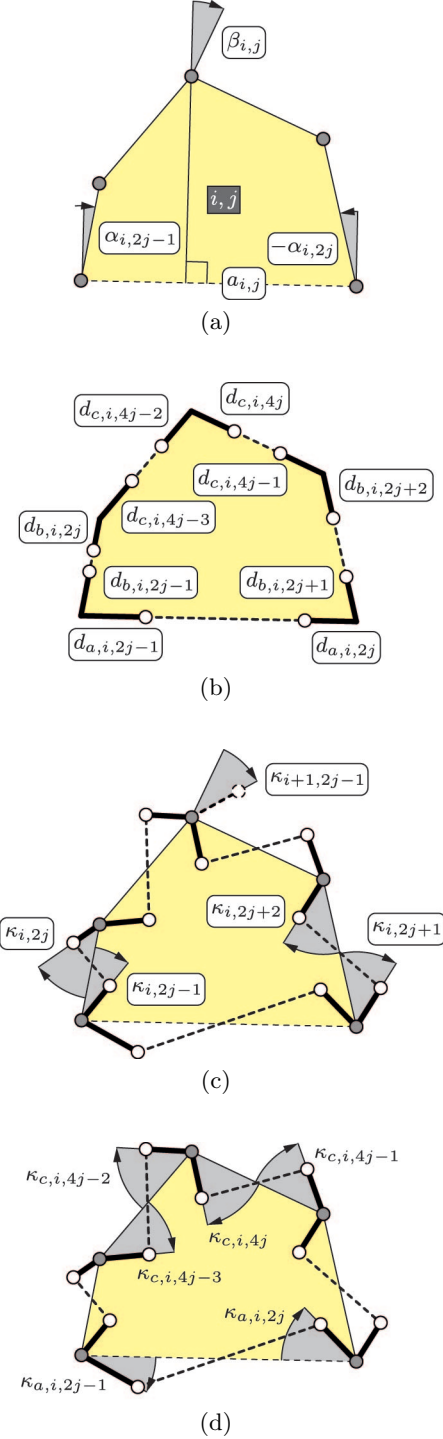
9.2 Mechanical Properties

9.2.1 Global State Variables

Additional global state variables for the stiffness of the axial \mathbf{m} and rotational \mathbf{n} springs are required to describe the strain energy of the mechanical model. These variables that are illustrated in Figure 9.5 can be fully derived from the geometric model and thus are invariant to cell side deformations. The equivalent axial spring stiffness m_k of the k -th rectangular cell side is

$$m_k(\mathbf{e}^G) = \frac{E^{\text{eff}} t_k^S}{v_k^S - \sum_{i=1}^2 (\xi_{k,i}(\mathbf{e}^G) + w_{k,i}(\mathbf{e}^G))} \quad (9.18)$$

Figure 9.4: Variables of the j -th pentagonal cell in the i -th cell row due to hinge eccentricities. (a) The local state variables \mathbf{u}^P are augmented by the global state variable β^P that describes the inclination of the cell side $b_{i+1,j}$ and thus serves as a reference for the upper cell corner rotation. Further local state variables include the (b) hinge eccentricities \mathbf{d}^P and the (c) cell corner rotations κ^P . (d) Internal variables κ_a and κ_c describe the angles between the rigid cell corners and the fictitious, straight cell sides a and c .



where the effective Young's modulus E^{eff} for the plane strain condition of a material with a Young's modulus E and a Poisson's ratio ν is

$$E^{\text{eff}} = \frac{E}{1 - \nu^2}. \quad (9.19)$$

The stiffness is computed with respect to the cell side length between the compliant hinges as the axial strains of both, hinges and cell corners are neglected. The ordering of the axial spring stiffness is similar to that of the effective cell side lengths \mathbf{v} .

The equivalent rotational spring stiffness \mathbf{n} of compliant hinges that are generated by circular cutouts can be analytically derived on the basis of the Euler-Bernoulli beam theory. However, the corresponding solution is rather bulky. It is therefore advantageous to derive the rotational spring stiffness from a rectangular beam with a unit length, a thickness s and a correction factor χ . The i -th spring stiffness of the k -th cell side thus becomes

$$n_{k,i}(\mathbf{e}^G) = \frac{E s_{k,i}^{\text{eff}S^2}}{12} \chi_{k,i}(\mathbf{e}^G). \quad (9.20)$$

Values for the correction factor are computed with the help of a finite element model as shown in Figure 9.6. The simulation results are then interpolated with an arctangent function so that

$$\chi_{k,i}(\mathbf{e}^G) \approx \frac{1}{\mu} + \frac{1}{4} \arctan \left(\frac{80 - 6\mu}{100} \left(\frac{t_k^S}{s_{k,i}^S} - 1 \right) \right). \quad (9.21)$$

The chosen interpolation function can be found in the major terms of the analytical solution so that it is not surprising that the interpolation error is relatively small.

The maximum hinge and cell side stresses depend on the central hinge thicknesses \mathbf{s} and the cell side thicknesses \mathbf{t} . Furthermore, the stiffness of the axial and rotational springs can be fully derived from the global state variables \mathbf{e}^G . It is therefore advantageous to augment the previously introduced global state variables \mathbf{e}^M that describe the geometry of the undeformed mechanical model with the stiffness terms \mathbf{m} , \mathbf{n} and thicknesses \mathbf{s} and \mathbf{t} so that

$$\mathbf{e}^M(\mathbf{e}^G) = [\mathbf{u}_0^\top \quad \mathbf{v}_0^\top \quad \mathbf{d}^\top \quad \mathbf{m}^\top \quad \mathbf{n}^\top \quad \mathbf{s}^\top \quad \mathbf{t}^\top]^\top. \quad (9.22)$$

9.2.2 Local State Variables

The additional local state variables of the k -th cell side due to the axial m and rotational \mathbf{n} spring stiffness are

$$m_k^S(\mathbf{e}^M) = m_k \quad (9.23)$$

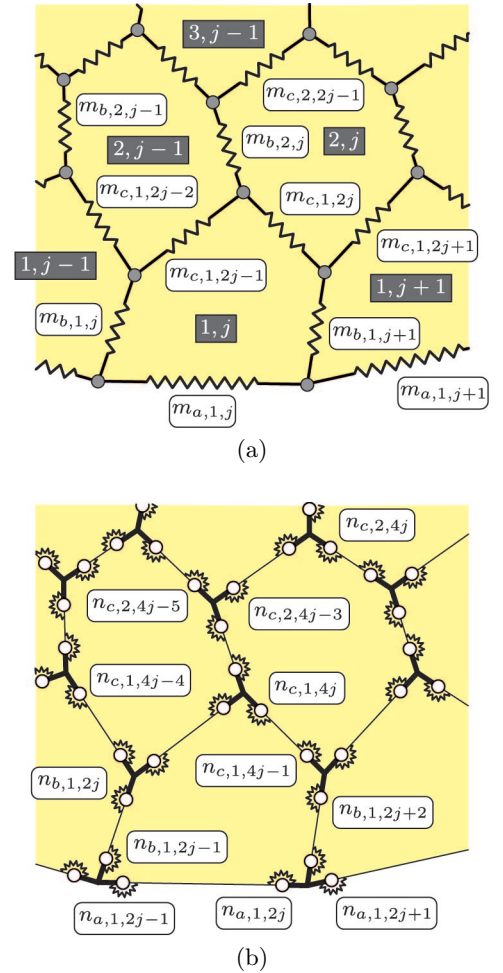


Figure 9.5: Additional global state variables that are required to describe the stiffness of the mechanical model. (a) Axial \mathbf{m} and (b) rotational \mathbf{n} cell side springs.

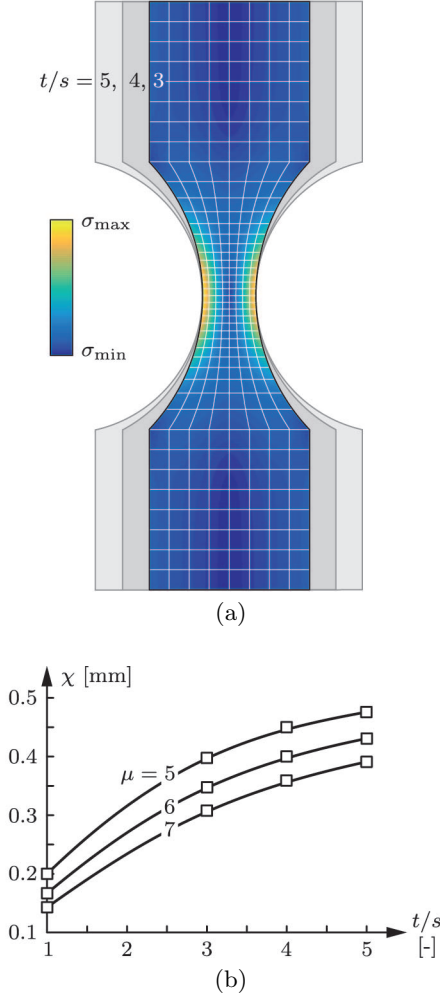


Figure 9.6: (a) Von Mises stresses of a compliant hinge with a thickness ratio $t/s = 3$ and an aspect ratio $\mu = 5$ due to end rotations. (b) Interpolated stiffness parameter χ for different thickness ratios t/s and aspect ratios μ .

and

$$\mathbf{n}_k^S(\mathbf{e}^M) = \begin{bmatrix} n_{k,1} & n_{k,2} \end{bmatrix}^\top. \quad (9.24)$$

Similarly the terms for the cell side t and hinge s thicknesses are

$$t_k^S(\mathbf{e}^M) = t_k \quad (9.25)$$

and

$$\mathbf{s}_k^S(\mathbf{e}^M) = \begin{bmatrix} s_{k,1} & s_{k,2} \end{bmatrix}^\top. \quad (9.26)$$

9.2.3 Dependent Variables

The stress resultants that act on the k -th cell side can be compute from the bending angles φ_k and the cell side elongation Δy_k . The bending moment $M_{k,i}^H$ at the center of the i -th cell side hinge is

$$M_{k,i}^H(\mathbf{e}^M, \mathbf{h}^M) = n_{k,i}^S(\mathbf{e}^M) \varphi_{k,i}(\mathbf{e}^M, \mathbf{h}^M) \quad (9.27)$$

and the axial cell side force F_k can be written as

$$F_k(\mathbf{e}^M, \mathbf{h}^M) = m_k^S(\mathbf{e}^M) (y_k(\mathbf{e}^M, \mathbf{h}^M) - y_{0,k}(\mathbf{e}^M)). \quad (9.28)$$

Unlike the normal force, the corresponding bending moment varies along the central cell side. Its maximum value M_k^S can be expressed with respect to the stress resultants \mathbf{M}_k^H and the differential pressure Δp_k so that

$$M_k^S = \begin{cases} \frac{\Delta p_k}{2} \zeta_k^2 - M_{k,2}^H & \text{if } \Delta p_k \neq 0 \text{ and } 0 < \zeta_k < y_k \\ \max(|M_{k,1}^H|, |M_{k,2}^H|) & \text{otherwise} \end{cases} \quad (9.29)$$

where the location ζ of the maximum bending moment is

$$\zeta_k = \frac{y_k}{2} + \frac{M_{k,1}^H + M_{k,2}^H}{\Delta p_k y_k}. \quad (9.30)$$

Hence, the maximum hinge σ^H and cell side σ^S stresses are

$$\sigma_{k,i}^H = \frac{\rho}{s_{k,i}^S} \left(\frac{6}{s_{k,i}^S} |M_{k,i}^H| + |F_k| \right) \quad (9.31)$$

and

$$\sigma_k^S = \frac{\rho}{t_k^S} \left(\frac{6}{t_k^S} |M_k^S| + |F_k| \right) \quad (9.32)$$

where the stress reduction factor ρ for the von Mises yield criterion is

$$\rho = \sqrt{1 - \nu + \nu^2}. \quad (9.33)$$

9.3 Summary

9.3.1 State Variables

In summary it can be said that the geometry of an undeformed mechanical model can be fully described by the global state variables \mathbf{u}_0 , \mathbf{v}_0 and \mathbf{d} . The stiffness of the mechanical model is described by the axial \mathbf{m} and rotational \mathbf{n} springs. Furthermore, the evaluation of maximum stresses requires hinge \mathbf{s} and cell side \mathbf{t} thicknesses. These global state variables are combined into a single vector

$$\mathbf{e}^M(\mathbf{e}^G) = [\mathbf{u}_0^\top \quad \mathbf{v}_0^\top \quad \mathbf{d}^\top \quad \mathbf{m}^\top \quad \mathbf{n}^\top \quad \mathbf{s}^\top \quad \mathbf{t}^\top]^\top \quad (9.34)$$

as they can be fully derived from the global state variables of the geometric model. Additional global state variables are required to describe the deformed geometry of the mechanical model. These variables include the global state variables \mathbf{u} and \mathbf{v} that define the centerline of the deformed configuration as well as $\boldsymbol{\kappa}$ that defines the cell corner rotations

$$\mathbf{h}^M = [\mathbf{u}^\top \quad \mathbf{v}^\top \quad \boldsymbol{\kappa}^\top]^\top. \quad (9.35)$$

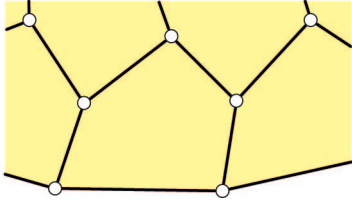
Global state variables can be transformed into the local state variables of pentagonal and triangular cells as well as cell sides. Their dependencies are

geometric primitive	local state variables
pentagonal cell	$\mathbf{u}_0^P(\mathbf{e}^M), \mathbf{v}_0^P(\mathbf{e}^M), \mathbf{u}^P(\mathbf{h}^M), \mathbf{v}^P(\mathbf{h}^M)$
triangular cell	$\mathbf{u}_0^T(\mathbf{e}^M), \mathbf{u}_0^T(\mathbf{e}^M), \mathbf{u}^T(\mathbf{h}^M), \mathbf{v}^T(\mathbf{h}^M)$
cell side	$v_0^S(\mathbf{e}^M), \mathbf{u}^S(\mathbf{e}^M, \mathbf{h}^M), v^S(\mathbf{h}^M), \mathbf{d}^S(\mathbf{e}^M)$ $m^S(\mathbf{e}^M), \mathbf{n}^S(\mathbf{e}^M), \mathbf{s}^S(\mathbf{e}^M), t^S(\mathbf{e}^M).$

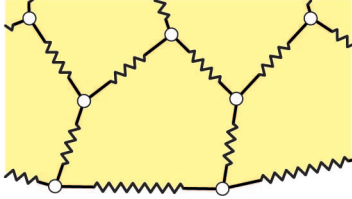
The local state variables of pentagonal and triangular cells are not separately considered in this chapter as they do not differ from the geometric model. Furthermore, cell corners are not a geometric primitive of the mechanical model. Their properties are merged into the local state variables of the cell sides through the hinge eccentricities \mathbf{d} and cell corner rotations \mathbf{u} .

9.3.2 Dependent Variables

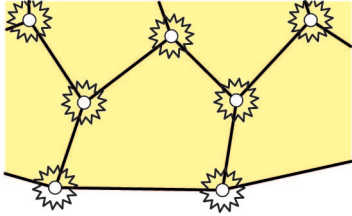
Additional geometric and mechanical properties that are required for the simulation and optimization of pressure actuated cellular structures can be derived from the local state variables of the geometric primitives. They include



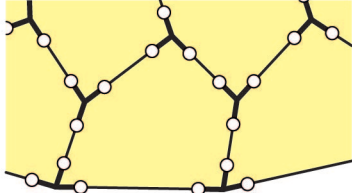
(a)



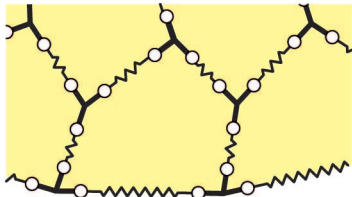
(b)



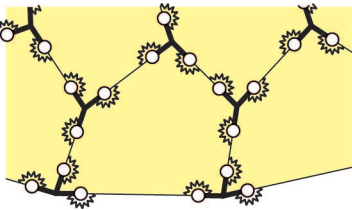
(c)



(d)



(e)



(f)

geometric primitive

pentagonal cell

triangular cell

cell side

local state variables $\gamma_0 (\mathbf{u}_0^P, \mathbf{v}_0^P), \gamma (\mathbf{u}^P, \mathbf{v}^P), A^P (\mathbf{u}^P, \mathbf{v}^P)$ $\psi_0 (\mathbf{u}_0^T, \mathbf{v}_0^T), \psi (\mathbf{u}^T, \mathbf{v}^T), A^T (\mathbf{u}^T, \mathbf{v}^T)$ $y_0 (v_0^S, \mathbf{d}^S), \varphi (\mathbf{d}^S, \mathbf{u}^S, v^S), y (\mathbf{d}^S, \mathbf{u}^S, v^S),$ $A^S (\mathbf{d}^S, \mathbf{u}^S, v^S), \sigma^S (v_0^S, \mathbf{d}^S, m^S, t^S, \mathbf{u}^S, v^S),$ $\sigma^H (\mathbf{d}^S, \mathbf{n}^S, \mathbf{s}^S, \mathbf{u}^S, v^S).$ **9.3.3 Special Cases****Centric Hinges**

The applicability of the geometric and mechanical model is by no means limited to compliant pressure actuated cellular structures. As shown in Figure 9.7, the complexity of the mechanical model can be successively reduced so that it can be applied to a wide range of structures. For example, a pressure actuated cellular structure with centric, frictionless hinges and rigid cell sides is fully described by the state variables

$$\mathbf{e}^M = \begin{bmatrix} \mathbf{v}_0^\top & \mathbf{t}^\top \end{bmatrix}^\top \quad (9.36)$$

$$\mathbf{h}^M = \mathbf{u}.$$

The geometric and mechanical model are thus coupled via the cell side lengths \mathbf{v}_0 and the cell side thicknesses \mathbf{t} . The latter are required for the computation of cell side stresses σ^S . An additional consideration of axial cell side springs leads to

$$\mathbf{e}^M = \begin{bmatrix} \mathbf{v}_0^\top & \mathbf{m}^\top & \mathbf{t}^\top \end{bmatrix}^\top \quad (9.37)$$

$$\mathbf{h}^M = \begin{bmatrix} \mathbf{u}^\top & \mathbf{v}^\top \end{bmatrix}^\top$$

as cell side elongations need to be taken into account. In contrast, an additional consideration of rotational springs leads to

$$\mathbf{e}^M = \begin{bmatrix} \mathbf{u}_0^\top & \mathbf{v}_0^\top & \mathbf{n}^\top & \mathbf{s}^\top & \mathbf{t}^\top \end{bmatrix}^\top \quad (9.38)$$

$$\mathbf{h}^M = \mathbf{u}.$$

Figure 9.7: The coupling between the geometric and mechanical model can be relaxed if hinge eccentricities or rotational springs are neglected or cell sides are assumed to be rigid. (a-c) The presence of centric hinges eliminates the global state variables \mathbf{d} and κ . Additional global state variables (a-b) \mathbf{u}_0, \mathbf{n} and (a),(c) \mathbf{m}, \mathbf{v} can be eliminated if rotational springs are negligible and cell sides are rigid, respectively. (d-f) The presence of hinge eccentricities increases the coupling between both models so that \mathbf{d} and κ can not be eliminated. However, the global state variables (d-e) \mathbf{n} and (d),(f) \mathbf{m}, \mathbf{v} can still be eliminated if rotational springs are negligible and cell sides are rigid, respectively.

The rotational spring stiffness of a mechanical model with eccentric and centric hinges can be transformed into each other if eccentricities are small. The relationship between cell corner and bending angles as illustrated in Figure 9.8 is

$$\begin{bmatrix} \Delta\theta_1 \\ \Delta\theta_2 \\ \Delta\theta_3 \end{bmatrix} = \begin{bmatrix} -1 & 0 & 1 \\ 1 & -1 & 0 \\ 0 & 1 & -1 \end{bmatrix} \begin{bmatrix} \varphi_1 \\ \varphi_2 \\ \varphi_3 \end{bmatrix}. \quad (9.39)$$

Previous matrix is rank deficient and thus not invertible. This can be overcome by additionally satisfying the equilibrium condition

$$\sum_{i=1}^3 n_i \varphi_i = 0 \quad (9.40)$$

so that the relationship between φ and $\Delta\theta$ becomes

$$\begin{bmatrix} \varphi_1 \\ \varphi_2 \\ \varphi_3 \end{bmatrix} = \frac{1}{n_1 + n_2 + n_3} \begin{bmatrix} -n_3 & n_2 & 0 \\ -n_3 & -n_1 - n_3 & 0 \\ n_1 + n_2 & n_2 & 0 \end{bmatrix} \begin{bmatrix} \Delta\theta_1 \\ \Delta\theta_2 \\ \Delta\theta_3 \end{bmatrix}. \quad (9.41)$$

Hence, the relationship between both kind of springs results in

$$\begin{bmatrix} n_1^* \\ n_2^* \\ n_3^* \end{bmatrix} = \frac{1}{n_1 + n_2 + n_3} \begin{bmatrix} n_1 n_3 \\ n_2 n_1 \\ n_3 n_2 \end{bmatrix} \quad (9.42)$$

as they need to preserve the total strain energy. Alternatively, rotational springs around centric hinges can originate from secondary structures such as internally placed elastic sealings. In this case it is not possible to derive the rotational spring stiffness \mathbf{n} from the geometric model. The same holds for the hinge thicknesses \mathbf{s} that are required for the computation of maximum bending stresses.

Eccentric Hinges

The coupling between the geometric and mechanical model increases considerably if hinge eccentricities are taken into account. The global state variables of a mechanical model without axial cell side springs is

$$\begin{aligned} \mathbf{e}^M &= [\mathbf{u}_0^\top \quad \mathbf{v}_0^\top \quad \mathbf{d}^\top \quad \mathbf{t}^\top]^\top \\ \mathbf{h}^M &= [\mathbf{u}^\top \quad \boldsymbol{\kappa}^\top]^\top. \end{aligned} \quad (9.43)$$

An additional consideration of axial cell side springs leads to

$$\begin{aligned} \mathbf{e}^M &= [\mathbf{u}_0^\top \quad \mathbf{v}_0^\top \quad \mathbf{d}^\top \quad \mathbf{m}^\top \quad \mathbf{t}^\top]^\top \\ \mathbf{h}^M &= [\mathbf{u}^\top \quad \mathbf{v}^\top \quad \boldsymbol{\kappa}^\top]^\top \end{aligned} \quad (9.44)$$

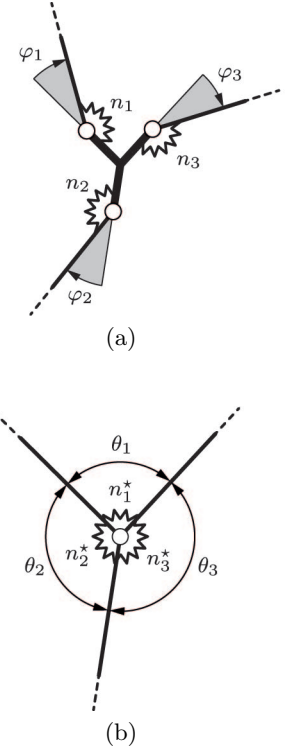


Figure 9.8: Cell corner with (a) eccentric and (b) centric hinges. The latter leads to different cell corner springs.

whereas an additional consideration of rotational springs leads to

$$\begin{aligned}\mathbf{e}^M &= \begin{bmatrix} \mathbf{u}_0^\top & \mathbf{v}_0^\top & \mathbf{d}^\top & \mathbf{n}^\top & \mathbf{s}^\top & \mathbf{t}^\top \end{bmatrix}^\top \\ \mathbf{h}^M &= \begin{bmatrix} \mathbf{u}^\top & \boldsymbol{\kappa}^\top \end{bmatrix}^\top.\end{aligned}\tag{9.45}$$

Chapter 10

Simulation

Despite their relatively simple geometry, analytical solutions for pressure actuated cellular structures can be only found for special cases. For example, a single variable is sufficient to describe the equilibrium configuration of a pentagonal cell row if it is assembled from identical, symmetric cells that consist of rigid cell sides and frictionless, centric hinges. The equilibrium configuration of such a structure is independent of the cell row pressure so that the variable needs to be computed such that it maximizes the cross sectional area. The number of variables that are required to describe the equilibrium configuration of a cellular structure increases dramatically if cells possess different geometries. Furthermore, a coupling between these variables occurs in structures with more than one cell row. Hence it is generally not possible to find analytical solutions for pressure actuated cellular structures even if they are made from rigid cell sides and frictionless, centric hinges. Further increases in complexity originate from elastic cell sides and compliant hinges that lead to complex cell corner geometries. It is subsequently shown how the previously introduced geometric and mechanical model can be efficiently used for the numerical simulation and optimization of compliant pressure actuated cellular structures.

10.1 Potential Energy

Equilibrium configurations of pressure actuated cellular structures maximize the difference between the pressure and strain energy. It is shown in the following how the potential energy of such a structure and its derivatives with respect to the global state variables \mathbf{e}^G of the geometric model can be assembled from the single contributions of their geometric primitives.

10.1.1 Geometric Primitives

The pressure potential Π^P of the j -th pentagonal cell in the i -th cell row is the product of its cross sectional area and the cell row pressure p so that

$$\Pi_{i,j}^P(\mathbf{h}^M) = -p_i A_{i,j}^P(\mathbf{h}^M) \quad (10.1)$$

if fictitious, straight cell sides are assumed. Similarly, the pressure potential of the corresponding triangular cell results in

$$\Pi_{i,j}^T(\mathbf{h}^M) = -p_{i+1} A_{i,j}^T(\mathbf{h}^M). \quad (10.2)$$

The potential energy of the k -th cell side is more complicated as it is composed of a pressure and strain part so that

$$\begin{aligned} \Pi_k^S(\mathbf{e}^M, \mathbf{h}^M) = & -\Delta p_k^S A_k^S(\mathbf{e}^M, \mathbf{h}^M) \\ & + \frac{1}{2} \left(m_k(\mathbf{e}^M) \Delta y_k(\mathbf{e}^M, \mathbf{h}^M)^2 + \sum_{i=1}^2 n_{k,i}(\mathbf{e}^M) \varphi_{k,i}(\mathbf{e}^M, \mathbf{h}^M)^2 \right) \end{aligned} \quad (10.3)$$

where Δp is the differential pressure that acts on the cell side and Δy is the elongation of the central cell side. Recall that $\Delta \varphi = \varphi$ since undeformed cell sides are straight. It can be seen that only the cell side potentials are a function of the reference (undeformed) configuration.

10.1.2 Structure

The potential energy of a cellular structure can be assembled from the contributions of its geometric primitives so that

$$\begin{aligned} \Pi(\mathbf{e}^M, \mathbf{h}^M) = & \sum_{i=1}^{nR} \left(\sum_{j=1}^{nP+1-i} (\Pi_{i,j}^P + \delta_i^1 \Pi_{a,j}^S + \Pi_{c,i,2j-1}^S + \Pi_{c,i,2j}^S) \right. \\ & \left. + \sum_{j=1}^{nP+2-i} \Pi_{b,i,j}^S + (1 - \delta_i^{nR}) \sum_{j=1}^{nP-i} \Pi_{i,j}^T \right) \end{aligned} \quad (10.4)$$

where δ is a Kronecker delta. The gradient $\mathbf{\Pi}^u = \partial \Pi / \partial \mathbf{u} \in \mathbb{R}^{nu}$ of the potential energy with respect to the global state variables \mathbf{u} is computed by summing up the contributions of single cell rows. The energy gradient $\mathbf{\Pi}_i^u$ incorporates only terms from cells and sides in the i -th cell row. It is expressed with respect to the state variables \mathbf{u}_i of a cellular structure

that solely consists of cell rows $i \dots n_R$

$$\begin{aligned}
\Pi_i^u = & \sum_{j=1}^{nP+1-i} \left(\Pi_{i,j}^{P,u} \frac{\partial \mathbf{u}_{i,j}^P}{\partial \mathbf{u}_i} + \Pi_{i,j}^{P,v} \frac{\partial \mathbf{v}_{i,j}^P}{\partial \mathbf{u}_i} \right) \\
& + \sum_{j=1}^{nP-i} \left(\Pi_{i,j}^{T,u} \frac{\partial \mathbf{u}_{i,j}^T}{\partial \mathbf{u}_i} + \Pi_{i,j}^{T,v} \frac{\partial \mathbf{v}_{i,j}^T}{\partial \mathbf{u}_i} \right) (1 - \delta_i^{n_R}) \\
& + \sum_{j=1}^{nP+1-i} \left(\Pi_{a,i,j}^{S,u} \frac{\partial \mathbf{u}_{a,i,j}^S}{\partial \mathbf{u}_i} + \Pi_{a,i,j}^{S,v} \frac{\partial v_{a,i,j}^S}{\partial \mathbf{u}_i} \right) \delta_i^1 \\
& + \sum_{j=1}^{nP+2-i} \left(\Pi_{b,i,j}^{S,u} \frac{\partial \mathbf{u}_{b,i,j}^S}{\partial \mathbf{u}_i} + \Pi_{b,i,j}^{S,v} \frac{\partial v_{b,i,j}^S}{\partial \mathbf{u}_i} \right) \\
& + \sum_{j=1}^{nP+1-i} \sum_{k=0}^1 \left(\Pi_{c,i,2j-k}^{S,u} \frac{\partial \mathbf{u}_{c,i,2j-k}^S}{\partial \mathbf{u}_i} + \Pi_{c,i,2j-k}^{S,v} \frac{\partial v_{c,i,2j-k}^S}{\partial \mathbf{u}_i} \right).
\end{aligned} \tag{10.5}$$

Terms such as $\partial \mathbf{u}_{i,j}^P / \partial \mathbf{u}_i$ map state variables of single cells or sides to the state variables \mathbf{u}_i . Adding and transforming the gradients of single cell rows from top to bottom leads to

$$\Pi^u = \frac{\partial \Pi}{\partial \mathbf{u}} = \left(\left(\Pi_{n_R}^u \frac{\partial \mathbf{u}_{n_R}}{\partial \mathbf{u}_{n_R-1}} + \dots + \Pi_3^u \right) \frac{\partial \mathbf{u}_3}{\partial \mathbf{u}_2} + \Pi_2^u \right) \frac{\partial \mathbf{u}_2}{\partial \mathbf{u}_1} + \Pi_1^u \tag{10.6}$$

where the terms $\partial \mathbf{u}_{i+1} / \partial \mathbf{u}_i$ are assembled from previously introduced transformation matrices. Gradients such as, for example, $\Pi^v = \partial \Pi / \partial \mathbf{v}$ can be computed in a similar manner.

10.2 Stationarity

10.2.1 Equilibrium Configurations

Cell pressures of compliant pressure actuated cellular structures are assumed to be constant throughout each cell row. Combinations of cell row pressures are subsequently referred to as pressure sets. A cellular structure is in equilibrium for a pressure set q if its potential energy is stationary i.e.

$$\mathbf{f}_q(\mathbf{e}^M, \mathbf{h}_q^M) = \mathbf{0} \tag{10.7}$$

where the force vector \mathbf{f}_q is

$$\mathbf{f}_q(\mathbf{e}^M, \mathbf{h}_q^M) = \begin{bmatrix} \Pi_q^u(\mathbf{e}^M, \mathbf{h}_q^M) & \Pi_q^v(\mathbf{e}^M, \mathbf{h}_q^M) & \Pi_q^\kappa(\mathbf{e}^M, \mathbf{h}_q^M) \end{bmatrix}^\top. \tag{10.8}$$

This nonlinear set of equations can be solved for the global state variables \mathbf{h}_q^M by using a Newton based approach. State variables of the $(i + 1)$ -th Newton iteration are

$$\mathbf{h}_q^{M,i+1} = \mathbf{h}_q^{M,i} - \mathbf{K}_q^{-1} \mathbf{f}_q \quad (10.9)$$

where the stiffness matrix \mathbf{K}_q is

$$\mathbf{K}_q = \begin{bmatrix} \Pi_q^{uu} & \Pi_q^{vu} & \Pi_q^{\kappa u} \\ \Pi_q^{uv} & \Pi_q^{vv} & \Pi_q^{\kappa v} \\ \Pi_q^{u\kappa} & \Pi_q^{v\kappa} & \Pi_q^{\kappa\kappa} \end{bmatrix}. \quad (10.10)$$

10.2.2 Sensitivities

The sensitivities of an equilibrium configuration with respect to the global state variables \mathbf{e}^G of the geometric model are subsequently derived. Infinitesimally small variations of the global state variables \mathbf{e}^M and \mathbf{h}_q^M of the mechanical model need to satisfy

$$\mathbf{f}_q(\mathbf{e}^M + \Delta\mathbf{e}^M, \mathbf{h}_q^M + \Delta\mathbf{h}_q^M) = \mathbf{0}. \quad (10.11)$$

Neglecting higher order terms leads to

$$\mathbf{f}_q + \frac{\partial \mathbf{f}_q}{\partial \mathbf{e}^M} \Delta\mathbf{e}^M + \frac{\partial \mathbf{f}_q}{\partial \mathbf{h}_q^M} \Delta\mathbf{h}_q^M = \mathbf{0} \quad (10.12)$$

so that the gradient \mathbf{G}_q becomes

$$\mathbf{G}_q = \frac{\partial \mathbf{h}_q^M}{\partial \mathbf{e}^G} = \frac{\partial \mathbf{h}_q^M}{\partial \mathbf{e}^M} \frac{\partial \mathbf{e}^M}{\partial \mathbf{e}^G} = -\mathbf{K}_q^{-1} \frac{\partial \mathbf{f}_q}{\partial \mathbf{e}^M} \frac{\partial \mathbf{e}^M}{\partial \mathbf{e}^G}. \quad (10.13)$$

Therefore, the sensitivities \mathbf{S}_q^S of the maximum axial cell side stresses σ_q^S can be written as

$$\mathbf{S}_q^S = \frac{\partial \sigma_q^S}{\partial \mathbf{e}^G} = \left(\frac{\partial \sigma_q^S}{\partial \mathbf{e}^M} + \frac{\partial \sigma_q^S}{\partial \mathbf{h}_q^M} \frac{\partial \mathbf{h}_q^M}{\partial \mathbf{e}^M} \right) \frac{\partial \mathbf{e}^M}{\partial \mathbf{e}^G} \quad (10.14)$$

and the sensitivities \mathbf{S}_q^H of the maximum hinge stresses σ_q^H are

$$\mathbf{S}_q^H = \frac{\partial \sigma_q^H}{\partial \mathbf{e}^G} = \left(\frac{\partial \sigma_q^H}{\partial \mathbf{e}^M} + \frac{\partial \sigma_q^H}{\partial \mathbf{h}_q^M} \frac{\partial \mathbf{h}_q^M}{\partial \mathbf{e}^M} \right) \frac{\partial \mathbf{e}^M}{\partial \mathbf{e}^G}. \quad (10.15)$$

However, only the maximum cell side stresses across all pressure sets are required for the optimization. For example, the n_R independent stress values of $\sigma_{q,i}^S$ of the i -th cell side can be condensed into a single value so that σ_i^S is

$$\sigma_i^S = \max [|\sigma_{1,i}^S| \quad \dots \quad |\sigma_{n_R,i}^S|] \quad (10.16)$$

where $i = 1, \dots, n_v$. Based on the previously used maximum stress norm, the corresponding matrices \mathbf{S}^S and \mathbf{S}^H for the sensitivities of the axial cell side and hinge stresses can be assembled in a similar manner. It should be noted that these gradients are discontinuous as the relevant pressure set for the corresponding stress values can vary during the optimization.

10.3 Target Shapes

10.3.1 Residuum

The state variables \mathbf{e}^G of the geometric model with n_R cell rows can be optimized such that the outer pentagonal cell corners are, depending on the pressure set q , located on n_R different C^1 continuous target shapes as illustrated in Figure 10.1. These shapes can be enforced by constraints for the pentagonal base sides angles $\alpha_q \subset \mathbf{u}_q$ that need to satisfy

$$\Delta\alpha_{q,1,j} = \alpha_{q,1,2j} - \alpha_{q,1,2j+1} \quad (10.17)$$

where $i = 1$ and $j = 1, \dots, n_P - 1$. The deviation between the target shape and an equilibrium configuration at the j -th cell corner is given by

$$r_{q,1,j} = \Delta\alpha_{q,1,j} - \alpha_{q,1,2j} + \alpha_{q,1,2j+1} \quad (10.18)$$

and gathered in the residual vector $\mathbf{r}_{q,1}$ for the q -th equilibrium configuration

$$\mathbf{r}_{q,1} = [r_{q,1,1} \dots r_{q,1,n_P-1}]^\top. \quad (10.19)$$

In turn, the residual vectors of all equilibrium configurations are gathered in

$$\mathbf{r} = [\mathbf{r}_1^\top \dots \mathbf{r}_{n_R}^\top]^\top. \quad (10.20)$$

The target angles $\Delta\alpha_{q,1,j}$ are a function of the base lengths $a_{1,j}$ and thus depend on the corresponding axial strains. However, their influence is neglected since these strains are usually small.

10.3.2 Sensitivities

Based on the gradients \mathbf{G}_q , the matrix \mathbf{R} relates the residual target shape vectors \mathbf{r} to the state variables \mathbf{e}^G of the geometric model for all n_R pressure sets so that

$$\mathbf{R} = \frac{\partial \mathbf{r}}{\partial \mathbf{e}^G} = [\mathbf{G}_1^\top \mathbf{B}^\top \dots \mathbf{G}_{n_R}^\top \mathbf{B}^\top]^\top \quad (10.21)$$

where \mathbf{B} is a Boolean matrix.

10.4 Optimization

The sensitivity matrix \mathbf{R} of the residual target shape vector \mathbf{r} is not quadratic and thus not invertible. Hence, there exists a null-space $\mathbf{N} = \text{null}(\mathbf{H})$ with $\dim(\mathbf{N}) = n_u + 4n_v - n_R(n_P - 1)$ where changes in state variables \mathbf{e}^G do not affect the residual target shape vector. In other

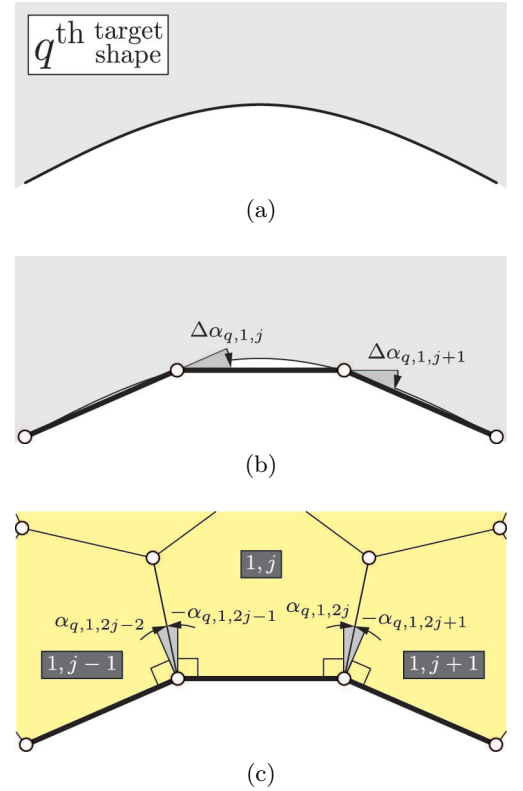


Figure 10.1: Approximation of continuous target shapes with equilibrium configurations of pressure actuated cellular structures. (a) Section of the q -th target shape. (b) Approximation of target shape with straight lines of given lengths. (c) The piecewise linear curve defines the required difference between the pentagonal base side angles α for the q -th pressure set.

words, it is possible to minimize an arbitrary objective function within the null-space where $\mathbf{r} = \mathbf{0}$. Hence, the underlying optimization problem for compliant pressure actuated cellular structures can be stated as

$$\begin{aligned} & \text{minimize} && \mathcal{F}(\mathbf{e}^G) \\ & \text{subject to} && \mathbf{r} = \mathbf{0} \\ & && \boldsymbol{\sigma} = \mathbf{1} \sigma_{\max} \end{aligned} \quad (10.22)$$

where $\boldsymbol{\sigma}$ is composed of the maximum cell side σ^S and hinge σ^H stresses, $\mathbf{1}$ is a vector of ones and σ_{\max} is the maximum allowed stress. This problem can be solved with Lagrange multipliers and the Newton method so that the Lagrangian

$$\mathcal{L}(\mathbf{e}^G, \boldsymbol{\lambda}_r, \boldsymbol{\lambda}_\sigma) = \mathcal{F}(\mathbf{e}^G) + \boldsymbol{\lambda}_r^\top \mathbf{r}(\mathbf{e}^G) + \boldsymbol{\lambda}_\sigma^\top \boldsymbol{\sigma}(\mathbf{e}^G) \quad (10.23)$$

is stationary if

$$\frac{\partial \mathcal{L}}{\partial \mathbf{e}^G} = \mathbf{0}, \quad \frac{\partial \mathcal{L}}{\partial \boldsymbol{\lambda}_r} = \mathbf{0} \quad \text{and} \quad \frac{\partial \mathcal{L}}{\partial \boldsymbol{\lambda}_\sigma} = \mathbf{0}. \quad (10.24)$$

In the following it is assumed that $\mathbf{e}^G = \{\mathbf{e}^G\} \setminus \{\mathbf{a}_0\}$ so that only reference cell side lengths other than the pentagonal base sides are varied during the optimization. An objective \mathcal{F} that minimizes the differences between state variables \mathbf{e}^G and target values $\mathbf{e}^{G,\text{tar}}$ can be defined as

$$\mathcal{F}(\mathbf{e}^G) = \frac{1}{2} (\mathbf{e}^G - \mathbf{e}^{G,\text{tar}})^\top (\mathbf{e}^G - \mathbf{e}^{G,\text{tar}}). \quad (10.25)$$

This choice is solely motivated by the objectives relatively simple gradient

$$\mathcal{F}^e = \frac{\partial \mathcal{F}}{\partial \mathbf{e}^G} = \mathbf{e}^G - \mathbf{e}^{G,\text{tar}} \quad (10.26)$$

and Hessian

$$\mathcal{F}^{ee} = \frac{\partial \mathcal{F}^e}{\partial \mathbf{e}^G} = \mathbf{I} \quad (10.27)$$

where \mathbf{I} is an identity matrix of size $n_u + 4n_v - n_P$. Therefore, the set of nonlinear equations for \mathbf{e}^G , $\boldsymbol{\lambda}_r$ and $\boldsymbol{\lambda}_\sigma$ that is iteratively solved with the Newton method is

$$\begin{bmatrix} \mathbf{I} + \boldsymbol{\mathcal{Z}}^i & \boldsymbol{\mathcal{R}}^{i\top} & \boldsymbol{\mathcal{S}}^{i\top} \\ \boldsymbol{\mathcal{R}}^i & \mathbf{0} & \mathbf{0} \\ \boldsymbol{\mathcal{S}}^i & \mathbf{0} & \mathbf{0} \end{bmatrix} \begin{bmatrix} \Delta \mathbf{e}^{G,i} \\ \Delta \boldsymbol{\lambda}_r^i \\ \Delta \boldsymbol{\lambda}_\sigma^i \end{bmatrix} = - \begin{bmatrix} \mathcal{F}^{e,i} + \boldsymbol{\mathcal{R}}^{i\top} \boldsymbol{\lambda}_r^i + \boldsymbol{\mathcal{S}}^{i\top} \boldsymbol{\lambda}_\sigma^i \\ \mathbf{r}^i \\ \boldsymbol{\sigma}^i - \sigma_{\max} \end{bmatrix} \quad (10.28)$$

where

$$\begin{bmatrix} \Delta \mathbf{e}^{G,i} \\ \Delta \boldsymbol{\lambda}_r^i \\ \Delta \boldsymbol{\lambda}_\sigma^i \end{bmatrix} = \begin{bmatrix} \mathbf{e}^{G,i+1} - \mathbf{e}^{G,i} \\ \boldsymbol{\lambda}_r^{i+1} - \boldsymbol{\lambda}_r^i \\ \boldsymbol{\lambda}_\sigma^{i+1} - \boldsymbol{\lambda}_\sigma^i \end{bmatrix}. \quad (10.29)$$

Furthermore, the derivatives of the sensitivity matrices $\mathcal{R} = \partial \mathbf{r} / \partial \mathbf{e}^G$ and $\mathcal{S} = \partial \boldsymbol{\sigma} / \partial \mathbf{e}^G$ are required to compute the nonlinear contributions of the constraint equations

$$\mathcal{Z}_{i,j} = \sum_{k=1}^{nR(nP-1)} \lambda_{r,k} \frac{\partial \mathcal{R}_{k,i}}{\partial \mathbf{e}_j^G} + \sum_{k=1}^{3nv} \lambda_{\sigma,k} \frac{\partial \mathcal{S}_{k,i}}{\partial \mathbf{e}_j^G}. \quad (10.30)$$

This requires third-order derivatives in \mathcal{Z} which are computationally expensive. On the other hand, neglecting these terms can slow down convergence. This problem can be overcome by sacrificing the objective function. If the target values $\mathbf{e}^{G,\text{tar}}$ are dynamically chosen at each iteration such that

$$\mathbf{e}^{G,i} - \mathbf{e}^{G,\text{tar}} = \mathbf{0} \quad (10.31)$$

then the Newton method reduces to

$$\begin{bmatrix} \mathbf{I} & \mathcal{R}^{i\top} & \mathcal{S}^{i\top} \\ \mathcal{R}^i & \mathbf{0} & \mathbf{0} \\ \mathcal{S}^i & \mathbf{0} & \mathbf{0} \end{bmatrix} \begin{bmatrix} \mathbf{e}^{G,i+1} - \mathbf{e}^{G,i} \\ \boldsymbol{\lambda}_r^{i+1} - \boldsymbol{\lambda}_r^i \\ \boldsymbol{\lambda}_\sigma^{i+1} - \boldsymbol{\lambda}_\sigma^i \end{bmatrix} = - \begin{bmatrix} \mathbf{0} \\ \mathbf{r}^i \\ \boldsymbol{\sigma}^i - \mathbf{1} \sigma_{\max} \end{bmatrix} \quad (10.32)$$

since $\mathcal{F}^e = \mathbf{0}$ and therefore $\boldsymbol{\lambda}_r = \mathbf{0}$ and $\boldsymbol{\lambda}_\sigma = \mathbf{0}$. Two iterations during the optimization of a pressure actuated cellular structure with a dynamic objective are visualized in Figure 10.2.

10.5 Examples

The complexity of pressure actuated cellular structures can vary greatly. For example, the use of frictionless instead of compliant hinges can eliminate the rigid cell corners and the hinge eccentricities of the geometric and mechanical model, respectively. However, it is not helpful to demonstrate the optimization of pressure actuated cellular structures for all possible simplifications and combinations thereof. Hence, two kind of example structures with extreme properties are subsequently used instead.

The first kind of structures possess centric, frictionless hinges and rigid cell sides. Their geometric and mechanical models are solely coupled via the cell side lengths and thicknesses. In contrast, the second kind of structures possess eccentric, compliant hinges and elastic cell sides so that their geometric and mechanical models are fully coupled. Example structures are optimized for two and three target shapes that range from circular arcs with moderate and extreme curvatures to the cruise and takeoff, landing configuration of a gapless leading edge. All

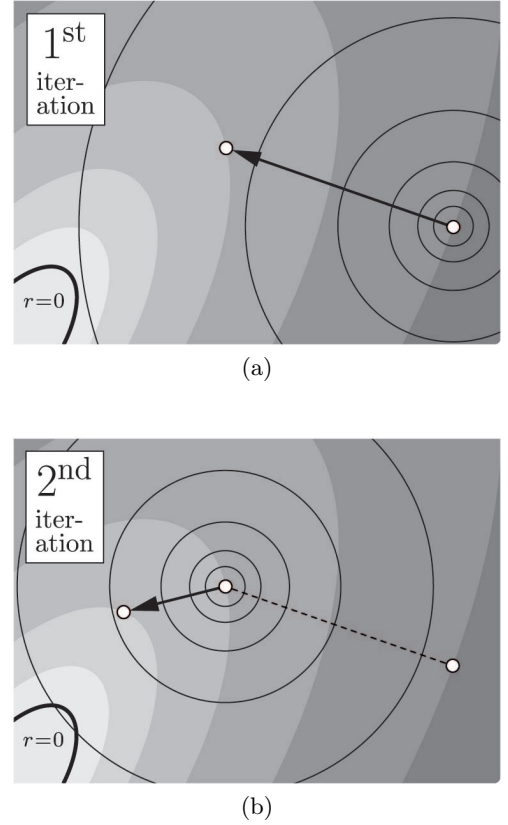


Figure 10.2: (a) First and (b) second iteration during the optimization of a pressure actuated cellular structure with a dynamic objective. The minimum of the objective moves with every iteration whereas the target shapes, constraints are enforced by Lagrange multipliers.

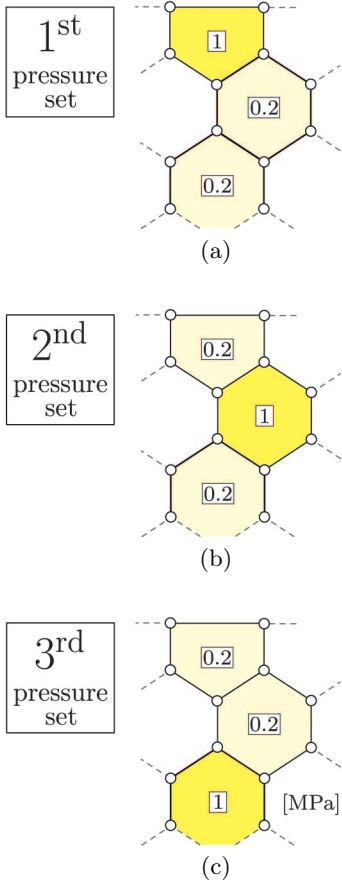


Figure 10.3: Pressure sets of example structures.

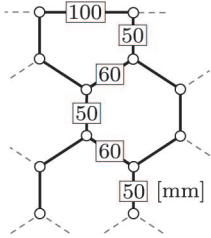


Figure 10.4: Initial cell side lengths of example structures with constant pentagonal base side lengths and centric, frictionless hinges.

of these structures have in common that they use cell row pressures of either $p = 0.2$ or 1 MPa as illustrated in Figure 10.3.

The shape changing potential of pressure actuated cellular structures is reduced at both ends by the decreasing number of cells in each additional cell row. It is thus assumed that, depending on the total number of cell rows, the shape changes between the first and the last n_R pentagonal base sides are zero. Furthermore, for the sake of simplicity, it is assumed that the maximum step length during the optimization is constant so that the total number of iterations could be potentially reduced with the help of a line search algorithm.

10.5.1 Rigid Body Structures

Shape changes of pressure actuated cellular structures with centric, frictionless hinges and rigid cell sides depend solely on the cell geometries and the pressure ratios between cell rows. Their shape changing potential is therefore an upper bound of what can be achieved by structures with compliant hinges and sides. Four different example structures are subsequently used to demonstrate the limits of pressure actuated cellular structures.

Extreme Curvatures

The achievable shape changes of pressure actuated cellular structures depend heavily on the target shapes and the associated pressure sets. This is demonstrated with the help of a structure that consists of two cell rows and twenty base pentagons. Its 119 cell side lengths¹ are optimized such that the equilibrium shapes resemble a convex and concave circular arc with an identical absolute curvature. Despite the constant curvature of the target shapes, edge effects prohibit the solution of this problem by investigating only a few cells.

As previously discussed, the computation of third order derivatives is avoided by using a dynamic objective that is updated after each iteration. As a consequence, the optimization results depend on the maximum step length during the optimization that is limited to $\Delta v_{\max} = 3$ mm and the initial cell side lengths that are summarized in Figure 10.4. The optimization results for the target shapes

$$\Delta\alpha_{q,i} = \begin{cases} 2.5^\circ & \text{for } q = 1 \\ -2.5^\circ & \text{otherwise} \end{cases}$$

¹The twenty pentagonal base side lengths are not varied during the optimization so that the total number of variables reduces from 139 to 119.

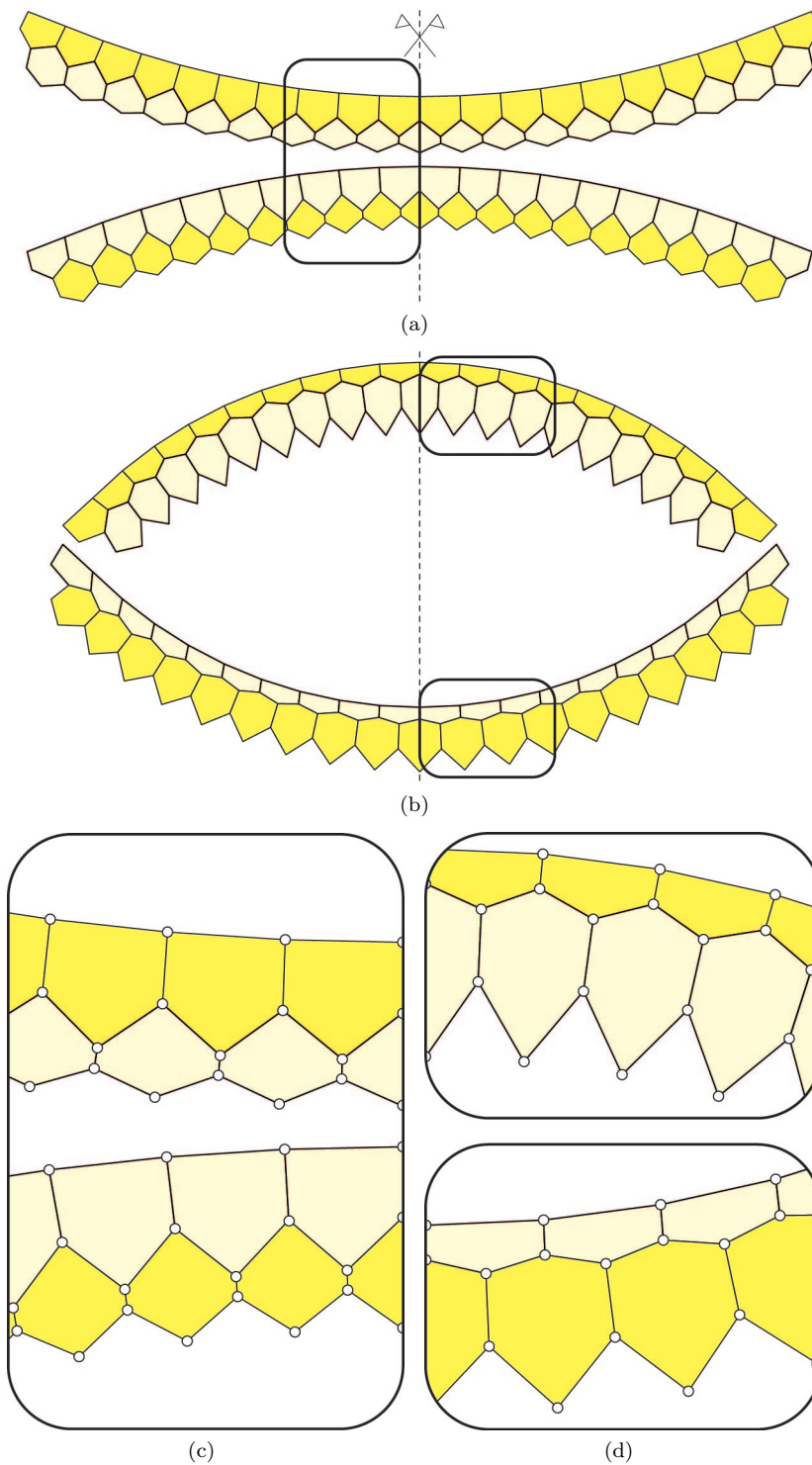


Figure 10.5: Pressure actuated cellular structure that consists of two cell rows and twenty base pentagons. The structure is assembled from centric, frictionless hinges and rigid cell sides. The cell side lengths are optimized such that the equilibrium shapes resemble convex, concave circular arcs with an identical absolute curvature. The maximum shape changes that can be achieved depend on the sign of the curvature for a given pressure set. Equilibrium shapes and detailed views of optimized structure for the (a),(c) first and (b),(d) second set of target shapes. (e) Convergence of the residual target shape vector.

and

$$\Delta\alpha_{q,i} = \begin{cases} -5^\circ & \text{for } q = 1 \\ 5^\circ & \text{otherwise.} \end{cases}$$

are shown in Figure 10.5. The non-zero shape changes between the pentagonal base sides are in both cases limited to $i = 2, \dots, 18$. It can be seen that the achievable absolute curvature is halved if the structure needs to deform into a convex arc for the first pressure set ($q = 1$). In both cases, the structures shape changing capability is limited by extreme pentagonal or hexagonal cell geometries.

The proposed algorithm requires at most fifteen iterations for the optimization of the example structure if a fixed maximum step length is used. Furthermore, the runtime is in each case less than twelve seconds on a single Intel i5-4250U core with 1.3 GHz and Matlab 2014b². This value can be seen as an upper bound as the symmetry and the small bandwidth of the stiffness matrix are not fully exploited. In general it can be said that practically relevant structures can be conveniently optimized even on aged hardware without the need for extremely refined software.

Moderate Curvatures

Pressure actuated cellular structures that fully utilize their shape changing potential suffer from extreme cell geometries. For example, the pentagonal cells of the previous example possess almost rectangular geometries for $\Delta\alpha_2 = 5^\circ$. These kind of cell geometries are disadvantageous as they lead to increased cell side forces and manufacturing sensitivities. The following example shows that balanced cell geometries can be obtained if pressure actuated cellular structures are optimized for moderate shape changes and appropriate cell row pressures. This is demonstrated with the help of a structure that consists of two cell rows and sixty base pentagons as illustrated in Figure 10.6. The 359 cell side lengths are optimized such that the equilibrium shapes resemble a half and a full circle with a convex curvature so that

$$\Delta\alpha_{q,i} = \begin{cases} 3^\circ & \text{for } q = 1 \\ 6^\circ & \text{otherwise.} \end{cases}$$

Similar to the previous example, the non-zero shape changes between pentagonal base sides are limited to $i = 2, \dots, 58$. Furthermore, the initial cell side lengths and the maximum step length during the optimization are unchanged.

²MathWorks claims that an average speedup of 2.1 can be achieved by simply upgrading from 2015a to 2018a.

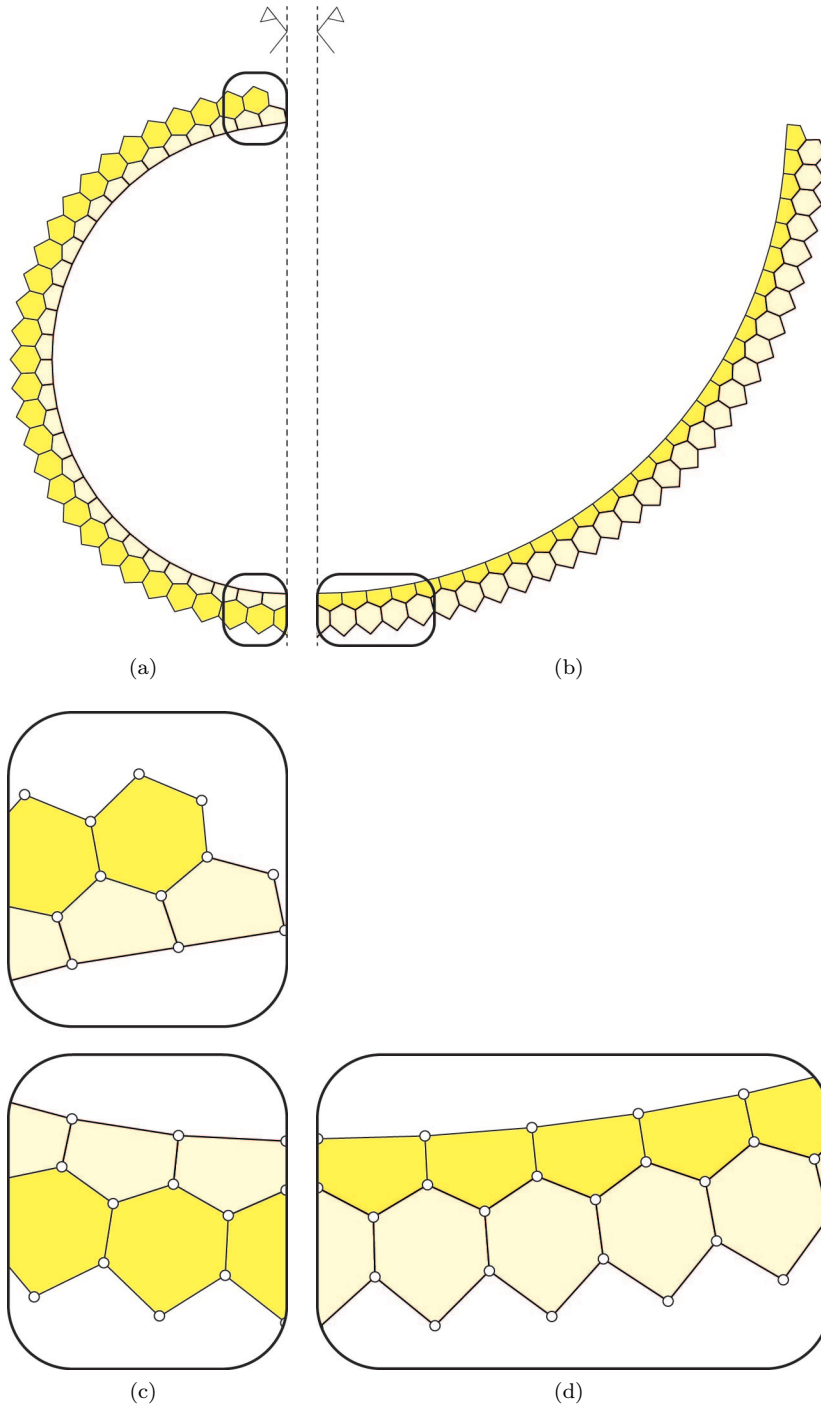


Figure 10.6: Pressure actuated cellular structure that consists of two cell rows and sixty base pentagons. The structure is assembled from centric, frictionless hinges and rigid cell sides. Cell side lengths are optimized such that the equilibrium shapes resemble a (a) half and (b) full circle with a convex curvature for the first and second pressure set, respectively. (c-d) Detailed views of equilibrium shapes. (e) Convergence of the residual target shape vector.

The difference between the pentagonal base side angles of both equilibrium shapes is $\Delta\alpha_2 - \Delta\alpha_1 = 3^\circ$ and thus considerably smaller than the 10° of the previous example. It can be seen that the moderate shape changing requirements in combination with an appropriate choice of cell row pressures leads to well balanced pentagonal and hexagonal cell geometries. This is also reflected by the required number of iterations that reduces from fifteen to six.

Euler Spiral

The presented framework for the optimization of pressure actuated cellular structures is by no means limited to two cell rows and target shapes with constant curvatures. This is demonstrated in the following with the help of a structure that consists of three cell rows and one-hundred base pentagons as illustrated in Figure 10.7. The 894 cell side lengths are optimized such that the equilibrium shapes resemble a convex and a concave circular arc with an identical absolute curvature as well as an Euler spiral

$$\Delta\alpha_{q,i} = \begin{cases} -1^\circ & \text{for } q = 1 \\ \frac{1}{47} (i - 50)^\circ & \text{for } q = 2 \\ 1^\circ & \text{otherwise.} \end{cases}$$

The potential shape changes at both ends are further reduced by the third cell row so that $i = 3, \dots, 97$. Hence, the angles between the first and the last three pentagonal base sides are constant. The initial cell side lengths and the maximum step length during the optimization are identical to the first two examples.

The consideration of three target shapes comes at the cost of a reduced shape changing capability. For example, the maximum difference between the pentagonal base side angles of all equilibrium shapes is $\Delta\alpha_3 - \Delta\alpha_1 = 2^\circ$ and thus smaller than in the previous examples. It can be seen that, unlike the previous examples, the structure does not possess a symmetry plane for any of the equilibrium shapes. Furthermore, it requires only five iterations to find an optimal solution that satisfies the target shapes. Hence, the convergence properties are not significantly affected by the varying curvature of the second target shape and the increased coupling between the state variables that is caused by the additional cell row.

Gapless Leading Edge

The shape changing potential of pressure actuated cellular structures with constant pentagonal base side lengths can not be fully utilized for arbitrary target shapes. This is disadvantageous as it leads to smaller

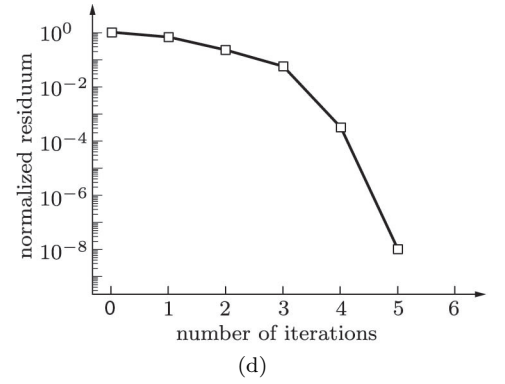
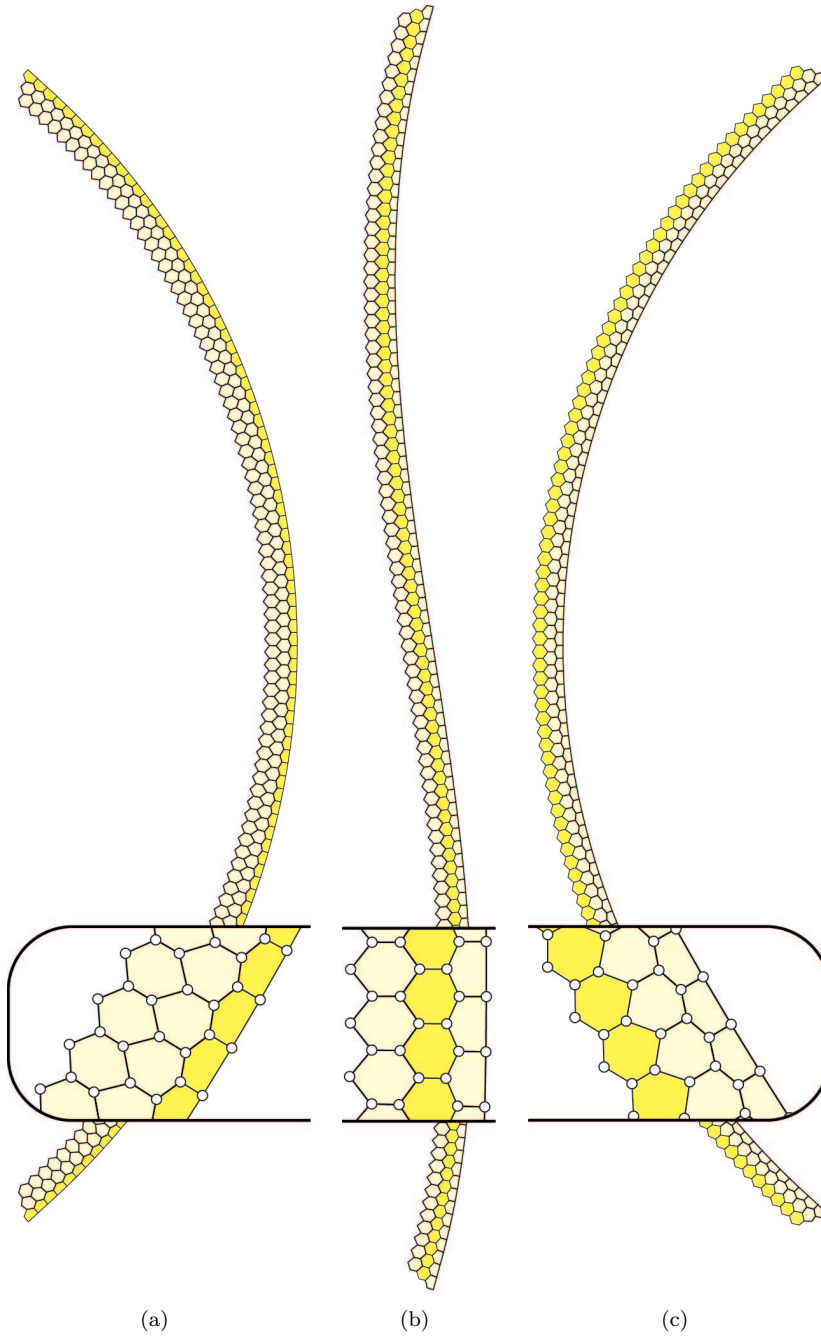


Figure 10.7: Pressure actuated cellular structure that consists of three cell rows and one-hundred base pentagons. The structure is assembled from centric, frictionless hinges and rigid cell sides. Cell side lengths are optimized such that the equilibrium shapes resemble a circular arc with a (a) concave and (c) convex curvature as well as an (b) Euler spiral. A detailed view of the structure is superimposed in these figures. (d) Convergence of the residual target shape vector.

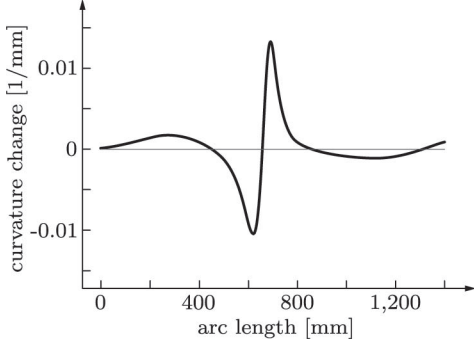


Figure 10.9: Curvature change of a gapless leading edge as a function of the arc length in counterclockwise direction. The curve is based on parametric least square interpolations with octic polynomials.

average cell sizes that depend on the maximum, local shape changing requirements. A structure that consists of two cell rows and one-hundred base pentagons is subsequently used to demonstrate the benefits of varying base side lengths. The 599 cell sides are optimized such that the equilibrium shapes resemble the cruise and high lift configuration of a gapless leading edge as illustrated in Figure 10.8. As for the previous examples, shape changes at both ends are assumed to be zero so that $i = 2, \dots, 98$.

The geometry of the leading edge is defined by discrete points whose coordinates can be found in the appendix. A set of parametric equations for the cruise and high lift configuration is obtained with the help of least square interpolations where the first and the last two coordinates are weighted³ to improve the continuity between the wing and the leading edge. Both configurations possess identical arc lengths so that axial strains during shape changes are avoided. The curvature changes of the leading edge are shown in Figure 10.9 for octic polynomials as a function of the arc length. It can be seen that the shape changing requirements vary considerably so that the use of constant pentagonal base side lengths is not optimal.

Instead it is better to choose the base side lengths such that the change of angles between neighbouring sides is constant. However, the computation of the corresponding side lengths is far from trivial and an interesting problem by itself. The base side length a_j of the j -th pentagonal cell is subsequently expressed with the help of a quadratic function

$$a_j = b_1 j^2 + b_2 j + b_3 \quad (10.33)$$

where \mathbf{b} are unknown coefficients. The arc length L of the leading edge needs to be identical to the sum of the n_P pentagonal base side lengths so that

$$L = \sum_{j=1}^{n_P} a_j = n_P \left(\frac{n_P + 1}{2} \left(\frac{2n_P + 1}{3} b_1 + b_2 \right) + b_3 \right). \quad (10.34)$$

Hence, the third coefficient becomes

$$b_3 = \frac{L}{n_P} - \frac{n_P + 1}{2} \left(\frac{2n_P + 1}{3} b_1 + b_2 \right) \quad (10.35)$$

and the remaining two coefficients are optimized such that the maximum change between base sides is minimal. An extension of this approach to polynomials with higher degrees is straightforward. The initial cell side

³The first and the last coordinate are weighted by a factor of ten whereas the second and penultimate coordinate are weighted by a factor of five.

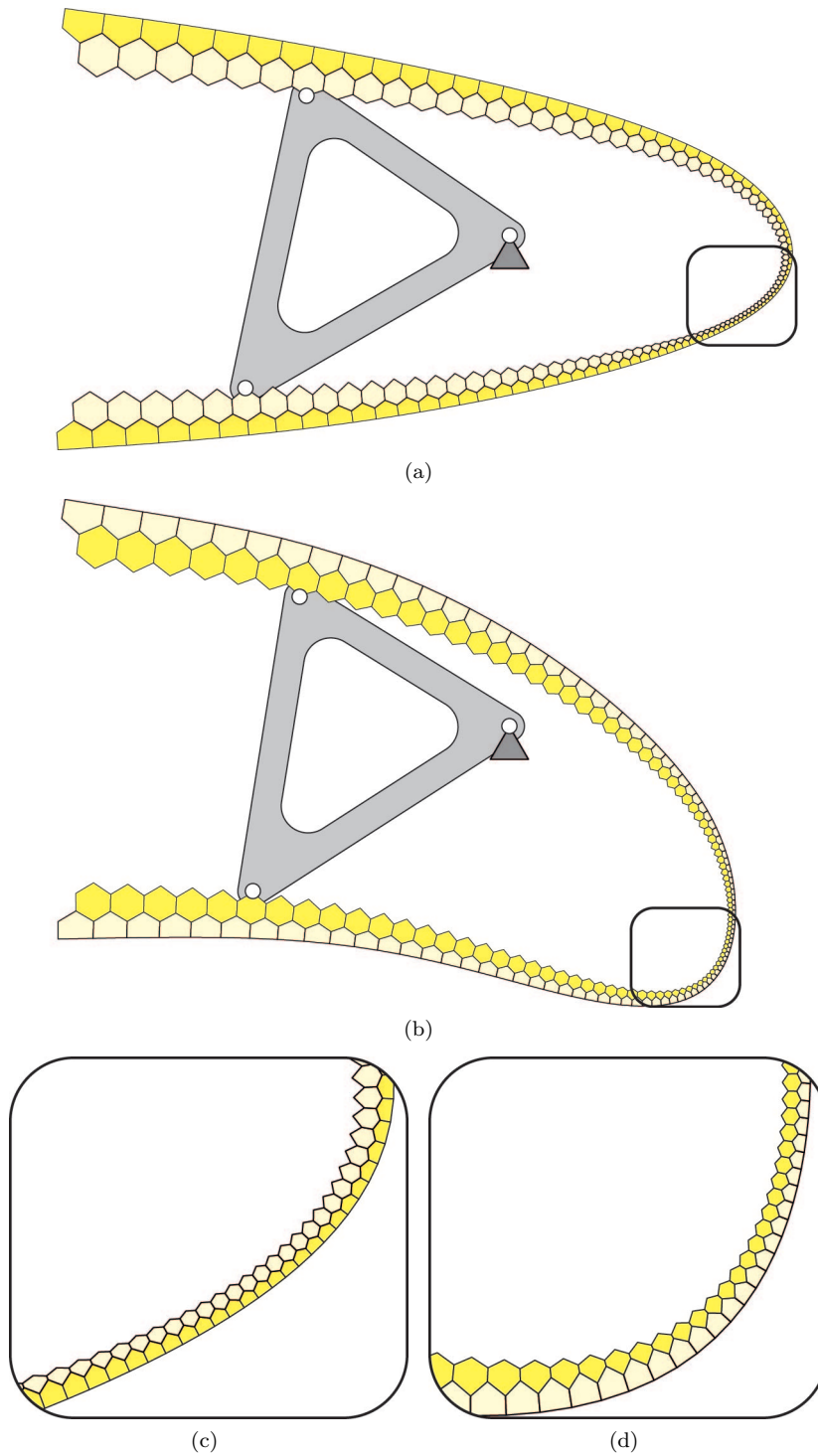


Figure 10.8: Pressure actuated cellular structure that consists of two cell rows and one-hundred base pentagons. The structure is assembled from centric, frictionless hinges and rigid cell sides. Cell side lengths are optimized such that the equilibrium shapes resemble the (a) cruise and (b) high lift configuration of a gapless leading edge for the first and second pressure set, respectively. The overall stiffness is increased by an internal, passive mechanism that connects the upper and lower surface. (c-d) Detailed views of equilibrium shapes. (e) Convergence of the residual target shape vector.

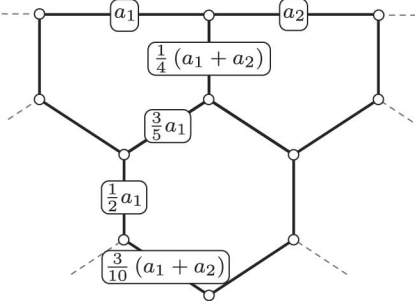


Figure 10.10: Initial cell side lengths of example structure with centric, frictionless hinges and varying pentagonal base side lengths.

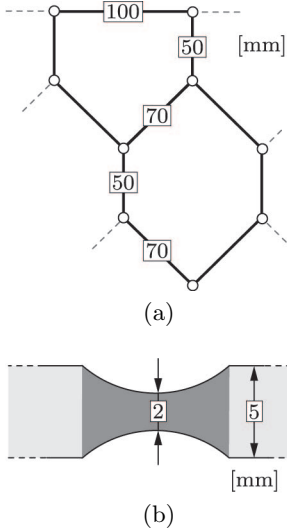


Figure 10.11: Initial (a) cell side lengths and (b) hinge, cell side thicknesses of compliant example structures.

lengths of the structure are then computed from the pentagonal base side lengths as illustrated in Figure 10.10.

The convergence of the optimization is not significantly affected by the relatively complex target shapes and the varying cell sizes as it requires only eight iterations to find an optimal solution. The stiffness of the structure can be enhanced by passive or active mechanisms that internally connect the upper and lower surface and thus provide additional supports. Constant distances between certain cell corners can be enforced with the help of constraints so that these mechanisms can be easily retrofitted. This is of great interest as the large variation of curvature changes leads to relatively thin regions that decrease the overall bending stiffness.

10.5.2 Compliant Structures

The first two examples are subsequently revisited to demonstrate the effects of compliant hinges and elastic cell sides on the shape changing potential of pressure actuated cellular structures. The equilibrium shapes of compliant structures depend additionally on the material properties and the geometry of the reference configuration. The initial cell side lengths and hinge, cell side thicknesses of both examples are summarized in Figure 10.11. Furthermore, it is assumed that the aspect ratio of hinges is $\mu = 4$ and that the target curvature of cell corners is $\kappa^{\text{tar}} = 0.5 \text{ mm}^{-1}$. The maximum step lengths during the optimization are limited to $\Delta v_{\text{max}} = 3 \text{ mm}$ and $\Delta s_{\text{max}} = \Delta t_{\text{max}} = 0.3 \text{ mm}$.

Depending on the considered target shapes, the reference state variables α_0 are chosen such that the required bending deformations of the pentagonal base side hinges are minimal. In contrast, the reference state variables β_0 are assumed to be zero. Furthermore, reference state angles are constrained during the optimization so that they remain unchanged. This is motivated by the different sensitivities of the equilibrium shapes with respect to cell side lengths, thicknesses and reference state angles. However, their values can be optimized in a subsequent step by minimizing the total bending energy of all equilibrium shapes for given cell row pressures, cell side lengths and thicknesses⁴.

It is subsequently assumed that the example structures are made from polyphenylsulfon⁵ so that the relevant material properties are

⁴This step can affect the structures equilibrium shapes so that it needs to be complemented by another optimization of the cell side lengths and hinge, cell side thicknesses.

⁵PPSU is a moldable plastic that is commonly used in rapid prototyping.

material

$E = 2,340$ MPa	Young's modulus
$\nu = 0.4$	Poisson's ratio
$\sigma_{\max} = 50$ MPa	yield strength.

It is usually not possible to fully utilize the yield strength of the material as it depends on the manufacturing process, environmental conditions, load history and size effects. However, the influence of these factors is difficult to quantify and thus not considered. As a consequence, the presented results are nonconservative and potential shape changes are likely to be (slightly) smaller.

Extreme Curvatures

It was previously shown that the shape changing potential of pressure actuated cellular structures with centric, frictionless hinges is limited by extreme cell geometries. This effect is magnified in compliant structures as each cell side needs to accommodate two cell corners and hinges with finite sizes. This increase the minimum cell side lengths and thus decrease the range of possible cell geometries. The shape changing potential is further reduced by the bending stiffness of compliant hinges and the elasticity of cell sides. Similar to the first example, this is demonstrated with the help of a structure that consists of two cell rows and twenty base pentagons.

The 536 optimization variables that include 119 cell side lengths, 139 cell side thicknesses and 278 hinge thicknesses⁶ are optimized such that the equilibrium shapes resemble a convex and concave circular arc with an identical absolute curvature. The corresponding target shapes are

$$\Delta\alpha_{q,i} = \begin{cases} 0.75^\circ & \text{for } q = 1 \\ -0.75^\circ & \text{otherwise} \end{cases}$$

and

$$\Delta\alpha_{q,i} = \begin{cases} -2^\circ & \text{for } q = 1 \\ 2^\circ & \text{otherwise} \end{cases}$$

as shown in Figure 10.12. As before, the non-zero shape changes between the pentagonal base sides are limited to $i = 2, \dots, 18$. The reference configuration is chosen such that the bending deformations of the base side hinges are minimal so that $\Delta\alpha_{0,i} = 0$.

It can be seen that the structures shape changing capabilities are severely limited by the minimum cell side lengths that are needed to

⁶The pentagonal base side lengths are assumed to be invariant whereas their hinge and cell side thicknesses are varied.

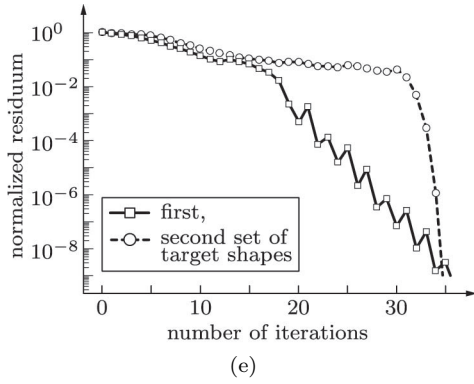
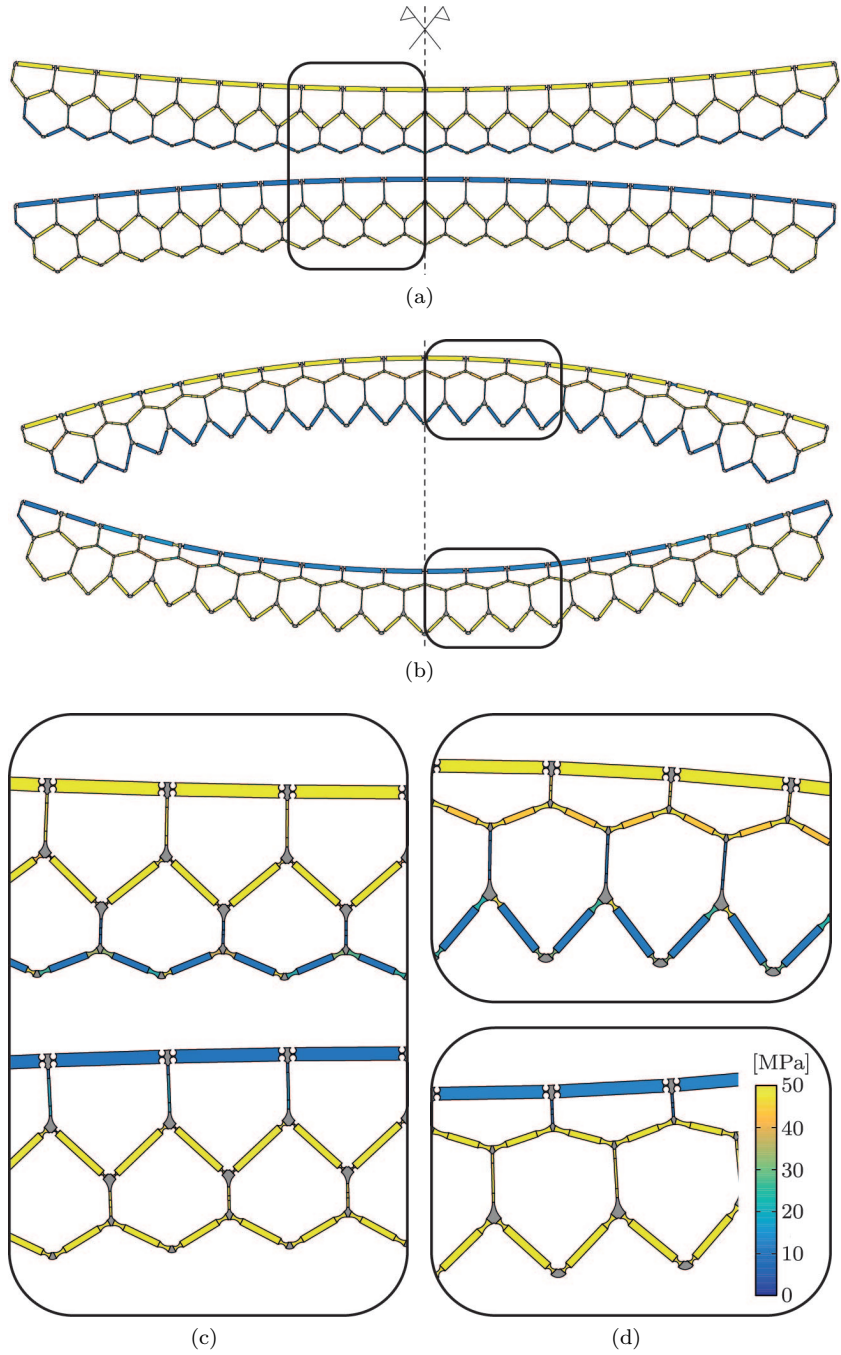


Figure 10.12: Compliant pressure actuated cellular structure that consists of two cell rows and twenty base pentagons. Cell side lengths and hinge, side thicknesses are optimized such that the equilibrium shapes resemble convex, concave circular arcs with an identical absolute curvature. The maximum shape changes that can be achieved depend on the sign of the curvature for a given pressure set. Equilibrium shapes, von Mises stresses and detailed views of the optimized structure for the (a),(c) first and (b),(d) second set of target shapes. (e) Convergence of the residual target shape and stress vector.



accommodate the rigid cell corners and compliant hinges. Furthermore, all cell sides and hinges are fully stressed for at least one of the two pressure sets. The corresponding stress constraints lead to a wide range of hinge geometries. For example, hinges of cell sides that are not exposed to differential pressures possess a nearly uniform thickness. In contrast, pentagonal base side hinges possess a large thickness variation due to the large bending angles and small axial cell side forces. This is problematic as the effect of transverse forces on the maximum hinge stresses is not considered. Hence it would be best to use an advanced hinge model instead that additionally takes the effects of transverse forces into account. Nonetheless, the proposed algorithm requires at most 35 iterations for the optimization despite the considerably increased nonlinearity of the underlying problem.

Moderate Curvatures

Finite cell corner and hinge sizes limit the minimum cell side lengths and thus the shape changing potential of compliant pressure actuated cellular structures. However, this is usually not a problem as moderate shape changing requirements lead to balanced cell geometries. Similar to the second example, this is demonstrated with the help of a structure that consists of two cell rows and sixty base pentagons as illustrated in Figure 10.13.

The 1,616 optimization variables that include 359 cell side lengths, 419 cell side thicknesses and 838 hinge thicknesses are optimized for a half and full circle with a convex curvature so that

$$\Delta\alpha_{q,i} = \begin{cases} 3^\circ & \text{for } q = 1 \\ 6^\circ & \text{otherwise} \end{cases}$$

where $i = 2, \dots, 58$. The reference configuration is chosen such that the bending deformations of the base side hinges are minimal. This is the case for $\Delta\alpha_{0,i} = 4.5^\circ$ so that the shape of the undeformed structure is between a half and full circle. It can be seen that the cell corners and hinges are easily integrated into the balanced cell geometries. Furthermore, if compared with the second example, the influence of compliant hinges and sides on the cell geometries is surprisingly small. As before, the optimization requires about 35 iterations.

10.5.3 Potential Improvements

The presented framework for the simulation and optimization of compliant pressure actuated cellular structures is remarkably efficient. With regards to the total number of cells and cell rows, there seems to be no

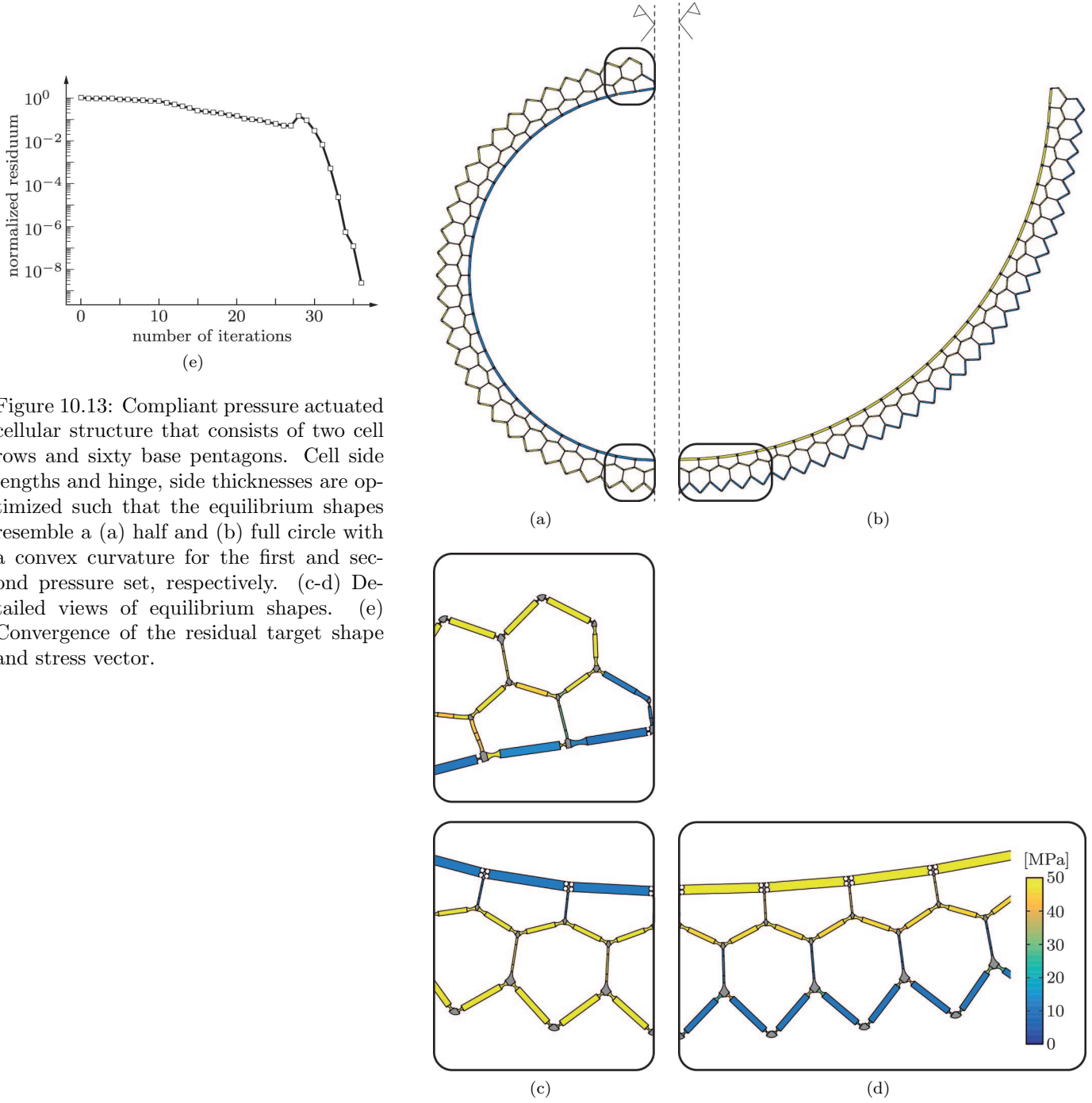


Figure 10.13: Compliant pressure actuated cellular structure that consists of two cell rows and sixty base pentagons. Cell side lengths and hinge, side thicknesses are optimized such that the equilibrium shapes resemble a (a) half and (b) full circle with a convex curvature for the first and second pressure set, respectively. (c-d) Detailed views of equilibrium shapes. (e) Convergence of the residual target shape and stress vector.

limit for the simulation and optimization of practically relevant structures. Nonetheless, several improvements can be made that range from the generation of input data to the software development. A brief outline of the main areas that need to be considered for a potential industrial use of this technology is given in the following.

Pre and Post Processor

The use of constant cell row pressures is only optimal if the sign of the curvature changes along the arc length of a target shape is invariant. In all other cases it is best to separate cell rows into regions with different cell pressures. This needs to be done in conjunction with an advanced algorithm that splits the parametric target shapes into pentagonal base sides of varying lengths such that the required shape changes between cells are uniform.

The optimization results of compliant pressure actuated cellular structures are provided in a vector graphic format (Scalable Vector Graphics) so that they can be directly send to a rapid prototyping machine. However, a direct integration of end caps, cytoskeletons, fluid channels and connection elements is currently not implemented.

Optimization

The required number of iterations for the optimization of pressure actuated cellular structures with centric, frictionless hinges and rigid cell sides is remarkably small and essentially independent of the total number of cells and cell rows. This does not significantly change for compliant structures despite the increased nonlinearity that mostly stems from the additional stress constraints. Nonetheless, it is possible to further reduce the number of iterations with the help of a line search algorithm particularly in the presence of large nonlinearities.

The exact consideration of an objective leads to optimization results that are independent of the initial state variables and step length. However, this requires the use of third order derivatives whose general implementation is particularly cumbersome. Fortunately, the corresponding implementation for a model with centric, frictionless hinges and rigid cell sides is manageable. Hence it is possible to reduce the sensitivity of the optimization results with respect to the initial state variables and step length by using a staged optimization approach with an increasing model complexity.

Mechanical Model

The presented framework is highly modular and enables the integration of different cell corner, hinge and cell side models. Potential im-

provements can be made with regard to the hinge model as it currently neglects the effects of axial strains and transverse forces. Hence, the required hinge thicknesses might be underestimated under certain conditions. Furthermore, it is beneficial to use advanced hinge geometries whose aspect ratios depend on the stress resultants and shape changes. Further improvements can be made with regard to cell sides. Their weight can be significantly reduced in the presence of differential pressures if cell side thicknesses are varied.

Software Development

The mechanical aspect of pressure actuated cellular structures is well understood and an integration of the previously discussed improvements into the existing framework is, at least from a theoretical point of view, straightforward. However, the corresponding development of a modular, highly versatile and efficient software is not trivial⁷.

Such a software should be able to seamlessly switch between different models and to interface with different pre and post processors. Furthermore, it needs to minimize the runtime by exploiting the one-dimensional nature of pressure actuated cellular structures that leads to sparse, symmetric matrices with a small bandwidth. This enables the efficient use of domain decomposition methods so that the computations can be distributed between several processors. However, the amount of time and effort that is required for the development of such a software can be hardly overestimated.

⁷The currently used software is a result of five major revisions. Although highly optimized, it encompasses nearly 10k lines of object oriented Matlab code.

Chapter 11

Additional Topics

An efficient numerical tool for the optimization of compliant pressure actuated cellular structures is necessary but not sufficient for their realization. Another equally important aspect is the pressure tight sealing of cells at both ends such that their shape changing capabilities are not significantly affected. Furthermore, there exists a number of different approaches that can be used to reduce their selfweight and to improve their stiffness and shape changing capabilities. For example, an optimal selection of cell sizes, cell row pressures and materials increases the ratio between the total pressure and bending energy. Further performance improvements can be achieved by using curved cell sides or subcellular structures. The latter is particularly interesting as it provides additional supports for the cell sides and thus carries a large part of the differential pressures via tension forces. It is subsequently shown how optimal materials for compliant pressure actuated cellular structure can be selected. Furthermore it is shown that cells can be efficiently sealed with the help of minimal surfaces and that cytoskeletons can be used to reduce the cell side moments due to differential pressures.

11.1 Material and Cell Sizes

The target shapes and stiffness requirements for pressure actuated cellular structures are known prior to their design whereas the optimal material, number of base pentagons and cell row pressures are usually unknown. It is subsequently shown that the material for pressure actuated cellular structures needs to be selected such that it minimizes the overall bending energy of compliant hinges. Furthermore, the dependencies between the material selection, cell row pressures and number of base pentagons are investigated.

11.1.1 Material Selection

Compliant pressure actuated cellular structures can be made from all kind of materials. A selection of materials with a particularly large ratio between yield strength σ_{\max} and Young's modulus E is shown in Figure 11.1. It can be seen that the yield strengths of these materials obey a power law

$$\sigma_{\max} = aE^b \quad (11.1)$$

where the parameters a and b are computed from a least square interpolation so that

$$a = 0.243 \quad \text{and} \quad b = 0.727. \quad (11.2)$$

Bending angles of compliant hinges are mainly driven by shape changing requirements whereas axial cell side forces are driven by cell pressures. Based on a constant thickness ratio t/s , the required central hinge thickness s for a given axial cell side force F and bending angle φ is

$$s = \frac{2\rho|F|}{2\sigma_{\max} - \rho\chi E^{\text{eff}}|\varphi|}. \quad (11.3)$$

Herein, E^{eff} denotes the effective Young's modulus, ρ the stress reduction factor for the von Mises yield criterion and χ the correction factor for the hinge geometry. Unlike the yield strength, the Poisson's ratio can not be expressed with the help of a power law. For example, a wide range of plastics and metals possess a similar Poisson's ratio [106]. Hence, its variation is not considered in the following. The bending energy

$$\Pi_n = \frac{\chi E^{\text{eff}}}{24} s^2 \varphi^2 \quad (11.4)$$

of a compliant hinge is minimal for

$$\tilde{E} = \left(\frac{\rho\chi|\varphi|}{2a(2b-1)(1-\nu^2)} \right)^{\frac{1}{b-1}} \propto |\varphi|^{-3.7} \quad (11.5)$$

so that the optimal Young's modulus \tilde{E} decreases exponentially for increasing bending angles. Therefore, the minimum bending energy $\tilde{\Pi}_n$ of a compliant hinge is proportional to

$$\tilde{\Pi}_n \propto |F|^2 |\varphi|^{\frac{1}{1-b}} \approx |F|^2 |\varphi|^{3.7}. \quad (11.6)$$

Hinges throughout a compliant pressure actuated cellular structure are usually subjected to different bending angles and axial cell side forces. As a consequence, it would be optimal if they are each made from a different material. If only one material is used throughout a structure it is best to select it such that it minimizes the overall bending energy.

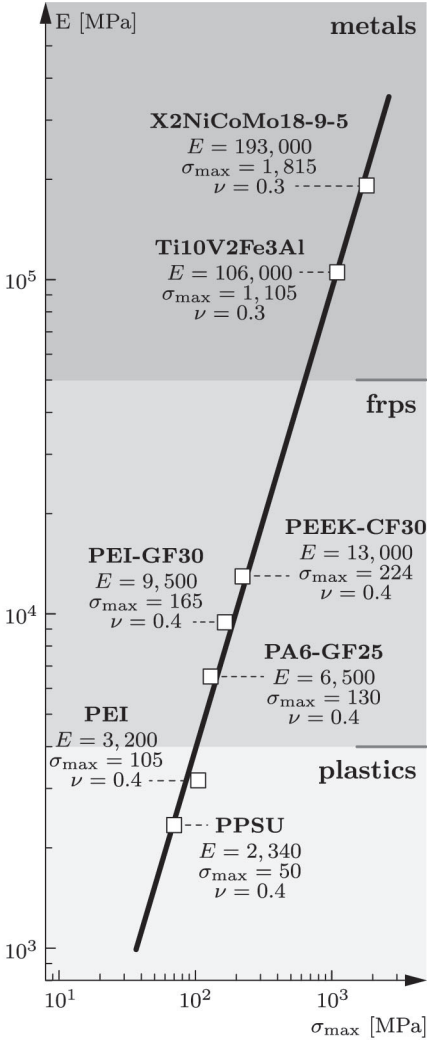


Figure 11.1: Yield strength σ_{\max} versus Young's modulus E of materials that range from plastics over fiber reinforced plastics (frps) to metals.

11.1.2 Scaling

As illustrated in Figure 11.2, the scaled cell side lengths \mathbf{v}_0^s and bending angles φ^s for a scaling factor $\eta \in \mathbb{R}$ are

$$\mathbf{v}_0^s = \eta^{-1} \mathbf{v}_0 \quad \text{and} \quad \varphi^s = \eta^{-1} \varphi. \quad (11.7)$$

The expression for the optimal, scaled Young's modulus \tilde{E}^s of a compliant hinge can thus be written as

$$\tilde{E}^s = \eta^{\frac{1}{1-b}} \tilde{E} \propto \eta^{3.7}. \quad (11.8)$$

As a consequence, a material with a thirteen times larger Young's modulus is required if the number of base pentagons is doubled. The corresponding expression for the bending energy $\tilde{\Pi}_n^s$ is harder to find as it additionally depends on the axial cell side force F^s . Doubling the number of base pentagons reduces the bending stiffness of pressure actuated cellular structures by a factor of eight so that the scaled differential pressure Δp^s that acts on a cell side is

$$\Delta p^s = \eta^3 \Delta p \quad (11.9)$$

if the overall bending stiffness needs to be preserved. The scaled cell side force F^s thus becomes

$$F^s = \eta^2 F \quad (11.10)$$

and the scaled bending energy of a hinge results in

$$\tilde{\Pi}_n^s = \eta^{\frac{3-4b}{1-b}} \tilde{\Pi}_n \propto \eta^{0.3} \quad (11.11)$$

since $F \propto \Delta p v_0$. The proportionality of the number of base pentagons and the ratio between the pressure Π_p and total bending $n_v \tilde{\Pi}_n$ energy of a compliant pressure actuated cellular structure follows from the previous equation¹

$$\frac{\Pi_p^s}{n_v^s \tilde{\Pi}_n^s} = \eta^{\frac{3b-2}{1-b}} \frac{\Pi_p}{n_v \tilde{\Pi}_n} \propto \eta^{0.7}. \quad (11.12)$$

Hence, the influence of the bending stiffness on the equilibrium shapes decreases for an increasing number of base pentagons. This might, at least partially, explain the small cell sizes and relatively large cell pressures that can be observed in nastic plants. However, structures with a very large number of cells are difficult to manufacture and therefore not of practical interest. Furthermore, safety and energy efficiency considerations limit the maximum cell pressures for most applications to about 5 MPa if gaseous pressure mediums are used. Cell pressures beyond that limit need to be generated with the help of comparatively heavy hydraulic fluids.

¹The number of scaled cell sides is proportional to $n_v^s \propto \eta$ so that the total bending energy is proportional to $n_v^s \tilde{\Pi}_n^s \propto \eta^{1.3}$. Furthermore, the scaled pressure energy is proportional to $\Pi_p^s \propto \eta^2$.

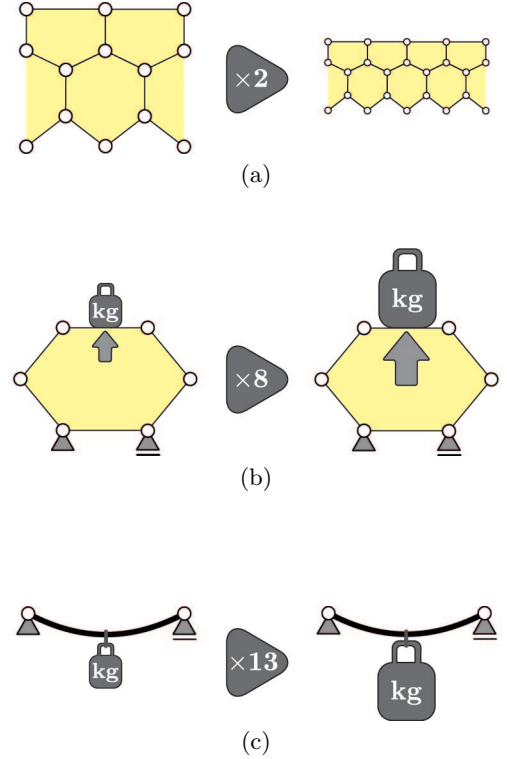


Figure 11.2: The following approximate changes are required if the overall stiffness and shape changing capabilities of a compliant pressure actuated cellular structure need to be preserved for a varying number of base pentagons. (a) The cross sectional area of each cell is quartered and the total cross sectional area of the structure is halved if the number of base pentagons is doubled ($\eta = 2$). (b) This leads to a reduced bending stiffness that needs to be compensated by an eightfold increase of cell pressures. (c) The reduced hinge rotations and increased axial cell side forces affect the material selection. Doubling the number of cells requires a material with a thirteen times higher stiffness.

11.2 Cytoskeletons

Pressure actuated cellular structures mimic the nastic movement of plants by combining several rows of equally pressurized prismatic cells with tailored cell side lengths. These structures are highly efficient as many of their sides are solely subjected to normal forces. However, compared to truss structures they have two drawbacks. The first is their relatively small stiffness due to their pressure stiffened, inherent degrees of freedom that enable large shape changes. The second is their relatively large weight that is caused by the pressure induced bending moments of cell sides along the boundary and between cell rows.

It is subsequently shown how the weight and stiffness of pressure actuated cellular structures can be improved with the help of cytoskeletons. These subcellular structures are relatively thin so that they can carry large tension but only minor compression forces. This is done on the basis of an adaptive module that consists of two cell rows that are assembled from identical cells with rigid sides and frictionless hinges as illustrated in Figure 11.3(a). The side lengths are chosen such that the subtended angles of the equilibrium shapes are $\alpha_{\min} = 60^\circ$ and $\alpha_{\max} = 100^\circ$ for cell row pressures of 0.4 and 2.0 MPa.

11.2.1 Stiffness

The stiffness of the adaptive module is enhanced by a cytoskeleton whose horizontal and vertical members restrain its shape changing capabilities and/or potential deformations. Two cytoskeletons with different member lengths are subsequently considered. The first cytoskeleton is designed such that its vertical and horizontal members are taut at α_{\min}

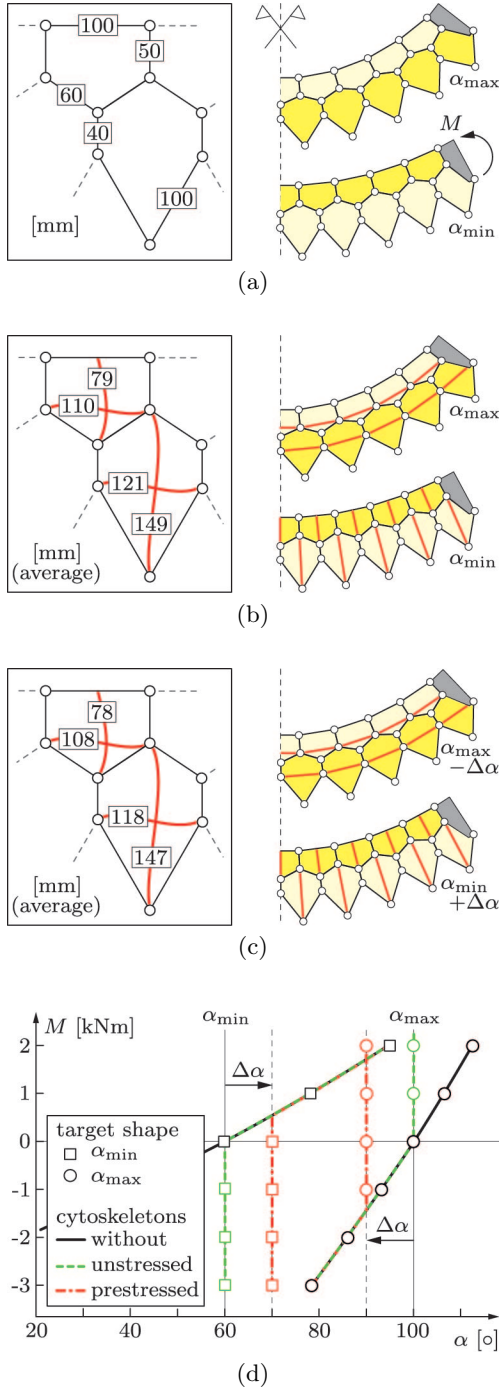


Figure 11.3: (a) Geometry of an adaptive module that consists of rigid cell sides and frictionless hinges. Subtended angles of equilibrium shapes are $\alpha_{\min} = 60^\circ$ and $\alpha_{\max} = 100^\circ$ for cell row pressures of 0.4 and 2.0 MPa. (b) Lengths of the vertical and horizontal cytoskeleton members are chosen such that they are taut and unstressed at α_{\min} and α_{\max} , respectively. Cytoskeleton members are slack if subjected to compression forces. (c) Reduced cytoskeleton lengths are chosen such that they restrain the subtended angles of the equilibrium shapes to $\alpha_{\min} + \Delta\alpha$ and $\alpha_{\max} - \Delta\alpha$ where $\Delta\alpha = 10^\circ$. (d) Subtended angles of modules with and without a cytoskeleton for both pressure sets as a function of the external bending moment M that acts on both ends. Depending on the cytoskeleton, taut members restrain deformations beyond $|\alpha_{\min}|$ and $|\alpha_{\max}|$ or $|\alpha_{\min} + \Delta\alpha|$ and $|\alpha_{\max} - \Delta\alpha|$. Furthermore, the prestress of the cytoskeleton with shorter members increases the module stiffness at the equilibrium shapes for bending moments with an arbitrary sign.

and α_{\max} , respectively and unstressed otherwise. In contrast, the second cytoskeleton is designed such that it restrains the subtended angles of the equilibrium shapes to $\alpha_{\min} + \Delta\alpha$ and $\alpha_{\max} - \Delta\alpha$ where $\Delta\alpha = 10^\circ$. It should be noted that the member lengths of the cytoskeleton differ slightly between neighbouring cells due to edge effects so that only average lengths are given in Figure 11.3(b-c).

The subtended angle α of the adaptive module with and without a cytoskeleton is shown in Figure 11.3(d) for both pressure sets as a function of the external bending moment M that acts on both ends. It can be seen that the stiffness of the module without a cytoskeleton is, depending on the cell pressures, between $7 - 19^\circ/\text{kNm}$. This corresponds to a steel plate with a thickness of 5-8 mm. The use of an unstressed cytoskeleton greatly increases the stiffness against deformations beyond $|\alpha_{\min}|$ and $|\alpha_{\max}|$ but does not affect the stiffness for deformations inbetween as its members become immediately slack if subjected to compression forces. In contrast, the prestressed cytoskeleton with shorter member lengths considerably increases the stiffness for a bending moment $|M|$ of up to 0.5-2.0 kNm at the cost of a reduced shape changing capability. Cytoskeletons can thus be used to improve the stiffness of pressure actuated cellular structures at equilibrium shapes. This is interesting as it potentially enables the use of reduced cell pressures and side thicknesses since the structural stiffness during shape changes is generally not a critical design criterion.

11.2.2 Weight

Unlike axial tension forces, bending moments can not be efficiently carried by cell sides as they lead to linear stress distributions that increase the required cell side thicknesses and thus the overall weight. It is therefore advantageous to minimize their impact with the help of advanced cell side geometries or subcellular structures. For example, curved cell sides can be used to minimize bending moments due to differential pressures. However, their applicability is limited as internal sides between cell rows are exposed to varying load directions. A curved cell side can thus lead to snap through buckling which increases the hinge deformations and decreases the fatigue life. Furthermore, pentagonal base sides need to provide a smooth surface so that their shapes depend on the target shapes. As a consequence, only the outer hexagonal cell sides can be potentially curved.

Alternatively, it is possible to reduce the bending moments of all cell sides with the help of a cytoskeleton that provides additional, equally spaced supports as illustrated in Figure 11.4. For the sake of simplicity, it is subsequently assumed that the cell side segments are connected

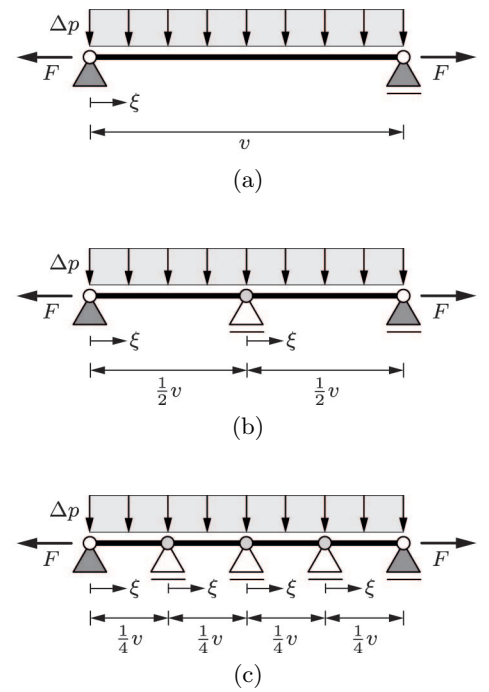


Figure 11.4: (a) Mechanical model of a cell side that is subjected to an axial force F and a differential pressure Δp . (b) Additional, equally spaced supports are provided by a cytoskeleton with a refinement level $q = 1$ and (c) $q = 2$.

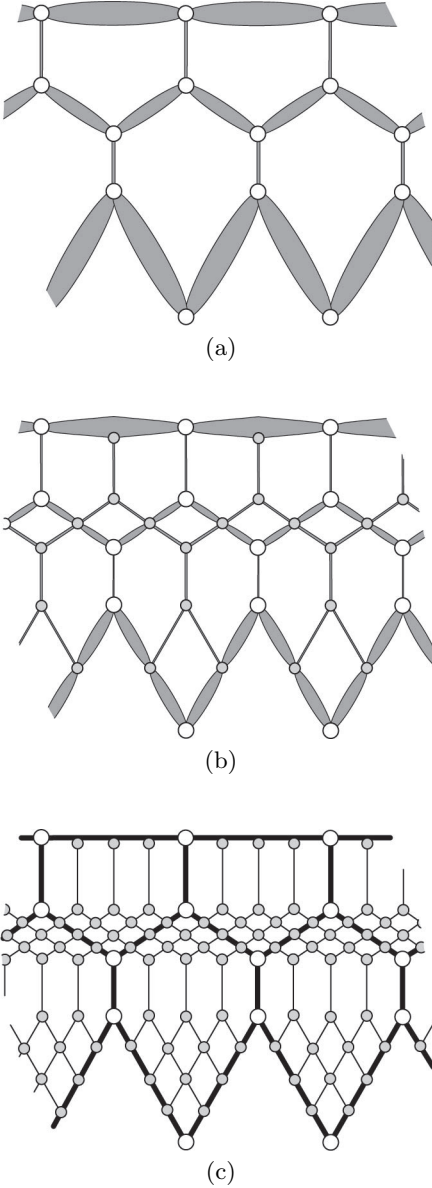


Figure 11.5: (a) Required cell side thicknesses of the adaptive module. (b) Thicknesses reduce considerably if a cytoskeleton with a refinement level $q = 1$ is used. (c) Cytoskeleton can be further refined ($q = 2$) to increase the number of equally spaced supports.

at intermediate supports via frictionless hinges. This is a conservative estimate that leads to larger bending moments in comparison to a continuous beam. The required cell side thickness t for an axial force F and bending moment M is

$$t(\xi, q) = \frac{|F| + \sqrt{F^2 + 24|M(\xi, q)|\sigma_{\max}}}{2\sigma_{\max}} \quad (11.13)$$

where σ_{\max} is the yield strength of the cell side material. The bending moment

$$M(\xi, q) = \frac{\Delta p v^2}{2 \cdot 4^q} (1 - \xi) \xi \quad (11.14)$$

depends on the position $\xi \in [0, 1]$ along the cell side and the number of supports

$$n_s = 1 + 2^q \quad (11.15)$$

that follows from the refinement level q of the cytoskeleton. The weight w is proportional to the thickness t of a cell side so that the weight ratio for different refinement levels ($q_2 > q_1$)

$$2^{q_1 - q_2} \leq \frac{w_{q_2}}{w_{q_1}} \leq 1 \quad (11.16)$$

is bounded by $F = 0$ and $\Delta p = 0$.

The required cell side thicknesses of the adaptive module for all possible cell row pressures are illustrated in Figure 11.5. It can be seen that the thicknesses are greatly reduced by a cytoskeleton with a refinement level $q = 1$. The uniformly stressed cytoskeleton members are relatively thin so that, depending on the cell material, weight reductions of up to 35 % can be achieved [222]. The cytoskeleton itself is based on four-bar linkages that provide additional supports but do not restrain the shape changing capabilities of the cells.

11.3 End Caps

The prismatic cells of pressure actuated cellular structures need to be sealed at both ends such that they can sustain significant differential pressures while being flexible enough to allow large cross sectional shape changes. Similar to tires, this can be done with the help of flexible inner tubes or compliant end caps that are seamlessly integrated into the cell sides. Elastic tubes are easy to manufacture and their integration into cellular structures that are not reinforced by a cytoskeleton is straightforward. However, they increase the overall weight and add potential

failure modes so that they are mainly of interest for the use in prototype structures.

In contrast, compliant end caps can be used in conjunction with cytoskeletons. However, their reduced part count and weight comes at the cost of an increased design and manufacturing complexity. Optimal end caps possess, similar to soap films, an isotropic stress state for all possible cell deformations. Unfortunately, it is not possible to construct such an end cap from a solid material. For the sake of simplicity, it is subsequently assumed that the stress variations of end caps due to shape changes are small. Hence their design reduces to the computation of minimal surfaces [25] for the reference, undeformed configurations.

Two different end cap designs for the pentagonal cells of the adaptive module are subsequently considered. The first consists of a thin membrane whereas the second is additionally reinforced by elastic tendons. It is assumed that the tendons that are connected at the cell center emerge from the central cell sides. The contour lines of the end caps are shown in Figure 11.6 for a membrane thickness $t = 1$ mm and a tendon stiffness of $EA = 0$ and 50 kN. Both, the membrane and tendons are made out of polyphenylsulfon so that the material properties and the underlying pressure load are

loading

$$p = 2.0 \text{ MPa} \quad \text{pressure}$$

material

$$\begin{aligned} E &= 2,340 \text{ MPa} && \text{Young's modulus} \\ \nu &= 0.4 && \text{Poisson's ratio} \\ \sigma_{\max} &= 50 \text{ MPa} && \text{yield strength.} \end{aligned}$$

It can be seen from the contour lines that the end cap geometries are improved with the help of uneven cell sides. The altitude z along each cell sides is described by a cubic polynomial with a point reflection symmetry

$$z = \begin{cases} 2\Delta z (\psi + 2(\psi - 1)(4\xi - 3)\xi) \xi & 0 \leq \xi \leq \frac{1}{2} \\ 2\Delta z (\psi - 2(\psi - 1)(4\xi - 1)(1 - \xi))(1 - \xi) & \frac{1}{2} < \xi \leq 1. \end{cases} \quad (11.17)$$

Herein, $\xi \in [0, 1]$ is the dimensionless coordinate along the cell side, Δz is the altitude at the cell side center ($\xi = 1/2$) and ψ is the gradient of the polynomial at $\xi = \{0, 0.5, 1\}$. It is subsequently assumed that $\Delta z = 15$ mm and that $\psi = 2$.

The smallest possible tendon stiffness EA , material volume V and deformation energy Π_n of an end cap as a function of the membrane thickness t are shown in Figure 11.7. The deformation energy is computed for the pentagonal state variables $\alpha = \pm 3/4^\circ$ such that the side

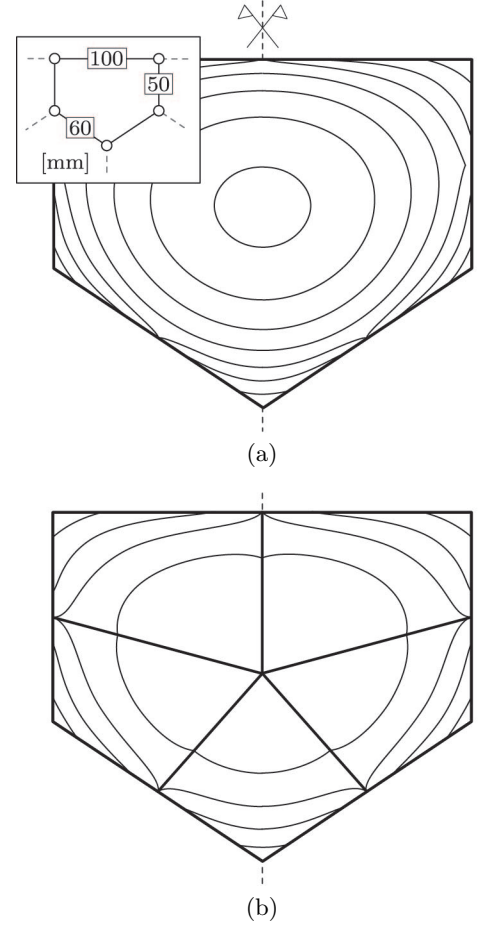


Figure 11.6: Contour lines of two end caps for a pentagonal cell that are based on minimal surfaces. The out of plane spacing of the contour lines is 5 mm. (a) End cap without and (b) with tendons that emerge from the cell side centers. The membrane thickness is, in both cases, $t = 1$ mm and the tendon stiffness is $EA = 50$ kN.

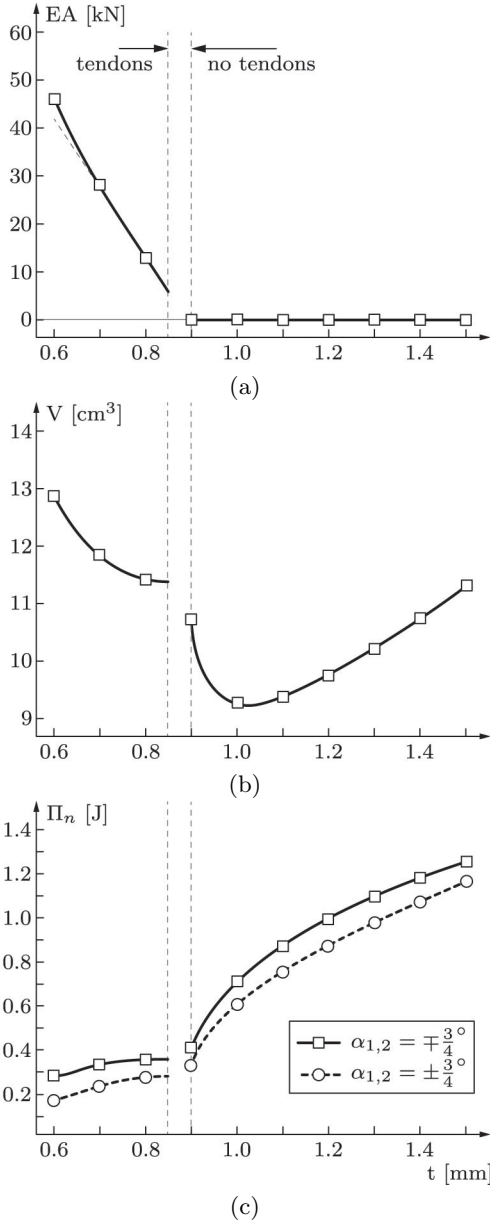


Figure 11.7: End cap properties as a function of the membrane thickness t . (a) Smallest possible tendon stiffness EA , (b) material volume V and (c) deformation energy Π_n for an angle α . The side lengths and reflection symmetry of deformed cells are preserved.

lengths and reflection symmetry of deformed cells are preserved. It can be seen that the smallest possible membrane thickness without tendons is about $t = 0.9$ mm. A further thickness reduction is only possible if local reinforcements are used. However, tendons are one-dimensional elements that can carry only uniaxial loads. As a consequence, the lightest possible end cap design does not possess any tendons and has a membrane thickness of about $t = 1$ mm. Although tendons increase the overall weight of an end cap, they can reduce the required deformation energy due to the higher curvature and smaller thickness of the membrane. Furthermore, their weight penalty can be avoided if local reinforcements are provided by a cytoskeleton that additionally supports the cell sides.

The influence of an end cap on a cells shape changing capabilities depends on the ratio between the end caps deformation energy and the variation of the cells pressure potential. The latter is

$$\Pi_p = \begin{cases} -14.4 \text{ J/m} & \text{for } \alpha_{1,2} = \pm 3/4^\circ \\ 5.8 \text{ J/m} & \text{for } \alpha_{1,2} = \mp 3/4^\circ \end{cases} \quad (11.18)$$

for a cell with a unit length and thus considerably larger than the energy needed to deform a well designed end cap. This is particularly remarkable as the undeformed cell geometry is already close to its maximum cross sectional area. As a consequence, the influence of well designed end caps on the simulation and optimization of pressure actuated cellular structures is negligible if cells are sufficiently long. In general it can be said that it is advantageous to use end cap materials with a large yield strength to stiffness ratio². The argument for this is as follows. The required membrane thickness of an end cap is proportional to

$$t \propto \frac{1}{\sigma_{\max}} = \frac{1}{\chi a E^b} \quad (11.19)$$

so that the additional energy density due to an unidirectional axial strain ε is

$$\Delta \Pi = \frac{1}{2} E t \varepsilon^2 \propto E^{1-b} = E^{0.27}. \quad (11.20)$$

Therefore, although only slightly, the energy required to deform an end cap increases with an increasing Young's modulus.

²For example, thermoplastic polyurethane (TPU) possesses a larger σ_{\max}/E ratio than titan.

Chapter 12

Conclusions

Commercial airplanes consist of a fuselage, wings, high lift devices, control surfaces and engines. These components are, as far as possible, independently developed and manufactured. They are incrementally improved within the limits of existing technologies until the required efforts outweigh the potential gains. Significant progress at this point can only be achieved by innovations that need to occur in one or more fields. Some of the most important innovations for the aerospace industry were made in material science. For example, great weight savings were achieved by the transition from wood to aluminium and the subsequent transition from aluminium to carbon fiber reinforced plastics. The latter occurred after the yield strength of newly developed aluminium alloys leveled off in the second half of the twentieth century as illustrated in Figure 12.1.

A myriad of similar innovation cycles within many fields led to highly optimized structures. It is therefore increasingly difficult to significantly improve the performance of airplanes by solely optimizing their components. On the other hand, the steadily increasing passenger numbers, oil prices and population densities around airports put a huge pressure on the airplane industry. Another aspect that adds to this pressure is the need for military airplanes with ever improving stealth properties. These opposing trends need to be countered by a shift towards an integrated development of airplane components. A complete fusion between wings and high lift devices seems to be particularly promising as they are a main source of noise emissions and radar reflections. Furthermore, they hinder the use of new technologies that improve the laminar flow around wings and thus the fuel consumption of airplanes.

Existing approaches towards gapless high lift devices lead to structures whose weight penalties and complexities are prohibitive. It is ironic that this is mostly due to their separate consideration of actuators, mechanisms and skins. In contrast, plants that can undergo large, rapid shape

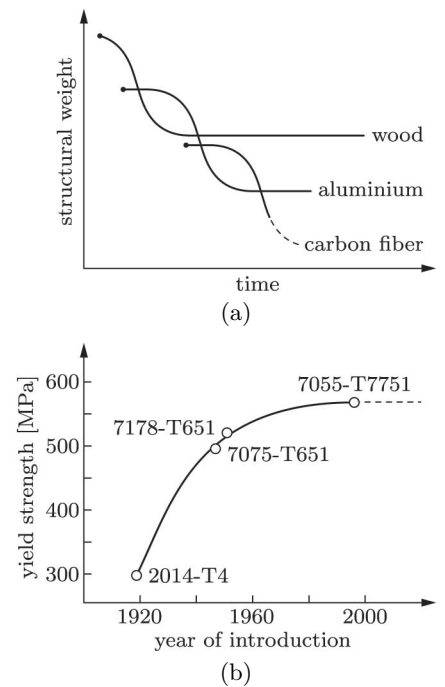


Figure 12.1: (a) Material based innovation cycles of airplane structures. (b) Maturation of aluminium alloys since the 1920s (data from [40]).

changes are highly integrated. It is virtually impossible to distinguish between their components. Nastic plants consist of a large number of three-dimensionally shaped cells with tailored geometries and material properties. Their overall shape and stiffness depends on the individual cell pressures that are varied through osmosis. The pressure induced biaxial tension forces are advantageous since they reduce potential instabilities due to external loads. This enables the use of relatively thin and flexible cell walls that, in return, minimize the deformation energy during shape changes. Another remarkable property of nastic plants is that they function without a central control system although they have to simultaneously control a large number of cell pressure.

Despite the attractive properties of nastic plants, the realization of bioinspired gapless high lift devices seemed to be elusive. It is believed by the author that some of these obstacles were overcome by the work in this thesis. It was shown that the cell geometries of pressure actuated cellular structures can be considerably simplified if their surfaces remain developable during shape changes¹. This enables the use of prismatic cells with tailored pentagonal or hexagonal geometries. A further simplification was achieved by the stacking of equally pressurized cell rows. A major problem that remained to be solved was the optimization of cell geometries for given target shapes, cell row pressures and material properties. This led to the development of a kinematic framework for compliant pressure actuated cellular structures that efficiently links their geometric and mechanical models. The optimisation itself is based on a second order approach that minimizes an arbitrary objective function and enforces the required target shapes with the help of Lagrange multipliers. An object-oriented design of the algorithm was implemented in Matlab together with a postprocessor that enables the direct use of rapid prototyping techniques. The outstanding properties of this approach were demonstrated by the optimization of various example structures with two and three cell rows. Different material properties, cell row pressures and target shapes were considered.

It was shown that compliant pressure actuated cellular structures can be made from a wide range of materials without significant performance degradations. Their shape changing capabilities and stiffness can be preserved if the use of increasingly stiff materials is compensated by decreasing cell sizes and increasing cell pressures. Particularly advantageous is the use of fiber reinforced composites whose material properties can be tailored to effectively carry the cell wall forces. Cytoskeletons that do not constrain the required shape changes can be used to support the cell walls that are exposed to differential pressures. This reduces their required thicknesses and thus the self-weight of pressure actuated cel-

¹The taper ratio of most wings is close to one so that their surfaces can be considered to be developable.

lular structures. The pressurization of prismatic cells requires hermetic seals at both ends. They can be realized as minimal surfaces that are reinforced by cytoskeletons. These end-caps possess an isotropic stress state in the undeformed configuration so that they are relatively thin and flexible. Despite their advantages, the integration of cytoskeletons and end-caps into compliant pressure actuated cellular structures is relatively complex. The use of hermetic, elastic tubes that are inserted into each cell instead is therefore often a good alternative particularly during prototyping.

Pressure actuated cellular structures with developable surfaces can be manufactured by using three-dimensional weaving or rapid prototyping techniques. Particularly the former seems to be promising since it leads, in conjunction with high strength fibers, to lightweight structures that can sustain large cell pressures while being flexible enough to undergo significant shape changes. In summary it can be said that the tight integration, shape changing capabilities, stiffness and simplicity of pressure actuated cellular structures is unique. Hence it seems likely that, in one way or another, they will find their way into future airplanes.

Nomenclature

Superscripts

$\tilde{\square}$	optimal value
\star	alternative value
eff	effective value
lin, nlin	linear, nonlinear
tar	target value
β, κ, u, v	derivatives with respect to global state variables
s	scaled
C	cell corner
G	geometric model
H	compliant hinge
M	mechanical model
P	pentagonal cell
S	cell side
T	triangular cell

Subscripts

min, max	minimum, maximum
0	reference configuration
σ, a, b, c, r	reference to stresses, cell sides, residuum
n, p	reference to bending (strain), pressure energy
q	pressure set

Numbers

n_κ	global state variables, cell corners
n_P	base pentagons
n_R	cell rows
n_T	triangular, hexagonal cells
n_s	cell sides at cell corner AND number of supports
n_u	global state variables
n_v	cell sides

Greek Letters

α	subtended angle of adaptive module AND global, local state variable
β	global state variable
γ, ω	internal angles
ε	strain
ψ	internal angle AND gradient
ζ, ξ	local coordinates
η	scaling factor
θ	cell corner angle
κ	fillet curvature
λ	global, local, dependent variable Lagrange multiplier
μ	ratio of width to central hinge thickness
ν	Poisson's ratio
ρ	stress reduction factor
σ	stress
v	variables for cell corner optimization
φ	bending angle of hinge
χ	stiffness parameter
Π	potential energy

Roman Letters

a, b, c	side lengths AND interpolation parameters
d	hinge eccentricity
e, h	set of design, state variables
f, g	force vector, gradient
i, j, k	integers
m, n	axial, rotational spring stiffness
p	cell row pressure
q	refinement level of cytoskeleton
r	residuum
s	central hinge thickness
t	cell side AND membrane thickness
u, v	global, local state variable
w	hinge width AND weight
x, y	internal lengths
z	internal length AND altitude
A	cross sectional area
B	Boolean matrix
C	constraint
E	Young's modulus
F	objective AND axial force
G	objective AND gradient

H	Hessian
K	stiffness matrix
L	arc length AND Lagrangian
M	bending moment
R, S	gradients
T	transformation matrix
V	volume
Z	constraint derivative

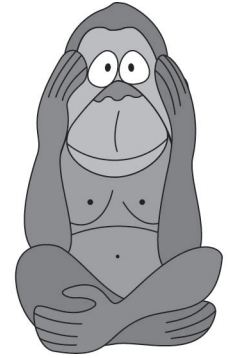
Appendix

This appendix serves three purposes. First, a thesis is probably the most boring and definitely an incomplete view of one's work life. Hence I could not resist to write a little bit about the journey that led to this point. This inevitably causes a slightly different, less scientific writing style which I hope will be forgiven. Second, it provides data that enables the verification of the load carrying capacity and shape changing capabilities of some pressure actuated cellular structures via simple hand calculations. Third, detailed information about the considered geometries of the passenger seat and the gapless high lift devices is provided. This data can be used to verify the presented results or serve as a basis for further investigations.

Distractions

The work on this thesis lasted far longer than I have initially anticipated. I first thought that it would take me about half a year to create a numerical tool for the efficient simulation and optimization of pressure actuated cellular structures. That was actually true for structures that consist of two cell rows, rigid cell sides and frictionless, centric hinges. However, I then started to extend the model towards compliant structures with an arbitrary number of cell rows, rigid cell corners, elastic cell sides and compliant hinges. This took me more than seven years during which I had a number of funny and well, less funny experiences that considerably slowed down the work on this thesis.

An article about a novel approach that tightly couples a structures geometric and mechanical model attracted my attention prior to this work. The presented results were intriguing so that I started to implement it myself. However, I just could not reproduce an important part of the results so that I threw away my complete code base after about half a year. Unfortunately, my simulation results were not affected by another, improved implementation of the algorithm. I annoyed the first author of the article until he admitted that it is common practice to



photoshop results if they don't fit one's expectations.

Early on in my career I had to supervise a PhD student who claimed to be smarter than Newton and Einstein. It is thus not particularly surprising that I was his third supervisor. The first one left the university and the other resigned from this duty. It took me some time to figure out that his revolutionary method solves the benchmark problems “numerically” by using the analytical solutions as ansatz functions. He was fully supported by the head of the institute so that he had five supervisors (of which three left) before he finally got his PhD.

Another PhD student that I had to supervise back home in Germany was funded by the military division of a large aerospace company. He told me in his first week that I should do the work and that he will take care of the marketing. He later published a part of my work under his name without even acknowledging it. This had no consequences for him and he received his PhD soon after. During that time I have been offered a new contract that would have allowed me to work from any place I want to. I refused. My last working day came and with it an e-mail that told me that I'm not allowed to take my remaining holidays and overtime. This was significant as I have collected the holidays of about two years during a three year period. Furthermore, my accumulated (unpaid) overtime was even more impressive. Anyhow, I had an excellent time watching the goodbye present that they gave to me. The first season of “The Walking Dead” is really classy.

A professor recently claimed in one of his books [267] that his co-worker coined the term “pressurized actuated cellular structures” in 2014. Disregarding the wrong grammar, a paper with the title “pressure actuated cellular structures” was published by me in 2012. I'm still trying to figure out how this works chronologically. The same guy actually wrote a research proposal about “pressure actuated cellular structures” that brought him quite a bit of money from a German research foundation. At least it was correctly written that time round. Congratulations.

Cantilever

At least one senior colleague was quite sceptical after I first came up with the idea of pressure actuated cellular structures. His scepticism grew as he could not verify the results of the tip loaded cantilever that was introduced in Chapter 7. This was worrying as he used commercial finite element packages during his lectures for postgraduate students. As a consequence, he assigned a master student to me who was supposed to prove me wrong. I supported his endeavors by providing nodal coordinates and axial cell side forces of the cantilever. This enabled a verification of the results with the help of simple hand calculations. The used node and cell side numbering is illustrated in Figure A1. The nodal coordinates of the equilibrium configurations for cell row pressures of either 0.4 or 2.0 MPa are summarized in Table A1 and the corresponding cell side forces are summarized in Table A2. In retrospective, I assume that his problems were due to the use of a tip load of 5 kN/mm instead of 5 kN/m. Well, units do matter and three orders of magnitude usually make a difference.

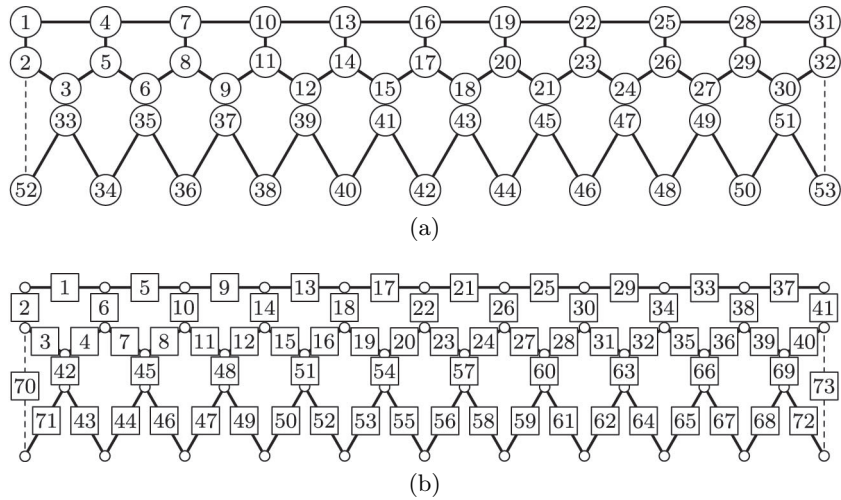


Figure A1: (a) Node and (b) cell side numbering of cantilever.

N	x_1 [mm]	y_1 [mm]	x_2 [mm]	y_2 [mm]
1	0	0	0	0
2	0	50.0000	0	50.0000
3	55.2935	73.2946	44.9419	89.7522
4	99.9717	2.3803	99.7155	7.5388
5	109.1154	46.7765	95.4444	57.3562
6	166.4943	64.3172	137.7908	99.8625
7	199.0197	16.1460	198.5391	22.8334
8	216.2532	30.7902	191.0712	72.2727
9	275.5689	39.8271	231.8457	116.2892
10	294.9835	44.2696	296.4087	43.3651
11	319.7106	0.8118	286.9084	92.4543
12	379.7027	1.7879	327.0753	137.0259
13	385.0069	87.8104	393.6093	66.8610
14	416.6285	49.0796	383.1809	115.7615
15	475.4671	60.8281	423.6836	160.0282
16	465.8645	146.6494	490.6004	91.2076
17	503.5866	113.8310	480.2891	140.1329
18	559.1272	136.5303	522.0143	183.2492
19	534.1871	219.6702	587.8749	114.3957
20	576.9816	193.8123	578.6864	163.5443
21	626.9387	227.0433	622.4210	204.6209
22	586.7487	304.7423	685.8386	134.4733
23	633.3788	286.6968	678.7550	183.9691
24	675.5251	329.4017	725.1370	222.0311
25	620.8486	398.7486	784.7016	149.5105
26	669.9165	389.1391	780.6846	199.3490
27	702.3229	439.6351	830.1427	233.3182
28	634.7420	497.7787	884.3763	157.5712
29	684.7360	496.9998	884.3378	207.5713
30	706.0260	553.0957	937.0112	236.3032
31	628.0109	597.5519	984.3722	156.6585
32	677.3280	605.7876	989.0510	206.4391
33	57.2529	113.2467	43.3326	129.7198
34	121.7017	189.7083	78.2896	223.4109
35	172.8900	103.8027	132.7541	139.5442
36	248.0438	169.7718	163.4523	234.7157
37	287.6632	77.9550	224.6643	155.6393
38	372.6743	130.6155	253.0009	251.5405
39	397.8790	33.8440	318.6826	176.1355
40	490.8541	70.6632	346.6743	272.1379
41	499.6303	28.9510	414.9356	199.0599
42	597.8391	10.1082	444.5336	294.5793
43	588.7928	109.6983	513.7245	222.3808
44	688.7908	110.3399	546.7814	316.7590
45	661.2429	206.4707	615.3785	243.9961
46	759.0693	227.2075	653.6184	336.3958
47	713.2453	316.0904	720.1230	261.7156
48	804.7591	356.4048	765.1069	351.0266
49	741.9552	434.2231	827.9739	273.2594
50	823.3175	492.3625	881.1414	357.9542
51	745.9406	555.7095	938.8169	276.2624
52	0	195.2352	0	219.8436
53	814.3314	628.6665	1002.8343	353.0854

Table A1: Nodal coordinates of the cantilever for a tip load of 5 kN/m and cell row pressures of either 0.4 or 2.0 MPa.

S	N_1	N_2	F_1 [kN/m]	F_2 [kN/m]	S	N_1	N_2	F_1 [kN/m]	F_2 [kN/m]
1	4	1	5.6967	101.1813	38	28	29	33.7915	204.0862
2	1	2	25.1299	97.0876	39	29	30	192.5062	133.5500
3	2	3	178.6629	92.2729	40	30	32	193.2165	131.7476
4	3	5	173.6615	90.7198	41	31	32	17.8448	98.2794
5	7	4	1.5200	95.6071	42	3	33	233.6901	33.7887
6	4	5	40.5616	192.2466	43	33	34	71.2196	10.0724
7	5	6	178.1628	96.3843	44	34	35	71.2196	10.0724
8	6	8	174.8691	95.1198	45	6	35	238.5784	35.8049
9	10	7	4.1023	89.7046	46	35	36	72.7398	10.5494
10	7	8	40.0964	195.0859	47	36	37	72.7398	10.5494
11	8	9	180.4924	100.7557	48	9	37	241.5641	37.3859
12	9	11	177.6238	99.5173	49	37	38	73.7565	10.9766
13	13	10	9.9525	83.6211	50	38	39	73.7565	10.9766
14	10	11	39.1389	197.4369	51	12	39	243.6188	38.8057
15	11	12	183.3486	105.1662	52	39	40	74.5794	11.3855
16	12	14	180.7461	103.9376	53	40	41	74.5794	11.3855
17	16	13	15.4578	77.3521	54	15	41	245.2704	40.1158
18	13	14	37.9728	199.3913	55	41	42	75.2853	11.7804
19	14	15	186.0857	109.6317	56	42	43	75.2853	11.7804
20	15	17	183.7634	108.4100	57	18	43	246.6331	41.3322
21	19	16	20.2787	70.8695	58	43	44	75.8726	12.1639
22	16	17	36.7531	200.9847	59	44	45	75.8726	12.1639
23	17	18	188.4157	114.1835	60	21	45	247.6905	42.4668
24	18	20	186.4534	112.9662	61	45	46	76.3101	12.5382
25	22	19	24.1811	64.1432	62	46	47	76.3101	12.5382
26	19	20	35.6046	202.2369	63	24	47	248.3767	43.5349
27	20	21	190.2044	118.8527	64	47	48	76.5516	12.9102
28	21	23	188.7079	117.6375	65	48	49	76.5516	12.9102
29	25	22	27.0161	57.1543	66	27	49	248.5886	44.5968
30	22	23	34.6538	203.1596	67	49	50	76.5321	13.3235
31	23	24	191.4190	123.6629	68	50	51	76.5321	13.3235
32	24	26	190.5010	122.4428	69	30	51	248.2835	45.8038
33	28	25	28.7356	49.9398	70	2	52	0	0
34	25	26	34.0214	203.7648	71	52	33	69.8304	9.6162
35	26	27	192.1228	128.6126	72	51	53	76.3720	13.7124
36	27	29	191.8973	127.3305	73	53	32	0	0
37	31	28	29.4297	42.7883					

Table A2: Cell side forces of the cantilever for a tip load of 5 kN/m and cell row pressures of either 0.4 or 2.0 MPa.

Applications

I thought hard about potential applications for pressure actuated cellular structures as I did not want to develop them primarily for airplanes. However, I think that I have failed in this regard as it seems inevitable that they will be first used in drones if they will be used at all. Anyhow, shape changing passenger seats could potentially benefit from pressure actuated cellular structures as many cars and trucks possess pneumatic

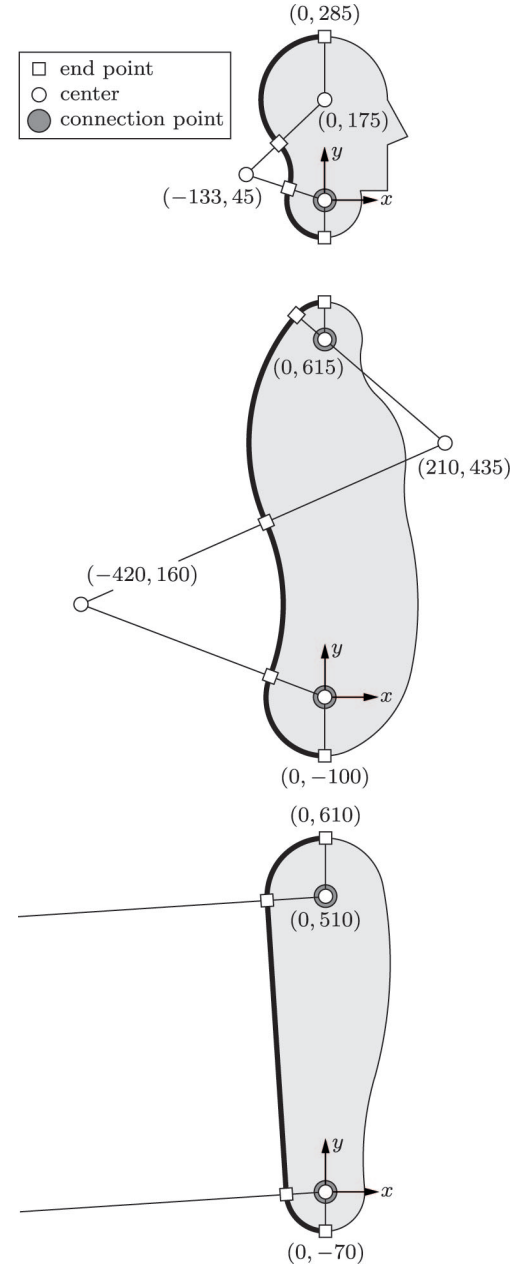


Figure A2: Coordinates of center, connection and end points of a two meter tall dummy. Center and end points define sequences of circular arcs that represent the boundaries of the head, torso and upper legs that are in contact with a seat.

systems. The target shapes for such a seat can be derived from a dummy with a rigid head, torso and extremities that are connected via hinges. The coordinates of the connection points and a description of the boundaries that are in contact with the seat is given in Figure A2 for a two meter tall dummy. The boundaries are described by C^1 continuous sequences of circular arcs² so that they are fully defined by the coordinates of their center and end points. The corresponding data for persons with different body sizes can be obtained by scaling. The considered seating postures for a forward, central and backward position are illustrated in Figure A3.

N	x [mm]	y [mm]	N	x [mm]	y [mm]	N	x [mm]	y [mm]
1	0	0	23	834.26	113.18	45	657.62	203.53
2	27.11	8.06	24	896.83	111.64	46	630.37	209.40
3	78.96	13.69	25	953.57	108.56	47	603.05	215.26
4	110.26	19.35	26	1003.82	104.50	48	575.52	221.11
5	141.37	25.02	27	1048.91	99.87	49	547.28	226.93
6	172.50	30.60	28	1090.23	94.89	50	518.30	232.72
7	203.38	36.37	29	1090.23	109.43	51	488.79	238.47
8	233.95	42.08	30	1060.82	115.19	52	458.76	244.20
9	264.58	47.77	31	1031.76	120.97	53	428.04	249.89
10	295.48	53.45	32	1003.11	126.76	54	396.53	255.54
11	326.65	59.12	33	974.87	132.58	55	364.29	261.14
12	358.04	64.78	34	947.01	138.42	56	331.30	266.71
13	389.73	70.41	35	919.54	144.28	57	297.46	272.22
14	421.98	76.02	36	892.51	150.15	58	262.70	277.68
15	455.23	81.57	37	865.90	156.05	59	226.95	283.06
16	490.02	87.02	38	839.69	161.96	60	190.22	288.39
17	526.84	92.33	39	813.87	167.89	61	152.45	293.64
18	566.29	97.46	40	788.21	173.83	62	113.55	298.81
19	609.27	102.29	41	762.90	179.78	63	73.44	303.88
20	656.78	106.67	42	736.98	185.70	64	32.04	308.85
21	710.06	110.32	43	715.17	190.44	65	0	312.48
22	770.05	112.69	44	682.42	197.91			

Table A3: Trailing edge coordinates for the cruise configuration.

However, existing passenger seats are inexpensive, lightweight and sufficiently comfortable so that it is unlikely that the integration of pressure actuated cellular structures would provide any noteworthy benefit. In contrast, shape changing airfoils would not only benefit from a reduced weight but also from a substantial improvement of aerodynamic and stealth properties. Optimal airfoil geometries for both high and low speed configurations were difficult to come by as most work focuses on gapless leading edges [149]. The cruise geometry of a trailing edge as used in this thesis is given by a number of discrete points whose coordinates are summarized in Table A3. The corresponding coordinates of a

²The approximation of the human body with circular arcs is by no means motivated by a potential discretization with shape changing modules.

leading edge for a high and low speed configuration are summarized in Table A4.

N	x_1 [mm]	y_1 [mm]	x_2 [mm]	y_2 [mm]	N	x_1 [mm]	y_1 [mm]	x_2 [mm]	y_2 [mm]
1	0	184.00	0	184.00	34	643.23	13.32	595.67	125.05
2	63.35	179.02	62.93	181.89	35	641.25	19.76	594.08	117.33
3	107.56	174.33	106.64	180.41	36	638.65	26.20	591.97	109.27
4	149.70	169.46	148.06	180.17	37	635.39	32.63	589.34	100.86
5	190.38	164.46	187.74	181.36	38	631.42	39.06	586.12	92.08
6	228.29	159.25	224.42	183.58	39	626.61	45.49	582.22	82.90
7	263.60	153.86	258.29	186.65	40	620.86	51.91	577.52	73.25
8	298.19	148.42	291.15	191.03	41	614.03	58.32	571.93	63.12
9	330.92	142.87	321.95	196.17	42	606.04	64.71	565.37	52.49
10	361.15	137.18	350.10	201.50	43	596.81	71.09	557.73	41.37
11	389.36	131.39	376.10	206.96	44	586.25	77.45	548.95	29.77
12	415.82	125.51	400.24	212.39	45	574.25	83.78	538.90	17.70
13	440.50	119.56	422.51	217.54	46	560.69	90.08	527.47	5.19
14	463.47	113.54	443.04	222.23	47	545.63	96.34	514.66	7.66
15	484.77	107.45	461.89	226.27	48	529.22	102.58	500.59	20.69
16	504.39	101.32	479.08	229.45	49	511.65	108.78	485.40	33.76
17	522.36	95.13	494.68	231.63	50	493.00	114.95	469.12	46.79
18	538.85	88.90	508.86	232.79	51	473.21	121.08	451.68	59.71
19	554.07	82.64	521.85	232.98	52	452.18	127.17	432.97	72.50
20	568.20	76.35	533.82	232.25	53	429.77	133.21	412.86	85.11
21	581.34	70.04	544.85	230.60	54	405.88	139.20	391.20	97.49
22	593.52	63.71	555.00	228.02	55	380.43	145.12	367.90	109.56
23	604.61	57.36	564.18	224.38	56	353.41	150.97	342.92	121.23
24	614.36	50.99	572.21	219.47	57	324.91	156.75	316.31	132.43
25	622.55	44.60	578.90	213.12	58	294.97	162.45	288.11	143.06
26	629.16	38.19	584.28	205.36	59	263.56	168.08	258.26	153.08
27	634.35	31.77	588.50	196.35	60	230.61	173.62	226.65	162.46
28	638.34	25.34	591.72	186.30	61	196.10	179.06	193.30	171.15
29	641.30	18.90	594.11	175.41	62	160.06	184.40	158.19	179.13
30	643.39	12.46	595.79	163.82	63	122.43	189.63	121.29	186.42
31	644.64	6.01	596.80	151.63	64	83.18	194.74	82.56	193.01
32	645.03	0	597.11	139.74	65	42.43	199.74	42.16	198.97
33	644.53	6.87	596.71	132.40	66	0	204.36	0	204.36

Table A4: Leading edge coordinates for the high and low speed configuration.

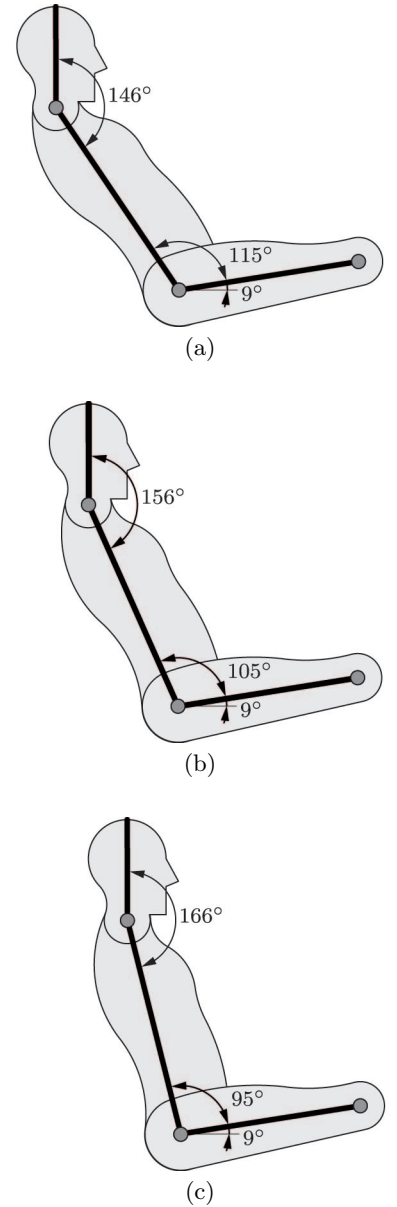


Figure A3: Seating postures of the dummy for the (a) backward, (b) central and (c) forward position.

Bibliography

- [1] N. Aage, E. Andreassen, B.S. Lazarov, and O. Sigmund. Giga-voxel computational morphogenesis for structural design. *Nature*, 550:84–86, 2017.
- [2] A. Airolidi, S. Fournier, E. Borlandelli, P. Bettini, and G. Sala. Design and manufacturing of skins based on composite corrugated laminates for morphing aerodynamic surfaces. *Smart Materials and Structures*, 26:1–22, 2017.
- [3] T. Akiyama and K. Shono. Controlled stepwise motion in polysilicon microstructures. *Journal of Microelectromechanical Systems*, 2:106–110, 1993.
- [4] K.L. Alderson, A. Alderson, G. Smart, V.R. Simkins, and P.J. Davies. Auxetic polypropylene fibres: Part 1 - manufacture and characterisation. *Plastics, Rubber and Composites*, 31:344–349, 2002.
- [5] H.G. Allen. *Analysis and Design of Structural Sandwich Panels*. Pergamon Press, Oxford, 1969.
- [6] D. Ambrosi, G.A. Ateshian, E.M. Arruda, S.C. Cowin, J. Dumas, A. Goriely, G.A. Holzapfel, J.D. Humphrey, R. Kemkemer, E. Kuhl, J.E. Olberding, L.A. Taber, and K. Garikipati. Perspectives on biological growth and remodeling. *Journal of the Mechanics and Physics of Solids*, 59:863–883, 2011.
- [7] A.-M. Ampère. *Théorie Mathématique des Phénomènes Électro-Dynamiques: Uniquement Déduite de l'Expérience*. Forgotten Books, London, 2017.
- [8] G.K. Ananthasuresh and S. Kota. Designing compliant mechanisms. *Mechanical Engineering*, 117:93–96, 1995.
- [9] M.F. Ashby. *Materials Selection in Mechanical Design*. Butterworth-Heinemann, Oxford, 2016.
- [10] T.S. Ashton. *Iron and Steel in the Industrial Revolution*. Augustus M. Kelley, New York, 1924.

- [11] H.S. Atamian, N.M. Creux, Brown E.A., A.G. Garner, B.K. Blackman, and S.I. Harmer. Circadian regulation of sunflower heliotropism, floral orientation, and pollinator visits. *Science*, 353:587–590, 2016.
- [12] J. Atulasimha and A.B. Flatau. A review of magnetostrictive iron-gallium alloys. *Smart Materials and Structures*, 20:1–15, 2011.
- [13] S. Babae, J. Shim, J.C. Weaver, E.R. Chen, N. Patel, and K. Bertoldi. 3-D soft metamaterials with negative Poisson’s ratio. *Advanced Materials*, 25:5044–5049, 2013.
- [14] E. Balaban, A. Saxena, P. Bansal, K.F. Goebel, P. Stoelting, and S. Curran. A diagnostic approach for electro-mechanical actuators in aerospace systems. In *Aerospace Conference*, Big Sky, MT, 2009.
- [15] P. Ball. Life’s lessons in design. *Nature*, 409:413–416, 2001.
- [16] R. Bannasch and L. Kniese. Flexible impact blade with drive device for a flexible impact blade. Patent US 8,323,062, 2007.
- [17] M. Barrett. *Survivability in the Digital Age: The Imperative for Stealth*. Mitchell Institute Press, Arlington, 2017.
- [18] C. Bartneck and E. Moltchanova. LEGO products have become more complex. *PLOS One*, 13:1–11, 2018.
- [19] R.H. Baughman. Conducting polymer artificial muscles. *Synthetic Metals*, 78:339–353, 1996.
- [20] R.H. Baughman, C. Cui, A.A. Zakhidov, Z. Iqbal, J.N. Barisci, G.M. Spinks, G.G. Wallace, A. Mazzoldi, D. De Rossi, A.G. Rinzler, O. Jaschinski, S. Roth, and M. Kertesz. Carbon nanotube actuators. *Science*, 284:1340–1344, 1999.
- [21] C.H. Beauchamp, L.M. Dean, and A.V. Raffa. Controllable camber fin. Patent US 5,367,970, 1993.
- [22] D.W. Bechert, M. Bruse, W. Hage, and R. Meyer. Fluid mechanics of biological surfaces and their technological application. *Naturwissenschaften*, 87:157–171, 2000.
- [23] H.C. Berg and R.A. Anderson. Bacteria swim by rotating their flagellar filaments. *Nature*, 245:380–382, 1973.
- [24] K. Bertoldi, P.M. Reis, S. Willshaw, and T. Mullin. Negative Poisson’s ratio behavior induced by an elastic instability. *Advanced Materials*, 22:361–366, 2010.

- [25] K.-U. Bletzinger and E. Ramm. A general finite element approach to the form finding of tensile structures by the updated reference strategy. *International Journal of Space Structures*, 14:131–145, 1999.
- [26] I. Boldea and S.A. Nasar. Linear electric actuators and generators. In *IEEE International Electric Machines and Drives Conference*, Milwaukee, WI, 1997.
- [27] B.A. Bolto, R. McNeill, and D.E. Weiss. Electronic conduction in polymers. III. *Australian Journal of Chemistry*, 16:1090–1103, 1963.
- [28] A.S. Borovik-Romanov. Piezomagnetism in the antiferromagnetic fluorides of cobalt and manganese. *Soviet Physics JETP*, 11:786–793, 1960.
- [29] M. Borrega, P. Ahvenainen, R. Serimaa, and L. Gibson. Composition and structure of balsa (*ochroma pyramidale*) wood. *Wood Science and Technology*, 49:403–420, 2015.
- [30] D. Bray. *Cell Movements*. Garland Science, New York, 2000.
- [31] L.C. Brinson. One-dimensional constitutive behavior of shape memory alloys: Thermomechanical derivation with non-constant material functions and redefined martensite internal variable. *Journal of Intelligent Material Systems and Structures*, 4:229–242, 1993.
- [32] A.H. Brown. Circumnutations: from Darwin to space flights. *Plant Physiology*, 101:345–348, 1993.
- [33] E.A. Bubert, B.K.S. Woods, K. Lee, C.S. Kothera, and N.M. Wereley. Design and fabrication of a passive 1D morphing aircraft skin. *Journal of Intelligent Material Systems and Structures*, 21:1699–1717, 2010.
- [34] W.J. Buehler, J.V. Gilfrich, and R.C. Wiley. Effect of low-temperature phase changes on the mechanical properties of alloys near composition TiNi. *Journal of Applied Physics*, 34:1475–1477, 1963.
- [35] M. Burrows and G. Sutton. Interacting gears synchronize propulsive leg movements in a jumping insect. *Science*, 341:1254–1256, 2013.
- [36] B.D. Caddock and K.E. Evans. Microporous materials with negative Poisson’s ratios. I. microstructure and mechanical properties. *Journal of Physics D: Applied Physics*, 22:1877–1882, 1989.

- [37] C. Calladine. *Theory Of Shell Structures*. Cambridge University Press, Cambridge, 1983.
- [38] L. Campanaro, N.J. Goldstone, and C.C. Shepherd. Rigidized evacuated structure. Patent 3,258,883, 1962.
- [39] L.F. Campanile and H. Hanselka. Aerodynamic structure, for a landing flap, an airfoil, an elevator unit or a rudder unit, with a changeable cambering. Patent US 6,010,098, 1997.
- [40] F.C. Campbell. *Manufacturing Technology for Aerospace Structural Materials*. Elsevier, Amsterdam, 2006.
- [41] D. Cao, X. Song, and M. Ahmadian. Editors' perspectives: road vehicle suspension design, dynamics, and control. *Vehicle System Dynamics*, 49:3–28, 2011.
- [42] F. Carpi, R. Kornbluh, P. Sommer-Larsen, and G. Alici. Electroactive polymer actuators as artificial muscles: are they ready for bioinspired applications? *Bioinspiration & Biomimetics*, 6, 2011.
- [43] C. Chary. Development and validation of a bird strike protection system for an enhanced adaptive droop nose. In P.C. Wöelcken and M. Papadopoulos, editors, *Smart Intelligent Aircraft Structures (SARISTU)*, pages 71–83. Springer, Cham, 2016.
- [44] A. Chaudhuri and N. Wereley. Compact hybrid electrohydraulic actuators using smart materials: A review. *Journal of Intelligent Material Systems and Structures*, 23:597–634, 2011.
- [45] J. Chen, H. Park, and K. Park. Synthesis of superporous hydrogels: Hydrogels with fast swelling and superabsorbent properties. *Journal of Biomedical Materials Research*, 44:53–62, 1999.
- [46] X. Chen, Y. Sun, and X. Gong. Design, manufacture, and experimental analysis of 3D honeycomb textile composites part I: Design and manufacture. *Textile Research Journal*, 78:771–781, 2008.
- [47] S.-J. Chiou and S. Kota. Automated conceptual design of mechanisms. *Mechanism and Machine Theory*, 34:467–495, 1999.
- [48] C.-P. Chou and B. Hannaford. Static and dynamic characteristics of McKibben pneumatic artificial muscles. In *IEEE International Conference on Robotics and Automation*, San Diego, CA, 1994.
- [49] R.R. Chutter. Pneumatic tubular construction. Patent 3,473,761, 1967.

- [50] A. Clausen, F. Wang, J.S. Jensen, O. Sigmund, and J.A. Lewis. Topology optimized architectures with programmable Poisson's ratio over large deformations. *Advanced Materials*, 27:5523–5527, 2015.
- [51] E.C. Cleary, R.A. Dolbeer, and S.E. Wright. Wildlife strikes to civil aircraft in the united states 1990-2005. Report of the Associate Administrator for Airports 12, 2006.
- [52] J.B. Cole. Variable camber airfoil. Patent US 3,941,334, 1975.
- [53] J.B. Cole. Variable-camber airfoil. Patent US 4,553,722, 1982.
- [54] N. Correll, C.D. Önal, H. Liang, E. Schoenfeld, and D. Rus. Soft autonomous materials - Using active elasticity and embedded distributed computation. In *International Symposium on Experimental Robotics*, New Delhi, 2010.
- [55] D.J. Cosgrove. Growth of the plant cell wall. *Nature Reviews Molecular Cell Biology*, 6:850–861, 2005.
- [56] R.A. Cowley, S.N. Gvasaliya, S.G. Lushnikov, B. Roessli, and G.M. Rotaru. Relaxing with relaxors: a review of relaxor ferroelectrics. *Advances in Physics*, 60:229–327, 2011.
- [57] J. Cui, Y.S. Chu, O.O. Famodu, Y. Furuya, J. Hattrick-Simpers, R.D. James, A. Ludwig, S. Thienhaus, M. Wuttig, Z. Zhang, and I. Takeuchi. Combinatorial search of thermoelastic shape-memory alloys with extremely small hysteresis width. *Nature Materials*, 5:286–290, 2006.
- [58] J. Curie and P. Curie. Phénomènes électriques des cristaux hémihédres à faces inclinées. *Journal de Physique Théorique et Appliquée*, 1:245–251, 1882.
- [59] F. Daerden and D. Lefeber. Pneumatic artificial muscles: actuators for robotics and automation. *European Journal of Mechanical and Environmental Engineering*, 47:10–21, 2002.
- [60] C. Dawson, J.F.V. Vincent, and A.-M. Rocca. How pine cones open. *Nature*, 390:668, 1997.
- [61] V.P. Dawson and M.D. Bowles. Taming liquid hydrogen: The centaur upper stage rocket 1958-2002. Report NASA-SP-2004-4230, NASA, 2004.
- [62] R. de Borst and E. Ramm. *Multiscale Methods in Computational Mechanics*. Springer, Dordrecht, 2010.
- [63] R.A.J. deBruyn, M. Paetkau, K.A. Ross, D.V. Godfrey, and C.R. Friedman. Thermogenesis-triggered seed dispersal in dwarf mistletoes. *Nature Communications*, 6:1–5, 2015.

- [64] R.D. Deegan. Finessing the fracture energy barrier in ballistic seed dispersal. *Proceedings of the National Academy of Sciences of the United States of America*, 109:5166–5169, 2012.
- [65] E. Denison and I. Stewart. *How to Read Bridges: A crash course spanning the centuries*. Bloomsbury Publishing, London, 2012.
- [66] J. Diamond. Transport mechanisms: The biology of the wheel. *Nature*, 302:572–573, 1983.
- [67] K. Dittrich. Cellular actuator device and methods of making and using same. Patent 7,055,782, EADS Deutschland GmbH, 2006.
- [68] Y. Duan and D.M. Ionel. A review of recent developments in electrical machine design optimization methods with a permanent-magnet synchronous motor benchmark study. *IEEE Transactions on Industry Applications*, 49:1268–1275, 2013.
- [69] J. Dumais and Y. Forterre. “Vegetable dynamics”: The role of water in plant movements. *Annual Review of Fluid Mechanics*, 44:453–478, 2012.
- [70] D. Eapen, M.L. Barroso, G. Ponce, M.E. Campos, and G.I. Cassab. Hydrotropism: root growth responses to water. *Trends in Plant Science*, 10:44–50, 2005.
- [71] J. Edwards, D. Whitaker, S. Klionsky, and M.J. Laskowski. A record-breaking pollen catapult. *Nature*, 435:164, 2005.
- [72] G. Eggeler, E. Hornbogen, A. Yawny, A. Heckmann, and M. Wagner. Structural and functional fatigue of NiTi shape memory alloys. *Materials Science and Engineering*, 378:24–33, 2004.
- [73] J.R. Ehleringer and O. Björkman. Pubescence and leaf spectral characteristics in a desert shrub, *Encelia farinosa*. *Oecologia*, 36:151–162, 1978.
- [74] T.P. Ehrhard. *Air Force UAVs*. Mitchell Institute Press, Arlington, 2010.
- [75] T. Eisner. Leaf folding in a sensitive plant: A defensive thorn-exposure mechanism? *Proceedings of the National Academy of Sciences of the United States of America*, 78:402–404, 1981.
- [76] R. Elbaum, L. Zaltzman, I. Burgert, and P. Fratzl. The role of wheat awns in the seed dispersal unit. *Science*, 316:884–886, 2007.
- [77] A.M. Ellison. Nutrient limitation and stoichiometry of carnivorous plants. *Plant Biology*, 8:740–747, 2006.

- [78] K.E. Evans and A. Alderson. Auxetic materials: Functional materials and structures from lateral thinking! *Advanced Materials*, 12:617–628, 2000.
- [79] K.E. Evans, J.P. Donoghue, and K.L. Alderson. The design, matching and manufacture of auxetic carbon fibre laminates. *Journal of Composite Materials*, 38:95–106, 2004.
- [80] E. Faran and D. Shilo. Ferromagnetic shape memory alloys - Challenges, applications, and experimental characterization. *Experimental Techniques*, 40:1005–1031, 2016.
- [81] A. Filippone. Data and performances of selected aircraft and rotorcraft. *Progress in Aerospace Sciences*, 36:629–654, 2000.
- [82] N.A. Fleck, V.S. Deshpande, and M.F. Ashby. Micro-architected materials: past, present and future. *Proceedings of the Royal Society A*, 466:2495–2516, 2010.
- [83] D.A. Fletcher and R. Dyche Mullins. Cell mechanics and the cytoskeleton. *Nature*, 463:485–492, 2010.
- [84] Y. Forterre, J.M. Skotheim, J. Dumais, and L. Mahadevan. How the venus flytrap snaps. *Nature*, 433:421–425, 2005.
- [85] P.J. Franks, T.N. Buckley, J.C. Shope, and K.A. Mott. Guard cell volume and pressure measured concurrently by confocal microscopy and the cell pressure probe. *Plant Physiology*, 125:1577–1584, 2001.
- [86] P. Fratzl and R. Weinkamer. Nature’s hierarchical materials. *Progress in Material Science*, 52:1263–1334, 2007.
- [87] J. Friml. Auxin transport - shaping the plant. *Current Opinion in Plant Biology*, 6:7–12, 2003.
- [88] S.C. Fry. *The growing plant cell wall: chemical and metabolic analysis*. Longman Group Limited, Harlow, 1988.
- [89] M. Gagliano, M. Renton, M. Depczynski, and S. Mancuso. Experience teaches plants to learn faster and forget slower in environments where it matters. *Oecologia*, 175:63–72, 2014.
- [90] M. Gagné and D. Therriault. Lightning strike protection of composites. *Progress in Aerospace Science*, 64:1–16, 2014.
- [91] L. Gaul, M. Kögl, and M. Wagner. *Boundary Element Methods for Engineers and Scientists*. Springer, Berlin, 2003.
- [92] C.F. Gauss. *General Investigations of Curved Surfaces*. The Princeton University Library, Princeton, 1902.

- [93] S. Geier, M. Kintscher, T. Mahrholz, P. Wierach, and H.-P. Monner. Experimental and finite element analyses of multifunctional skins for morphing wing applications. In *Sensors and Smart Structures Technologies for Civil, Mechanical, and Aerospace Systems*, pages 1–11, Las Vegas, NV, 2016. SPIE.
- [94] L.V. Gibiansky and S. Torquato. Thermal expansion of isotropic multiphase composites and polycrystals. *Journal of the Mechanics and Physics of Solids*, 45:1223–1252, 1997.
- [95] L.J. Gibson. The hierarchical structure and mechanics of plant materials. *Journal of the Royal Society Interface*, 9:2749–2766, 2012.
- [96] L.J. Gibson, M.F. Ashby, G.S. Schajer, and C.I. Robertson. The mechanics of two-dimensional cellular materials. *Proceedings of the Royal Society A*, 382:25–42, 1982.
- [97] L.J. Gibson, K.E. Easterling, and M.F. Ashby. The structure and mechanics of cork. *Proceedings of the Royal Society A*, 377:99–117, 1981.
- [98] R.H. Goddard. Aircraft construction. Patent 2,090,038, 1934.
- [99] M.R. Golabchi and S.D. Guest. Morphing multistable textured shells. In *Proceedings of the International Association for Shell and Spatial Structures*, Universidad Politecnica de Valencia, 2009.
- [100] J.P. Gong, Y. Katsuyama, T. Kurokawa, and Y. Osada. Double-network hydrogels with extremely high mechanical strength. *Advanced Materials*, 15:1155–1158, 2003.
- [101] Goodyear. Airmat materials investigation of one-place inflator-plane. Report GER 102070, Goodyear Aircraft Corporation, 1961.
- [102] Z. Goraj. An overview of the deicing and antiicing technologies with prospects for the future. In *International Congress of the Aeronautical Sciences*, Yokohama, Japan, 2004.
- [103] S.J. Gould. Kingdoms without wheels. *Natural History*, 90:42–48, 1983.
- [104] R. Grant. *The Radar Game*. Mitchell Institute Press, Arlington, 2010.
- [105] R.G. Grant. *Flight: The Complete History*. DK Publishing, London, 2007.
- [106] G.N. Greaves, A.L. Greer, R.S. Lakes, and T. Rouxel. Poisson’s ratio and modern materials. *Nature Materials*, 10:823–837, 2011.

- [107] K.E. Griffin, R.P. Guillot, and D.J. Siler. Rotary beam variable stiffness wing spar. Patent 6,000,660, 1998.
- [108] R.E. Grip, J.J. Brown, N.A. Harrison, B.K. Rawdon, and J.C. Vassberg. Morphing airfoil leading edge. Patent US 9,598,167, 2014.
- [109] Q. Guo, E. Dai, X. Han, S. Xie, E. Chao, and Z. Chen. Fast nastic motion of plants in bioinspired structures. *Journal of the Royal Society Interface*, 12, 2017.
- [110] O. Gutfleisch, M.A. Willard, E. Brück, C.H. Chen, S.G. Sankar, and J.P. Liu. Magnetic materials and devices for the 21st century: Stronger, lighter, and more energy efficient. *Advanced Materials*, 23:821–842, 2011.
- [111] C.S. Haines, N. Li, G.M. Spinks, A.E. Aliev, J. Di, and R.H. Baughman. New twist on artificial muscles. *Proceedings of the National Academy of Sciences of the United States of America*, 113:11709–11716, 2016.
- [112] C.S. Haines, M.D. Lima, N. Li, G.M. Spinks, J. Foroughi, J.D.W. Madden, S.H. Kim, S. Fang, M.J. de Andrade, F. Göktepe, Ö. Göktepe, S.M. Mirvakili, S. Naficy, X. Lepró, J. Oh, M.E. Kozlov, S.J. Kim, X. Xu, B.J. Swedlove, G.G. Wallace, and R.H. Baughman. Artificial muscles from fishing line and sewing thread. *Science*, 343:868–872, 2014.
- [113] T.C. Hales. The honeycomb conjecture. *Discrete & Computational Geometry*, 25:1–22, 2001.
- [114] K. Haraguchi and T. Takehisa. Nanocomposite hydrogels: A unique organic-inorganic network structure with extraordinary mechanical, optical, and swelling/de-swelling properties. *Advanced Materials*, 14:1120–1124, 2002.
- [115] M.J. Harrington, K. Razghandi, F. Ditsch, L. Guiducci, M. Rueggeberg, J.W.C. Dunlop, P. Fratzl, C. Neinhuis, and I. Burgert. Origami-like unfolding of hydro-actuated ice plant seed capsules. *Nature Communications*, 2:1–7, 2011.
- [116] R.G. Harris and F.B. Bradfield. Model experiments with variable camber wings. Report 677, Aeronautical Research Council London, 1920.
- [117] F.G. Hawksworth. Ballistics of dwarf mistletoe seeds. *Science*, 130:504, 1959.
- [118] M. Hayashi, K.L. Feilich, and D.J. Ellerby. The mechanics of explosive seed dispersal in orange jewelweed (*impatiens capensis*). *Journal of Experimental Botany*, 60:2045–2053, 2009.

- [119] A. Hedenström and L.C. Johansson. Bat flight: aerodynamics, kinematics and flight morphology. *The Journal of Experimental Biology*, 218:653–663, 2015.
- [120] S. Heimbs, J. Cichosz, M. Klaus, S. Kilchert, and A.F. Johnson. Sandwich structures with textile-reinforced composite fold-cores under impact loads. *Composite Structures*, 92:1485–1497, 2010.
- [121] Z. Hejnowicz and A. Sievers. Proton efflux from the outer layer of the peduncle of tulip in gravitropism and circumnutation. *Botanica Acta*, 108:7–13, 1995.
- [122] C.T. Herakovich. Composite laminates with negative through-the-thickness Poisson’s ratios. *Journal of Composite Materials*, 18:447–455, 1984.
- [123] A.S. Herrmann, P.C. Zahlen, and I. Zuardy. Sandwich structures technology in commercial aviation. In Thomsen O., Bozhevolnaya E., and Lyckegaard A., editors, *Sandwich Structures 7: Advancing with Sandwich Structures and Materials*, pages 13–26. Springer, Cham, 2005.
- [124] P.J. Hine, R.A. Duckett, and I.M. Ward. Negative Poisson’s ratios in angle-ply laminates. *Journal of Materials Science Letters*, 16:541–544, 1997.
- [125] R. Hooke. *Micrographia*. The Royal Society, London, 1665.
- [126] J.B. Hopkins and M.L. Culpepper. Synthesis of multi-degree of freedom, parallel flexure system concepts via freedom and constraint topology (fact) - Part I: Principles. *Precision Engineering*, 34:259–270, 2010.
- [127] L.J. Hornbeck. Deformable-mirror spatial light modulators. *SPIE Critical Reviews Series*, 1150:86–102, 1989.
- [128] W. Huang. On the selection of shape memory alloys for actuators. *Materials and Design*, 23:11–19, 2002.
- [129] J.E. Huber, N.A. Fleck, and M.F. Ashby. The selection of mechanical actuators based on performance indices. *Proceedings of the Royal Society A*, 453:2185–2205, 1997.
- [130] A. Hughes and B. Drury. *Electric Motors and Drives*. Elsevier, Amsterdam, 2013.
- [131] S. Inwood. *The Forgotten Genius: The Biography Of Robert Hooke 1635-1703*. MacAdam/Cage, San Francisco, 2005.

- [132] P.L. Jakab. Wood to metal: The structural origins of the modern airplane. *Journal of Aircraft*, 36:914–918, 1999.
- [133] J.M. Jani, M. Leary, A. Subic, and M.A. Gibson. A review of shape memory alloy research, applications and opportunities. *Materials and Design*, 56:1078–1113, 2014.
- [134] F. Javid, E. Smith-Roberge, M.C. Innes, A. Shanian, J.C. Weaver, and K. Bertoldi. Dimpled elastic sheets: a new class of non-porous negative Poisson’s ratio materials. *Scientific Reports*, 5:1–9, 2015.
- [135] D. Jenn. *Radar and Laser Cross Section Engineering*. AIAA, Reston, 2005.
- [136] B. Ji and J. Gao. Mechanical properties of nanostructure of biological materials. *Journal of the Mechanics and Physics of Solids*, 52:1963–1990, 2004.
- [137] W. Jo, R. Dittmer, M. Acosta, J. Zang, C. Groh, E. Sapper, K. Wang, and J. Rödel. Giant electric-field-induced strains in lead-free ceramics for actuator applications - status and perspective. *Journal of Electroceramics*, 29:71–93, 2012.
- [138] B.M. Jordan and J. Dumais. Biomechanics of plant cell growth. In *Encyclopedia of Life Sciences*, pages 1–8. Wiley, Chichester, 2010.
- [139] J.P. Joule. On the effects of magnetism upon the dimensions of iron and steel bars. *Philosophical Magazine and Journal of Science*, 30:76–87, 1847.
- [140] J.W. Judy. Microelectromechanical systems (MEMS): fabrication, design and applications. *Smart Materials and Structures*, 10:1115–1134, 2001.
- [141] H. Junkers. Abdeckung für Flugzeugtragflächen und dergleichen. Patent DE310040, 1915.
- [142] N. Kanzawa, Y. Hoshino, M. Chiba, D. Hoshino, H. Kobayashi, N. Kamasawa, Y. Kishi, M. Osumi, M. Sameshima, and T. Tsuchiya. Change in the actin cytoskeleton during seismonastic movement of *Mimosa pudica*. *Plant and Cell Physiology*, 47:531–539, 2006.
- [143] H. Kawai. The piezoelectricity of poly (vinylidene fluoride). *Japanese Journal of Applied Physics*, 8:975–976, 1969.
- [144] S. Kawamura, T. Yamamoto, D. Ishida, T. Ogata, Y. Nakayama, O. Tabata, and S. Sugiyama. Development of passive elements with variable mechanical impedance for wearable robots. In *IEEE Conference on Robotics & Automation*, Washington, DC, 2002.

- [145] A.L. Kay. *Junkers Aircraft and Engines, 1913-1945*. Naval Institute Press, Annapolis, 2004.
- [146] R.A. Khire, S. van Dessel, A. Messac, and A.A. Mullur. Study of a honeycomb-type rigidified inflatable structure for housing. *ASCE Journal of Structural Engineering*, 132:1664–1672, 2006.
- [147] O. Kim, H. Kim, U.H. Choi, and M.J. Park. One-volt-driven superfast polymer actuators based on single-ion conductors. *Nature Communications*, 7:1–8, 2016.
- [148] Y.-J. Kim, S. Cheng, S. Kim, and K. Iagnemma. Design of a tubular snake-like manipulator with stiffening capability by layer jamming. In *IEEE International Conference on Intelligent Robots and Systems*, Vilamoura, 2012.
- [149] M. Kintscher, J. Kirn, S. Storm, and F. Peter. Assessment of the SARISTU enhanced adaptive droop nose. In P.C. Wöelcken and M. Papadopoulos, editors, *Smart Intelligent Aircraft Structures (SARISTU)*, pages 113–140. Springer, Cham, 2016.
- [150] M. Kirschner and T. Mitchison. Beyond self-assembly: From microtubules to morphogenesis. *Cell*, 45:329–342, 1986.
- [151] T. Kobori, M. Takahashi, T. Nasu, N. Niwa, and K. Ogasawara. Seismic response controlled structure with active variable stiffness system. *Earthquake Engineering Structural Dynamics*, 22:925–941, 1993.
- [152] K. Koch, B. Bhushan, and W. Barthlott. Multifunctional surface structures of plants: An inspiration for biomimetics. *Progress in Material Science*, 54:137–178, 2009.
- [153] C. Körner and Y. Liebold-Ribeiro. A systematic approach to identify cellular auxetic materials. *Smart Materials and Structures*, 24:1–10, 2015.
- [154] D.J. Korteweg. Ueber die Veränderung der Form und des Volumens dielectricischer Körper unter Einwirkung electricischer Kräfte. *Annalen der Physik*, 245:48–61, 1880.
- [155] U. Kosidlo, M. Omastová, M. Micusík, G. Ćirić-Marjanović, H. Randriamahazaka, T. Wallmersperger, A. Aabloo, I. Kolaric, and T. Bauernhansl. Nanocarbon based ionic actuators - a review. *Smart Materials and Structures*, 22:1–30, 2013.
- [156] B. Kost and N.-H. Chua. The plant cytoskeleton: Vacuoles and cell walls make the difference. *Cell*, 108:9–12, 2002.
- [157] S. Kota. Twistable wings take flight. *IEEE Spectrum*, 53:28–33, 2016.

- [158] S. Kota and J.A. Hetrick. Adaptive compliant wing and rotor system. Patent US 2006/0186269, 2003.
- [159] J. Krauel. *Inflatable Art, Architecture & Design*. Links, Barcelona, 2013.
- [160] I.K. Kuder, A.F. Arrieta, W.E. Raither, and P. Ermanni. Variable stiffness material and structural concepts for morphing applications. *Progress in Aerospace Sciences*, 63:33–55, 2013.
- [161] M. LaBarbera. Why the wheels won’t go. *The American Naturalist*, 121:395–408, 1983.
- [162] G. Lachmann. Tragflügel für Flugzeuge mit hohem, vorn verdicktem Profil. Patent DE 347,884, 1922.
- [163] V.M. Levin. Thermal expansion coefficients of heterogeneous materials. *Mekhanika Tverdogo Tela*, 2:88–94, 1967.
- [164] T.-C. Lim. *Auxetic Materials and Structures*. Springer, Singapore, 2015.
- [165] M.D. Lima, N. Li, M.J. de Andrade, S. Fang, J. Oh, G.M. Spinks, M.E. Kozlov, C.S. Haines, D. Suh, J. Foroughi, S.J. Kim, Y. Chen, T. Ware, M.K. Shin, L.D. Machado, A.F. Fonseca, J.D.W. Madden, W.E. Voit, D.S. Galvão, and R.H. Baughman. Electrically, chemically, and photonically powered torsional and tensile actuation of hybrid carbon nanotube yarn muscles. *Science*, 338:928–932, 2012.
- [166] A.J. Liu and S.R. Nagel. Jamming is not just cool any more. *Nature*, 396:21–22, 1998.
- [167] C. Llorens, M. Argentina, N. Rojas, J. Westbrook, J. Dumais, and X. Noblin. The fern cavitation catapult: mechanism and design principles. *Journal of the Royal Society Interface*, 13:1–13, 2016.
- [168] F.E. Lloyd. *The Carnivorous Plants*. Chronica Botanica Company, Waltham, 1942.
- [169] N. Lobontiu. *Compliant Mechanisms: Design of Flexure Hinges*. CRC, Boca Raton, 2003.
- [170] L.N. López de lacalle, J. Pérez, J.I. Llorente, and J.A. Sánchez. Advanced cutting conditions for the milling of aeronautical alloys. *Journal of Materials Processing Technology*, 100:1–11, 2000.
- [171] M.A. Lorell and H.P. Levaux. *The Cutting Edge*. RAND, Santa Monica, 1998.
- [172] Varioplane Ltd. Tragfläche für Flugzeuge. Patent DE366693, 1915.

- [173] H.Y. Luo and E.W. Abel. A comparison of methods for the training of NiTi two-way shape memory alloy. *Smart Materials and Structures*, 16:2543–2549, 2007.
- [174] D.A. Lutes. Air-supported structures. Report CBD 137, National Research Council Canada, 1971.
- [175] J. Lv, H. Liu, and H.W. Zhang. A multiscale co-rotational method for geometrically nonlinear shape morphing of 2D fluid actuated cellular structures. *Mechanics of Materials*, 79:1–14, 2014.
- [176] D.G. Lyon. Variable shaped airfoil. Patent US 3,076,623, 1960.
- [177] B.J. Maclean, B.F. Carpenter, J.L. Draper, and M.S. Misra. A shape memory actuated compliant control surface. *Smart Structures and Intelligent Systems*, 1917:809–818, 1993.
- [178] A. Mamada, T. Tanaka, D. Kungwachakun, and M. Irie. Photoinduced phase transition of gels. *Macromolecules*, 23:1517–1519, 1990.
- [179] J.-C. Maré. *Aerospace Actuators: Signal-by-Wire and Power-by-Wire*. Wiley, Hoboken, 2017.
- [180] W. Martin, H.-F. Siegling, M. Kuhn, and N. Himmel. Load carrying structure having variable flexibility. Patent 6,182,929, 1998.
- [181] P. Martins, A.C. Lopes, and S. Lanceros-Mendez. Electroactive phases of poly(vinylidene fluoride): Determination, processing and applications. *Progress in Polymer Science*, 39:683–706, 2014.
- [182] K. Matsumoto, S. Nobuki, and T. Miyata. Thermo-responsive gels that absorb moisture and ooze water. *Nature Communications*, 9:1–7, 2018.
- [183] L. Matthews, V.B. Sundaresan, V. Giurgiutiu, and D.J. Leo. Bioenergetics and mechanical actuation analysis with membrane transport experiments for use in biomimetic nastic structures. *Journal of Materials Research*, 21:2058–2067, 2006.
- [184] K. Maute, M.L. Dunn, R. Bischel, M. Howard, and J.M. Pajot. Multiscale design of vascular plates. In *ASME International Mechanical Engineering Congress and Exposition*, Orlando, FL, 2005.
- [185] J.C. Maxwell. *The Electrical Researches Of The Honourable Henry Cavendish F.R.S.* Nabu Press, Charleston, 2010.
- [186] C.R. McClung. Plant circadian rhythms. *The Plant Cell*, 18:792–803, 2006.
- [187] G.P. McKnight and W. Barvosa-Carter. Variable stiffness structure. Patent 7,550,189, 2009.

- [188] G.A. Medrano-Cerda, C.J. Bowler, and D.G. Caldwell. Adaptive position control of antagonistic pneumatic muscle actuators. In *IEEE International Conference on Intelligent Robots and Systems*, Pittsburgh, PA, 1995.
- [189] P.W. Merlin. Design and development of the blackbird: Challenges and lessons learned. In *AIAA Aerospace Sciences Meeting*, Orlando, FL, 2009.
- [190] M. Miki and Y. Murotsu. The peculiar behavior of the Poisson's ratio of laminated fibrous composites. *JSME International Journal. Ser.1, Solid mechanics, strength of materials*, 32:67–72, 1989.
- [191] R. Miller and D. Sawers. *Technical Development of Modern Aviation*. Routledge & Kegan Paul PLC, Abingdon-on-Thames, 1968.
- [192] W. Miller, P.B. Hook, C.W. Smith, X. Wang, and K.E. Evans. The manufacture and characterisation of a novel, low modulus, negative Poisson's ratio composite. *Composite Science and Technology*, 69:651–655, 2009.
- [193] G.W. Milton. Composite materials with Poisson's ratios close to -1. *Journal of the Mechanics and Physics of Solids*, 40:1105–1137, 1992.
- [194] T. Mirfakhrai, J.D.W. Madden, and R.H. Baughman. Polymer artificial muscles. *Materials Today*, 10:30–38, 2007.
- [195] A. Miriyev, K. Stack, and H. Lipson. Soft material for soft actuators. *Nature Communications*, 8:1–8, 2017.
- [196] S. Miyata, M. Yoshikawa, S. Tasaka, and M. Ko. Piezoelectricity revealed in the copolymer of vinylidene cyanide and vinyl acetate. *Polymer Journal*, 12:857–860, 1980.
- [197] R. Morillon, D. Liénard, M.J. Chrispeels, and J.-P. Lassalles. Rapid movements of plants organs require solute-water cotransporters or contractile proteins. *Plant Physiology*, 127:720–723, 2001.
- [198] D. Müller. Lift body having a variable camber. Patent US 6,152,405, 1996.
- [199] M. Muller. A novel classification of planar four-bar linkages and its application to the mechanical analysis of animal systems. *Philosophical Transactions of the Royal Society B*, 351:689–720, 1996.
- [200] C. Neinhuis and W. Barthlott. Characterization and distribution of water-repellent, self-cleaning plant surfaces. *Annals of Botany*, 79:667–677, 1997.

- [201] Y. Nemirovsky, I. Zelniker, O. Degani, and G. Sarusi. A methodology and model for the pull-in parameters of magnetostatic actuators. *Journal of Microelectromechanical Systems*, 14:1253–1264, 2005.
- [202] D. Niarchos. Magnetic MEMS: key issues and some applications. *Sensors and Actuators A*, 109:166–173, 2003.
- [203] G.K. Nikas. Eighty years of research on hydraulic reciprocating seals: Review of tribological studies and related topics since the 1930s. *Proceedings of the Institution of Mechanical Engineers, Part J: Journal of Engineering Tribology*, 224:1–23, 2010.
- [204] M.A. Nkansah, K.E. Evans, and I.J. Hutchinson. Modelling the effects of negative Poisson’s ratios in continuous-fibre composites. *Journal of Materials Science*, 28:2687–2692, 1993.
- [205] R.K. Norris. Historical perspective on inflatable wing structures. In *AIAA Structures, Structural Dynamics, and Materials Conference*, Palm Springs, CA, 2009.
- [206] S. Ogden, L. Klintberg, G. Thornell, K. Hjort, and R. Bodén. Review on miniaturized paraffin phase change actuators, valves, and pumps. *Microfluidics and Nanofluidics*, 17:53–71, 2014.
- [207] K. Oguro, N. Fujiwara, K. Asaka, K. Onishi, and S. Sewa. Polymer electrolyte actuator with gold electrodes. *Smart Structures and Materials: Electroactive Polymer Actuators and Devices*, 3669:64–71, 1999.
- [208] A.G. Olabi and A. Grunwald. Design and application of magnetostrictive materials. *Materials & Design*, 29:469–483, 2008.
- [209] A. Ölander. An electrochemical investigation of solid cadmium-gold alloys. *Journal of the American Chemical Society*, 54:3819–3833, 1932.
- [210] K.R. Olympio and F. Gandhi. Zero- ν cellular honeycomb flexible skins for one-dimensional wing morphing. In *AIAA Structures, Structural Dynamics, and Materials Conference*, Honolulu, HI, 2007.
- [211] M. Pagitz. The future of scientific ballooning. *Philosophical Transactions of the Royal Society A*, 365:3003–3017, 2007.
- [212] M. Pagitz. Stability of lobed superpressure balloons during ascent. *Journal of Aircraft*, 48:2042–2049, 2011.
- [213] M. Pagitz and M. Abdalla. Simulation of tension fields with in-plane rotational degrees of freedom. *Computational Mechanics*, 46:747–757, 2010.

- [214] M. Pagitz and J. Bold. Shape-changing shell-like structures. *Bioinspiration & Biomimetics*, 8, 2013.
- [215] M. Pagitz, J. Bold, and C. Hühne. Formändernde Struktur. Patent DE 102,012,109,889, 2012.
- [216] M. Pagitz and J. Hol. A morphing structure and method for morphing a structure. Patent NL 2,006,936, 2012.
- [217] M. Pagitz and J. James. Symmetry transformation matrices for structures. *Proceedings of the Royal Society A*, 463:1563–1583, 2007.
- [218] M. Pagitz, E. Lamacchia, and J. Hol. Pressure-actuated cellular structures. *Bioinspiration & Biomimetics*, 7, 2012.
- [219] M. Pagitz and R.I. Leine. Continuum model for pressure actuated cellular structures. *arXiv*, 1403:4033v4, 2017.
- [220] M. Pagitz and R.I. Leine. Shape optimization of compliant pressure actuated cellular structures. *International Journal of Non-Linear Mechanics*, In Press, 2017.
- [221] M. Pagitz and J.M. Mirats-Tur. Finite element based form-finding algorithm for tensegrity structures. *International Journal of Solids and Structures*, 46:3235–3240, 2009.
- [222] M. Pagitz, M.H. Pagitz, and C. Hühne. A modular approach to adaptive structures. *Bioinspiration & Biomimetics*, 9, 2014.
- [223] M. Pagitz and S. Pellegrino. Buckling pressure of “pumpkin” balloons. *International Journal of Solids and Structures*, 44:6963–6986, 2007.
- [224] M. Pagitz and S. Pellegrino. Maximally stable lobed balloons. *International Journal of Solids and Structures*, 47:1496–1507, 2010.
- [225] S. Pamidighantam, R. Puers, and K. Baert. Pull-in voltage analysis of electrostatically actuated beam structures with fixed-fixed and fixed-free end conditions. *Journal of Micromechanics and Microengineering*, 12:458–464, 2002.
- [226] D.S. Parker and C.G. Hodge. The electric warship. *Power Engineering Journal*, 12:5–13, 1998.
- [227] A. Parr. *Hydraulics and Pneumatics*. Elsevier, Oxford, 2011.
- [228] J. Perez. Mechanism for at least regionally adjusting the curvature of airfoil wings. Patent US 6,644,599, 2000.

- [229] M. Peters, J. Kumpfert, C.H. Ward, and C. Leyens. Titanium alloys for aerospace applications. *Advanced Engineering Materials*, 5:419–427, 2003.
- [230] W.A. Petka, J.L. Harden, K.P. McGrath, D. Wirtz, and D.A. Tirrell. Reversible hydrogels from self-assembling artificial proteins. *Science*, 281:389–392, 1998.
- [231] L. Petrini and F. Migliavacca. Biomedical applications of shape memory alloys. *Journal of Metallurgy*, 2011:1–15, 2011.
- [232] K.L. Pickering, M.G. Aruan Efendy, and T.M. Le. A review of recent developments in natural fibre composites and their mechanical performance. *Composites: Part A*, 83:98–112, 2016.
- [233] M. Piening and H.P. Monner. Aerofoil profile with variable profile adaption. Patent US 6,164,599, 1997.
- [234] D.H. Plettenburg. Pneumatic actuators: a comparison of energy-to-mass ratio’s. In *International Conference on Rehabilitation Robotics*, Chicago, IL, 2005.
- [235] P. Polygerinos, S. Lyne, Z. Wang, L.F. Nicolini, B. Mosadegh, G.M. Whitesides, and C.J. Walsh. Towards a soft pneumatic glove for hand rehabilitation. In *International Conference on Intelligent Robots and Systems*, Tokyo, 2013.
- [236] S. Poppinga, N. Nestle, A. Šandor, B. Reible, T. Masselter, B. Bruchmann, and T. Speck. Hygroscopic motions of fossil conifer cones. *Scientific Reports*, 7:1–4, 2017.
- [237] H. Pottmann, M. Eigensatz, A. Vaxman, and J. Wallner. Architectural geometry. *Computers & Graphics*, 47:145–164, 2015.
- [238] D.R. Poulter. *The Design of Gas-Cooled Graphite-Moderated Reactors*. Oxford University Press, Oxford, 1963.
- [239] D. Prall and R.S. Lakes. Properties of a chiral honeycomb with a Poisson’s ratio of -1. *International Journal of Mechanical Sciences*, 39:305–314, 1997.
- [240] F. Previtali, A.F. Arrieta, and P. Ermanni. Performance of a three-dimensional morphing wing and comparison with a conventional wing. *AIAA Journal*, 52:2101–2113, 2014.
- [241] K.S. Ramadan, D. Sameoto, and S. Evoy. A review of piezoelectric polymers as functional materials for electromechanical transducers. *Smart Materials and Structures*, 23:1–26, 2014.
- [242] D. Reckzeh. Aerodynamic design of the high-lift-wing for a megaliner aircraft. *Aerospace Science and Technology*, 7:107–119, 2003.

- [243] F. Reuleaux. *The Kinematics of Machinery*. Macmillan and Co., London, 1876.
- [244] D.S. Richeson. *Euler's Gem: The Polyhedron Formula and the Birth of Topology*. Princeton University Press, Princeton, 2012.
- [245] J. Roncali. Conjugated poly(thiophenes): Synthesis, functionalization, and applications. *Chemical Reviews*, 92:711–738, 1992.
- [246] J.A. Rosero, J.A. Ortega, E. Aldabas, and L. Romeral. Moving towards a more electric aircraft. *IEEE Aerospace and Electronic Systems Magazine*, 8:175–191, 1961.
- [247] I.D. Rowland and T. Noble Howe. *Ten Books on Architecture*. Cambridge University Press, Cambridge, 2001.
- [248] P.K.C. Rudolph. *High-Lift Systems on Commercial Subsonic Airlines*. NASA, Moffett Field, 1996.
- [249] E.K. Sackmann, A.L. Fulton, and D.J. Beebe. The present and future role of microfluidics in biomedical research. *Nature*, 507:181–189, 2014.
- [250] A. Sakes, M. van der Wiel, P.W.J. Henselmans, J.L. van Leeuwen, D. Dodou, and Breedveld P. Shooting mechanisms in nature: A systematic review. *PLOS One*, 11:1–46, 2016.
- [251] J.K. Salisbury. Active stiffness of a manipulator in cartesian coordinates. In *IEEE Conference on Decision and Control*, Albuquerque, NM, 1980.
- [252] A.W. Sanders. Drone swarms. MSc thesis, United States Army Command and General Staff College, 2017.
- [253] H. Scherngell and A.C. Kneissl. Generation, development and degradation of the intrinsic two-way shape memory effect in different alloy systems. *Acta Materialia*, 50:327–341, 2002.
- [254] K. Schweizerhof and E. Ramm. Displacement dependent pressure loads in nonlinear finite element analyses. *Computers & Structures*, 18:1099–1114, 1984.
- [255] E. Seedhouse. *Bigelow Aerospace*. Springer, Berlin, 2014.
- [256] C. Semini, M. Baker, K. Laxman, V. Chandan, T. Maruthiram, R. Morgan, M. Frigerio, V. Barasuol, D.G. Caldwell, and G. Rey. A brief overview of a novel, highly-integrated hydraulic servo actuator with additive-manufactured titanium body. In *IEEE International Conference on Intelligent Robots and Systems*, Daejeon, 2016.

- [257] J.E. Shafizadeh, J.C. Seferis, E.F. Chesmar, and R. Geyer. Evaluation of the in-service performance behavior of honeycomb composite sandwich structures. *Journal of Materials Engineering and Performance*, 8:661–668, 1999.
- [258] M. Shahinpoor and K.J. Kim. Ionic polymer-metal composites: I. fundamentals. *Smart Materials and Structures*, 10:819–833, 2001.
- [259] Y. Shan, M. Philen, A. Lotfi, S. Li, C.E. Bakis, C.D. Rahn, and K.W. Wang. Variable stiffness structures utilizing fluidic flexible matrix composites. *Journal of Intelligent Material Systems and Structures*, 20:443–456, 2009.
- [260] H. Shirakawa, E.J. Louis, A.G. MacDiarmid, C.K. Chiang, and A.J. Heeger. Synthesis of electrically conducting organic polymers: Halogen derivatives of polyacetylene, (CH)_x. *Journal of the Chemical Society, Chemical Communications*, 0:578–580, 1977.
- [261] O. Sigmund. Materials with prescribed constitutive parameters: An inverse homogenization problem. *International Journal of Solids and Structures*, 31:2313–2329, 1994.
- [262] O. Sigmund. Tailoring materials with prescribed elastic properties. *Mechanics of Materials*, 20:351–368, 1995.
- [263] O. Sigmund. On the design of compliant mechanisms using topology optimization. *Mechanics of Structures and Machines*, 25:493–524, 1997.
- [264] O. Sigmund. Design of multiphysics actuators using topology optimization - Part I: One-material structures. *Computer methods in applied mechanics and engineering*, 190:6577–6604, 2001.
- [265] O. Sigmund. Design of multiphysics actuators using topology optimization - Part II: Two-material structures. *Computer methods in applied mechanics and engineering*, 190:6605–6627, 2001.
- [266] V.R. Simkins, A. Alderson, P.J. Davies, and K.L. Alderson. Single fibre pullout tests on auxetic polymeric fibres. *Journal of Materials Science*, 40:4355–4364, 2005.
- [267] J.M. Sinapius. *Adaptronik*. Springer, Berlin, 2018.
- [268] R. Slayton and G. Spinardi. Radical innovation in scaling up: Boeing’s dreamliner and the challenge of socio-technical transitions. *Technovation*, 47:47–58, 2016.
- [269] A.M.O. Smith. High-lift aerodynamics. *Journal of Aircraft*, 128:501–530, 1975.

- [270] G.D. Smith. *Numerical solution of partial differential equations*. Clarendon Press, Oxford, 1985.
- [271] J.W. Smith, W.P. Lock, and G.A. Payne. Variable-camber systems integration and operational performance of the AFTI/F-111 mission adaptive wing. Report 4370, NASA, 1992.
- [272] G.A. Smolenskii and A.I. Agranovskaya. Dielectric polarization and losses of some complex compounds. *Soviet Physics Technical Physics*, 3:1380–1389, 1958.
- [273] N.E. Stamp. Self-burial behaviour of *Erodium cicutarium* seeds. *Journal of Ecology*, 72:611–620, 1984.
- [274] E. Stanewsky. Adaptive wing and flow control technology. *Progress in Aerospace Sciences*, 37:583–667, 2001.
- [275] M. Stolarz. Circumnutation as a visible plant action and reaction. *Plant Signaling and Behavior*, 4:380–387, 2009.
- [276] D.R. Strong and T.S. Ray. Host tree location behavior of a tropical vine (*Monstera gigantea*) by skototropism. *Science*, 190:804–806, 1975.
- [277] C.G. Suits. Double-wall portable shelter. Patent 2,649,101, 1952.
- [278] J.A. Sumovski. Tubular structure filled with gaseous fluid. Patent 511,472, 1893.
- [279] H. Sun, Z. Xu, and C. Gao. Multifunctional, ultra-flyweight, synergistically assembled carbon aerogels. *Advanced Materials*, 25:2554–2560, 2013.
- [280] M.D. Swaine and T. Beer. Explosive seed dispersal in *Hura crepitans* L. (Euphorbiaceae). *New Phytologist*, 78:695–708, 1977.
- [281] A.A. Syed and M.K. Dinesan. Review: Polyaniline - a novel polymeric material. *Talanta*, 38:815–837, 1991.
- [282] O. Tabata, S. Konishi, P. Cusin, Y. Ito, F. Kawai, S. Hirai, and S. Kawamura. Micro fabricated tunable bending stiffness devices. *Sensors and Actuators A*, 89:119–123, 2001.
- [283] T. Tanaka. Collapse of gels and the critical endpoint. *Physical Review Letters*, 40:820–823, 1978.
- [284] T. Tanaka, I. Nishio, S.-T. Sun, and S. Ueno-Nishio. Collapse of gels in an electric field. *Science*, 218:467–469, 1982.
- [285] W.C. Tang, T.-C. H. Nguyen, M.W. Judy, and R.T. Howe. Electrostatic-comb drive of lateral polysilicon resonators. *Sensors and Actuators A*, 21:328–331, 1990.

- [286] E.D. Tate, M.O. Harpster, and P.J. Savagian. The electrification of the automobile: From conventional hybrid, to plug-in hybrids to extended-range electric vehicles. *SAE International Journal of Passenger Cars*, 1:156–166, 2009.
- [287] P.E. Taylor, G. Card, J. House, M.H. Dickinson, and R.C. Flagan. High-speed pollen release in the white mulberry tree, *Morus alba* L. *Sexual Plant Reproduction*, 19:19–24, 2006.
- [288] T.D.C. Thanh and K.K. Ahn. Nonlinear PID control to improve the control performance of 2 axes pneumatic artificial muscle manipulator using neural network. *Mechatronics*, 16:577–587, 2006.
- [289] C. Thill, J. Etches, I. Bond, K. Potter, and P. Weaver. Morphing skins. *The Aeronautical Journal*, 112:117–139, 2008.
- [290] C. Thill, J.A. Etches, I.P. Bond, K.D. Potter, and P.M. Weaver. Composite corrugated structures for morphing wing skin applications. *Smart Materials and Structures*, 19:1–10, 2010.
- [291] T.C.T. Ting and T. Chen. Poisson’s ratio for anisotropic elastic materials can have no bounds. *The Quarterly Journal of Mechanics & Applied Mathematics*, 58:73–82, 2005.
- [292] R. Tiwari, M.A. Meller, K.B. Wajcs, C. Moses, I. Reveles, and E. Garcia. Hydraulic artificial muscles. *Journal of Intelligent Material Systems and Structures*, 23:301–312, 2012.
- [293] G.E. Totten and V.J. De Negri. *Handbook of Hydraulic Fluid Technology*. CRC, Boca Raton, 2012.
- [294] S.W. Tsai and H.T. Hahn. *Introduction to Composite Materials*. Technomic Publishing, Lancaster, PA, 1980.
- [295] K. Uchino. *Piezoelectric Actuators and Ultrasonic Motors*. Kluwer, Boston, 1997.
- [296] S.C. Ugbolue, Y.K. Kim, S.B. Warner, Q. Fan, C.-L. Yang, and O. Kyzymchuk. Auxetic fabric structures and related fabrication methods. Patent US 8,772,187, 2007.
- [297] K. Ullakko. Magnetically controlled shape memory alloys: A new class of actuator materials. *Journal of Materials Engineering and Performance*, 5:405–409, 1996.
- [298] M. Vaezi, S. Chianrabutra, B. Mellor, and S. Yang. Multiple material additive manufacturing - Part 1: a review. *Virtual and Physical Prototyping*, 8:19–50, 2013.
- [299] D. van den Bossche. The A380 flight control electrohydrostatic actuators, achievements and lessons learnt. In *25th International Congress of the Aeronautical Sciences*, Hamburg, 2006.

- [300] X.M. van der Burgt. Explosive seed dispersal of the rainforest tree *Tetraberlinia moreliana* (Leguminosae - Caesalpinioideae) in gabon. *Journal of Tropical Ecology*, 13:145–151, 1997.
- [301] W.G. van Doorn and U. van Meeteren. Flower opening and closure: a review. *Journal of Experimental Botany*, 54:1801–1812, 2003.
- [302] J.L. van Leeuwen. Launched at 36,000 g. *Science*, 329:395–396, 2010.
- [303] S. Vasista and L. Tong. Design considerations of a pressure driven morphing wing structure. In *International Congress of the Aeronautical Sciences*, Brisbane, 2012.
- [304] K.C. Vaughn, A.J. Bowling, and K.J. Ruel. The mechanism for explosive seed dispersal in *Cardamine hirsuta* (Brassicaceae). *American Journal of Botany*, 98:1276–1285, 2011.
- [305] E. Venkatragavaraj, B. Satish, P.R. Vinod, and M.S. Vijaya. Piezoelectric properties of ferroelectric PZT-polymer composites. *Journal of Physics D: Applied Physics*, 34:487–492, 2001.
- [306] W. Voigt. *Lehrbuch der Kristallphysik*. Springer, Wiesbaden, 1966.
- [307] R. Vos. Mechanics and applications of pressure adaptive honeycomb. PhD thesis, University of Kansas, 2009.
- [308] P. Waide and C. Brunner. Energy-efficiency policy opportunities for electric motor-driven systems. Report, International Energy Agency, 2011.
- [309] K.J. Waldron, G.L. Kinzel, and S.K. Agrawal. *Kinematics, Dynamics, and Design of Machinery*. Wiley, Hoboken, 2016.
- [310] D. Weaire and R. Phelan. A counter-example to Kelvin’s conjecture on minimal surfaces. *Philosophical Magazine Letters*, 69:107–110, 1994.
- [311] U.G.K. Wegst, H. Bai, E. Saiz, A.P. Tomsia, and R.O. Ritchie. Bioinspired structural materials. *Nature Materials*, 14:23–36, 2015.
- [312] Z.G. Wei, R. Sandström, and S. Miyazaki. Shape-memory materials and hybrid composites for smart systems. *Journal of Materials Science*, 33:3743–3762, 1998.
- [313] D.L. Whitaker and J. Edwards. Sphagnum moss disperses spores with vortex rings. *Science*, 329:406, 2010.
- [314] D.L. Whitaker, L.A. Webster, and J. Edwards. The biomechanics of *Cornus canadensis* stamens are ideal for catapulting pollen vertically. *Functional Ecology*, 21:219–225, 2007.

- [315] O. Wichterle and D. Lim. Hydrophilic gels for biological use. *Nature*, 185:117–118, 1960.
- [316] E.P. Wohlfarth. *Handbook of Ferromagnetic Materials - Chapter 7*. North-Holland, Amsterdam, 1980.
- [317] O. Wright and J.M.H. Jacobs. Airplane. Patent 1,504,663, 1921.
- [318] H. Xu, Z.-Y. Cheng, D. Olson, T. Mai, and Q.M. Zhang. Ferroelectric and electromechanical properties of poly(vinylidene-fluoride-trifluoroethylene-chlorotrifluoroethylene) terpolymer. *Applied Physics Letters*, 78:2360–2362, 2001.
- [319] J.J. Yao, S.C. Arney, and N.C. MacDonald. Fabrication of high frequency two-dimensional nanoactuators for scanned probe devices. *Journal of Microelectromechanical Systems*, 1:14–22, 1992.
- [320] C.Y. Yap, C.K. Chua, Z.L. Dong, Z.H. Liu, D.Q. Zhang, and L.E. Loh. Review of selective laser melting: Materials and applications. *Applied Physics Reviews*, 2, 2015.
- [321] R. Yeh, S. Hollar, and K.S.J. Pister. Single mask, large force, and large displacement electrostatic linear inchworm motors. *Journal of Microelectromechanical Systems*, 11:330–336, 2002.
- [322] B.P.M. Yeung and P.W.Y. Chiu. Application of robotics in gastrointestinal endoscopy: A review. *World Journal of Gastroenterology*, 22:1811–1825, 2016.
- [323] T. Yokozeki, S. Takeda, T. Ogasawara, and T. Ishikawa. Mechanical properties of corrugated composites for candidate materials of flexible wing structures. *Composites: Part A*, 37:1578–1586, 2006.
- [324] N. Zarubova and V. Novák. Phase stability of CuAlMn shape memory alloys. *Materials Science and Engineering A*, 378:216–221, 2004.
- [325] S.-T. Zhang, A.B. Kounga, W. Jo, C. Jamin, K. Seifert, T. Granzow, J. Rödel, and D. Damjanovic. High-strain lead-free antiferroelectric electrostrictors. *Advanced Materials*, 21:4716–4720, 2009.
- [326] O.C. Zienkiewicz, R.L. Taylor, and D.D. Fox. *The Finite Element Method for Solid and Structural Mechanics*. Butterworth-Heinemann, Oxford, 2014.
- [327] H. Zimmer. Transverse force-connected body with variable profiling, particularly an airplane wing. Patent 4,252,287, 1979.

